



**UNIVERSIDAD NACIONAL AUTÓNOMA DE MÉXICO**  
PROGRAMA DE POSGRADO EN ASTROFÍSICA

**Centro de Radioastronomía y Astrofísica**

ESTUDIO QUÍMICO-DINÁMICO  
EN REGIONES DE FORMACIÓN ESTELAR MASIVA

TESIS  
PARA OPTAR POR EL GRADO DE:  
DOCTOR EN CIENCIAS (ASTROFÍSICA)

PRESENTA:  
JOSÉ VICENTE HERNÁNDEZ HERNÁNDEZ

TUTORES  
DR. STANLEY E. KURTZ SMITH  
CENTRO DE RADIOASTRONOMÍA Y ASTROFÍSICA, UNAM  
DR. LUIS A. ZAPATA GONZÁLEZ  
CENTRO DE RADIOASTRONOMÍA Y ASTROFÍSICA, UNAM

MEXICO, D.F. JUNIO 2014



Universidad Nacional  
Autónoma de México

Dirección General de Bibliotecas de la UNAM

**Biblioteca Central**



**UNAM – Dirección General de Bibliotecas**  
**Tesis Digitales**  
**Restricciones de uso**

**DERECHOS RESERVADOS ©**  
**PROHIBIDA SU REPRODUCCIÓN TOTAL O PARCIAL**

Todo el material contenido en esta tesis esta protegido por la Ley Federal del Derecho de Autor (LFDA) de los Estados Unidos Mexicanos (México).

El uso de imágenes, fragmentos de videos, y demás material que sea objeto de protección de los derechos de autor, será exclusivamente para fines educativos e informativos y deberá citar la fuente donde la obtuvo mencionando el autor o autores. Cualquier uso distinto como el lucro, reproducción, edición o modificación, será perseguido y sancionado por el respectivo titular de los Derechos de Autor.



# Abstract

## Chemical-Dynamical Study in Massive Star Forming Regions

The formation of massive stars ( $> 8 M_{\odot}$ ) in the Universe is one of the most important topics in contemporary astronomy. Massive star forming regions (MSFRs) influence dynamically the interstellar medium (ISM) and play an important role in the evolution of the entire galaxy through movement of gas and dust; HII regions, strong stellar winds and—in their final stages—supernovae events that push on the surrounding gas and promote the formation of new generation of stars. Massive stars are born deeply embedded in the gas and dust associated with giant molecular clouds, in clusters. Most of the Galactic MSFRs are far from the Sun ( $\gtrsim 5$  kpc), in turbulent environments, and have hundreds of magnitudes of visual extinction. MSFRs host a large number of molecular species that are useful to trace different phenomena such as outflows, accretion, rotation, and maser emission, and to estimate physical and chemical parameters. In an extragalactic context, MSFRs are the only star forming activities observable toward other galaxies.

Due to all these characteristics and to their relatively short lifetimes ( $< 10^6$  yr), the earliest phases of the high-mass stars are challenging objects to study.

Observational evidence suggests that massive stars begin their life within massive cores of gas associated with *infrared dark clouds* (IRDCs; Rathborne et al. 2007). These massive cores show high column densities ( $\sim 10^{23}$ – $10^{25}$  cm $^{-2}$ ) and low temperatures ( $< 25$  K). Observed with millimeter and submillimeter telescopes, these cores show strong dust continuum emission, revealing small sizes ( $< 1$  pc) and masses from  $\sim 10$  to  $\sim 1000 M_{\odot}$ . Finally, shocked gas, outflows and maser emission indicate that these massive cores are nurseries of massive stars.

Another phenomenon associated with the early stages of massive star formation is the so-called hot molecular core phase (HMCs; Kurtz et al. 2000; Cesaroni 2005). This phase is characterized by molecular gas condensations at relatively high temperatures ( $> 100$  K) and high densities ( $\sim 10^5$ – $10^8$  cm $^{-3}$ ), attributed to compact ( $< 0.1$  pc), luminous ( $> 10^4 L_{\odot}$ ), and massive ( $\sim 10$ – $1000 M_{\odot}$ ) molecular cores. HMCs show a forest of molecular lines, especially from organic species (e.g., Comito et al. 2005). Many of

---

these molecules probably were formed in gas-phase or on ice mantles of dust grains during a previous cold phase, while others were produced by gas-phase reactions after “parent species” were evaporated from the grains by the strong radiation of embedded or nearby protostars (e.g., [Herbst & van Dishoeck 2009](#)). HMCs are proposed as an intermediate stage between the massive cores in IRDCs and the ultracompact HII regions.

Despite their great importance, the early physical and chemical processes of MSFRs are still poorly understood. For example, the timescale of each evolutionary phase is unclear, as well as the chemical evolution of important molecular tracers during the MSFR lifetime.

In this doctoral thesis we study physical and chemical properties of massive cores in IRDCs and HMCs associated with MSFRs, in order to determine how some molecular species were formed and evolved. Also, we test the common assumption that HMCs are internally heated.

In a first project we study the 1.3 mm continuum emission and the CH<sub>3</sub>CN ( $12_K-11_K$ ) line emission of 17 HMCs with SubMillimeter Array (SMA) observations. The angular resolution of the observations ranges from 1''0 to 4''0. The continuum observations reveal large (>3500 AU) dusty structures with gas masses from 3 to 580 M<sub>⊙</sub>, that probably surround multiple young stars. The CH<sub>3</sub>CN line emission is detected toward all the molecular cores at least up to the  $K = 6$ -component and is mostly associated with the emission peaks of the dusty objects. We used the multiple  $K$ -components of CH<sub>3</sub>CN and both the rotational diagram method and a simultaneous synthetic local thermodynamic equilibrium model with the XCLASS program to estimate the temperatures and column densities of the cores. For all sources, we obtained reasonable fits from XCLASS by using a model that combines two components: an extended and warm envelope, and a compact hot core of molecular gas, suggesting internal heating by recently formed massive stars. The rotational temperatures lie in the range of 40-132 K and 122-485 K for the extended and compact components, respectively. From the continuum and CH<sub>3</sub>CN results, we infer fractional abundances for this molecule from  $10^{-9}$  to  $10^{-7}$  toward the compact inner components, that increase with the rotational temperature. Our results agree with a chemical scenario in which the CH<sub>3</sub>CN molecule is efficiently formed in the gas phase above 100-300 K,

---

and its abundance increases with temperature. These results have been published in Hernández-Hernández, V., et al. 2014, *The Astrophysical Journal*, 786, 38.

In a second project we study the molecular line emission of methanol ( $\text{CH}_3\text{OH}$ ) toward 12 MSFRs, at 247 GHz, using the APEX telescope with an angular resolution of  $25''$ . Eight of the regions are hot molecular cores while the other four regions are massive cores embedded in IRDCs. Most of the hot cores show a rich molecular line spectra, but the strength of different species and transitions varies from source to source. In contrast, the massive cores do not show significant molecular line emission. Multiple  $\text{CH}_3\text{OH}$  transitions are detected toward seven of the hot cores; one of these transitions has been proposed to be a Class II maser by radiative models (e.g., Sobolev et al. 1997; Cragg et al. 2005). We found that most of the detected  $\text{CH}_3\text{OH}$  lines are thermal in nature although maser emission may be present in some cases. Five sources, all of them hot cores, show sufficient transitions to use the rotation diagram method to estimate rotational temperatures and column densities. The temperatures lie in the range of 105-170 K and column densities from  $4 \times 10^{13}$  to  $2 \times 10^{14} \text{ cm}^{-2}$ . Using the average line parameters from  $\text{CH}_3\text{OH}$  we estimate virial masses from 700 to 6000  $M_\odot$ . We discuss possible scenarios to explain the chemical differences between hot cores and massive cores. This work is in preparation to be submitted to *The Astrophysical Journal*.

# Resumen

## Estudio Químico Dinámico en Regiones de Formación Estelar Masiva

La formación de estrellas masivas ( $>8 M_{\odot}$ ) en el Universo es uno de los más importantes tópicos en la astronomía contemporánea. Las regiones de formación de estrellas masivas (MSFRs, por sus siglas en inglés) influyen de manera dinámica el medio interestelar (ISM, por sus siglas en inglés) y juegan un rol importante en la evolución de toda la galaxia por medio de movimiento de gas y polvo; regiones HII, fuertes viento estelares y —en sus etapas finales— eventos de supernova que empujan sobre los alrededores de gas y promueven la formación de nuevas generaciones de estrellas. Las estrellas masivas nacen profundamente embebidas en el gas y polvo asociado con nubes gigantes de gas molecular, en cúmulos. La mayoría de las MSFRs galácticas se encuentran lejos del Sol ( $\gtrsim 5$  kpc), en ambientes turbulentos y tienen cientos de magnitudes de extinción visual. Las MSFRs albergan un gran número de especies moleculares que son útiles para trazar diferentes fenómenos como flujos, acreción, rotación y emisión maser, y para estimar parámetros físicos y químicos. En un contexto extragaláctico, las MSFRs son las únicas actividades de formación estelar que se observan en otras galaxias.

Debido a todas estas características y a sus relativamente cortos tiempos de vida ( $< 10^6$  años), las primeras fases de las estrellas de alta masa son objetos difíciles de estudiar.

La evidencia observacional sugiere que las estrellas masivas comienzan su vida dentro de núcleos masivos de gas asociado con *nubes oscuras infrarrojas* (IRDCs, por sus siglas en inglés; [Rathborne et al. 2007](#)). Estos núcleos masivos muestran altas densidades de columna ( $\sim 10^{23}$ – $10^{25}$  cm $^{-2}$ ) y bajas temperaturas ( $< 25$  K) observados con telescopios milimétricos y submilimétricos, estos núcleos muestran fuerte emisión en el continuo de polvo, tienen tamaños pequeños ( $< 1$  pc) y masas de 10 a 1000  $M_{\odot}$ . Finalmente, gas chocado, flujos y emisión maser indica que estos núcleos masivos son semilleros de estrellas masivas.

Otro fenómeno asociado con las primeras etapas de la formación de estrellas masivas es la fase llamada núcleo molecular caliente (HMCs, por sus siglas en idioma inglés; [Kurtz et al. 2000](#); [Cesaroni 2005](#)). Esta fase esta caracterizada por condensaciones

de gas molecular a relativamente altas temperaturas ( $>100$  K) y altas densidades ( $\sim 10^5\text{--}10^8$   $\text{cm}^{-3}$ ), atribuidas a núcleos moleculares compactos ( $< 0.1$  pc), luminosos ( $> 10^4 L_{\odot}$ ) y masivos ( $\sim 10\text{--}1000 M_{\odot}$ ). HMCs muestran una multitud de líneas moleculares, particularmente de especies orgánicas (e.g., [Comito et al. 2005](#)). Muchas de estas moléculas probablemente fueron formadas en una fase gaseosa o en mantos de hielo sobre los granos de polvo durante una fase fría previa, mientras que otras fueron producidas por reacciones en fase gas una vez que las “especies progenitoras” fueron evaporadas desde los granos por la fuerte radiación de las protoestrellas embebidas o cercanas (e.g., [Herbst & van Dishoeck 2009](#)). HMCs son propuestos como un estado intermedio entre los núcleos masivos en IRDCs y las regiones HII ultracompactas.

A pesar de su gran importancia, los procesos físicos y químicos tempranos de las MSFRs aún son poco entendidos. Por ejemplo, las escalas de tiempo de cada fase evolutiva no son claros, así como la evolución química de importantes trazadores moleculares a lo largo de la vida de las MSFRs.

En esta tesis doctoral se estudian las propiedades físicas y químicas de los núcleos masivos en IRDCs y HMCs asociados con MSFRs, con el fin de determinar cómo se formaron y evolucionaron algunas especies moleculares. Además, ponemos a prueba la presunción de que los HMCs son calentados internamente.

En un primer proyecto estudiamos la emisión del continuo a 1.3 mm y la emisión de línea de  $\text{CH}_3\text{CN}$  ( $12_K\text{--}11_K$ ) de 17 HMCs con observaciones del arreglo submilimétrico (SMA). La resolución angular de las observaciones va de  $1''.0$  a  $4''.0$ . Las observaciones del continuo revelan largas estructuras de polvo con masas en gas de 3 a  $580 M_{\odot}$ , que probablemente rodean varias estrellas jóvenes. La emisión de las líneas de  $\text{CH}_3\text{CN}$  es detectada hacia todos los núcleos moleculares al menos hasta la componente  $K=6$  y está mayormente asociada con el pico de emisión de los objetos polvosos. Usamos las múltiples componentes  $K$  del  $\text{CH}_3\text{CN}$  para estimar temperaturas y densidades de columna mediante los métodos de diagramas de rotación y modelos sintéticos en equilibrio termodinámico local con el programa XCLASS. Para todas las fuentes obtuvimos razonables ajustes con XCLASS usando un modelo que combina dos componentes: una envolvente extendida y tibia, y un núcleo compacto y caliente de gas molecular, sugiriendo calentamiento interno por estrellas masivas recién formadas. Las temperaturas



---

rotacionales están en el intervalo de 40-132 K y 122-485 K para las componentes extendida y compacta, respectivamente. De la emisión del continuo y del CH<sub>3</sub>CN inferimos abundancias fraccionales para esta molécula de 10<sup>-9</sup> a 10<sup>-7</sup> hacia las componentes compactas, que se incrementa con la temperatura rotacional. Nuestros resultados concuerdan con un escenario químico en el que la molécula de CH<sub>3</sub>CN es eficientemente formada en fase gaseosa por arriba de 100-300 K y su abundancia se incrementa con la temperatura. Estos resultados han sido publicados en Hernández-Hernández, V. et al. 2014, *The Astrophysical Journal*, 786, 38.

En un segundo proyecto estudiamos la emisión de línea molecular de metanol (CH<sub>3</sub>OH) hacia 12 MSFRs a 247 GHz usando el telescopio APEX con una resolución angular de 25''. Ocho de las regiones son HMCs mientras que el resto son núcleos masivos embebidos en IRDCs. La mayoría de los HMCs muestra un rico espectro abundante en líneas moleculares, pero la fuerza de las distintas especies varía de fuente a fuente. En contraste, los núcleos masivos no muestran emisión de línea significativa. Múltiples transiciones de CH<sub>3</sub>OH son detectadas hacia siete de los HMCs; una de esas transiciones ha sido propuesta para ser maser Clase II por modelos radiativos (e.g., Sobolev et al. 1997; Cragg et al. 2005). Encontramos que la mayoría de las líneas de CH<sub>3</sub>OH detectadas son de naturaleza térmica aunque emisión maser podría estar presente en algunos casos. Cinco fuentes, todas ellas HMCs, muestran suficientes transiciones para usar el método de diagramas de rotación para estimar temperaturas rotacionales y densidades de columna. Las temperaturas están en el rango de 105-170 K y las densidades de columna de  $4 \times 10^{13}$  a  $2 \times 10^{14}$  cm<sup>-2</sup>. Usando los parámetros promedio de las líneas de CH<sub>3</sub>OH estimamos masas viriales de 700 a 6000  $M_{\odot}$ . Discutimos escenarios posibles para explicar las diferencias químicas entre los HMCs y los núcleos masivos. Este trabajo está en preparación para ser enviado a *The Astrophysical Journal*.

# *Agradecimientos*

Quiero agradecer en primer lugar a Stan por todo su apoyo, sus conocimientos, tiempo y paciencia puestos en el desarrollo de esta tesis y los artículos que la componen. A Luis Zapata por compartir sus conocimientos y proponerme el proyecto con las observaciones del SMA. A Guido por su apoyo, hospitalidad y gran ayuda durante mi estancia en Chile.

A todas las personas que durante este tiempo han pertenecido al CRyA y de las cuales tengo valiosos recuerdos. A Roberto, Charly, Jesús, Gaby, Alvaro y Karla por su amistad *pragmática*, su ayuda *incondicional* y los grandes momentos que vivimos juntos.

A los amigos que hice, compañeros e investigadores. A Rosy, Ramiro, Sergio, Manuel y Yetli. A Javier, Laurent, Rosa, Luis Felipe, Stan, Susana, Adriana y Luis Zapata. A Karin por hacer nuestra vida más fácil, por su paciencia y el gran trabajo en CRyA. A todos muchas gracias.

De manera especial, siempre estaré agradecido y me sentiré profundamente afortunado por haber conocido a Yolanda y Paola. Ambas dejaron un recuerdo imborrable en todos los que convivimos con ellas.

A los Álamo, mi segunda familia, por su alegría, entusiasmo y comprensión. A Don Jorge, a Claudia, Luis y Jorge, y sus respectivas familias. A Lupita por su ánimo y vigor constantes.

A mis padres por su ejemplo en todo momento, por la educación que me dieron, por los valores que me transmitieron y la fuerza con que mantuvieron a la mejor de las familias. Ellos son los pilares eternos de ese hogar maravilloso. A Eli y Mónica por su incondicional compañía y total apoyo. A Ramiro y Cesar, gracias.

Finalmente, gracias a Karla, mi pequeña, por dejarme llegar a su vida y permitirme ser el hombre más feliz. Por su paciencia conmigo, su grandeza ante los retos y su carácter con la vida. Gracias por dejarme encontrarte, gracias por dejarme buscarte. Mi lugar es y seguirá siendo donde estés tú (y Beka).

*Que Ramirin, Eli y Violeta  
tengan el mejor de los futuros  
(¡las cosas que ellos verán!).*

# Contents

<b>Abstract</b>	<b>i</b>
<b>Resumen</b>	<b>iv</b>
<b>Agradecimientos</b>	<b>vii</b>
<b>1 A General Perspective of Star Formation</b>	<b>1</b>
1.1 High-mass <i>vs</i> low-mass Star Formation . . . . .	2
1.2 The Study of Massive Star Forming Regions . . . . .	6
1.2.1 UC HII regions . . . . .	6
1.2.2 Hot Molecular Cores . . . . .	8
1.2.3 Massive Cores in Infrared Dark Clouds . . . . .	11
1.2.4 This thesis . . . . .	14
<b>2 Hot Molecular Cores</b>	<b>16</b>
2.1 The number and lifetime of HMCs . . . . .	21
2.2 Dust Emission . . . . .	28
2.3 Molecules and Chemistry . . . . .	32
2.3.1 Chemical reactions . . . . .	34
2.3.2 Chemical Evolution in MSFRs . . . . .	36
2.3.3 Molecules in this thesis . . . . .	40
2.4 Dynamics . . . . .	42
<b>3 Spectral Lines As Tracers</b>	<b>46</b>
3.1 CH <sub>3</sub> OH Molecular Emission . . . . .	48
3.1.1 CH <sub>3</sub> OH Masers . . . . .	48
3.2 CH <sub>3</sub> CN Molecular Emission . . . . .	51
3.3 Estimation of Physical Conditions Through Molecular Transitions . . . . .	53
3.3.1 Rotation Diagram Method . . . . .	53
3.3.2 Modelling Emission . . . . .	56

---

<b>4</b>	<b>SMA millimeter observations of Hot Molecular Cores</b>	<b>59</b>
4.1	Introduction . . . . .	59
4.2	Observations and Data Reduction . . . . .	61
4.3	Results and Analysis . . . . .	65
4.3.1	Millimeter continuum data . . . . .	65
4.3.2	Molecular line emission . . . . .	79
4.3.3	Temperature and density of the CH <sub>3</sub> CN gas . . . . .	84
4.3.4	Virial masses and velocity gradients . . . . .	90
4.4	Comments on Individual Sources . . . . .	91
4.4.1	W3OH . . . . .	91
4.4.2	W3TW . . . . .	93
4.4.3	I16547 . . . . .	93
4.4.4	I17233 . . . . .	96
4.4.5	G5.89 . . . . .	97
4.4.6	G8.68 . . . . .	97
4.4.7	G10.47 . . . . .	100
4.4.8	G10.62 . . . . .	100
4.4.9	I18182 . . . . .	103
4.4.10	G23.01 . . . . .	103
4.4.11	G28.20N . . . . .	104
4.4.12	G31.41 . . . . .	104
4.4.13	I18566 . . . . .	105
4.4.14	G45.07 . . . . .	105
4.4.15	G45.47 . . . . .	106
4.4.16	W51e2 . . . . .	106
4.4.17	W51e8 . . . . .	107
4.5	Discussion . . . . .	108
4.5.1	Mass and density from 1.3 mm continuum . . . . .	108
4.5.2	Spatial distribution with respect to the CH <sub>3</sub> CN . . . . .	109
4.5.3	Temperature, density, and virial mass . . . . .	109
4.5.4	Fractional Abundances . . . . .	112
4.5.5	HMC and UCHII regions . . . . .	114
<b>5</b>	<b>APEX observations of CH<sub>3</sub>OH emission toward MSFRs</b>	<b>116</b>
5.1	Introduction . . . . .	116
5.2	Observations and Data Reduction . . . . .	118
5.3	Results and Discussion . . . . .	121
5.3.1	Detection of molecular line emission . . . . .	121
5.3.2	Rotation diagram analysis . . . . .	128
5.3.3	Detection of CH <sub>3</sub> OH toward our sample . . . . .	133
5.3.4	Nature of the CH <sub>3</sub> OH emission . . . . .	135

---

5.3.5	Virial Masses . . . . .	136
<b>6</b>	<b>Conclusions</b>	<b>137</b>
6.1	SMA observations of Hot Molecular Cores . . . . .	137
6.2	APEX observations of CH <sub>3</sub> OH . . . . .	138
	<b>Bibliography</b>	<b>140</b>

# Chapter 1

## A General Perspective of Star Formation

The formation of massive stars ( $> 8M_{\odot}$ ) in the Universe is one of the most important topics in contemporary astronomy; hence the study of the massive star forming regions (MSFRs) plays a major role in astrophysics. Young massive stars influence dynamically the interstellar medium, promoting the movement of material, mixing the gas and the dust, and pushing the gas to form new, mainly low-mass stars. Furthermore, MSFRs develop a diversity of chemical conditions in regions of ionized, atomic and molecular gas. The interaction of the stellar radiation field, and sometimes shock fronts, with the ubiquitous dust of the interstellar medium (ISM) plays an important role in this chemical diversity. Clouds and cores of gas surrounding young massive protostars show one of the richest and most complex organic chemistries in the Universe, comparable, for example, to comets in the Solar System. Life as we know it today is probably linked to the early astrochemistry phenomena in MSFRs. In an extragalactic context, MSFRs are the only star forming activities observable toward other galaxies.

Despite their importance, the early chemical and dynamical processes in MSFRs are still poorly understood; and unlike low-mass stars, whose formation process is well established (see next Section), a clear evolutionary sequence has not yet emerged for massive stars.

The present work has the goal of contributing to the answer of *how massive stars form?*, using millimetric observations of the continuum and molecular line emission toward MSFRs in different evolutionary stages. Our specific goal is to search for observational evidence for a connection between the chemical abundances of some molecular species and the physical parameters and evolution of MSFRs.

In the next Section, I present a brief overview of MSFRs, their initial conditions and the molecular and ionized gas found toward these regions.

## 1.1 High-mass *vs* low-mass Star Formation

Both low-mass and high-mass stars begin their lives as contracting clouds of gas and dust. However, these clouds in MSFRs are much more massive ( $\sim 100\text{-}1000 M_{\odot}$ ), denser ( $\sim 10^5\text{-}10^6 \text{ cm}^{-3}$ ), show much more turbulence and a wider range of temperatures — from some tens of Kelvin (K) in starless-cores to some hundreds of K in hot cores. Another difference is that for low-mass and intermediate-mass stars the timescales of the various formation stages are well known —not so for high-mass stars.

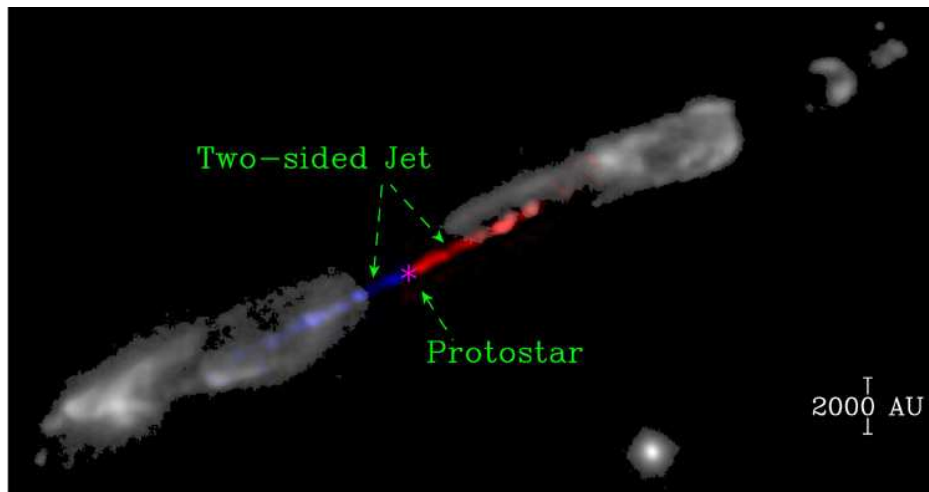


FIG. 1.1: Image of the Herbig-Haro 211 object showing submm data from the Submillimeter Array (blue and red) and near-infrared data from the European Very Large Telescope (gray scale). The SMA data were color-coded blue for approaching (blue-shifted) material and red for receding (red-shifted) material. The VLT reveals shocked molecular hydrogen emission produced by the jet. Figure from <http://www.cfa.harvard.edu> SMA/Chin-Fei Lee & VLT/Naomi Hirano.



The current model of low-mass star formation, summarized by [Shu et al. \(1987\)](#), begins with molecular clouds, identified as Bok globules (see [Table 1.1](#); [Bok & Reilly 1947](#); [Lada 1999](#)), in which some portions become gravitationally unstable, forming fragments or cores with masses of the order of the Jeans-mass that collapse by their own gravity. This collapse typically results in one or two central protostars and a flattened accretion disk. These protostellar cores have low temperatures ( $\sim 10$  K), compact sizes ( $\sim 0.05$  pc), low masses ( $0.5$ - $5 M_{\odot}$ ) and high densities ( $\sim 10^4$ - $10^5 \text{ cm}^{-3}$ ) (see [Table 1.1](#)). As the protostar is formed, it transfers linear and angular momentum and mechanical energy to its surroundings and forms a bipolar jet that moves molecular gas from the circum-protostellar environment creating molecular outflows. Herbig-Haro objects are an indirect manifestation of these jets (see [Figure 1.1](#)). After the reservoir of molecular gas disperses, the young star becomes optically visible in the pre-main-sequence — a phase called T Tauri. Finally, once the CNO cycle dominates, the star reaches the Zero Age Main Sequence. A picture of the main stages of low-mass star formation is shown in [Figure 1.2](#).

An analogous model for massive stars is more challenging to develop because massive stars are born deeply embedded in massive clumps (see [Table 1.1](#)) associated with the giant molecular clouds, in clusters of other stars, and at large distances from the Sun ( $\sim 5$  kpc). Paraphrasing [Kurtz et al. \(2000\)](#) “O stars do not form as single [nearby] spies but in [faraway] battalions”. Also, massive stars have relatively short lifetimes (a few  $10^6$  yr). Moreover, in the formation of a massive star, there is only a short time, on the order of  $10^4$  yr, before a contracting massive protostar begins core hydrogen burning and the stellar radiation becomes significant.

The timescale for collapse of the parent molecular gas is given by the *free-fall* time

$$t_{\text{ff}} = \left( \frac{3\pi}{32G\rho} \right)^{0.5} = 3.4 \times 10^7 n^{-0.5} \text{ yr}, \quad (1.1)$$

where  $\rho$  is the average mass density,  $n$  is the number density, and  $G$  is the gravitational constant. For example, toward massive cores a typical value of  $n$  is  $\sim 10^4 \text{ cm}^{-3}$  and the free fall time is  $t_{\text{ff}} \sim 3.4 \times 10^5 \text{ yr}$ , which gives a lower limit on the timescale for formation of massive stars.

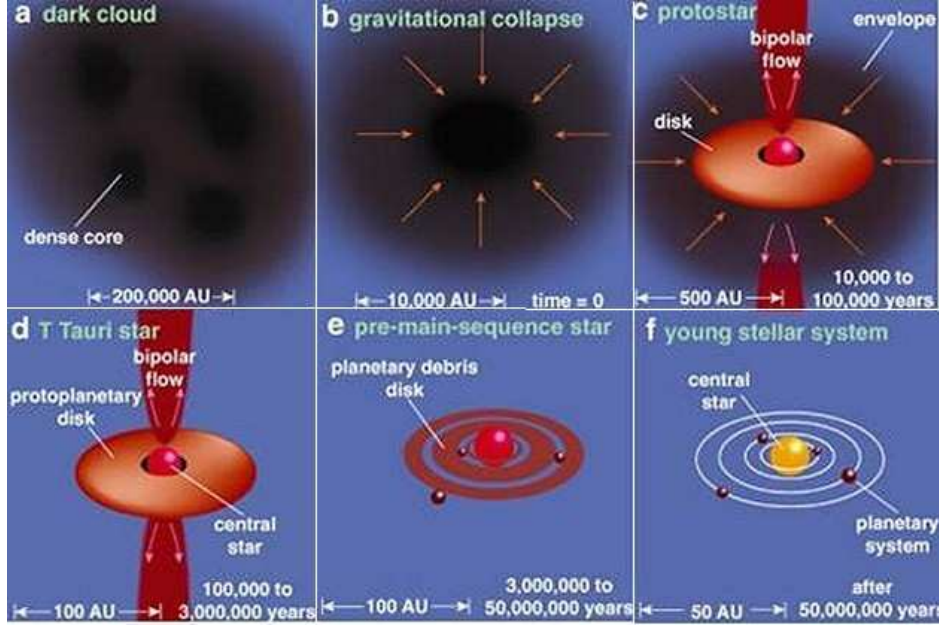


FIG. 1.2: Picture of the stages of low-mass star formation. Source: Spitzer Science Center.

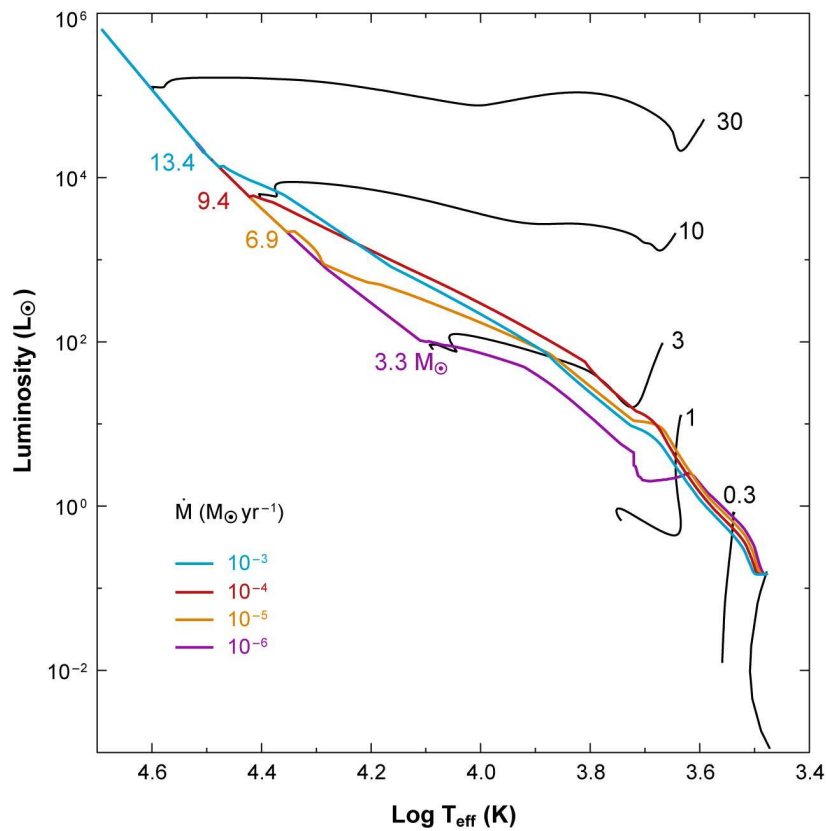
As the cores collapse, protostars are formed and their gravitational potential energy is converted to thermal energy on the Kelvin-Helmholtz timescale,  $t_{\text{KH}}$ ,

$$t_{\text{KH}} \approx \frac{GM_{\star}^2}{R_{\star}L_{\star}}, \quad (1.2)$$

which is an estimate for the protostellar lifetime before the star joins the main sequence;  $M_{\star}$ ,  $R_{\star}$  and  $L_{\star}$  are mass, radius and luminosity of the protostar, respectively. For example, assuming that all the mass of a protostar collapses, for a  $1 M_{\odot}$  star this time is  $t_{\text{KH}} \approx 3 \times 10^7$  yr, while for a  $50 M_{\odot}$  ( $\sim 10^5 L_{\odot}$ ) star  $t_{\text{KH}} \approx 3 \times 10^4$  yr.

Thus, for stars with masses  $> 8 M_{\odot}$  we have that  $t_{\text{ff}} > t_{\text{KH}}$ , and fusion begins before collapse ceases. In other words, massive stars reach the main sequence while they are still accreting material (see figure 1.3). This is problematic because the strong radiation pressure should stop further growth of the central objects. Theoretical calculations have shown that the radiation pressure is so high that it can decrease or even halt the infall (e.g., [Wolfire & Cassinelli 1987](#)), contradicting the observational existence of star with masses of 100-150  $M_{\odot}$ . This paradox is one of the principal problems in the current understanding of massive star formation (see [Garay & Lizano 1999](#)).

To circumvent the strong radiation pressure dilemma, several proposals have been made: theoretical models of mass build-up through disk accretion (McKee & Tan 2002; Yorke & Sonnhalter 2002), accretion with extremely large (Nakano et al. 2000) or increasing (e.g., Behrend & Maeder 2001) infall rates, accretion through photoionized regions (Keto & Wood 2006; Keto & Klaassen 2008), and coalescence of less massive stars in young and dense cluster environments (Bonnell et al. 1998) have been proposed. Other attempts to resolve the dilemma include the assumption of different dust properties, non-spherical symmetry, and so-called competitive accretion (see McKee & Tan 2003; Krumholz et al. 2007; Zinnecker & Yorke 2007; Bonnell & Bate 2006; McKee & Ostriker 2007).




 Zinnecker H, Yorke HW. 2007.  
Annu. Rev. Astron. Astrophys. 45:481–563

FIG. 1.3: Evolutionary tracks in the Hertzsprung-Russell diagram for protostars accreting at a constant rate (colored lines) are contrasted to the tracks of nonaccreting stars (black lines).

Of course, the above models are not necessarily mutually exclusive of each other and massive stars may form by more than one of these mechanisms. For example, there are

models and direct observational evidence of accretion onto photoionized regions with photoevaporating disks (Keto & Wood 2006; Keto & Klaassen 2008); and recent observations have confirmed the formation of accretion disks, jets, and molecular outflows in some MSFRs (Zapata et al. 2009a, 2010; Beltrán et al. 2011). This evidence suggests that massive stars could form in a manner similar to their lower mass counterparts (i.e., McKee & Tan 2003).

## 1.2 The Study of Massive Star Forming Regions

The radiation from young massive stars profoundly alters their immediate environment by heating the surrounding interstellar gas and exerting direct pressure on dust grains within the gas. Once hydrogen burning begins in a massive star, energetic photons are released that ionize the hot, dense molecular gas surrounding the star(s). These ionized regions are known as HII regions and we will discuss them in the following sub-section.

Historically, first compact ionized regions and then hot molecular cores were the objects observationally associated with the earliest phases of massive star evolution (see Garay & Lizano 1999; Kurtz et al. 2000). This was a consequence of radio interferometers applied first to centimeter continuum observations and only later to centimeter and millimeter spectral line observations.

### 1.2.1 UC HII regions

The spectral energy distribution (SED) of HII regions peaks at around  $100 \mu\text{m}$  due to the reprocessed emission of dust in the vicinity of young massive stars. At wavelengths longer than  $3 \text{ mm}$  the dust emission falls rapidly and the dominant emission is thermal free-free –produced when an electron passes near an ion and the former loses energy by emitting a photon. Thus, because of their characteristic spectrum, HII regions are best detected with infrared observations or at radio wavelengths (see Figure 1.4). The free-free emission of ionized gas from an homogeneous HII region has a frequency spectrum  $S_\nu \propto \nu^2$  if it is optically thick (i.e.,  $\tau_\nu \gg 1$  or  $\nu \ll \nu_0$ ) and  $S_\nu \propto \nu^{-0.1}$  if optically thin (i.e.,  $\tau_\nu \ll 1$  or  $\nu \gg \nu_0$ ), where  $S_\nu$  and  $\tau_\nu$  represent the flux and the

optical depth at frequency  $\nu$ , respectively, and  $\nu_0$  is the turn-over frequency defined as  $\tau_{\nu_0} = 1$ , which depends of the emission measure,  $EM$  (Mezger & Henderson 1967). Note that for ionized hydrogen in an homogeneous medium with depth  $L$ ,  $EM = n_e^2 L$ , where  $n_e$  is the electron density. In Figure 1.4 we show both optically thick and thin regions of the spectrum.

The first radio continuum observations of the free-free emission from HII regions were correctly interpreted as an indication of the birthplace of young massive stars (Mezger & Henderson 1967). However, until the decade of 1990s—and with the high angular resolution of radio interferometry—large campaigns of radio observations found hundreds of small HII regions with typical sizes of 0.1 pc and electron densities of  $10^4 \text{ cm}^{-3}$ . Such objects were called ultracompact HII regions or UC HII regions for short.

For example, the seminal works of Wood & Churchwell (1989a,b) reported over 1600 UC HII candidates using the IRAS Point Source Catalog and the far-infrared (FIR) colour criteria  $\log(F_{60}/F_{12}) \geq 1.30$ ,  $\log(F_{25}/F_{12}) \geq 0.57$  (where  $F_\lambda$  represents the *IRAS* flux in the waveband centred at  $\lambda$  microns), effectively observing the thermal dust component of the UC HII regions. Follow-up surveys confirmed the effectiveness of the selection criteria: Garay et al. (1993); Miralles et al. (1994); Kurtz et al. (1994, 1999). Despite a variety of morphologies, physical parameters and dynamics, UC HII regions were correctly understood as the birthplace of O-stars (see Churchwell 2002, for a comprehensive review of UC HII regions).

Afterwards, these source catalogs were used to search for other star formation phenomena and measure physical parameters toward MSFRs. For example, CS line emission to trace dense gas (Bronfman et al. 1996), methanol maser emission to signpost disks, jets or shock fronts (Ellingsen et al. 1996; Caswell 1996), CO to trace molecular outflows (Snell et al. 1990), water masers (Palla et al. 1993, 1991; Comoretto et al. 1990; Brand et al. 1994) to trace, some times, massive star formation, and  $\text{NH}_3$  to trace warm molecular gas (Blake et al. 1996; Cesaroni et al. 1991; Churchwell et al. 1990). With the development of (sub)millimetric radio astronomy, observations of molecular transitions and continuum emission—with single dish and interferometers—were available and essential to study the gaseous molecular cores associated with UC HII regions.

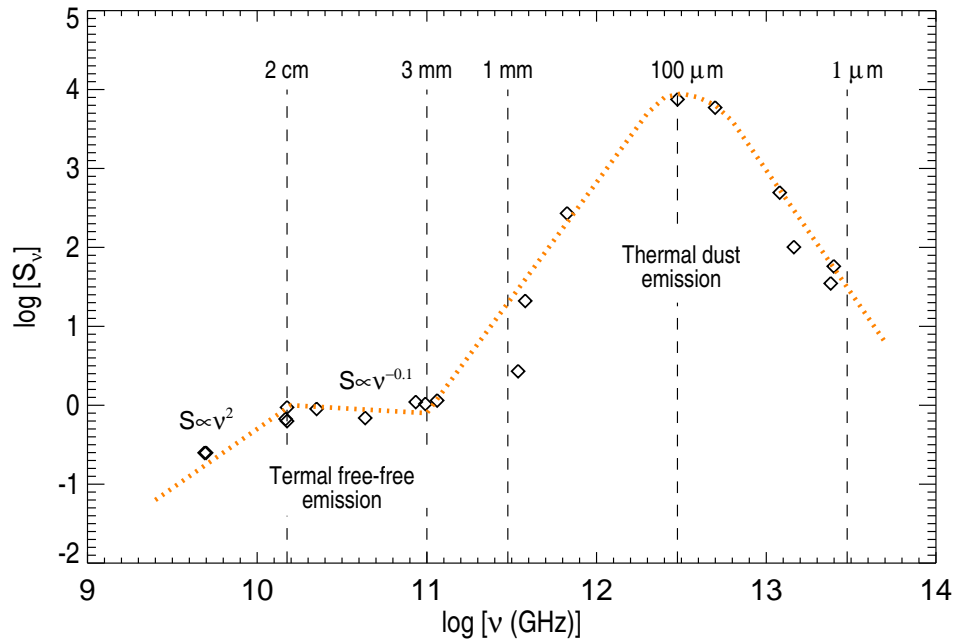


FIG. 1.4: Spectral energy distribution of the UCHII region G45.07+0.13.

### 1.2.2 Hot Molecular Cores

Prior to the development of IRAS color criteria to identify large numbers of MSFRs, only a handful of better-known MSFRs had been observed in high density gas tracers. For example, ammonia—an excellent thermometer for gas in star forming regions—was observed toward G10.62–0.38 (Mauersberger et al. 1986a; Keto et al. 1988), G15.04–0.68 (Guesten & Fiebig 1988; Massi et al. 1988), G34.26+0.15 (Henkel et al. 1987; Heaton et al. 1985; Andersson & Garay 1986) the W51N region (Mauersberger et al. 1987; Ho et al. 1983), S140 (Ungerechts et al. 1986; Torrelles et al. 1985), Cep A (Torrelles et al. 1986; Guesten et al. 1984) and NGC 7538 (Mauersberger et al. 1986b; Henkel et al. 1984). Maser emission of H<sub>2</sub>O and OH was also sampled (Henkel et al. 1986; Garay et al. 1985; Walmsley et al. 1986, e.g.) and molecules such as HCN (Pratap et al. 1989, e.g.). Notably, interferometric observations of high excitation ammonia transitions by Garay & Rodriguez (1990) showed that G34.26+0.15 has distinct molecular gas regions, with higher density and temperature toward the inner-most parts, associated with an UCHII region.

The development of the IRAS criteria permitted systematic surveys of molecular tracers toward large samples of MSFRs. These surveys showed a strong correlation between UCHII regions and warm-dense molecular gas. For example, Churchwell et al. (1990) found ammonia gas tracing temperatures of 25–65 K toward 70% of sources selected by FIR colors (64 UCHII regions and 20 candidates) using single dish observations (a resolution of  $\sim 40''$ ). In this study 67% of the targets also showed H<sub>2</sub>O maser emission. This work was a first step to further line observations at 1.3 mm and 3 mm of <sup>13</sup>CO, CS, and CH<sub>3</sub>CN (Churchwell et al. 1992) and C<sup>34</sup>S (Cesaroni et al. 1991), and high excitation transitions of ammonia (Cesaroni et al. 1992). A conclusion of these studies was that the molecular gas toward some UCHII regions is dense and hot, typically  $n_{\text{H}_2} \geq 10^5 \text{ cm}^{-3}$  and  $T \geq 100 \text{ K}$  (See Figure 1.5).

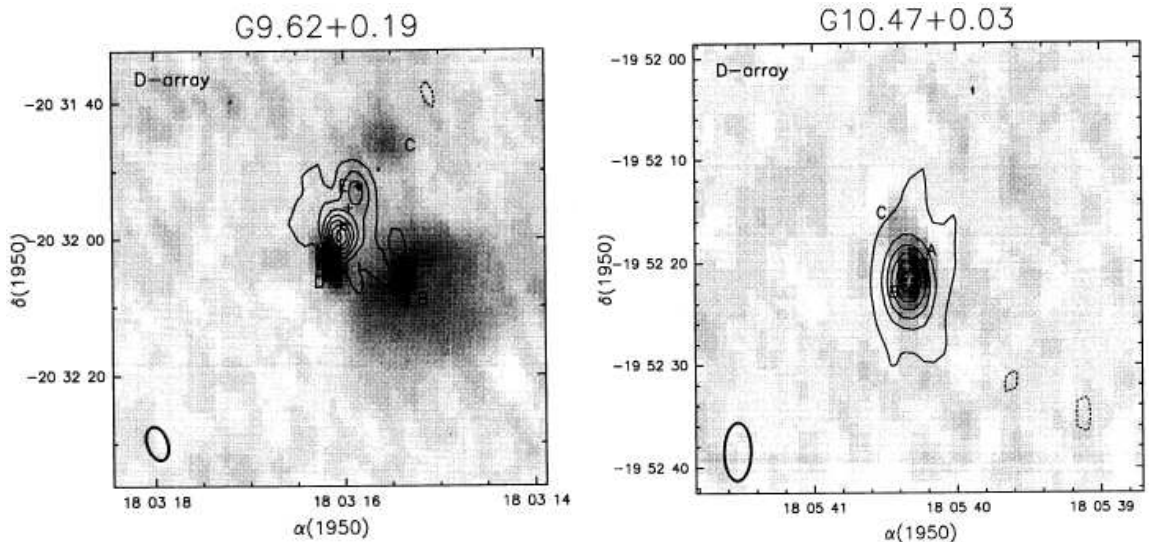


FIG. 1.5: Maps of G9.62+0.19 and G10.47+0.03 in the NH<sub>3</sub>(4,4) line emission (contours) overlapped with the 1.3 cm continuum emission (gray scale). Figure of Cesaroni et al. (1994a).

The term *hot core* had been used in some “exotic” sources such as Orion BN/KL (Genzel & Stutzki 1989; Wilson & Walmsley 1989) —rare due to the large number of molecular lines—, even prior to the above surveys. The idea of a dense and hot core of gas very near to or surrounding massive protostars was generalized as a stage of massive star formation somewhat later (e.g., Hofner et al. 1996; Cesaroni et al. 1998; Kaufman et al. 1998).

In addition to high excitation line transitions, HMCs are abundant in complex organic molecules. This rich chemistry is understood as the end result of the evaporation of ice

mantles from dust grains heated above 90–100 K and subsequent gas phase reactions. We describe this chemistry in the next section.

Finally, HMCs show dynamical phenomena such as rotation, infalling motions and molecular outflows, similar to the case of young low-mass stars. Furthermore, observations and models show that HMCs are collapsing and accreting mass onto a central source(s) at rates of  $10^{-4} - 10^{-3} M_{\odot} \text{yr}^{-1}$  (Osorio et al. 2009; Zapata et al. 2009a). These intense mass accretion rates are high enough to prevent the development of an ionized region around the massive star(s), at least in the early phases (Osorio et al. 1999), suggesting that most HMCs are predecessors of the UC HII regions (Kurtz et al. 2000; Wilner et al. 2001). All the above evidence indicates that HMCs are an earlier stage than UC HII regions in the formation of massive stars.

An important question is if HMCs are heated by internal protostars, i.e., hosting embedded young stellar objects, or if they are externally heated and hence not necessarily undergoing star formation. Recently, Zapata et al. (2011) and Goddi et al. (2011) found that the prototypical HMC Orion BN/KL is not internally heated by a protostar but rather is a pre-existing dense clump that is externally illuminated. This source suggests that the physical interpretation of objects matching the defining physical characteristics of HMC may not be unambiguous. *Are there more cases of “external heating” in HMCs? How different are the physical and chemical conditions between “internally” and “externally” heated HMCs? Will externally heated HMCs eventually form stars?* We will address these questions in this thesis work. As we will see in Chapter 4, the case of Orion BN/KL appears to be the exception and not the rule.

In short, HMCs and UC HII regions appear to be two linked pieces in a evolutionary scheme with HMCs being earlier than HII regions. Naturally, one might ask, *what kind of objects precede the HMCs? What would be the physical and chemical environment of this even earlier cores?* Recent works suggest an evolutionary sequence starting from massive cores in infrared dark clouds (IRDCs Rathborne et al. 2009, 2006; Pillai et al. 2006; Simon et al. 2006; Jackson et al. 2008).

In the next section we will discuss IRDCs and their massive cores.



### 1.2.3 Massive Cores in Infrared Dark Clouds

The *Infrared Space Observatory* (ISO; Perault et al. 1996) and *Midcourse Space Experiment* (MSX; Egan et al. 1998) surveys toward the Galactic plane identified dark filamentary clouds seen in absorption against the bright mid-IR background. These molecular infrared dark clouds show high densities ( $n > 10^5 \text{ cm}^{-3}$ ), high column densities ( $\sim 10^{23}\text{-}10^{25} \text{ cm}^{-2}$ ), and in general low temperatures ( $< 25 \text{ K}$ ) (Simon et al. 2006; Carey et al. 2000). Follow-up molecular and millimeter continuum observations indicated that IRDCs have sizes of  $\sim 5 \text{ pc}$  and masses of  $\sim \text{few } 10^3 M_{\odot}$  (Jackson et al. 2008; Ragan et al. 2009).

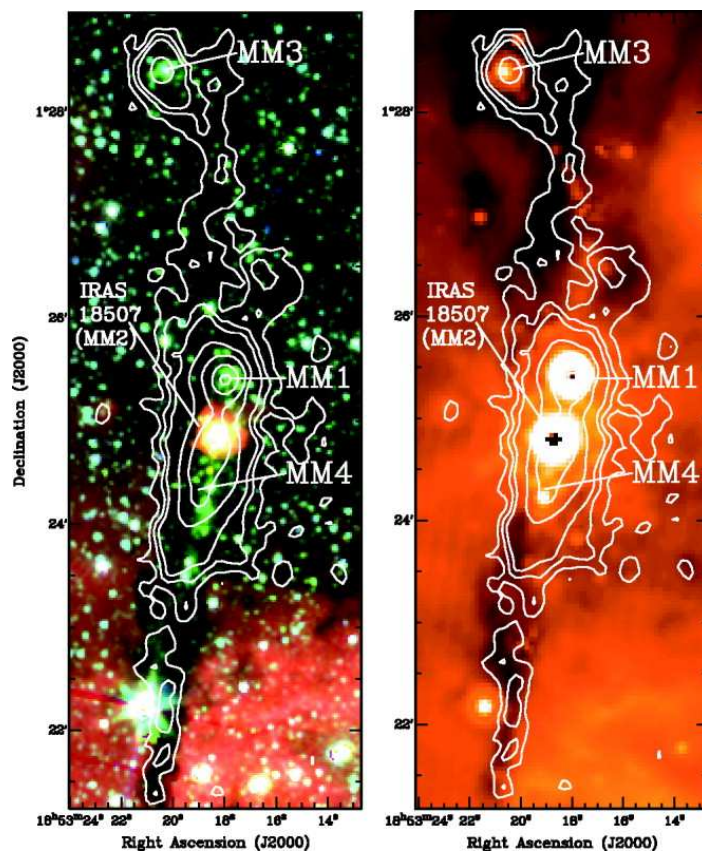


FIG. 1.6: IRDC G034.43+00.24. *Left:* *Spitzer*/IRAC three-color image ( $3.6 \mu\text{m}$  in blue,  $4.5 \mu\text{m}$  in green (EGOs or , and  $8.0 \mu\text{m}$  in red) overlaid with contours of IRAM/MAMBO-II 1.2 mm continuum emission. *Right:* *Spitzer*/MIPS  $24 \mu\text{m}$  image. MM1 shows a rich chemistry similar to that of a HMC. MM2 is associated with an UC HII region, and MM3 is considered to be a massive core in an early evolutionary stage (Rathborne et al. 2005, 2011).

Within IRDCs multiple compact and cold cores have been identified, and they show physical characteristics with potential to harbour massive protostars: strong mm and sub(mm) continuum emission (Garay et al. 2010, 2004; Sridharan et al. 2005; Ragan et al. 2013), infall evidence (Chen et al. 2010), molecular outflows (Beuther & Sridharan 2007; Cyganowski et al. 2008; Sanhueza et al. 2010; Jiménez-Serra et al. 2010),  $4.5\ \mu\text{m}$  emission indicating probable outflow [Extended Green Objects (EGOs Cyganowski et al. 2008)], bright  $24\ \mu\text{m}$  emission indicating the presence of warm dust; maser emission in multiple species (Wang et al. 2006; Leurini et al. 2007b; Cyganowski et al. 2009) and large bolometric luminosities in some cases. Thus, these IRDC massive cores are considered to be the cradles of massive star formation, some of them harbouring embedded protostars (Rathborne et al. 2006, 2008; Jackson et al. 2008). Hereafter we will refer to them as **massive cores**.

The masses and sizes of massive cores are similar to those of HMCs (see Table 1.1), but with considerably lower temperatures (Sridharan et al. 2002; Pillai et al. 2006). In terms of chemical abundances, most massive cores show low complexity of molecular species (Rathborne et al. 2007, 2011). This can be explained if we consider that owing to their extreme youth and low temperatures the ice mantles on the dust grains are still intact.

However, simple species such as  $\text{HC}_3\text{N}$ ,  $\text{N}_2\text{H}^+$ ,  $\text{CSS}$ ,  $\text{H}_2\text{O}$ ,  $\text{NH}_3$ , and  $\text{CH}_3\text{OH}$  are commonly found in massive cores (Gibson et al. 2009; Rathborne et al. 2007; Ragan et al. 2006; Sakai et al. 2008; Cyganowski et al. 2013; Wang et al. 2008). Also,  $\text{CH}_3\text{OH}$  maser emission has been detected toward dozens of massive cores (Cyganowski et al. 2009; Chambers et al. 2014, 2011; Bayandina et al. 2012; Lim et al. 2012) In particular, Class II  $\text{CH}_3\text{OH}$  masers —often found very close to protostars (see chapter 3), and exclusively tracing MSFRs (Ellingsen 2005; Minier et al. 2003)— has been detected. Part of this thesis work was an observational study to search for Class II  $\text{CH}_3\text{OH}$  maser emission toward a group of HMCs and massive cores in IRDCs, at submillimeter wavelengths. In Chapter 3 we will summarize theoretical and observational details about  $\text{CH}_3\text{OH}$  emission and in Chapter 5 we will present our study using this tracer.

Finally, from molecular abundances and chemical evolution models, Gibson et al. (2009) established chemical ages for massive cores between  $10^{4.5}$  and  $10^{5.5}$  years for more-evolved cores and  $<10^{4.5}$  years for younger, and probably starless cores.

If these massive cores are precursors of HMCs, they will begin to heat their surroundings and evaporate the dust ice mantles giving rise to the molecular complexity of the HMC phase. For example, Rathborne et al. (2007, 2008, 2011) made millimeter and submillimeter observations of three massive cores within IRDCs and found abundant line emission from complex molecules, at temperatures  $\gtrsim 200$  K,  $\text{CH}_3\text{CN}$  column densities of  $\gtrsim 1 \times 10^{17} \text{ cm}^{-2}$ , and with gas masses from dust continuum emission between 10 and  $26 M_\odot$ . These massive cores are considered a very early phase in the hot core stage Rathborne et al. (2011).

TABLE 1.1: Typical physical properties of star forming regions and cores

Properties	Star Forming Regions			Star Forming Cores			UCHII Regions
	Bok Globules	Massive Clumps	IRDCs	Low-mass Protostellar	Hot Cores	Massive Cores in IRDCs	
Sizes (pc)	0.1-1	0.5-3	5-10	$\sim 0.05$	$< 0.1$	0.02-0.8	$< 0.1$
Mass ( $M_\odot$ )	$1-10^2$	$10^2-10^3$	$10^2-10^4$	0.5-5	$\sim 10-10^3$	$10-10^3$	*
Density ( $\text{cm}^{-3}$ )	$10^3-10^4$	$10^4-10^6$	$10^2-10^4$	$10^5-10^6$	$10^5-10^8$	$10^3-10^7$	$> 10^4$
Temperature (K)	10-20	50-100	10-20	10	$> 100$	15-30	$\sim 10^4$
References	1,2,3	4,5	6	7,8	9,10,11	12,13	14

References—(1)Leung 1985; (2)Clements & Barvainis 1998; (3)(Bourke et al. 1995); (4)(Lada & Lada 2003); (5)(Motte et al. 2003); (6)(Rathborne et al. 2006); (7)Myers & Benson 1983; (8)(Ward-Thompson et al. 1994); (9)(Garay & Lizano 1999); (10)(Kurtz et al. 2000); (11)(Churchwell 2002); (12)(Rathborne et al. 2006); (13)(Rathborne et al. 2005); (14)(Churchwell 2002). \*Emission measures  $> 10^7 \text{ pc cm}^{-6}$ .

In summary, the interstellar medium has star forming regions with substructures (clouds, filaments, clumps, and cores) showing different physical characteristics. Nonetheless, the scales on which star formation takes place allow us to state typically values—somewhat artificial and overlapped some times (see table 1.1).

Regarding to an evolutionary sequence for MSFRs, some authors have proposed that massive stars begins their lives in IRDCs and massive clumps of dense gas at the heart of giant molecular clouds. Part of these dark clouds and clumps collapse into massive cores via mergers or accretion, forming massive protostellar objects. Once heat and radiation from protostars produce a hot molecular core, high temperatures and rich chemistry is detected through organic molecules. Then, central objects begin burning hydrogen brightly enough to ionize its surroundings, and will form an UCHII region which continues to expand as the protostar evolves toward the main sequence.

Of course, this is an *ideal evolutionary sequence* and the transition between stages is not well established. We note, for example, that there are IRDCs showing massive cores, HMCs, and UCHII regions in the same filament of gas and dust (Rathborne et al. 2011, 2009). This is the case of G34.43+00.24 (figure 1.6). Also, some HMCs have little or no observable radio continuum emission, at least with  $\sim 0.1$  mJy sensitivity, for example G8.68-0.37 (Longmore et al. 2011), IRAS 18182-1433 (Beuther et al. 2006) and G23.01-0.41 (Furuya et al. 2008). Finally, some MSFRs associated with high luminosities ( $>10^5 L_{\odot}$ ) do not lie in filamentary IRDCs.

Today, even with recent high-frequency interferometers (e.g., SMA and ALMA) and robust computational models of physical and chemical characteristics, our knowledge about the evolutionary sequence of massive star formation is incomplete. In particular, some interesting questions are: *How does the chemical composition vary between massive cores? Which chemical species could be useful to study dynamics and evolutionary states?* Wide bandwidth observations at submillimeter wavelengths and chemical models are two indispensable tools in order to study the chemical composition and its relationship with physical parameters and evolution of the MSFRs.

#### 1.2.4 This thesis

Considering the observational evidence in the previous sections, we can summarize the two principal topics of interest in this thesis as follows:

- **Massive cores in IRDCs.** Massive cores associated with filaments of gas and dust (IRDCs) and with physical parameters that likely represent the initial conditions of massive star formation. Some of them appear to be more evolved and show molecular line emission of complex species.
- **HMCs.** Massive, dense, and hot molecular cores, commonly showing high luminosities, and characterized by very rich chemistry. HMCs without detected free-free emission are assumed to be younger than those associated with UCHII regions.

This thesis consists of an observational study at (sub)millimeter wavelengths of continuum emission and molecular line emission of CH<sub>3</sub>CN and CH<sub>3</sub>OH toward HMCs and massive cores. Our main goal is to address the following questions:

- *Are there other HMCs that are externally heated, as is the case of Orion BN/KL?*
- *How different is the chemical composition between HMCs?*
- *How do molecular abundances evolve in HMCs? Are there chemical abundances correlated with physical parameters such as density or temperature?*
- *How different is the chemical composition between massive cores associated with IRDCs? Which molecules could be important to determine their evolutionary state?*

In the following Chapter we summarize recent observations and models toward HMCs in order to describe their physical parameters. In Chapter 3 we describe the molecular lines used in this work and the methods to estimate density, temperature and abundance in HMCs and massive cores. In Chapter 4 we present an observational study toward 17 HMCs, using interferometric data at 220 GHz. In Chapter 5 we present our results from single dish observations at 247 GHz of CH<sub>3</sub>OH emission, toward a group of MSFRs that include HMCs and massive cores in IRDCs. Finally, in Chapter 6 we present the conclusions of this thesis.

# Chapter 2

## Hot Molecular Cores

Hot molecular cores (HMCs) are knots of dense, compact and warm molecular gas detected mostly through line transitions at centimetric, millimetric and submillimetric wavelengths. They reside inside larger molecular clumps (with mean size of 1-3 pc, density of  $10^4$ - $10^6$   $\text{cm}^{-3}$ , and mass of  $10^2 - 10^3 M_{\odot}$ ) and they are frequently associated with UC HII regions. These characteristics suggest that HMCs are sites of (or with nearby) newly formed O-stars still embedded in their natal clouds.

Early single-dish observations had insufficient angular resolution to disentangle the confused star forming environments and the link between the hot gas and other tracers of massive stars, such as maser emission, continuum dust emission, and UC HII regions was far from clear. As interferometers were used to observe these phenomena with high resolution, the most embedded molecular and ionized gas was characterized. Figure 2.1 from [Furuya et al. \(2011\)](#) illustrates the complexity of structures and multiplicity of tracers toward the HMC G19.61-0.23. The central hot core is traced by dust emission at submillimetric wavelengths and  $\text{CH}_3\text{CN}$  (18-17) emission from hot gas.

From an observational point of view, HMCs are characterized as molecular gas condensations at relatively high temperatures ( $>100$  K) and high densities ( $\sim 10^5$ - $10^8$   $\text{cm}^{-3}$ ), that are compact ( $< 0.1$  pc), luminous ( $> 10^4 L_{\odot}$ ), and massive ( $\sim 10$ - $1000 M_{\odot}$ ); (e.g., [Walmsley et al. 1995](#); [Kurtz et al. 2000](#); [Cesaroni 2005](#)).

HMCs show a forest of molecular lines (see figure 2.2), especially from organic species (e.g., [Comito et al. 2005](#)). The only astronomical objects known to present a similarly

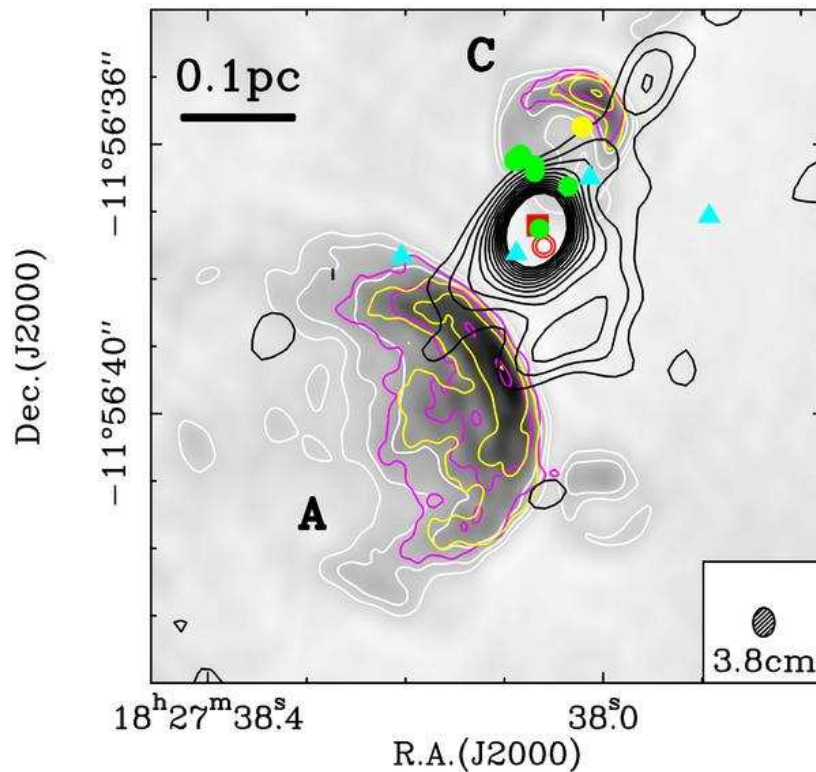


FIG. 2.1: Image of the region G19.61-0.23 comparing the 6 cm (greyscale plus white contours), 3.8 cm (magenta contours), 1.3 cm (yellow contours), and  $890\ \mu\text{m}$  (black contours) continuum emission. The filled red rectangle and double red circle indicate the peak positions of the 3 mm and  $890\ \mu\text{m}$  continuum emission, respectively. The filled green circles and light-blue triangles show the positions of the OH (Garay et al. 1985) and  $\text{H}_2\text{O}$  (Hofner & Churchwell 1996) masers, respectively. Labels A and C refer to UCHII regions, and the filled yellow circle marks the position of an isolated 7 mm emission peak. Figure from (Furuya et al. 2011).

complex chemistry are comets and the atmospheres of moons and planets in our Solar System. Many of these molecules probably were formed in a cold gas-phase or in surface reactions of grain ice-mantles, while others were likely produced by gas-phase reactions after “parent species” were evaporated or sublimated from the grains by the strong radiation of embedded or nearby protostars (see Herbst & van Dishoeck 2009). Formation of some species is better explained by dynamical phenomena such as shocks and accretion (Millar et al. 1997; Nomura & Millar 2004; Garrod & Herbst 2006; Doty et al. 2006; Lintott et al. 2005). In figure 2.3, from Wright et al. (1996), one can appreciate the diversity of molecules observed toward Orion BN/KL. We will discuss the chemistry and dynamics of HMCs in this chapter.

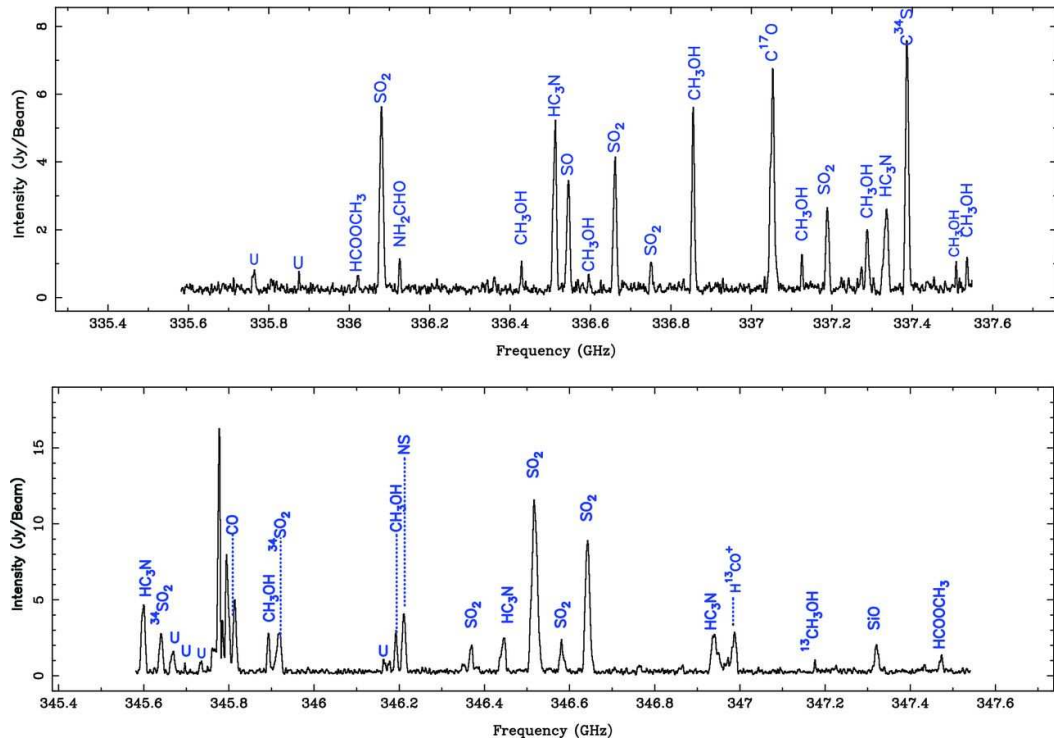


FIG. 2.2: Figure of Xu & Wang (2013). SMA spectra extracted from the line data cubes in the HMC G20.08–0.14N. The spectra are averaged over one beam centred on the peak of the continuum.

The most accepted scenario for HMCs is that one or more central protostars are embedded within a massive envelope collapsing and accreting mass at rates of  $10^{-3} - 10^{-4} M_{\odot} \text{ yr}^{-1}$  (Osorio et al. 2009, 1999). These intense mass accretion rates are high enough to prevent the development of an ionized region around the central stars, at least in early phases. In this scenario, HMCs without free-free emission should be younger (or have higher accretion rates) than those that have developed UC HII regions, while UC HII without any remaining vestige of the parent HMC should be in a later evolutionary phase. That is, HMCs are thought to precede the UC HII phase (Walmsley et al. 1995; Kurtz et al. 2000).

Although the general scenario pre-supposes the presence of embedded young massive stellar objects, without their direct observations it is difficult to establish the heating source(s). Detection of ionized or molecular gas infall, rotating structures such as toroids or accretion disks, or molecular outflows or jets, also would indicate embedded sources.



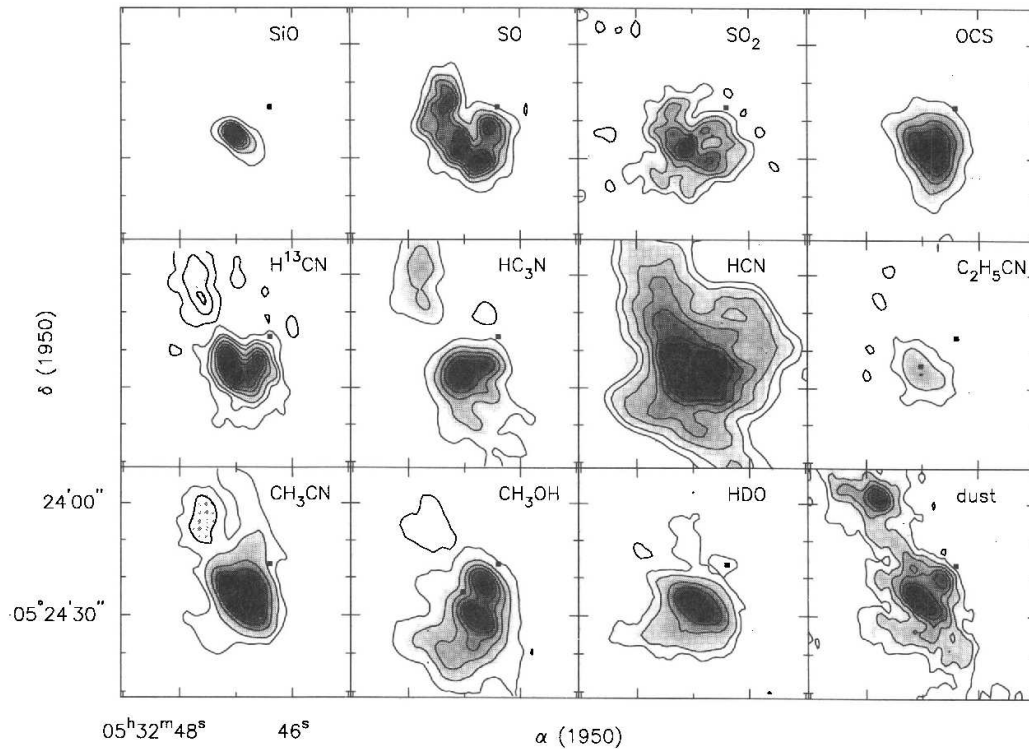


FIG. 2.3: Molecular observations of Orion BN/KL, a prototypical HMC (figure from Wright et al. 1996).

For example, in the case of G19.61-0.23, two “cometary” UC HII regions one on each side of the central molecular core, suggest that pressure from the expanding UC HII regions may be responsible for compressing and heating the gas, thus creating the hot core (see figure 2.1). However, in G19.61-0.23 the hottest gas is found toward the centre of the core, and the velocity field of hot  $\text{CH}_3\text{CN}$  (18-17) emission shows a clear velocity gradient, indicative of systematic motions of gas, resembling a toroid (see figure 14 of Furuya et al. (2011)).

This kind of rotating structure has been detected toward other HMCs as well (e.g., Beltrán et al. 2011, 2006; Klaassen et al. 2009; Cesaroni et al. 2011, 2006, 2005). Furthermore, infall or accretion of molecular and ionized gas have also been observed and modelled (Keto & Klaassen 2008; Keto & Wood 2006; Keto & Zhang 2010; Beltrán et al. 2006; Zapata et al. 2008b). At least in these cases, one has strong evidence of embedded protostars in HMCs.

However, another scenario for HMCs is suggested by recent high angular resolution observations toward Orion BN/KL (see Figure 2.4). In this case, Zapata et al. (2011)

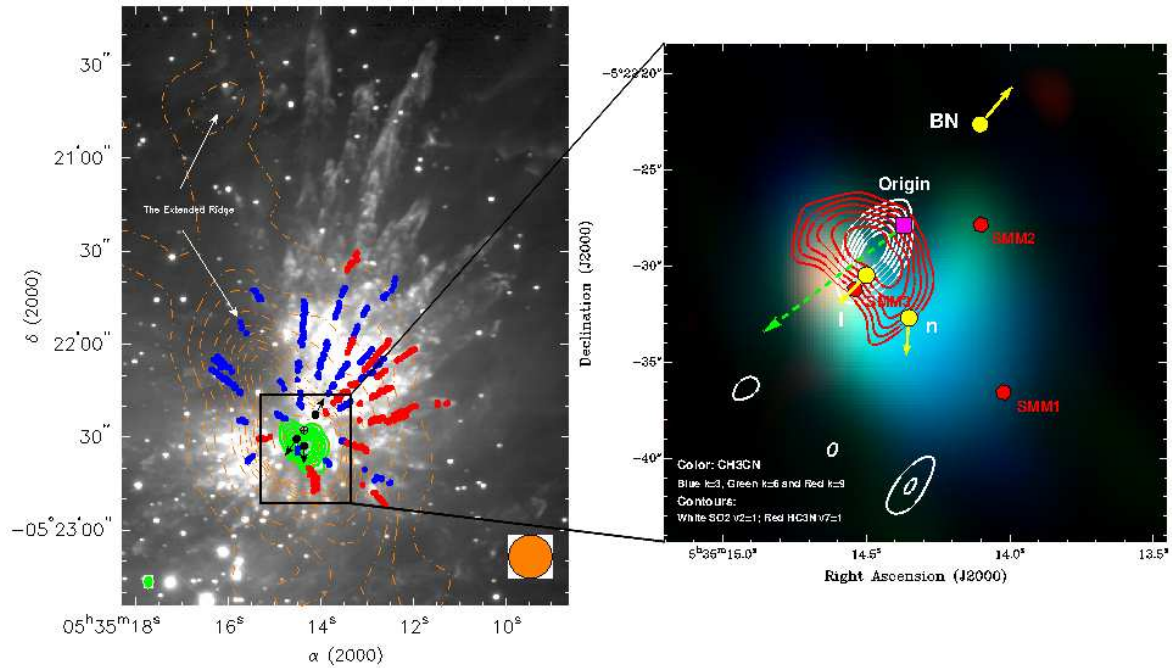


FIG. 2.4: *Left*:  $\text{H}_2$  image of the Orion KL region (Bally et al. 2011) overlaid with SMA map of  $\text{CH}_3\text{CN}$  ( $12_K-11_K$ )  $k = 3$  in green contours. The black circles with vectors mark the positions and orientations of the proper motions of the radio and infrared sources BN, I and n. *Right*:  $\text{CH}_3\text{CN}$  ( $12_K-11_K$ ) composite image showing the rotational transitions  $k = 3$  (blue),  $k = 6$  (green), and  $k = 9$  (red). Red and white contours correspond to  $\text{HC}_3\text{N}$  (37-36) and  $\text{SO}_2$  ( $21_{2,20}-21_{1,20}$ ), respectively. The pink square represents the origin of the Orion KL molecular outflow. The red hexagons mark the positions of the three submillimeter sources SMM1, SMM2, and SMM3. (figure from Zapata et al. (2011)).

found that high-excitation transitions trace a shell around a submillimeter continuum source. Also, they find filamentary CO structures of a previous explosive flow from a close dynamical interaction of three protostars (Zapata et al. 2009b). They propose that “the CO-shadow” behind the Orion KL hot core and the shell of hot gas indicate that the HMC is not internally heated by a protostar but rather is a pre-existing clump that is externally illuminated (Zapata et al. 2011; Goddi et al. 2011). In this scenario, no internal protostellar source for heating is necessary and external heating could explain the nature of this prototypical source. However, additional sub-arcsecond observations at millimetric and submillimetric wavelengths, and models are required to confirm this heating scenario. (As we note in Chapter 4, one of our goals in this thesis was to search for evidence of external heating toward other HMCs).

In any case, we consider that Orion BN/KL is the exception and not the rule. Many

observational works have identified the central source(s) for a number of HMCs, using high angular resolution mid-IR, submillimeter and millimeter continuum emission (e.g., De Buizer et al. 2003; Beltrán et al. 2004a; Galván-Madrid et al. 2009; Cesaroni et al. 2010). These detections strengthen the idea that HMCs are objects associated with the early phase of massive stars.

One consideration is that the typical size of a HMC is  $\sim 0.05$  pc, while its distance is in most cases  $> 5$  kpc, implying an angular diameter  $< 2''$ . Only recently have millimeter interferometers such as ALMA and SMA been able to achieve angular resolutions below  $0''.5$ , which are sufficient to resolve some HMC and study their internal structure and dynamics. In this regard, radial profiles of density and temperature (Cesaroni et al. 2010), and some evidence of infall and rotation of gas inside HMCs has been reported (Sollins et al. 2005a; Zhang et al. 1998b; Cesaroni et al. 2005; Beltrán et al. 2005; Rolffs et al. 2011; Mayen-Gijon et al. 2014). We will discuss internal dynamics of HMCs in the last section of this chapter.

## 2.1 The number and lifetime of HMCs

One of the pending issues is the number of HMCs and their estimated ages. Using the number ratio of HMCs to UC HII regions toward two different MSFRs, Wilner et al. (2001) and Furuya et al. (2011) estimated that HMCs live at least 25% of the time of UC HII regions ( $\sim 10^5$  yr; Wood & Churchwell 1989a), or a few  $10^4$  yr. This implies about one HMC for each four UC HII regions, i.e., of order 400 HMCs in the Galaxy. Similarly, self-consistent models of the physical structure of HMCs suggest ages less than  $10^5$  yr (Osorio et al. 2009, 1999).

Additionally, chemical models require  $10^4 - 10^5$  yr to reach the chemical richness observed in HMCs (e.g., Charnley 1995; Herbst & van Dishoeck 2009), which implies from a few hundreds to thousands of HMCs (the latter similar to the number of UC HII regions). Although these are rough measures and the studies of Wilner et al. (2001) and Furuya et al. (2011) are only two cases, clearly there is a discrepancy between the low number of HMCs observed ( $\sim 60$ ) and the numbers suggested by these lifetime arguments. If we assume that high-mass star formation is continuous, uncorrelated

with the environment around each MSFR, and we are sampling cores at a random point in time, then we should observe many more HMCs (Furuya et al. 2005).

However, determining the relative number of HMCs with respect to other objects such as UC HII regions (e.g., Wilner et al. 2001; Furuya et al. 2011), requires unbiased observations of large regions at high angular resolution to ensure that the results are statistically reliable. To date, only a few dozens of HMCs have been detected, most of them from molecular line observations toward cores showing indicators of active massive star formation: UC HII (e.g., Cesaroni et al. 1992; 1994; Churchwell et al. 1992; Olmi et al. 1993; Hatchell et al. 1998), CH<sub>3</sub>OH masers (Purcell et al. 2006), and multiple indicators (Pankinin et al. 2001).

No single census of HMCs exists in the literature. We searched the published literature for MSFRs in the HMC phase, based on previous detections of molecular species indicating warm-hot and dense gas such as CH<sub>3</sub>CN, NH<sub>3</sub> and CH<sub>3</sub>OH. These molecules are commonly used to study HMCs (e.g., Churchwell et al. 1990, 1992; Olmi et al. 1993; Kalenskii et al. 1997, 2000). A list of catalogues surveys used to search for probable HMCs is shown in Table 2.1.

TABLE 2.1: Observational surveys

Paper	Lines	Beam size arcsec	Targets Type/number	Detection	Notes
Churchwell et al. 1990	NH <sub>3</sub> (1,1)-(2,2)	40	UC HII/84	70%	50% has $T_k > 25$ K
Churchwell et al. 1992	CH <sub>3</sub> CN(6-5), (12-11)	25	UC HII/11	45%	—
Pankinin et al. 2001	CH <sub>3</sub> CN(12-11)	35	MSFR-UC HII/48	52%	—
Purcell et al. 2006	CH <sub>3</sub> CN(5-4)-(6-5)	35	MSFR/77	70%	—
Longmore et al. 2007	NH <sub>3</sub> (1,1)-(5,5)	11-8	MSFR/21	100%	—
Beuther et al. 2009	NH <sub>3</sub> (4,4)-(5,5)	1	MSFR/12	91%	—

We compiled a list of almost 70 objects of which most are associated with UC HII regions, strong (sub)millimeter continuum emission, molecular outflows, or maser emission. In Table 2.2 we present the list of probable HMC, their positions, LSR velocities, distances, luminosities (derived from IRAS fluxes in most cases), and temperatures estimated from molecular tracers. We add some notes about the nature, environment or phenomena associated with the HMCs.

We used this list of probable HMCs to search in the database of SMA observations. We sought observations at  $\sim 220$  GHz, with compact or extended configurations and with publically available data. This work is presented in Chapter 4.

TABLE 2.2: Hot molecular cores

Name	R.A. (J2000)	Dec (J2000)	$V_{\text{LSR}}$ ( $\text{km s}^{-1}$ )	d (kpc)	$L(10^5)^*$ ( $L_{\odot}$ )	$T_{\text{rot}}^{**}$ (K)	Other name	Comments <sup>†</sup>
G301.13–0.23	12 35 35.0	-63 02 29	-40	4.4	3.8	50(c,6); 91(b,7)	I12326-6245	(18), E
G305.20–0.20	13 11 14.0	-62 34 26	-41	3.9	1.5	102(c,6)	I13079-6218	(51)
G305.79–0.25	13 16 43.0	-62 58 30	-33	4.2	0.6	236(c,6)	I13134-6242	E305.77/80, $\text{CH}_3\text{OH}^{\text{M}}$
G316.81–0.06	14 45 27.9	-59 49 14	-39	2.7	1.32	>200(a,10), 73(b,5)	I14416-5937	$\text{CH}_3\text{OH}^{\text{MII}}$ , E
G318.05–0.09	14 53 41.6	-59 08 54	-50	4.3	0.58	295(b,7)	I14498-5856	E318.05/04
G323.46–0.08	15 29 19.6	-56 31 23	-67	4.9	2.13	112(b,7)	I15254-5621	
G323.74–0.26	15 31 45.5	-56 30 50	-50	3.3	0.53	>200(a,10), 67(b,5)	I15278-5620	EG323.74, $\text{CH}_3\text{OH}^{\text{MII}}$ , E
G327.30–0.60	15 53 06.0	-54 36 24	-46	3.1/11.2	1.0	>200(a,10)	I15492-5426	EG327.30, $\text{CH}_3\text{OH}^{\text{MII}}$
G328.31+0.43	15 54 06.0	-53 11 38	-92	7.2/5.6	9.6	134(b,7)	I15502-5302	
G328.81+0.63	15 55 48.4	-52 43 06	-41	3.0	2.1	>200(a,10)	I15520-5234	EG328.81, $\text{CH}_3\text{OH}^{\text{MII}}$
G330.94–0.18	16 09 51.4	-51 55 07	-91	5.5/9.4	7.8/23.8	170(b,18)	I16060-5146	EG330.95
G330.87–0.36	16 10 20.0	-52 06 13	-100	4.0/10.8	3.0/21.2	220(b,18), 133(c,6)	I16065-5158	EG330.88
G331.28–0.19	16 11 26.9	-51 41 57	-88	5.4	2.3	74(b,5), >200(a,10)	I16067-5134	$\text{CH}_3\text{OH}^{\text{MII}}$
G336.02–0.83	16 35 09.3	-48 46 47	-48	3.6/12.0		>200(a,10)	I16313-4840	EG336.02, $\text{CH}_3\text{OH}^{\text{MII}}$
G340.06–0.25	16 48 11.9	-45 21 35	-54	3.4		130/550(c,6)	I16445-4516	EG340.05
IRAS16547-4247	16 58 17.3	-42 52 07	-30	2.9	0.6	245(b,52)		$\text{H}_2\text{O}^{\text{M}}$
G345.50+0.35	17 04 24.6	-40 43 57	-16	1.8	0.5		I17008-4040	(53), EG345.51
G345.00–0.22	17 05 10.9	-41 29 06	-27	2.9/13.5	0.10	>200(a,10)		EG345.00
IRAS17233-3606	17 26 42.8	-36 09 17	2	2.2	0.14	>200(a,10), 210(b,17,33)		E, $\text{H}_2\text{O}^{\text{M}}$ , $\text{CH}_3\text{OH}^{\text{MII}}$
NGC6334I	17 20 53.4	-35 46 57	-3	1.7	2.6	>200(a,10)		
NGC6334I(N)	17 20 55.0	-35 45 05	-3	1.7	0.32	170(b,9)		
SgrB2(M-N)	17 47 21.0	-28 23 00	-3	8.0	1.0	150(a,56)		
G0.55–0.85	17 50 15.0	-28 54 30	18	7.7/9.4	8.55	>200(a,10); 63(b,5)		

Table 2.2 – continued from previous page

Name	R.A. (J2000)	Dec (J2000)	$V_{\text{LSR}}$ (km s <sup>-1</sup> )	d (kpc)	$L(10^5)^*$ ( $L_{\odot}$ )	$T_{\text{rot}}^{**}$ (K)	Other name	Comments <sup>†</sup>
G5.89–0.39	18 00 30.4	-24 04 00	+10	2.0	1.47	125(a,1), 75(b,2); 150(b,30)		
G8.67–0.36	18 06 19.0	-21 37 30	+24	4.6				(35), H <sub>2</sub> O <sup>M</sup> , UCHII
G8.68–0.37	18 06 23.4	-21 37 10	+37	4.8	0.2	100–200(b,19)		(19), NCE, E
G9.62+0.19	18 06 15.0	-20 31 40	+4	5.7	2.8	95(a,1), 123(b,4), 135(b,2)		
G10.30–0.15	18 08 56.1	-20 05 50	+12	6.0	6.50	68(a,1), 32(b,5), 34(b,4)	I18060-2005	EG10.29/34
G10.32–0.16	18 09 01.5	-20 05 08	12	2.2	0.8	53(b,5)		
G10.47+0.03	18 08 38.2	-19 51 49	+68	5.8	18.2	196(b,2), 64(b,5), 165(a,22)		
G10.62–0.38	18 10 28.7	-19 55 50	-3	4.8	11.0	55(a,4), 103(b,2), 87(b,34)		
G11.92-0.61	18 13 57.8	-18 54 14	+35	3.8	0.1	166(b,25)		E, H <sub>2</sub> O <sup>M</sup> , CH <sub>3</sub> OH <sup>MII</sup>
G12.21–0.10	18 12 39.8	-18 24 17	+24	13.5	14.8	72(b,4)	G12.22–0.12	
G12.68–0.18	18 13 54.7	-18 01 48	+56	11.5	3.3	>50(a,54)		E, OH <sup>M</sup> , CH <sub>3</sub> OH <sup>M</sup>
G12.89+0.49	18 11 51.4	-17 31 28	+33	3.6	0.34	131(b,5),350(b,27)	I18089-1732	
G12.91–0.26	18 14 39.5	-17 52 00	+37	3.9	0.7	94(b,5)	W33A	
HH80-81	18 19 12.1	-20 47 30	+13	1.7	0.1	>100(57)	I18162-2048	
G15.04–0.68	18 20 24.8	-16 11 35	+19	2.1	1.63	78(b,5), 52(b,4)		
G16.59–0.05	18 21 09.0	-14 31 49	+59	4.5	0.2	150(b,23)	I18182-1433	
G19.01-0.03	18 25 44.8	-12 22 45	+60	4.2	0.1	114(b,25)		E, CH <sub>3</sub> OH <sup>MII,I</sup> , IRDC
G19.47+0.17	18 25 54.3	-11 52 30	+20	1.9	0.1	>200(a,10), 55(b,5)		
G19.61–0.23	18 27 38.1	-11 56 38	+42	12.6	20	208(b,14)		NCE or UCHII <sup>b,21</sup>
G20.08-0.14N	18 28 10.3	-11 28 48	+42	12.3	6.6	230(b,20)		
G23.01–0.41	18 34 40.3	-09 00 38	+77	8.5	10.0	121(b,11),58(a,12)		(44), E
G23.71+0.17	18 33 53.5	-08 07 25	+113	9.0	4.3	56(b,4), 35(b,4), 43(a,4)		
G24.33+0.11MM1	18 35 08.1	-07 35 04	+110	6.3	0.14	>100(31)		IRDC, H <sub>2</sub> O <sup>M</sup>
G24.78+0.08	18 36 12.5	-07 12 11	+110	7.7	2.0	87(a,12), 81(b,5)		(45)

Table 2.2 – continued from previous page

Name	R.A. (J2000)	Dec (J2000)	$V_{\text{LSR}}$ (km s <sup>-1</sup> )	d (kpc)	$L(10^5)^*$ ( $L_{\odot}$ )	$T_{\text{rot}}^{**}$ (K)	Other name	Comments <sup>†</sup>
G25.65+1.05	18 34 20.8	-05 59 42	+60	3.3	0.33	197(b,2), 166(b,5)	I18316-0602	
G25.83-0.18	18 39 03.6	-06 24 10	+90	5.6		>50(b,5),(a,58)		(44), H <sub>2</sub> CO <sup>M</sup> , CH <sub>3</sub> OH <sup>M</sup>
G28.20-0.04	18 42 58.1	-04 13 56	+96	6.8	1.7	74(b,5)		(24)
G30.71-0.06	18 47 36.5	-02 00 31	+93	5.8		75(b,5)	W43	IRDC, E, CH <sub>3</sub> OH <sup>M</sup>
G30.82-0.05	18 47 46.5	-01 54 17	+97	6.0	0.27	78(b,5)	W43	
G31.41+0.31	18 47 34.3	-01 12 46	+97	7.9	1.85	292(b,2), 98(b,5), (a,22)		(45)
G31.97+0.07	18 49 36.3	-00 45 45	+98	6.9	0.4			IRDC, E, CH <sub>3</sub> OH <sup>M</sup>
G32.80+0.19	18 50 30.6	-00 01 59	+17	13	3.5	60(a,26)		(35), H <sub>2</sub> O <sup>M</sup>
G33.92+0.11	18 52 50.0	+00 55 29	+107	8.2	2.50	52(b,4), 36(b,4), 39(a,4)		
G34.26+0.15	18 53 18.5	+01 14 58	+58	3.7	5.22	219(b,2)		
G34.43+0.24MM1	18 53 18.0	+01 25 24	+57	3.4	0.19	100(41)		IRDC, E
G35.58-0.03	18 56 22.6	+02 20 27	+62	3.3	0.41	—(a,24)	I18538+0216	
IRAS18566+0408	18 59 09.8	+04 12 13	—	6.7	0.6	70(a,13)		
W49N	19 10 13.4	+09 06 14	—	—	—	—(b,15)		5-6 sources
G43.80-0.13	19 11 54.0	+09 35 50	+42	9.0	3.50	—(a,24)		
G45.07+0.13	19 13 22.0	+10 50 54	+62	6.3	14.1	113(b,2)		
G45.12+0.13	19 13 27.8	+10 53 37	+62	6.3	7.6	120—		
G45.47+0.05	19 14 25.6	+11 09 26	+62	6.3	1.1	81(b,2), 59(a,3), 44(b,4)		
W51IRS2	19 23 40.0	+14 31 06	55	5.1	30	535(b,2)	W51N or W51d	(39), (40)
W51e2 + W51e8	19 23 43.9	+14 30 15	55	5.1	15	460(b,16), 350(b,16)		(39), (40)
IRAS19442+2427	19 46 20.9	+24 35 14	+22	—	0.30	41(a,4)		
G61.48+0.08	19 46 49.0	+25 12 47	+1	2.5	0.91	70(a,26)	SH 2-88	
G69.54-0.98	20 10 09.0	+31 31 34	+12	1.8	0.1	98(b,2)	ON1	
G75.78-0.34	20 21 44.1	+37 26 39	0	4.1	1.90	88(b,4), 34(a,4), 89(b,2)		

Table 2.2 – continued from previous page

Name	R.A. (J2000)	Dec (J2000)	$V_{\text{LSR}}$ (km s $^{-1}$ )	d (kpc)	$L(10^5)^*$ ( $L_{\odot}$ )	$T_{\text{rot}}^{**}$ (K)	Other name	Comments $^{\dagger}$
G78.12+3.63	20 14 26.0	+41 13 32	-3	1.7	0.13	115(b,2)	I20126+4104	NCE <sup>(28)</sup>
G78.89+0.71	20 29 24.9	+40 11 21	-6	4.3	2.60	152(b,2)	AFGL 2591	
G81.87+0.78	20 38 36.1	+42 37 34	+7	2.0		135(b,2)	W75N	
G81.68+0.54	20 39 01.1	+42 22 49	-2	2.0	0.5	>71(b,2)	DR21(OH), W75S	
IRAS21397+5802	21 40 42.0	+58 16 10	-3	0.7		>50(d,45)	G175.58+2.45	(45)
CepA-HW2	22 56 17.9	+62 01 49	-2	0.7	0.2	>250(61)	I22543+6145	
NGC7538IRS1	23 13 45.4	+61 28 10	-56	2.8	1.3	310(b,16)		
NGC7538S	23 13 44.0	+61 26 50	-56	2.8	0.15	>50(b,29)		
IRAS23151+5912	23 17 21.0	+59 28 49	-54	5.7	1.0	150(a,d,9)		
W3(TW)	02 27 03.8	+61 52 25	-48	2.4	1.0	181(b,2)		(43)
AFGL5142	05 30 48.0	+33 47 54	-1	1.8	0.1	250(b,8)		H <sub>2</sub> O <sup>M</sup> , CH <sub>3</sub> OH <sup>M</sup>
OrionIRc2	05 35 14.5	-05 22 31	+7	0.46	0.1	179(b,2)		
Orion(OMC1S)	05 35 14.0	-05 24 02	+5	0.46	0.1	>100(b,60)		
IRAS05358+3543	05 39 13.1	+35 45 50	-17	1.8	0.63	220(b,55)		
S255N	06 12 53.0	+18 00 27	+8	2.6	1.0	>100(d,59)		H <sub>2</sub> O <sup>M</sup> , CH <sub>3</sub> OH <sup>M</sup>

Notes—(\*)IRAS luminosities unless other indicate; (\*\*)Temperature(Molecule $^{\dagger}$ ,Reference\*);

\*References—(1)(Cesaroni et al. 1992); (2)(Pankonin et al. 2001); (3)(Hofner et al. 1999); (4)(Olmi et al. 1993); (5)(Purcell et al. 2006); (6)(Zinchenko et al. 2000); (7)(Araya et al. 2005a); (8)(Zhang et al. 2007a); (9)(Beuther et al. 2007); (10)(Beuther et al. 2009); (11)(Furuya et al. 2008); (12)(Codella et al. 1997); (13)(Zhang et al. 2007b); (14)(Furuya et al. 2011); (15)(Wilner et al. 2001); (16)(Klaassen et al. 2009); (17)(Leurini et al. 2008); (18)(Dedes et al. 2010); (19)(Longmore et al. 2011); (20)(Galván-Madrid et al. 2009); (21)(Wu et al. 2010); (22)(Cesaroni et al. 2010); (23)(Beuther et al. 2006); (24)(Sollins et al. 2005a); (25)(Cyganowski et al. 2011); (26)(Gomez et al. 1995); (27)(Beuther et al. 2005); (28)(Cesaroni et al. 2005); (29)(Sandell & Wright 2010); (30)(Su et al. 2009); (31)(Rathborne et al. 2007); (32)(Zhang et al. 2009); (33)(Leurini et al. 2011); (34)(Beltrán et al. 2011); (35)(Hofner & Churchwell 1996); (36)(Cyganowski et al. 2008);



(37)(Beuther et al. 2006); (38)(de Vicente et al. 2000); (39)(Zhang & Ho 1997); (40)(Zhang et al. 1998a); (41)(Rathborne et al. 2008); (41)(Su et al. 2009); (42)(Araya et al. 2009); (43)(Wyrowski et al. 1999b); (44)(Araya et al. 2008); (45)(Beltrán et al. 2004a); (46)(Shi et al. 2010); (47)(Zapata et al. 2008b); (48)(Hunter et al. 2006); (49)(Beuther & Walsh 2008); (50)(Franco-Hernández et al. 2009); (51)(Longmore et al. 2007b); (52)(Hernández-Hernández et al. 2014); (53)(López et al. 2011); (54)(Cyganowski et al. 2013); (55)(Leurini et al. 2007a); (56)(Carlstrom & Vogel 1989); (57)(Fernández-López et al. 2011); (58)(Longmore et al. 2007a); (59)(Cyganowski et al. 2007); (60)(Zapata et al. 2007); (61)(Jiménez-Serra et al. 2007).

‡Molecules—(a)Ammonia ( $\text{NH}_3$ ); (b)Methylcyanide ( $\text{CH}_3\text{CN}$ ); (c)HCNO; (d)Methanol ( $\text{CH}_3\text{OH}$ ).

†Comments—M: Maser emission; E: EGO (Cyganowski et al. 2008); NCE: No centimetric emission detected.

## 2.2 Dust Emission

Although the  $\text{H}_2$  molecule is the main component of clouds, clumps, and cores associated with MSFRs, as a symmetric rotor its rotational transitions do not emit dipole radiation. Instead, other molecular species and dust must be used to measure the gas properties.

Dust grains are mixed with the molecular gas and absorb photons from stars that in turn emit thermal radiation at far-infrared and (sub)millimeter wavelengths. Thermal dust emission is optically thin at wavelengths longer than  $200\mu\text{m}$  (Hildebrand 1983), thus its (sub)millimeter continuum flux density is proportional to the temperature and number density of dust grains in the telescope beam.

In fact, the [Wood & Churchwell \(1989a\)](#) color criteria to identify UC HII regions are based precisely on the FIR emission from dust grains. The IRAS satellite was an all-sky mission, and the full Galactic plane was included. Hence, its Point Source Catalog provides a nearly complete census of MSFRs.

Mainly through single-dish observations, several works have found that dust associated with MSFRs is present in massive cores showing temperatures of  $\sim 25\text{-}60$  K, column densities of some  $10^{23}\text{ cm}^{-2}$ , masses of  $10^3\text{-}10^4 M_\odot$ , and luminosities in the range of  $10^5\text{-}10^4 L_\odot$  ([Beuther et al. 2002a](#); [Faúndez et al. 2004](#); [Williams et al. 2007](#); [Garay et al. 2007](#)). Such properties indicate that a luminous energy source has been already formed inside in most of them (see figures 2.5 and 2.6). Some of these massive cores are found toward IRDCs (e.g. [Rathborne et al. 2006](#)).

In order to estimate column density and mass of gas from millimeter-submillimeter emission of dust we follow [Hildebrand \(1983\)](#). Since emissivity of grains,  $Q_\nu$ , varies with frequency as  $\nu^\beta$  (e.g. [Hunter et al. 2000](#)), they emit with a modified Planck spectrum  $B_\nu(T_d)$ . Thus, the flux density  $F_\nu$  at frequency  $\nu$  from an optically-thin cloud at a distance  $D$  containing  $N$  dust grains at uniform temperature  $T_d$  with a geometric cross sectional area  $\sigma$  for each dust grain is related by:

$$F_\nu = \frac{N\sigma Q_\nu B_\nu(T_d)}{D^2} = \frac{N\sigma Q_\nu}{D^2} \frac{2h\nu^3}{c^2[\exp(h\nu/kT_d) - 1]}. \quad (2.1)$$

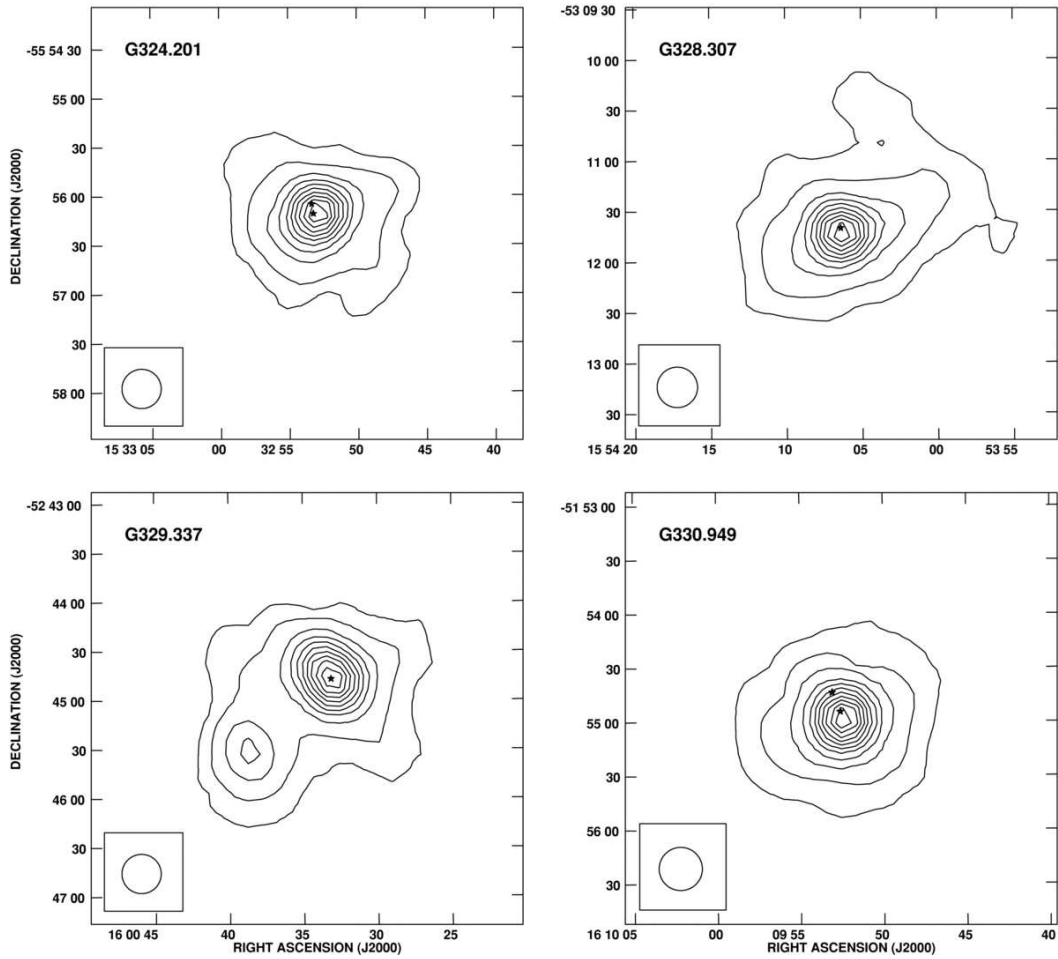


FIG. 2.5: Image of 1.2mm dust emission from SEST/SIMBA maps toward four massive cores. Stars mark the positions of the compact radio continuum. Masses derived from dust emission range from  $10^3$ - $10^4 M_{\odot}$ . Figure of [Garay et al. \(2010\)](#)

Since  $F_{\nu} \propto \sigma a \propto \mathcal{V}_{\text{grain}}$ , that is, the volume of a grain (where  $a$  is the grain radius), we can estimate the total mass of a cloud with flux density  $F_{\nu}$  as follows. The total volume of grain dust in a cloud is  $V = N\mathcal{V}_{\text{grain}} = 4N\pi a^3/3$ , thus eliminating  $N$  from Eq. 2.1 we have

$$F_{\nu} = \frac{3V\sigma Q_{\nu} B_{\nu}(T_d)}{4\pi a^3 D^2}, \quad (2.2)$$

but  $V = M_d/\rho_d$ , where  $\rho_d$  is the grain mass density and  $\sigma = \pi a^2$ . Thus

$$M_d = \frac{4a\rho_d F_{\nu} D^2}{3B_{\nu}(T_d)Q_{\nu}} \quad (2.3)$$

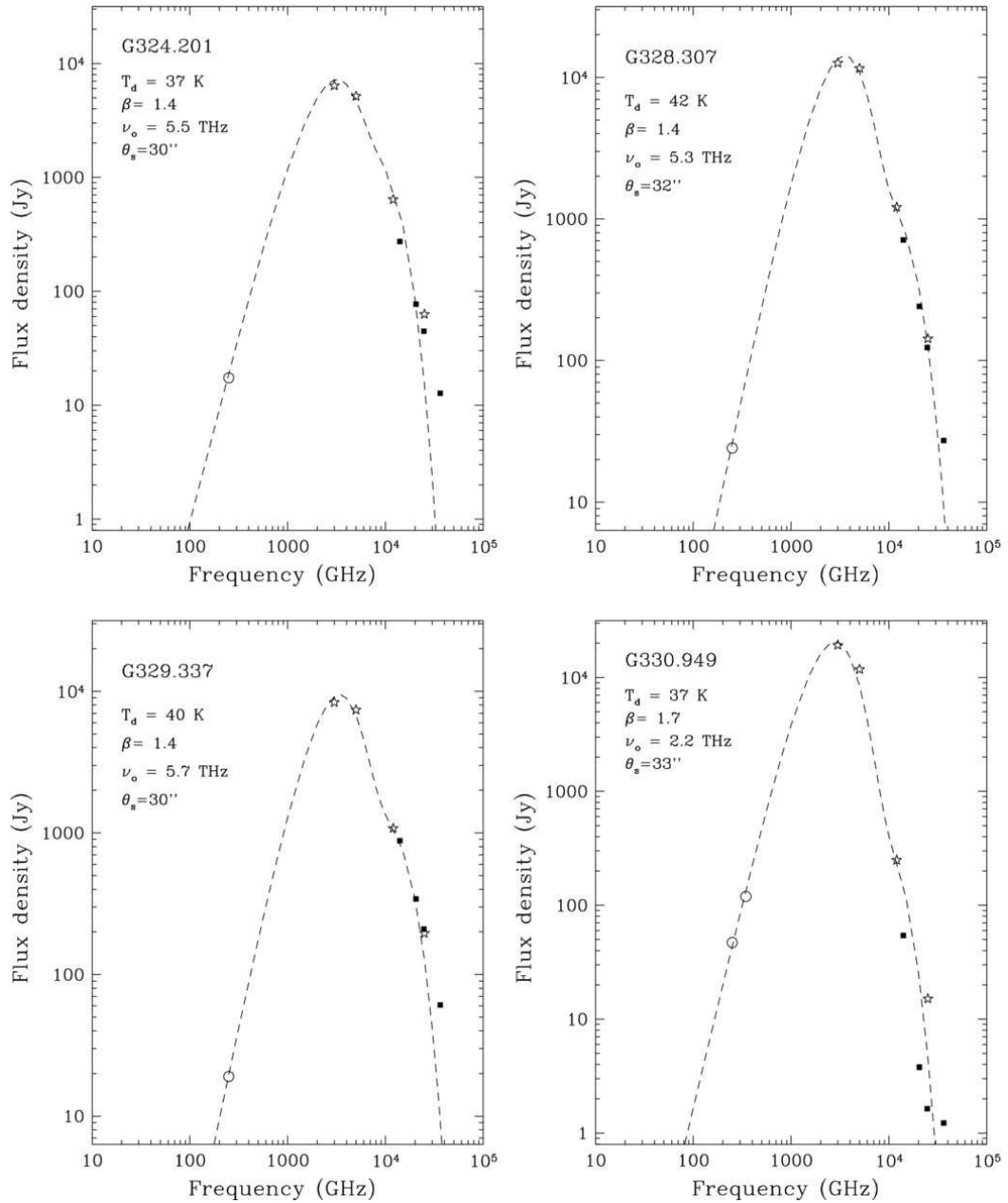


FIG. 2.6: SEDs of the four massive cores of figure 2.5. Stars mark *IRAS* fluxes, squares indicate *MSX* fluxes and the circle shows the SIMBA (1.2 mm) flux. The dashed curve is a fit to the spectrum using two modified blackbody functions of the form  $B_\nu(T_d[1 - \exp(\nu/\nu_o)^\beta])$  with different temperatures. The parameters derived from the fits, for the colder dust component, are given below the name of each source. Figure of Garay et al. (2010)

and

$$M_{\text{H}_2} = \frac{4R_d a \rho_d F_\nu D^2}{3B_\nu(T_d) Q_\nu} \quad (2.4)$$

where  $R_d$  is the gas to dust mass ratio, commonly assumed to be 100. Note that the inverse of  $4\rho_d a/3Q_\nu$  is  $\kappa_\nu$ , the mass absorption coefficient, which does not have a well-determined value and converts Eq. 2.4 in the common relationship  $M_{\text{H}_2} = F_\nu D^2 R_d / B_\nu(T_d) \kappa_\nu$ . Ossenkopf & Henning (1994) suggest  $\kappa_{1.3\text{mm}} = 1.0 \text{ cm}^2 \text{ g}^{-1}$ . In order to estimate  $\kappa_\nu$ , it is common to use  $Q_\nu = Q_{\nu_0} (\nu/\nu_0)^\beta$ , empirically scaled with  $Q_{\nu_0} = 7.5 \times 10^{-4}$  at  $\nu_0 = 2.4 \text{ THz}$  (Hildebrand 1983; Hunter et al. 2000), where  $\beta$  is the dust emissivity index.

Using typical values, i.e.,  $a = 0.1 \mu\text{m}$  and  $\rho_d = 3 \text{ g cm}^{-3}$ , and in the millimeter range ( $h\nu \ll kT$ ) we have the equations:

$$\left[ \frac{M_{\text{H}_2}}{M_\odot} \right] = 1.14 \left[ \frac{F_\nu}{\text{Jy}} \right] \left[ \frac{D}{\text{kpc}} \right]^2 \left[ \frac{T}{\text{K}} \right]^{-1} \left[ \frac{\nu}{1.2\text{THz}} \right]^{-2-\beta} \quad (2.5)$$

$$\left[ \frac{N_{\text{H}_2}}{\text{cm}^{-2}} \right] = \frac{6.25 \times 10^{13}}{\theta^2} \left[ \frac{F_\nu}{\text{Jy}} \right] \left[ \frac{T}{\text{K}} \right]^{-1} \left[ \frac{\nu}{1.2\text{THz}} \right]^{-2-\beta} \quad (2.6)$$

where  $\theta$  is the source size (diameter) in radians. Using  $\beta = 1.5$  at  $\nu = 220 \text{ GHz}$ ,

$$\left[ \frac{M_{\text{gas}}}{M_\odot} \right] = 432.0 \left[ \frac{F_\nu}{\text{Jy}} \right] \left[ \frac{D}{\text{kpc}} \right]^2 \left[ \frac{T}{\text{K}} \right]^{-1} \quad (2.7)$$

$$\left[ \frac{N_{\text{H}_2}}{\text{cm}^{-2}} \right] = \frac{2.36 \times 10^{16}}{\theta^2} \left[ \frac{F_\nu}{\text{Jy}} \right] \left[ \frac{T}{\text{K}} \right]^{-1} \quad (2.8)$$

where  $\theta$  is the source size (diameter) in radians.

In MSFRs and HMCs the dust would be expected to have a distribution of temperatures with the hottest grains near the young embedded stars and cooler grains lying in the outer parts —if there are no external heating sources. Thus, a single fit to the entire IR through millimeter spectrum with a modified Planck function of a single

temperature is difficult. However, accurate estimates of the gas mass can be obtained by considering one or two dust temperature components (see figure 2.6).

One important issue at radio-frequencies is that continuum emission from MSFRs can be produced both by thermal bremsstrahlung of ionized gas and by the warm dust. Confusion at millimetric wavelengths could be important. We must remove the former emission in order to correctly estimate column density and gas mass. To derive a rough estimate of the free-free contribution from UCHII regions, we can extrapolate the centimetric emission assuming optically thin free-free emission, that is  $S_\nu \propto \nu^{-0.1}$  (see chapter 1). Thus we assume that the remaining continuum emission is due to thermal dust. We apply this procedure to the 17 HMCs observed at 1.3 mm; the results are presented in chapter 4.

## 2.3 Molecules and Chemistry

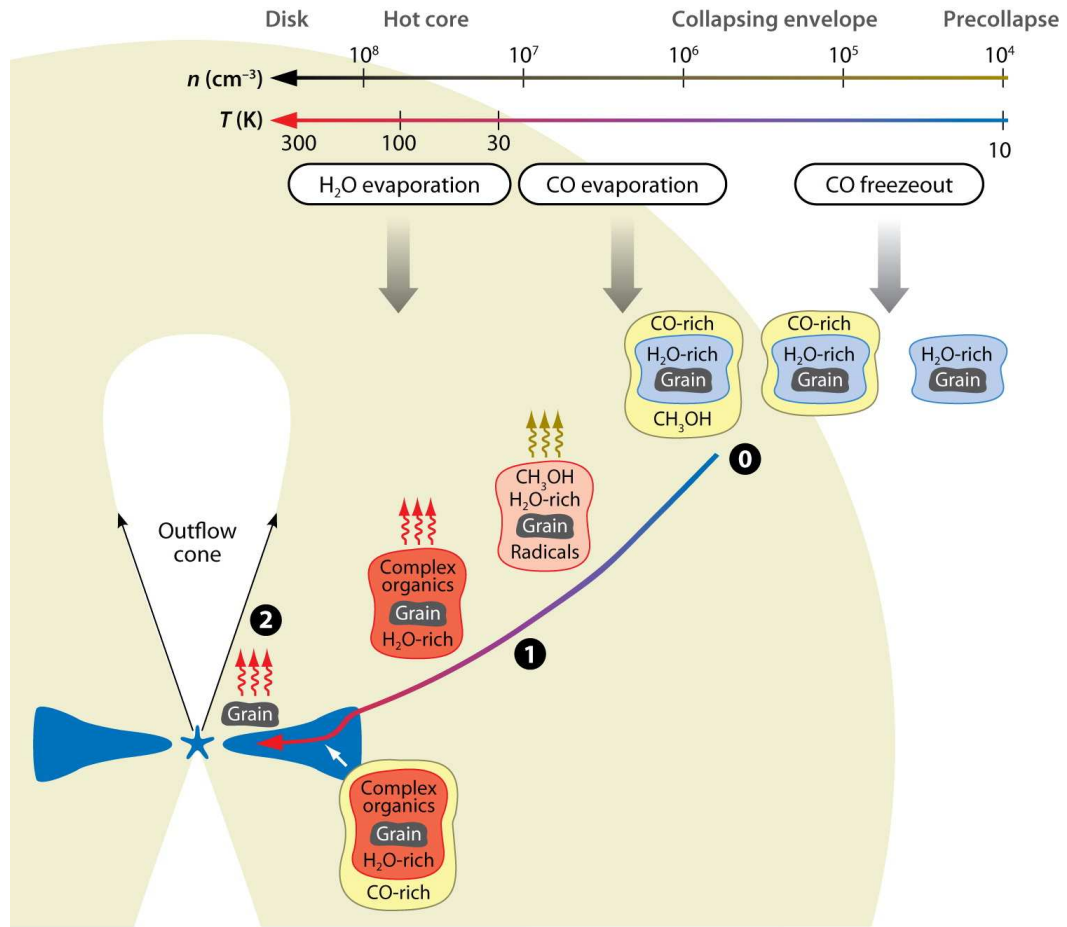
Early centimeter-wave observations of HMCs concentrated on a few molecular species, such as  $\text{NH}_3$ , OH,  $\text{H}_2\text{CO}$ , and  $\text{H}_2\text{O}$ . Particularly useful was the symmetric top  $\text{NH}_3$  (Ho & Townes 1983) to estimate density and temperature, and the OH and  $\text{H}_2\text{O}$  maser spots to obtain very precise positional information (Reid & Moran 1983). However, during the last three decades, molecular surveys at mm and submm wavelengths have shown an impressive number of molecular species—some of them organic and closely associated with prebiotic chemistry—, toward the HMCs (see Figure 2.2). Until the late 1970's such a variety of exotic chemical compounds had been detected only toward comets. To date, over 120 molecules have been detected in MSFRs and cold clouds through rotational transitions, primarily at millimetric wavelengths.

Millimeter wave rotational transitions provide a useful probe of the physical conditions in molecular clouds. The line intensity is related to the density and temperature of the gas, while the shape of the line profile shows dynamical phenomena such as velocity of the material. If we measure the density of a region by means of a particular molecular species, we can estimate its abundance, and thus study the chemical characteristics.

The chemical species found in MSFRs are often indicators of current (or past) physical conditions and gas dynamics. For example, molecules such as SiO, CO, and H<sub>2</sub>CO — and their isotopes — are commonly found in molecular outflows, while CH<sub>3</sub>CN, NH<sub>3</sub>, HC<sub>3</sub>N, and HCOOCH<sub>3</sub> are associated with the inner-most parts of cores, probably tracing structures such as toroids and disks (a schematic of a HMC is shown in figure 2.7). In some cases, the same species appears to trace both outflows and hot cores (e.g. [Leurini et al. 2011](#)). Of course, high angular resolution is necessary to disentangle different structures. Also, it is interesting that although the same chemical species are usually present, there can be substantial variation in their abundances from source to source. This suggests that the interstellar medium is probably homogeneous before the formation of protostellar objects, and chemical differences are a consequence of formation and destruction rates, and the particular physical conditions of gas and dust.

Astrochemical models of HMCs published to date assume that they are internally heated by protostars (e.g., [Blake et al. 1987](#); [Brown et al. 1988](#); [Charnley et al. 1992](#)) (see [Herbst & van Dishoeck 2009](#), for an extensive review). As the protostars evolve, heat and radiation evaporate grain mantles, releasing molecular species formed earlier in a cold-gas phase or on dust grains in surface-chemistry reactions. Expelling these molecules into a warm-hot gas phase fuels a much more complex and rich chemistry ([van Dishoeck & Blake 1998](#)). Eventually, the embedded protostar ionizes the surrounding environment, forming an UC HII region and complex molecules are destroyed owing to exposure to a harder radiation field.

Because MSFRs evolve rapidly ( $\sim 10^5$  yr) the chemical reactions often do not have time to establish a steady state equilibrium. Thus, the relative abundances of molecular species will probably be unique in time, under similar physical conditions. This supposition opens a window to the use of accurate models of chemical networks and observations, using the so called “chemical clocks”: molecules that can be used to determine the age of MSFRs (e.g. [Charnley 1997](#); [Wakelam et al. 2004](#)).




 Herbst E, van Dishoeck EF. 2009.  
Annu. Rev. Astron. Astrophys. 47:427–80

FIG. 2.7: Schematic of a HMC. Figure of [Herbst & van Dishoeck \(2009\)](#).

### 2.3.1 Chemical reactions

Chemical reactions describe how atoms, ions, and molecules can generate other species. They are the building blocks of chemical models to simulate steady state chemical conditions or time dependent chemical evolution. If we consider a simple chemical reaction as





then  $A$  and  $B$  are precursors while  $C$  and  $D$  are products. The reaction rate can be written as

$$d[A]/dt = d[B]/dt = -k_1[A][B], \quad (2.10)$$

where  $[A]$  and  $[B]$  are the concentrations of  $A$  and  $B$ , and  $k_1$  is the rate coefficient (see Herbst 1999). The reaction rate from  $A$  and  $B$  to  $C$  and  $D$  depends on the concentrations of  $A$ ,  $B$  and  $k_1$ . If the reaction can occur in the opposite direction from  $C$  and  $D$  to  $A$  and  $B$  simultaneously, the reaction rate depends on  $A$ ,  $B$ ,  $C$  and  $D$  and the reverse reaction coefficient. The rate coefficient depends on the energy barrier of the chemical reaction  $E_b$ , temperature and a slightly temperature-dependent parameter  $\alpha(T)$  as

$$k_1 = \alpha(T)e^{-E_b/kT}, \quad (2.11)$$

where  $k$  is the Boltzmann constant (Herbst 1999). We note that  $A$ ,  $B$ ,  $C$  and  $D$  can be photons, electrons, atoms, ions or molecules in gas phase. The chemical networks include a large range of reaction types, including various neutral–neutral reactions, ion–molecule reactions, and the electron recombination of ions, as well as ionization and photodissociation processes. Due to cosmic rays penetrate within star forming regions, some degree of ionization is present in the gas (typically  $X_e > 10^{-9}$ ), thus ions drive much of the gas-phase chemistry.

At low densities typical in molecular clouds, reactions in the gas phase involve two bodies. Three-body reactions only play a role in shocks and in the inner regions of protoplanetary disks, where molecular densities exceed  $\sim 10^{12} \text{ cm}^{-3}$  (Hogerheijde 2005). At low temperatures the chemistry is dominated by gas phase ion-molecule reactions, with typical reaction rates of  $\sim 10^{-9} \text{ cm}^{-3} \text{ s}^{-1}$ . Neutral-neutral reactions have rates between  $\sim 10^{-12}$  and  $\sim 10^{-10} \text{ cm}^{-3} \text{ s}^{-1}$ , and large activation energy barriers, thus they only take place efficiently in warm, dense gas (Hogerheijde 2005).

The process of molecules forming within ice mantles and evaporating from grain surfaces can be described by a reaction equation similar to chemical reactions,



where  $:$  means adsorption of a species, and  $\mathcal{G}$  is the dust grain. The desorption rate of molecules from grain surfaces is similar to the rate coefficient,

$$k_s = \nu_m e^{-E_s/kT}, \quad (2.13)$$

where  $\nu_m$  is a vibrational frequency of the molecule and  $E_s$  is the desorption energy.

The grain surface acts as a catalyst for reactions at low temperatures (van der Tak 2005); due to the long time over which species remain bound, reactions with large activation energies can proceed on the grains. For example, atomic hydrogen is extremely mobile on the grain surfaces and can lead to the production of hydrogenated species such as  $\text{H}_2$ ,  $\text{CH}_4$ , and  $\text{NH}_3$ . Moreover, the dominant water ice in grain mantles is produced by the sequential hydrogenation of O atoms landing on a grain:  $\text{O} : \mathcal{G} : \text{OH} \rightarrow \mathcal{G} : \text{H}_2\text{O}$ . Likewise,  $\text{CH}_3\text{OH}$  is formed once CO —produced in the gas phase— accretes onto grains and is hydrogenated via another sequence of reactions (Charnley et al. 1997).

### 2.3.2 Chemical Evolution in MSFRs

The formation of molecules in MSFRs is generally considered to follow three stages (Herbst & van Dishoeck 2010):

(1) **A cold phase** dominated by low-temperature ( $< 10$  K) in clouds of gas with density of  $> 10^4 \text{cm}^{-3}$ . Gas-phase chemistry is dominated by ion-molecule and neutral-neutral reactions, where main products are small radicals and unsaturated molecules —species that contain carbon-carbon double bond ( $\text{C}=\text{C}$ ) or triple bond ( $\text{C}\equiv\text{C}$ ). However, abundance of more saturated species such as  $\text{CH}_3\text{OH}$ ,  $\text{CH}_3\text{CHCH}_2$ , and  $\text{CH}_3\text{CHO}$  are not well explained only by gas-phase reactions, and dust chemistry is necessary.

During the early, cold era massive cores begin an isothermal collapse and single atoms and molecules, such as  $\text{CO}$ ,  $\text{C}_2\text{H}_2$  and unsaturated carbon chains, are adsorbed onto dust

grains (carbon and silicon) and form ice-mantles. The resulting increase in density causes molecules to condense on dust grains at timescales of  $t_{\text{accr}} \sim 2 \times 10^9 (n_{\text{H}} g_s)$  sec, where  $g_s$  is the probability that a molecule sticks on the grain (Hogerheijde 2005; Williams 1993) and  $n_{\text{H}}$  is the density of atomic hydrogen. Surface chemistry produces a new set of complex molecules such as  $\text{CH}_3\text{OH}$ ,  $\text{H}_2\text{O}$ ,  $\text{CO}_2$ ,  $\text{H}_2\text{CO}$ , and  $\text{HCOOCH}_3$ . (see Charnley et al. 2001; Garrod et al. 2006). While hydrides are formed on the grain surface, atomic hydrogen may also react with other hydrogen atoms to form  $\text{H}_2$ , which rapidly desorbs from the grain. Other atomic species may also be sufficiently mobile at low temperatures to react with each other or with radicals to form partially hydrogenated species such as  $\text{OH}$ ,  $\text{NH}_2$ , and  $\text{CH}_3$ .

An important hydrogenation involves the  $\text{CO}$ , which results in the formation of two key species: formaldehyde and methanol. (For more details about formation of  $\text{CH}_3\text{OH}$  see the next section).

Except  $\text{H}_3^+$ , practically all species will condense onto the dust grains over time, and molecules formed from  $\text{H}_3^+$  such as  $\text{N}_2\text{H}^+$  and  $\text{HCO}^+$ , may remain as good tracers of early collapsing cores (Bergin & Langer 1997; Hogerheijde et al. 1997; Rawlings et al. 2004) or may trace relic outflows (e.g. Klaassen & Wilson 2007; Hunter et al. 2008).

Ices will remain on the grains until protostars begin to heat the environment, rising the dust temperature.  $\text{CO}$  ice will desorb above 20 K and  $\text{H}_2\text{O}$  at  $\sim 90$  K (e.g., Tielens & Hagen 1982; Tielens 2005).

(2) **A warm phase** in which massive cores show high accretions rates and the first protostellar objects increase the temperature of dense gas by some tens of Kelvins. The sublimation of ice mantles does not occur in a simple manner, and recent works have combined chemical models with results of so-called temperature-programmed desorption (TDP) experiments Collings et al. 2004 (e.g. Garrod & Herbst 2006; Viti et al. 2004) When molecules come in contact with grain surface, they minimize their energy by forming a bond with the grain. As temperature increases, the energy transferred to the absorbed species will cause it to desorb. The temperature at which this happens is known as the desorption temperature. The TDP approach allows complex phase changes within the ices during warming to be included. Nowadays, gas–grain chemical

models alone cannot reproduce such behaviour, due to the lack of a compatible microscopic treatment for phase changes (see [Garrod & Widicus Weaver 2013](#), for a recent chemical review).

However, models show that at  $> 20$  K, H atoms no longer reside long enough on the grain surfaces to be the dominant reactants and some molecules such as CO, CH<sub>4</sub>, and N<sub>2</sub> begin to sublime from grain ice-mantles. The heavier species remaining on the grain surfaces (e.g., H<sub>2</sub>O, H<sub>2</sub>CO, and CH<sub>3</sub>OH) begin to diffuse more quickly and subsequent chemical reactions produce much more complex molecules such as methyl formate (HCOOCH<sub>3</sub>), dimethyl ether (CH<sub>3</sub>OCH<sub>3</sub>), and formic acid (HCOOH) (e.g. [Garrod & Herbst 2006](#); [Garrod et al. 2008](#)). These molecules are examples of a first generation of organic complex molecules.

(3) **A hot core phase** in which high temperatures ( $>100$  K) sublime all ice-mantles, and only gas phase chemistry is possible, including exothermic and endothermic reactions. At this stages high densities ( $10^5 - 10^8$  cm<sup>-3</sup>) of molecular hydrogen are estimated; dynamical phenomena such as high accretion rates, rotating gas, jets and molecular outflows could be affect the chemical evolution and modify abundances of some molecular species (see the last section in this chapter).

Chemical abundance of some molecules in HMCs, CH<sub>3</sub>OH for example, are well-explained by sublimation of the hydride-rich species in ice mantles, formed through surface chemical reactions at an earlier phase. However, for other complex molecules, such as CH<sub>3</sub>CN, CH<sub>3</sub>COOH (acetic acid), or CH<sub>3</sub>COCH<sub>3</sub> (Acetone), chemical processes in a hot gas-phase reproduce adequately their abundances. However, this simple picture may be more complex than previously thought.

Seminal works of hot-core chemical models considered the gas-phase reactions as the focus to explain their molecular richness. For example, Blake et al. (1987) presented a gas-phase model to explain the oxygen-containing complex molecules in the Orion Compact Ridge. Millar et al. (1991) used much of the chemistry of Blake et al. (1987) but found that it was necessary that methanol be injected into the source in order to explain abundances in that region. In the important work of Charnley et al. (1992) they started with warm gas-phase initial molecular abundances (rich in ammonia and methanol) and found reasonable agreement with CH<sub>3</sub>CN observations of the Orion Hot Core at a time of  $6.3 \times 10^4$  years, and with the Compact Ridge at  $10^4$  years. However,

these results have been called into question by recent works (e.g., Garrod & Herbst 2006), in which some O-rich complex species may be produced by surface reactions of radicals derived from  $\text{H}_2\text{O}$ ,  $\text{H}_2\text{CO}$ , and  $\text{CH}_3\text{OH}$ .

In general, past models considered two temperature values to model the hot-core chemistry, a low value of the order of 10 K that correspond to the early stage of ice formation and a later stage with high temperature, of  $>100$  K. Some models (e.g., Lintott et al. 2005) include an isothermal collapse in the cold stage, allowing the evolution from a diffuse cloud to a dense core. The hot stage usually begins with the instantaneous ejection of species, once sublimation of ice mantles on dust occurs. However, recent models include gas-phase and surface chemistries through cold, warm and hot stages.

Both in past and recent models, neutral–neutral and ion–molecule reactions play a main role in gas-phase complex molecule production in HMCs; for example, such processes lead to the formation of various sulfur-bearing and nitrogen-bearing molecules following sublimation of hydride-species and production of single molecules (i.e.,  $<6$  atoms). Fully hydrogenated molecules in the hot gas-phase are common, including  $\text{H}_2\text{O}$ ,  $\text{NH}_3$ ,  $\text{HCN}$ ,  $\text{HNC}$ ,  $\text{HNCO}$ ,  $\text{H}_2\text{S}$ ,  $\text{CH}_3\text{CN}$  among others.  $\text{HCN}$ , for example, is routinely detected toward HMCs, traces gas of many hundreds of Kelvin and show high abundances up to  $10^{-5}$  relative to  $\text{H}_2$  (Rolffs et al. 2011). Moreover,  $\text{HCN}$  appears to be formed in the hot gas phase with abundance increasing with time, as more complex species are destroyed by ion–molecule reactions.  $\text{HCN}$  is a precursor of  $\text{CH}_3\text{CN}$ , which has been used in this thesis work to estimate temperature, density and abundance toward 17 HMCs. The  $\text{CH}_3\text{CN}$  formation through  $\text{HCN}$  is discussed in the next subsection.

In summary, simulations of hot-core chemistry have seen great advance during the two past decades. Nowadays, great emphasis has been placed on including both gas-phase and grain/ice- surface reactions, through the cold, warm, and hot stages. Recent experimental studies have shown that many complex species detected toward HMCs may be formed in terrestrial laboratory ices under similar conditions of temperature, pressure, and radiation. In general, the simulations agree with observations for the most abundant molecular species.

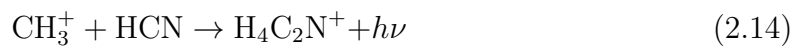
However, gas–grain models including TDP and new measurements of gas-phase reaction rates are necessary in order to explain some hot-core abundances (e.g., Garrod &

Weaver 2013). Also, dynamics of MSFRs have not yet been totally coupled with chemical reaction networks, and only a few chemical-dynamical models have been reported (e.g., Lintott et al. 2005).

### 2.3.3 Molecules in this thesis

#### CH<sub>3</sub>CN

CH<sub>3</sub>CN (figure 2.8) is a classical hot core tracer (e.g., Araya et al. 2005a; Pankonin et al. 2001). It forms from evaporated grain mantles, thus it is a “daughter molecule”. Although alternative formation routes through grain surface chemistry are proposed (Millar et al. 1997), the dominant gas-phase formation route is through radiative association (Charnley et al. 1992; Millar et al. 1997; Mackay 1999):



followed by dissociative recombination



The precursor HCN is formed in the gas phase through the reaction of atomic N with HCO, CH<sub>2</sub> or CH<sub>3</sub><sup>+</sup>.

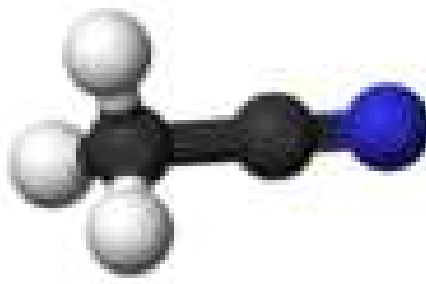


FIG. 2.8: Diagram of the methyl cyanide molecule.

One major conclusion from this thesis (see chapter 4) is that CH<sub>3</sub>CN increases in abundance at higher temperatures, which is consistent with an increased production

of HCN in N-rich environments. Above  $\sim 200$  K reactions of O and OH with  $H_2$  operate very efficiently to convert all the initial oxygen into  $H_2O$  (Charnley 1997) and cores at higher temperatures are expected to be rich in N-bearing species (Rodgers & Charnley 2001). For example, the following reactions become important at high temperatures:



Steady state models (Schilke et al. 1992) predict that the HCN abundance and the HNC/HCN ratio decline with increasing temperature and density. Support for this scenario comes from Wyrowski et al. (1999) who measured the peak position of the N-bearing species to be at a higher temperature than the peak of the O-bearing species in the W3 star forming complex. Goldsmith et al. (1981) observed this trend toward four molecular clouds, and our results, presented in chapter 4, also support this scenario.

### CH<sub>3</sub>OH

Methanol (figure 2.9) is ubiquitous and associated with different star forming regions, from cold dark clouds, where abundance is only  $\sim 10^{-9}$ , to HMCs where reach  $\sim 10^{-7} - 10^{-6}$  (Menten et al. 1988).  $CH_3OH$  emission has been used as tracer of density and temperature, and molecular outflows (Walmsley et al. 1988; Menten et al. 1988; Kalenskii et al. 1997; Bachiller et al. 1998; Sutton et al. 2004)

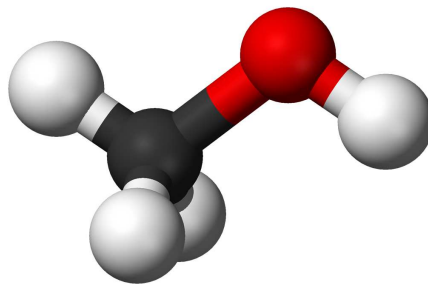
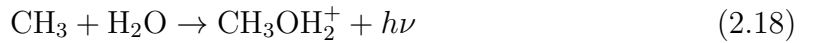


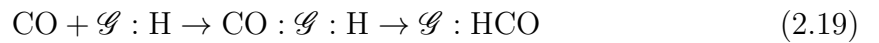
FIG. 2.9: Diagram of the methanol molecule.

At temperatures below 100 K, production of  $CH_3OH$  in the gas phase is governed by the radiative association reaction



followed by electronic recombination to form  $\text{CH}_3\text{OH}$  plus an hydrogen atom (Lee et al. 1996). However, the initial reaction was found to be much slower than the earlier theoretical prediction (Luca, Voulot & Gerlich 2002). In addition, this reaction set yields abundances of only  $\sim 10^{-11}$ , insufficient to explain the observations.

Thus, the primary formation route of methanol is the hydrogenation sequence on dust grains ( $\mathcal{G}$ ) of CO:



which is an efficient reaction at temperatures of  $\sim 10$  K (Charnley et al. 1997; Watanabe & Kouchi 2002) but not at higher temperatures because the residence time of hydrogen atoms on grains becomes too short. By  $10^6$  yr at 10 K, the fractional abundance of  $\text{CH}_3\text{OH}$  in the ice mantle on dust grains reaches  $\sim 10^{-5}$ . Thus, its formation by surface chemistry is favoured by most works (Grim et al. 1991; Dartois et al. 1991; Pontoppidan et al. 2004; Tielens & Allamandola 1987; Allamandola et al. 1992; van der Tak et al. 2000; Menten et al. 1988).

## 2.4 Dynamics

MSFRs have a very strong dynamical impact on their surroundings caused by stellar winds, expanding ionized regions, outflows and jets, accretion and collapse, rotation of disks and toroids, and motions of the stars and the entire region through molecular clouds.



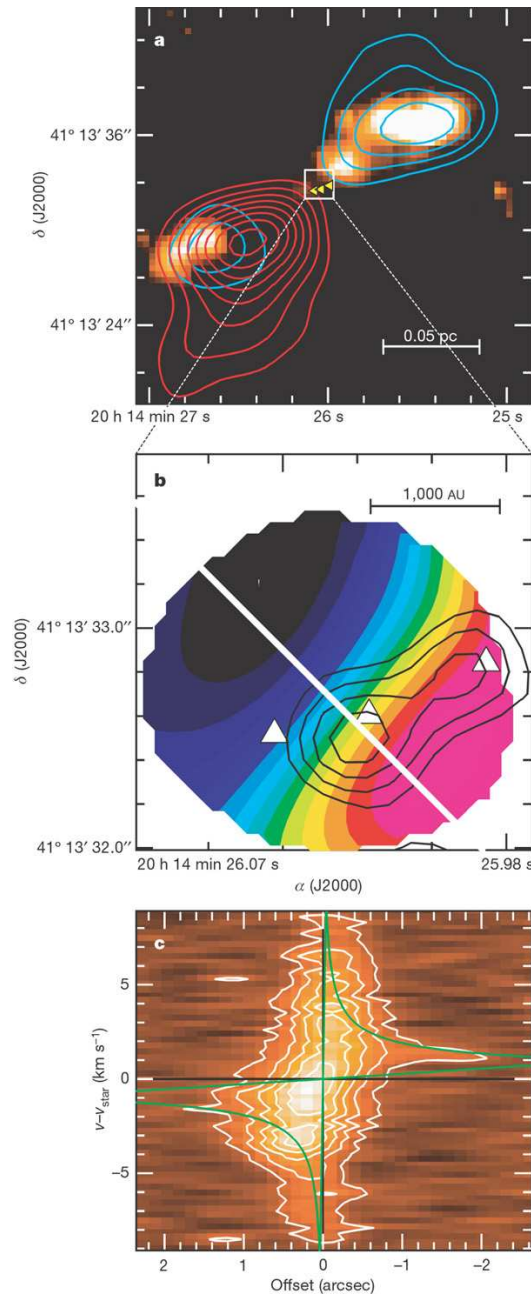


FIG. 2.10: Figure of Cesaroni et al. 2006. Circumstellar disk and associated bipolar outflow in the MSFR IRAS 20126+4104. **a**, red- and blueshifted  $\text{HCO}^+(1-0)$  contours tracing the outflow and overlaid on the  $2.2 \mu\text{m}$   $\text{H}_2$  emission. **b**, contours of the  $3.6 \text{ cm}$  continuum are overlaid on a velocity map of  $\text{C}^{34}\text{S}(5-4)$ . A velocity gradient perpendicular to the outflow is shown by the color scale. The triangles mark the positions of the  $\text{H}_2\text{O}$  maser spots. **c**, position-velocity diagram of  $\text{C}^{34}\text{S}(5-4)$  line emission outlined by the white line in **b**. Green lines denote the region from which emission is expected in the case of keplerian rotation about a  $7M_{\odot}$  star.

Moreover, recent observations of HMCs and young massive protostars have detected rotating structures called “toroids” (Cesaroni 2005), in sources such as G24.78+0.08 (Beltran et al. 2004, 2005), G28.20–0.05 (Sollins et al 2005), IRAS 18089–1732 (Beuther & Walsh 2008), NGC 7538 S (Sandell et al 2003) and G20.08–0.14N (Galvan-Madrid et al. 2009), and IRAS 20126+4104 (see figure 2.10; Cesaroni et al. 2006).

One way to study the central HMCs and search for observational signatures of rotation is to detect high density tracing molecules to see whether a velocity gradient perpendicular to the outflow exist. As yet there is no consensus on what molecular species best traces rotating structures (Beuther et al. 2007; Leurini et al. 2011). But it turns out that organic species with low optical depths are associated with the innermost structures, and they could be particularly useful as tracers of temperature, density and dynamics of gas around the central embedded protostars (Araya et al. 2005). This is the case of CH<sub>3</sub>CN which is commonly used. One result of our observations (see chapter 4) is that we confirm rotational motions of dense gas in most of our sources; some of them previously unreported.

These structures are somewhat different from the classical low-mass disks in the sense that show typical radii of thousands of AU and masses similar to or slightly larger than the mass of the central source. High angular resolution observations have shown that most of these toroids are in Keplerian rotation, and may be feeding inner accretion disks, surrounding multiple protostars (e.g., Zapata et al. 2009).

Recently, chemical models have been used to understand the effects of infall and evolution of high-mass protostars. These are interesting examples of how chemistry in HMCs could be affected by the dynamics of the cores. For example, chemical models of Lintott et al. (2005) predict an enhancement of CS and reduction of N<sub>2</sub>H<sup>+</sup> abundance toward massive cores collapsing above the free-fall rate (accelerated collapse). Low-mass star forming regions show the opposite behaviour. Lintott and collaborators suggest that high densities would be achieved before freeze-out had removed the molecules responsible for N<sub>2</sub>H<sup>+</sup> loss, while the high densities promote CS formation. Their results are similar even if the free-fall rate is doubled.

Their model is confirmed by observations of CS and other species that show similar behaviour (Pirogov et al. 2007). However, discrepancies between the model and observations show that the SO abundance would have a similar distribution to N<sub>2</sub>H<sup>+</sup>,

whereas observations of the star forming region S255 show it to be more similar to CS. Also, systematic collapse motions predicted by this model should give asymmetric or self-absorbed profiles of optically thick lines, (e.g., CS), which are not observed in most of the sources (Pirogov et al. 2007). However, this last effect could be due to unresolved clumps with a low volume-filling factor, in which low optical depth produces nearly symmetric profiles. The observations of Pirogov et al. have low angular resolution ( $\sim 22''$ ) and the sources were selected by the presence of embedded clusters of stars or high IR-luminosities. Interferometric studies toward earlier evolutionary stages of MSFRs are necessary to test the predictions of Lintott and collaborators.

Also, Doty et al. 2006 used a model to trace chemical evolution in a collapsing massive protostar, including evolution of the central source and adsorption/desorption of ice mantles on grain dust. They find that infall of grains from cold exterior regions toward the warmer inner regions, reproduces and explains observed water abundances and distribution. Their results suggest a lifetime of  $\sim 10^5$  yr for HMCs and that massive star disks should contain most of the complex species on scales of less than few hundred AU.

Future high resolution observations and robust time-dependent chemical models are essential to understand the role of dynamical phenomena toward MSFRs and their chemistry.

# Chapter 3

## Spectral Lines As Tracers

Molecular astrophysics began with the first molecule to be discovered, CH, in 1937 by [Swings & Rosenfeld \(1937\)](#). Later, the new field of radio astronomy in 1960s and 1970s showed that a vast number of different molecules, transitions and its isotopes can be used to study the conditions of clouds, star clusters, and galaxies. Molecular astrophysics and astrochemistry joined as valuable fields to understand a large number of astronomical phenomena. Today, around 200 molecules have been detected (including deuterated molecules) in the interstellar medium and circumstellar shells. The detection of molecules in the space is one of the most important discoveries in modern astronomy.

Gas in star forming regions emits and absorbs spectral line and continuum radiation, that can be used to estimate their physical and chemical conditions. In this chapter we will summarize how radiation and molecules interact to form line spectra at millimeter wavelengths, allowing the derivation of physical parameters toward HMCs and massive cores in IRDCs.

Molecules mainly have three kinds of transitions: electronic, vibrational and rotational, depending of the molecular configurations and energies. **Electronic transitions** are very energetic, typically a few eV and corresponding to frequencies of some  $10^{15}$  Hz, that is, lines in the visual or UV regions of the spectrum. **Vibrational transitions** occur by oscillations of nuclei relative to equilibrium positions. Typical energies are 0.1–0.01 eV, corresponding to frequencies of some  $10^{13}$  Hz, in the infrared portion of

the spectrum. Finally, **rotational transitions** are due to rotation of the molecule as a whole (including nuclei), they have energies of some  $10^{-4}$  eV, and emit at cm and mm wavelengths. Thus, vibrational energy ( $E_{\text{vib}}$ ) and rotational energy ( $E_{\text{rot}}$ ) correspond to the (slow) motion of the nuclei of the molecule, while electronic energy ( $E_{\text{el}}$ ) depends on the (fast) motions of the electrons.

Transitions between different electronic states will produce spectral lines in the UV-optical range, thus for the radio-mm-submm part of the spectrum we can confine our study to rotational and some times vibrational transitions. Moreover, if we consider that molecular clouds have excitation temperatures between 10 K in cold clouds and some hundreds of Kelvin in HMCs, then we can expect excitation energies ( $kT_{\text{K}}$ ) less than  $\sim 0.05$  eV which correspond to rotational and vibrational transitions.

Molecular hydrogen ( $\text{H}_2$ ) is the most abundant molecule in the Universe and its formation occurs on dust grains—which act as a catalytic converter—where density of H atoms is  $\gtrsim 50 \text{ cm}^{-3}$ . Unfortunately,  $\text{H}_2$  is among the most difficult species to detect, because it is a homonuclear diatomic molecule (like  $\text{O}_2$  or  $\text{N}_2$ ), and thus does not have an electric dipole moment,  $\mu$ . Polar molecules such as CO, CS,  $\text{HCO}^+$  and their isotopes are strong emitters in rotational transitions and hence are workhorse probes of the interstellar medium (e.g. Turner 1974, 1991).

Despite the large number of species detected, only a handful have been used to estimate physical parameters of star forming regions. This is because of the difficult mechanic quantum treatment of the molecular structure and the complicated spectra of complex organic molecules. Also, the chemical behaviour of single molecules (i.e.,  $<6$  atoms) is rather better understood than that of more complex species. Thus, molecules such as SiO, HCN,  $\text{NH}_3$ , HNC,  $\text{CH}_3\text{OH}$ , and  $\text{CH}_3\text{CN}$  have been used as tracers of chemical evolution, lifetime of star forming regions, density and temperature, and phenomena such as molecular outflows and rotation of structures.

In this chapter, we will focus on the use of  $\text{CH}_3\text{CN}$  and  $\text{CH}_3\text{OH}$  as tracers of physical and chemical parameters. Their symmetric and slightly asymmetric rotor structures, respectively, make both species excellent tracers of temperature and density. Movement of gas—as rotation and outflows—can also be detected by these molecules. Moreover,  $\text{CH}_3\text{OH}$  shows maser emission, that has been used as velocity tracer in disks, toroids, and molecular outflows.

## 3.1 CH<sub>3</sub>OH Molecular Emission

CH<sub>3</sub>OH was discovered in the ISM by Ball et al. in 1970, using the 140-foot radiotelescope, of NRAO in Green Bank, West Virginia, observing at 834 MHz ( $\sim 36$  cm). Since then, over 200 transitions have been observed at radio frequencies, 20 of them showing maser emission. Both thermal and maser emission are considered as very useful tracers of MSFRs.

The molecular structure of the methanol molecule can be divided into the CH<sub>3</sub> group – with a tetrahedron structure – that rotates with respect to the OC bond. The presence of the H atom bond to the O makes the molecule an asymmetric top. The torsional motion of the OH with respect to the methyl group is “hindered” by the small increase in potential when the OH aligns with the H atoms of the CH<sub>3</sub> group.

The threefold symmetric torsional barrier in methanol leads to the existence of three torsional symmetry states, designated  $A$ ,  $E_1$ , and  $E_2$ . Transition selection rules only allow transitions from one  $A$ -level to another  $A$ -level, and the same between  $E$ -levels. Thus,  $A$ - and  $E$ -methanols can be considered as two distinct species. Both  $A$ - and  $E$ -type can generate maser emission.

Rotation states of methanol are characterized by  $J_K$ , in which  $J$  is the total angular momentum of the molecule and  $K$  is the component along the molecular symmetry axis.  $A$ -levels are torsionally degenerate, splitting the  $K$  levels into two pairs,  $A^+$  and  $A^-$ , and one uses  $K = |k|$  to designate levels, in which the quantum number  $k$  can be positive or negative. On the other hand,  $E$ -levels are doubly degenerate and are represented by  $K = (\pm)k$ .

For reviews of CH<sub>3</sub>OH emission as diagnostic tool see Leurini et al. (2004), Sutton et al. (2004), and Helmich et al. (1994).

### 3.1.1 CH<sub>3</sub>OH Masers

MASER or Microwave Amplification by Stimulated Emission of Radiation is the equivalent of the LASER for light at optical wavelengths. The first maser laboratory experiments were made by Charles Townes in 1954 (Gordon, Zeiger and Townes 1955).

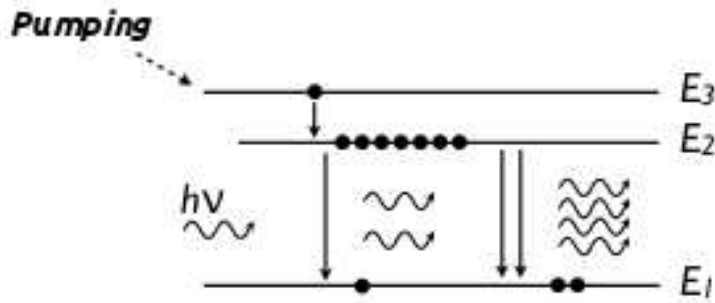


FIG. 3.1: Schematic of maser emission.

However, under terrestrial conditions most molecules are in their ground state without any amplification of their emission. To generate maser emission, the interstellar conditions must have at least three properties: the gas is out of thermal equilibrium with a population inversion of the energy states (high levels over-populated), a radiation field with *seed* photons with the same frequency as the maser emission, and sufficient coherent path length for the amplification.

Population inversion occurs when  $n_2/g_2 > n_1/g_1$  and the density must be below the critical density of the transition, otherwise the masers would be quenched by collisional de-excitation. This implies negative excitation temperatures (not physical temperature) and negative optical depth. Thus, the intensity of a maser line is  $T_L^0 \simeq |T_{ex}|e^{|\tau_0|}$ , i.e., radiation is exponentially amplified when interacting with the interstellar material.

Another important factor is that a pumping mechanism is required to sustain the population inversion, which can be either collisional or radiative pumping. To illustrate this situation (see Figure 3.1), consider that a molecular species has only three energy levels, in which  $E_1 < E_2 < E_3$ . Now consider that molecules excite from level 1 to 3, through (stimulated) absorption or collisional excitation, and then relax into the level 2 (process  $P_{12}$ ). De-excitation from level 2 to 1, through level 3 also is possible,  $P_{21}$ . If the transition rate of  $P_{12}$  is higher than  $P_{21}$ , then more and more molecules will populate the  $E_2$  level. The *inversion* occurs when more molecules are in state 2 than in 1. If a photon with a energy  $h\nu = E_2 - E_1$  passes through a region of gas with the above conditions and interacts with a molecule in the excited level 2, it will stimulate the emission of a second coherent photon at the same frequency, travelling in the same direction and with the same phase. These two photons can then stimulate the emission of two more photons and so on.

The emission observed in radio telescopes results from a huge number of individual photons with a preferential direction of de-excitation; then, the path length is determined by the length of the gas cloud with population inversion. Also, maser photons will only interact with molecules whose transition frequency has not been Doppler shifted outside the linewidth. We can say that such emission is beamed and strongly depends on the physical conditions of the interstellar medium.

Finally, maser emission comes from small regions, of the order of  $\sim 10^{13}$  cm, having well-defined positions and velocities. Molecular species that show maser emission toward MSFRs are H<sub>2</sub>O, OH, H<sub>2</sub>CO, HCN, NH<sub>3</sub>, and CH<sub>3</sub>OH, which can occur in either *A*- or *E*-type.

The CH<sub>3</sub>OH maser is characterized by two distinct classes, I and II. Collisionally excited **Class I** CH<sub>3</sub>OH masers are observationally well correlated with molecular outflows in MSFRs (Plambeck & Menten 1990; Johnston et al. 1992; Cragg et al. 1992; Kurtz et al. 2004). In the largest interferometric survey to date, Kurtz et al. (2004) found that 44 GHz Class I CH<sub>3</sub>OH masers were common in MSFRs and well correlated with shocked gas in outflows as traced by SiO and H<sub>2</sub>. Based on the relation of 95 GHz Class I CH<sub>3</sub>OH maser emission to molecular cores traced by CS and outflow shocks traced by H<sub>2</sub> in DR21 and on the close-to-systemic velocities of the masers ( $v_{\text{maser}} \sim v_{\text{LSR}_{\text{gas}}}$ ), Plambeck & Menten (1990) suggested that Class I CH<sub>3</sub>OH masers may be excited specifically in interface regions where outflows encounter surrounding molecular material.

On the other hand, **Class II** CH<sub>3</sub>OH masers, radiatively pumped by IR emission from warm dust (Cragg et al. 1992, 2005, and references therein), are associated exclusively with massive protostellar objects (e.g., Minier et al. 2003, Walsh et al. 2003). Sensitive searches toward low-mass protostars ( $L \lesssim 10^3 L_{\odot}$ ,  $M \lesssim 3M_{\odot}$ ; Minier et al. 2003; Bourke et al. 2005; Xu et al. 2008,  $3\sigma \lesssim 0.2$  Jy), including hot corinos (Pandian et al. 2008,  $3\sigma \sim 0.003$  Jy), have uniformly yielded null results. In addition to being an observationally robust result, the lack of 6.7 GHz Class II CH<sub>3</sub>OH masers toward low-mass protostars may be understood theoretically in the context of the excitation models: the energetics of low-mass objects do not produce regions with the necessary combination of dust temperature, density, and CH<sub>3</sub>OH abundance for 6.7 GHz maser emission (Minier et al. 2003; Pandian et al. 2008).



Class II CH<sub>3</sub>OH maser emission requires the presence of warm dust ( $T_d \geq 125$  K), which both releases CH<sub>3</sub>OH from icy grain mantles into the warm gas phase and emits the IR photons that pump the population inversions (Cragg et al. 1992; Minier et al. 2003; Cragg et al. 2005, and references therein). As a consequence, Class II masers may only be excited relatively near the central protostar, where dust temperatures are high.

### 3.2 CH<sub>3</sub>CN Molecular Emission

The CH<sub>3</sub>CN is a symmetric molecule with large dipolar momentum (3.91 Debyes) whose rotational levels, or  $K$ -ladders, are populated through collisions. Thus CH<sub>3</sub>CN is an excellent tracer of temperature in clumps and cores of molecular gas (Boucher et al. 1980). (NH<sub>3</sub>, HC<sub>3</sub>N, and CH<sub>3</sub>Cl molecules are examples of symmetric rotors).

CH<sub>3</sub>CN is a member of the  $c_{3v}$  group of symmetric tops, whose rotational energy levels may be described by two quantum numbers:  $J$ , the total angular momentum and  $K$ , the projection of  $J$  along the axis of symmetry. Individual  $J \rightarrow (J - 1)$  transitions are grouped into ‘rotational ladders’ labelled by their  $K$  values. (see Loren & Mundy 1984 for a detailed description).

For each  $J \rightarrow (J - 1)$  transition, selection rules prohibit radiative transitions between the  $K$  ladders and their relative populations are determined exclusively by collisional excitation. Assuming local thermal equilibrium and optically thin lines, the relative intensities of the  $K$ -components yield a direct measure of the kinetic temperature and column density.

The energy spacings between individual  $J$  levels are almost independent of  $K$  ladder, however, increasing centrifugal distortion causes successive  $K$ -components to shift to progressively lower frequencies. The offset in frequency is slight, and the  $K$ -components of a particular  $J \rightarrow (J - 1)$  transition may be observed simultaneously in a single bandpass, minimizing errors in their relative calibration. Spin statistics of the hydrogen nuclei divide CH<sub>3</sub>CN into two spin states, dubbed A and E.

Energy levels with  $K = 3n$ ,  $n = 0, 1, 2 \dots$  belong to the A state, while those with  $K \neq 3n$ ,  $n = 0, 1, 2 \dots$  belong to the E state. The A states have twice the statistical

weight of the E states. Neither radiation nor collisions convert between states; if formed in equilibrium conditions the A/E abundance ratio is expected to be  $\sim 1$  (Minh et al. 1993).

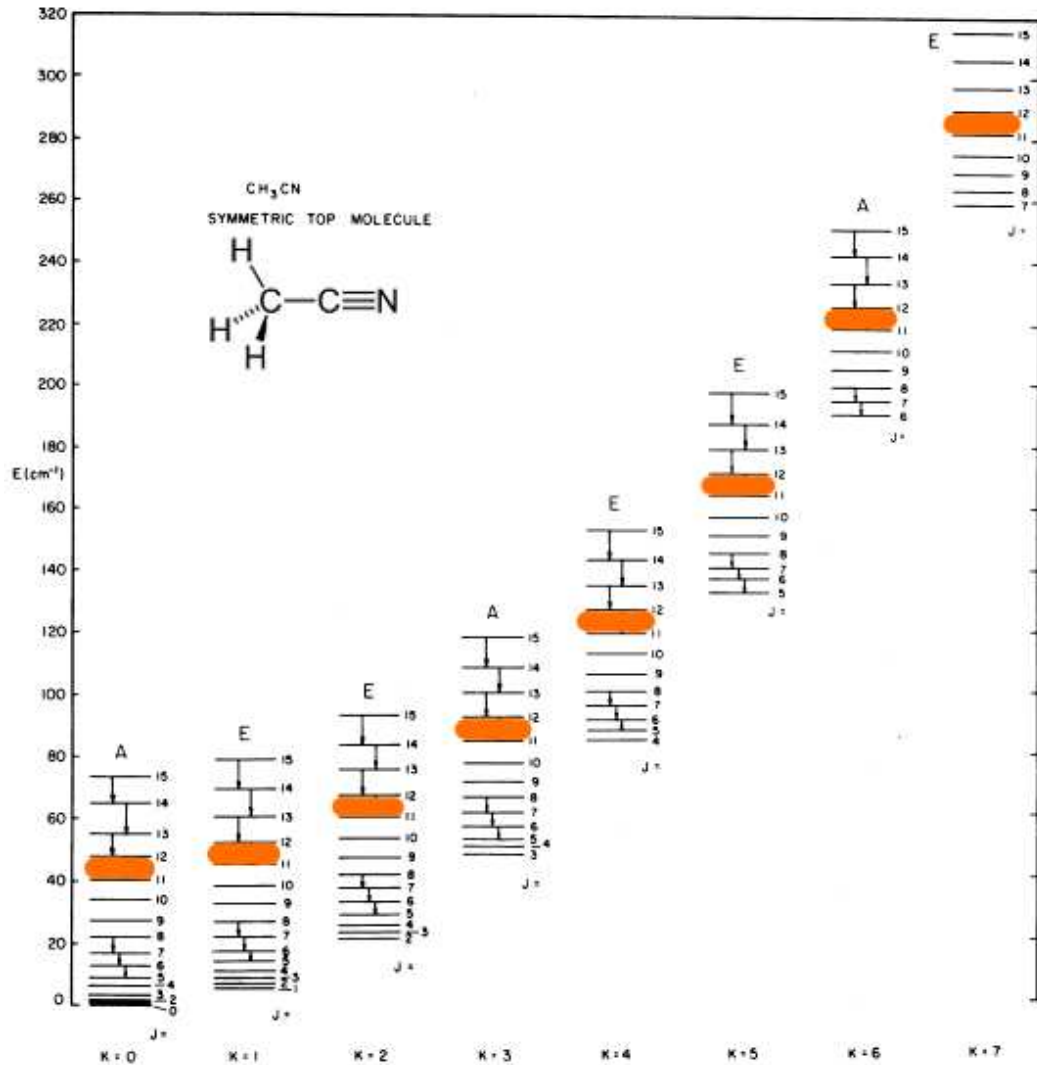


FIG. 3.2: The energy level of  $\text{CH}_3\text{CN}$  taken from Loren & Mundy (1984). Orange marks are the  $K$  ladders for the  $J = 12$  transition.

### 3.3 Estimation of Physical Conditions Through Molecular Transitions

Our interest in the line emission observations is to determine physical conditions such as kinetic temperature, density and abundance toward the molecular gas. Under the assumption of optically thick lines, the brightness saturates at the excitation temperature; under LTE conditions this is equal to the kinetic temperature,  $T_{\text{ex}}=T_{\text{kin}}$ . If we assume optically thin conditions the intensity of a spectral line is proportional to the number of molecules emitting and their excitation temperature. In this case we can estimate the number density of molecules if the excitation temperature is known.

In the physical conditions of dense molecular gas it is common to use both optically thick line tracers to measure the excitation temperature and optically thin lines to measure the column density. However, we need a practical method to measure both physical parameters simultaneously through the observable line emission.

#### 3.3.1 Rotation Diagram Method

The rotation diagram method (e.g., Hollis et al. 1981; Hollis 1982; Loren & Mundy 1984) is often used to estimate simultaneously the rotation temperature ( $T_{\text{rot}}$ ) and total column density ( $N_{\text{tot}}$ ) assuming LTE conditions and optically thin transitions; if the energy levels are populated according to a Boltzmann distribution, we can consider the excitation temperature as the rotational temperature (Loren & Mundy 1984; Goldsmith & Langer 1999). This method is based on a straightforward linear relationship between the integrated intensities observed and the two physical parameters above. At high densities, the rotation temperature will approach to the kinetic temperature of the gas.

In the next, we present a brief description of the rotation diagram method, following more detailed works (e.g., Loren & Mundy 1984; Goldsmith & Langer 1999; Araya et al. 2005).

In a molecular gas region, the number of molecules, at a particular rotational energy will be governed by the Boltzmann distribution

$$\frac{n_u}{n_l} = \frac{g_u}{g_l} e^{h\nu/kT} \quad (3.1)$$

where  $n_l$  is the number density of molecules in the lowest rotational state (e.g.,  $J=0$ ),  $n_u$  is the number density of molecules in the upper rotational state (e.g.,  $J+1$ ) and,  $g_u$  and  $g_l$  are the statistical weights for such states.  $h$  is the Planck constant,  $\nu$  is the frequency of the transition,  $k$  is the Boltzmann constant, and  $T$  is the excitation temperature, equal to the kinetic temperature under LTE conditions.

Thus, in LTE the absorption coefficient,  $\kappa_\nu$ , can be written as

$$\kappa_\nu = \frac{c^2 g_u}{8\pi\nu^2 g_l} n_l A_{ul} (1 - e^{h\nu/kT}) \phi(\nu) \quad (3.2)$$

where  $c$  is the speed of light,  $A_{ul}$  is the Einstein  $A$  coefficient, and  $\phi(\nu)$  is the line profile function. Equation 3.2 can be expressed in terms of the optical depth  $\tau_\nu$ , defined as  $\tau_\nu = \int \kappa_\nu dz$  and  $N_l = \int n_l dz$ ,

$$\tau_\nu = \frac{c^2 g_u}{8\pi\nu^2 g_l} N_l A_{ul} (1 - e^{h\nu/kT}) \phi(\nu) \quad (3.3)$$

thus from equation 3.1 to use  $N_u$ , and applying the Taylor series expansion of the parenthesis term (in the radio range  $h\nu \ll kT$ ),

$$\tau_\nu = \frac{hc^2}{8\pi\nu kT} N_u A_{ul} \phi(\nu) \quad (3.4)$$

Integrating with respect to  $\nu$  we have the normalized line profile,  $\int_0^\infty \phi(\nu) d\nu = 1$ , in the right side of the last equation. If we use  $\int \tau_\nu d\nu = (\nu/c) \int \tau_\nu dv$  in order to express the optical depth in terms of velocity, one obtains

$$\int \tau_\nu dv = \frac{hc^3}{8\pi\nu^2 kT} N_u A_{ul} \quad (3.5)$$

Assuming optically thin emission and introducing the *brightness temperature*,  $T_b$ ,  $T_b \approx \tau_\nu T$ ,

$$\int T_b dv = \frac{hc^3}{8\pi\nu^2 kT} N_u A_{ul} \quad (3.6)$$

or in terms of the upper level column density, and using  $W = \int T_b dv$ , to obtain

$$N_u = \frac{8\pi\nu^2 k}{hc^3 A_{ul}} W \quad (3.7)$$

For a molecule in LTE, all the energy levels are populated according to a single temperature  $T_{rot}$ , the rotational temperature. Thus, the upper state column density is related to the total column density,  $N$ , by

$$N_u = \frac{N}{Q_{rot}} g_n e^{E_u/kT_{rot}} \quad (3.8)$$

where  $g_n = g_u g_k g_I$  is the total degeneracy of the upper state;  $g_u$ ,  $g_k$ , and  $g_I$  correspond to the rotational degeneracy, the  $K$ -level degeneracy, and the reduced nuclear spin degeneracy, respectively.  $E_u$  is the energy of the upper state and  $Q_{rot}$  is the partition function (for a detailed description of  $Q_{rot}$ ,  $g_u$ ,  $g_k$ , and  $g_I$  see Turner 1991; Araya et al. 2005). From equation 3.8, one gets the fundamental formula of rotation diagrams:

$$\ln\left(\frac{N_u}{g_u}\right) = \ln\left(\frac{N}{Q_{rot}}\right) - \frac{E_u}{kT_{rot}} \quad (3.9)$$

this is a linear equation in which the slope is  $(-1/T_{rot})$  and  $\ln(N/Q_{rot})$  the intercept. The left-hand side of this equation contains the column density per statistical weight of the molecular energy levels and represents the integrated intensity per statistical weight. In this way, plotting the natural logarithm of  $N_u/g_u$  versus  $E_u/k$  and calculating the best linear fit,  $T_{rot}$  and  $N$  can be inferred.

In our analysis (Chapters 4 and 5) we used the partition function for  $\text{CH}_3\text{CN}$  quoted in Araya et al (2005),

$$Q_{rot} = \frac{3.89T_{rot}^{1.5}}{(1 - e^{-524.8/T_{rot}})^2} \quad (3.10)$$

and for CH<sub>3</sub>OH we adopted a general equation of Turner (1991) for species having one internal rotor,

$$Q_{rot} = Q_{rot}(A) + Q_{rot}(E) = 2 \left[ \frac{\pi (kT_{rot})^3}{h^3 ABC} \right]^{1/2} \quad (3.11)$$

where A, B, and C are the rotational constants of the molecule.

### 3.3.2 Modelling Emission

The analysis of molecular line emission have the main goal of estimate physical conditions of the observed regions. For example, column densities and temperatures can be derived through different approaches, typically assuming LTE and optically thin lines. Traditional methods such as rotation diagram or population diagram involve by-hand fitting of the line features: integrated intensity, linewidth, LSR velocity, and some times multiple velocity components, for every species. With the large bandwidth offered by new (sub)mm receptors, this procedure is extremely time-consuming. Also, line blending and optically thick lines are common in spectra of sources such as HMCs. Finally, for complex sources with two or more regions with different densities and temperatures the rotation diagram method will not provide a good linear fit. In brief, a large multi-line study the rotation diagram method could be impractical.

Better results might be obtained if the analysed parameters are simultaneously estimated and then directly compared with observations. An innovative technique proposed by Schilke et al. (1990) and Comito et al (2005), is based on the simultaneous fit of all the lines in a spectrum with a synthetic spectrum computed under LTE conditions. This approach produces the following representation of the spectrum:

$$T_\nu = \sum_m \sum_c \eta(\theta_{m,c}) [J(T_{ex}^{m,c})] (1 - e^{-\tau^{\nu,m,c}}) \quad (3.12)$$

where the indices  $m$  and  $c$  correspond to molecules and components respectively.  $\theta$  is the source size,  $T_{ex}$  is the excitation temperature, and  $\eta$  is the filling factor which is explained below.

The synthetic spectrum will be derived for multiple molecular lines, toward different regions with different physical characteristics, i.e., a small and dense hot core, and a larger, less dense warm envelope, for example.

The optical depth is defined as

$$\tau^{\nu,m,c} = \sum_l \tau_l^{\nu,m,c} = \sum_l \frac{c^3}{8\pi\nu_l^3} A_{if} N_{tot}^{m,c} \frac{g_i e^{-E_i/kT_{ex}^{m,c}}}{Q(m, T_{ex}^{m,c})} (1 - e^{-h\nu/kT_{ex}}) \phi^{\nu,m,c} \quad (3.13)$$

where the indice  $l$  refers to the molecular lines. Similarly to equation 3.3,  $A_{if}$  is the Einstein  $A$  coefficient,  $N_{tot}$  is the total molecular column density;  $g_i$ ,  $E_i$  and  $Q$  are the statistical weights, excitation energies and the partition function for each molecule, respectively. The line profile function is

$$\phi^{\nu,m,c} = \frac{2\sqrt{\log 2}}{\sqrt{\pi}\Delta v^{m,c}} e^{-\frac{(\nu-\nu_l+\nu_{off})^2}{2\sigma^2}} \quad (3.14)$$

with velocity width  $\Delta v$  and velocity offset  $v_{off}$  for each line. Finally the filling factor is given by

$$\eta(\theta_{m,c}) = \frac{\theta_{m,c}^2}{\theta_t^2 + \theta_{m,c}^2} \quad (3.15)$$

where  $\theta_t$  is the telescope beam size. Line parameters are obtained from online catalogs of the JPL line catalogs (Pickett et al 1998) and the Cologne Database for Molecular Spectroscopy (CDMS, Muller et al. 2001).

The optical depth for each molecule in each component at each frequency is derived by summing over all lines of all isotopomers, and isotopomeric lines are treated like main lines with line strengths reduced by the isotopic ratio.

For optically thick or thin lines, equation 3.12 can be approximated by

$$T_\nu = \sum_m \sum_c \eta(\theta_{m,c}) [J(T_{ex}^{m,c})] \quad (\text{optically thick}) \quad (3.16)$$

$$T_\nu = \sum_m \sum_c \eta(\theta_{m,c}) [J(T_{ex}^{m,c})] \tau^{\nu,m,c} \text{ (optically thin)} \quad (3.17)$$

In the optically thick lines, source size and excitation temperatures cannot be determined independently, while the same is true for source size and column density in the optically thin case. However, most complex molecules display a mixture of optically thick and thin lines and the above degeneracy is not important.

The above method has been implemented as a command in an extended version of CLASS, called XCLASS. We use this program in order to estimate densities and temperatures toward 17 HMCs. In the next chapter we present the results with XCLASS.



# Chapter 4

## SMA millimeter observations of Hot Molecular Cores

*This chapter is based on the paper Hernandez-Hernandez, V., Zapata, L., Kurtz, S. & Garay, G. 2014, ApJ, 786, 38*

### 4.1 Introduction

Massive stars ( $M > 8 M_{\odot}$ ) are born inside of dense cores located in large and massive molecular clouds (e.g., [Garay & Lizano 1999](#); [Cesaroni 2005](#)). These massive star-forming regions (MSFRs) have a substantial impact on the evolution of the interstellar medium (ISM) and make important contributions to its dynamics and chemistry. For example, molecular outflows, jets, stellar winds and supernovae associated with MSFRs push into their surroundings, promoting additional star formation and mixing the ISM.

One of the first manifestations of massive star formation is the so-called hot molecular core phase (HMCs; [Kurtz et al. 2000](#); [Cesaroni 2005](#)). This phase is characterized by molecular gas condensations at relatively high temperatures ( $>100$  K) and high densities ( $\sim 10^5$ – $10^8$  cm $^{-3}$ ), associated with a compact ( $< 0.1$  pc), luminous ( $> 10^4 L_{\odot}$ ), and massive ( $\sim 10$ – $1000 M_{\odot}$ ) molecular core.

HMCs show a forest of molecular lines, especially from organic species (e.g., [Comito et al. 2005](#)). Many of these molecules probably were formed on grain mantles during a previous cold phase, while others were produced by gas-phase reactions after “parents species” were evaporated from the grains by the strong radiation of embedded or nearby protostars (see [Herbst & van Dishoeck 2009](#)).

Both models and observations suggest that massive HMCs are collapsing and accreting mass onto a central source(s) at rates of  $10^{-4} - 10^{-3} M_{\odot} \text{yr}^{-1}$  ([Osorio et al. 2009](#); [Zapata et al. 2009a](#)). These intense mass accretion rates are high enough to prevent the development of an ionized region around the massive star(s) at least in the early stages ([Osorio et al. 1999](#)). Thus, HMCs probably precede ultracompact HII regions (UCHII; [Kurtz et al. 2000](#); [Wilner et al. 2001](#)). Indeed, sub-arcsecond observations argue in favor of this scenario, particularly those showing embedded UC HII-regions, strong (sub)millimeter emission from dust condensations, or strong mid-IR emission from internal objects (e.g.; [Cesaroni et al. 2010, 2011](#)).

In the above scenario a HMC corresponds to the most internal clump of molecular material collapsing and probably feeding other structures and the massive stars inside ([Cesaroni 2005](#); [Wilner et al. 2001](#)). However, recent sensitive high angular resolution observations suggest that the prototypical HMC, Orion BN/KL, may not follow this model. In this case, a close dynamical interaction of three young protostars produced an explosive flow and illuminated a pre-existing dense clump, thus creating the HMC ([Zapata et al. 2011](#); [Goddi et al. 2011](#)). Also, toward G34.26+0.15 (another prototypical HMC), [Mookerjea et al. \(2007\)](#) failed to find any embedded protostars within the hot core. The different natures of internally and externally heated HMC makes it important to distinguish between them.

With this in mind, we present a study using Submillimeter Array<sup>1</sup> (SMA) archival observations of  $\text{CH}_3\text{CN}$  ( $12_K-11_K$ ) and 1.3 mm continuum emission, toward 17 MSFRs in the HMC stage.  $\text{CH}_3\text{CN}$  (methyl cyanide) is frequently used as an effective thermometer and to estimate gas density toward HMCs (e.g., [Araya et al. 2005a](#); [Pankonin et al. 2001](#)). Our main goal is to use the same molecular tracer toward a relatively large group of sources to study the innermost and hottest material, estimating densities,

---

<sup>1</sup>The Submillimeter Array is a joint project between the Smithsonian Astrophysical Observatory and the Academia Sinica Institute of Astronomy and Astrophysics and is funded by the Smithsonian Institution and the Academia Sinica.

temperatures, masses, abundances, and the spatial distribution of the dust emission and CH<sub>3</sub>CN molecular gas.

In Section 4.2 we describe the archival observations presented in this study. In Section 4.3 we report the results and analysis of the millimeter continuum data and the molecular line emission. In Section 4.4 we comment briefly on each source, giving the physical characteristics from the literature and from our results. In Section 4.5 we discuss our results, first comparing the spatial distribution of the continuum emission and molecular emission, and then estimating the temperatures and densities of the regions from an LTE analysis of the CH<sub>3</sub>CN (12<sub>K</sub>–11<sub>K</sub>) spectra and through the rotation diagram method. Finally, in Chapter 6, we present our main conclusions.

## 4.2 Observations and Data Reduction

TABLE 4.1: Observed Sources.

Source Name	Short Name	R.A. (J2000)	Dec. (J2000)	V <sub>lsr</sub> (km/s)	Distance (kpc)	$L$ (10 <sup>5</sup> L <sub>⊙</sub> )	UCHII	Refs
W3(OH)	W3OH	02 27 03.9	+61 52 24	−48.0	2.0	0.10	Y	1
W3(H <sub>2</sub> O)TW	W3TW	02 27 04.8	+61 52 24	−48.0	2.0	0.30	N	1
IRAS 16547–4247	I16547	16 58 17.3	−42 52 07	−30.0	2.9	0.62	N	2,3
IRAS 17233–3606	I17233	17 26 42.8	−36 09 17	−03.4	1.0	0.14	Y	4,5
G5.89–0.37	G5.89	18 00 30.4	−24 04 00	+10.0	3.0	1.50	Y	1
G8.68–0.37	G8.68	18 06 23.4	−21 37 10	+37.2	4.8	0.20	N	6,7
G10.47+0.03	G10.47	18 08 38.2	−19 51 50	+68.0	8.5	7.00	Y	1
G10.62–0.38	G10.62	18 10 28.7	−19 55 49	−03.0	5.0	9.20	Y	1
IRAS 18182–1433	I18182	18 21 09.0	−14 31 49	+59.1	3.6	0.19	N	1
G23.01–0.41	G23.01	18 34 40.3	−09 00 38	+77.0	4.6	1.00	N	1
G28.20–0.04N	G28.20N	18 42 58.1	−04 13 57	+95.6	5.7	1.60	Y	8,9
G31.41+0.31	G31.41	18 47 34.3	−01 12 46	+96.5	7.9	2.50	Y	10,11
IRAS 18566+0408	I18566	18 59 09.8	+04 12 13	+85.0	6.7	0.60	Y	12
G45.07+0.13	G45.07	19 13 22.0	+10 50 53	+60.0	8.0	11.0	Y	1
G45.47+0.05	G45.47	19 14 25.6	+11 09 25	+59.0	8.0	11.0	Y	1
W51e2	W51e2	19 23 44.0	+14 30 35	+55.0	5.4	15.0	Y	1
W51e8	W51e8	19 23 43.9	+14 30 28	+55.0	5.4	15.0	Y	1

**Notes.**— Units of right ascension are hours, minutes, and seconds, and for declination are degrees, arcminutes, and arcseconds. Positions, V<sub>lsr</sub>, distances, luminosities, and UCHII regions are taken from the cited references.

**References.**— (1) (Reid et al. 2014); (2) Rodríguez et al. (2008); (3) Franco-Hernández et al. (2009); (4) Faúndez et al. (2004); (5) Leurini et al. (2011); (6) Purcell et al. (2006); (7) Longmore et al. (2011); (8) Sollins et al. (2005a); (9) Qin et al. (2008); (10) Pandian et al. (2008); (11) Cesaroni et al. (2010); (12) Zhang et al. (2007b)

We searched the literature for MSFRs in the HMC phase, based on previous detections of molecular species indicating warm and dense gas such as CH<sub>3</sub>CN, NH<sub>3</sub> and CH<sub>3</sub>OH. These molecules are commonly used to trace HMCs (e.g., Churchwell et al. 1990, 1992;

Olmi et al. 1993; Kalenskii et al. 1997, 2000). We compiled a list of almost 60 objects of which most are associated with UCHII regions, strong (sub)millimeter emission, molecular outflows, or maser emission; i.e., they are young MSFRs. Then we searched in the SMA archive for observations that included the CH<sub>3</sub>CN (12<sub>K</sub>–11<sub>K</sub>) transitions at  $\sim 220.7$  GHz. Of the nearly 60 objects, 17 were previously observed in the compact or extended configurations and their data are public.

In Table 4.1 we list the observed sources, their coordinates, *lsr* velocities, distances, and luminosities, and indicate whether a UCHII region is present. If the 1.3 mm continuum or CH<sub>3</sub>CN (12<sub>K</sub>–11<sub>K</sub>) data were previously published, we list the paper in Table 4.2. Distances range from 1 to 8.5 kpc, with a mean of 5.0 kpc. Luminosities were in most cases estimated from IRAS fluxes and range from  $10^4$  to some  $10^5 L_{\odot}$ . Twelve of the MSFRs (70%) host UCHII regions.

The HMCs were observed with the SMA (Ho et al. 2004) in the compact and/or extended configuration at epochs from April 2004 to April 2010. The maximum projected baselines of the visibility data ranged from  $\sim 53$  to  $\sim 174$  k $\lambda$ , with different numbers of antennas at different epochs. The SMA correlator was operated with the double-sideband receiver covering 2 GHz in both the lower-sideband (LSB) and the upper-sideband (USB). For G23.01 a single receiver with 4 GHz bandwidth was used. The lower-sideband covered the frequencies of the CH<sub>3</sub>CN (12<sub>K</sub>–11<sub>K</sub>) *K*-components, which range from 220.74726 GHz ( $K = 0$ ) to 220.2350 GHz ( $K = 11$ ), with uniform spectral resolution of 0.406 MHz ( $\sim 0.53$  km s<sup>-1</sup>) or 0.812 MHz ( $\sim 1.1$  km s<sup>-1</sup>) for different sources (see Table 4.2). The primary beam of the SMA at 220 GHz has FWHM  $\sim 55''$ .

The gain, flux, and bandpass calibrators used at each epoch are listed in Table 4.2. Based on the SMA monitoring of quasars, we estimate the uncertainty in the fluxes to be between 15% and 20%. The visibilities from each observation were calibrated with the IDL-based MIR package (adapted for the SMA<sup>2</sup>), and were then exported to MIRIAD for further processing. The 1.3 mm continuum emission was derived from the line-free channels of the LSB in the visibility domain. All the line data were smoothed

---

<sup>2</sup>The MIR cookbook by Charlie Qi at <http://www.cfa.harvard.edu/~cqi/mircook.html>

---

to a spectral resolution of 0.812 MHz or  $\sim 1.1 \text{ km s}^{-1}$  to improve the sensitivity and provide uniform spectra. The synthesized beam sizes range from  $1''.47 \times 0''.83$  to  $5''.34 \times 2''.95$ . In Table 4.2 we summarize the relevant information concerning the observations.

TABLE 4.2: Observational Parameters

Source Name	Observation Epoch	Frequency range of LSB (GHz)	Spectral resolution (MHz)	Calibrators			$S_\nu$ of gain calibrators <sup>a</sup> (Jy)	Synthesized beam		Published data
				Bandpass	Gain	Flux		FWHM (arcsec)	PA (deg)	
W3OH	2004 Oct 24	219.50–221.48	0.812	0359+509	0102+584	Uranus	1.41	2.97×1.93	+69.1	
W3TW	2004 Oct 24	219.50–221.48	0.812	0102+584	0102+584	Uranus	1.41	2.97×1.93	+69.1	
					0359+509		3.10			
I16547	2006 Jun 06	219.21–221.19	0.812	3C273	1745-290	Uranus	3.09	1.97×1.18	–6.3	
					1604-446		1.32			
I17233	2007 Apr 10	219.45–221.43	0.406	3C454.3	1626-298	Callisto	1.22	4.85×2.14	+32.1	1
					1713-269		0.30			
G5.89	2008 Apr 18	219.37–221.34	0.406	3C454.3	1921–293	Uranus	1.11	3.25×2.00	+60.4	2
G8.68	2008 Sep 17	220.28–222.27	0.406	3C273	1733-130		0.71			
					3C454.3	1911–201	Uranus	1.89	3.71×2.79	+10.8
G10.47	2008 Jun 21	220.24–222.22	0.406	3C273	1733-130	Uranus	1.39	3.26×1.91	+63.9	
					3C454.3	1911–201		1.05		
G10.62	2009 Jan 31	220.32–222.30	0.406	3C454.3	1733-130	Uranus	2.07	5.34×2.95	–0.9	
I18182	2004 Apr 30	219.42–221.07	0.812	3C273	1733-130	Uranus	1.48	3.84×2.59	+15.9	4
					1908-201		1.64			
G23.01	2010 Apr 28	216.90–220.88(b)	0.812	3C273	1743-038	Uranus	0.97	3.52×3.16	–43.7	
					3C454.3	1911-201		1.55		
G28.20N	2008 Jun 21	220.25–222.22	0.406	3C273	1733–130	Uranus	1.39	3.31×1.60	–72.0	
					3C454.3	1911-201		1.05		
G31.41	2007 Jul 09	219.30–221.30	0.406	3C273	1751+096	Uranus	1.59	3.53×1.70	+66.0	
					1830+063		0.46			
I18566	2007 Jul 09	219.30–221.30	0.812	3C273	1751+096	Uranus	1.59	3.48×1.65	+66.7	
					1830+063		0.46			
G45.07	2007 Apr 13	219.45–221.43	0.812	3C273	1751+096	Callisto	8.88	3.31×1.60	+78.7	
					1925+211		1.65			
G45.47	2008 Jun 30	219.15–221.13	0.406	3C454.3	1925+211	Titan	0.63	3.40×1.68	+77.2	
					1911-201		1.41			
W51e2	2005 Sep 01	220.25–222.23	0.406	3C454.3	1751+096	Uranus	1.41	1.47×0.83	–86.9	5
					2025+337		0.74			
W51e8	2005 Sep 01	220.25–222.23	0.406	3C454.3	1751+096	Uranus	1.41	1.47×0.83	–86.0	5
					2025+337		0.74			

**Notes.**– (a) We estimated bootstrapped flux for gain calibrators with an uncertainty of 15%–20%. (b) A single sideband of 4 GHz bandwidth. **References.**– 1: [Leurini et al. \(2011\)](#); 2: [Su et al. \(2009\)](#); 3: [Longmore et al. \(2011\)](#); 4: [Beuther et al. \(2006\)](#); 5: [Klaassen et al. \(2009\)](#)

## 4.3 Results and Analysis

### 4.3.1 Millimeter continuum data

In Figures 4.1 to 4.8 we show the 1.3 mm continuum emission images overlaid with three  $K$ -lines ( $K = 3, 5$  and  $7$ ) of  $\text{CH}_3\text{CN}$  ( $12_K-11_K$ ) emission toward the 17 HMCs. Table 4.3 shows the corresponding continuum emission parameters, derived using line-free channels from the LSB. Using the task *imfit* in MIRIAD, we found the position of the peak, and the peak and integrated flux densities. The deconvolved source sizes were determined from two dimensional Gaussian fits.

Since HMCs are chemically rich, the continuum emission may be contaminated by some molecular lines, particularly for extremely rich sources such as I17233, G10.62, G31.41, W51e2 and W51e8. Although we were careful to avoid any obvious contamination during the reduction process, we consider the peak and integrated fluxes as upper limits.

Some HMCs show embedded or very nearby UC HII regions and the 1.3 mm continuum emission may have contributions from both ionized gas emission and from the dust. To estimate the free-free contribution at 1.3 mm we extrapolated the emission between 10 and 45 GHz reported in the literature, assuming optically thin emission, i.e., considering  $S_\nu \propto \nu^{-0.1}$ . For G45.07, G45.47, and W51e2 we choose  $\sim 100$  GHz for extrapolation of the free-free emission due to their high turnover frequencies. In Figures 4.9 to 4.12 we show the flux density distribution for the sources. We note that the flux densities shown were obtained with a variety of instruments, and discrepancies between observed values for the sources are due to this issue.

Finally, we derived the dust continuum emission for the HMCs which ranges from 0.31 Jy for I18566 to 5.88 Jy for I17233. The measured fluxes and the contribution from thermal dust are presented in Table 4.3.

To estimate the gas mass and average column density we follow Hildebrand (1983). Assuming optically thin dust emission and a constant gas-to-dust ratio, the gas mass is:

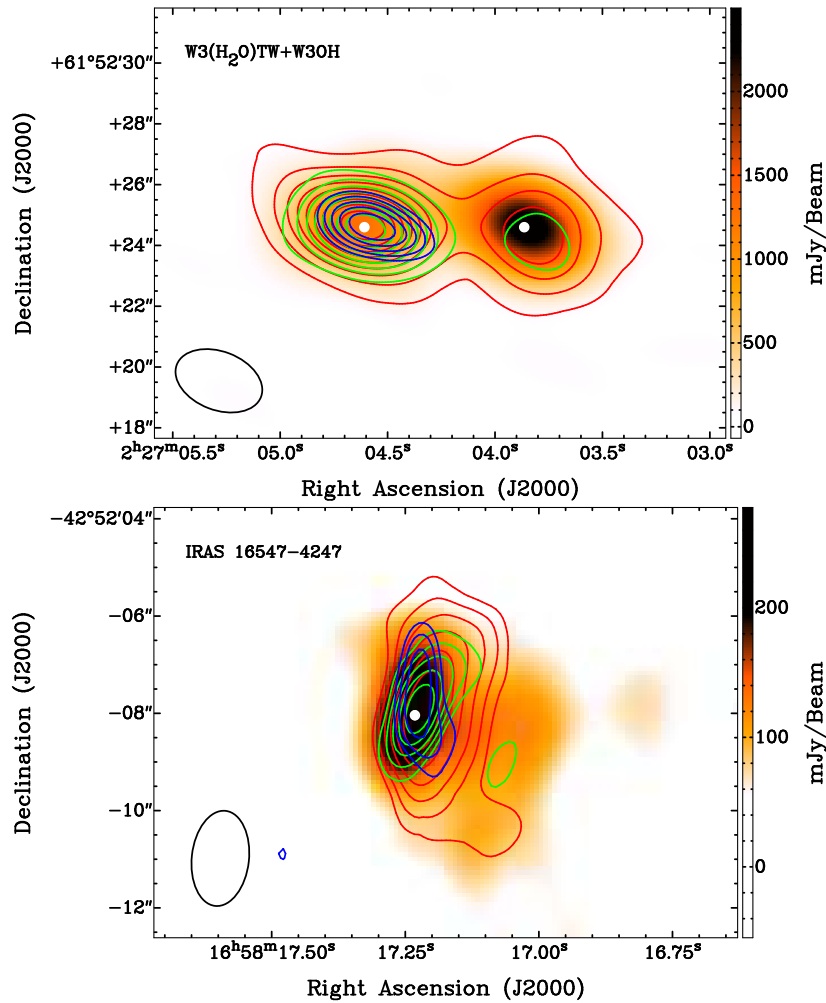


FIG. 4.1: SMA line-free continuum maps at 1.3 mm (color scale) and velocity-integrated emission (moment 0, contours) of CH<sub>3</sub>CN ( $12_K-11_K$ ) for  $K = 3$  (red),  $K = 5$  (green) and  $K = 7$  (blue) lines. Contour levels have steps of 10% until 90% of the integrated emission shown in Table 6. Contour levels for the W3OH-region begin at 10% ( $K = 3$ ), 20% ( $K = 5$ ), and 50% ( $K = 7$ ). Contour levels for I16547 begin at 40% ( $K = 3$ ), 50% ( $K = 5$ ), and 70% ( $K = 7$ ). White dot marks the peak position of 1.3 mm continuum emission (Table 4.3), and the synthesized beam (Table 4.3) is shown at the bottom-left.

$$M_{\text{gas}} = \frac{F_{\nu} D^2 R_d}{B_{\nu}(T_d) \kappa_{\nu}} \quad (4.1)$$

where  $F_{\nu}$ ,  $D$ ,  $R_d$ ,  $\kappa_{\nu}$  and  $B_{\nu}(T_d)$  are the flux density, distance to the core, gas-to-dust ratio, the dust opacity per unit dust mass, and the Planck function at the dust temperature ( $T_d$ ), respectively (see Section 2.2). Note that  $\kappa_{\nu}$  ranges from 0.2 to 3.0 at 1.3 mm, depending on its scaled value with frequency as  $\nu^{\beta}$ , where  $\beta$  is the dust emissivity index (e.g., Hunter et al. 2000; Henning et al. 1995). Following Ossenkopf & Henning (1994) and using  $\beta=1.5$ , we obtain  $\kappa_{1.3\text{mm}} = 0.74\text{ cm}^2\text{ g}^{-1}$ , corresponding



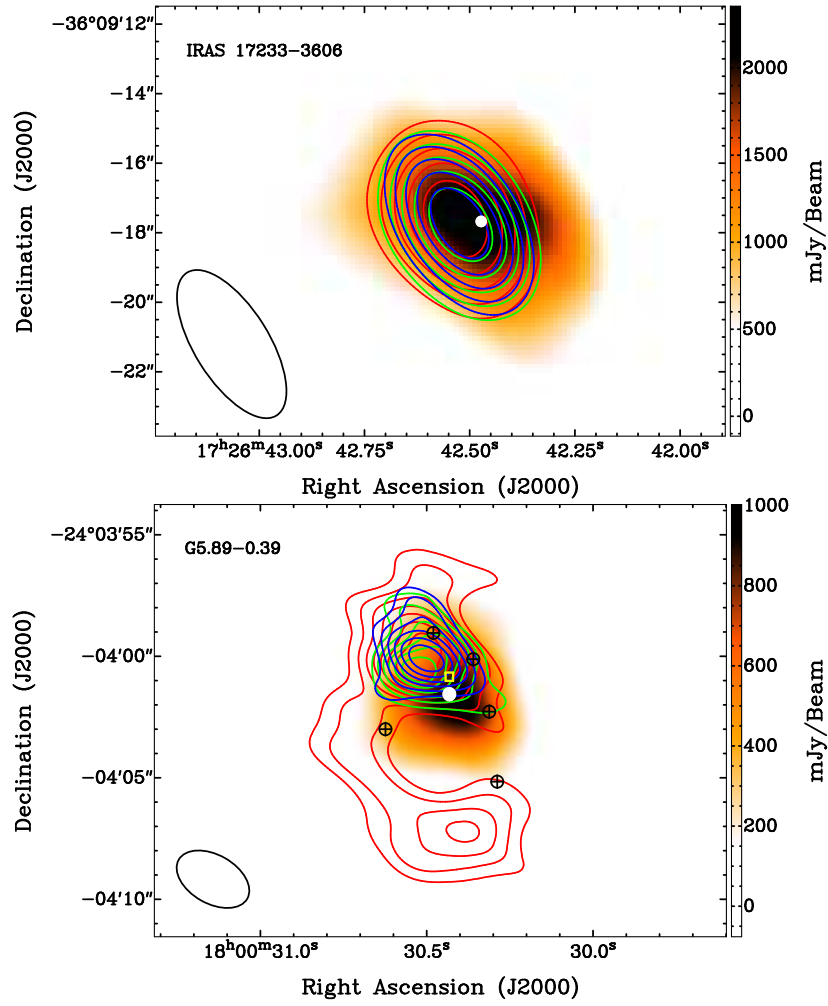


FIG. 4.2: Same as Figure 4.1. Contour levels for I17233 begin at 50% ( $K = 3$ ,  $K = 5$ , and  $K = 7$ ). For G5.89 we used the  $K$ -lines 3, 5, and 6 with contour levels beginning at 30%, 40%, and 40%, respectively. Yellow box marks the position of the Feldt’s star (Feldt et al. 2003), and circles with crosses show condensations with excess  $870 \mu\text{m}$  emission reported by Hunter et al. (2008).

to a median grain size  $a = 0.1 \mu\text{m}$  and a grain mass density  $\rho_d = 3 \text{ g cm}^{-3}$ . Our value of  $\kappa_\nu$  is very similar to other estimates toward HMCs (e.g., Hunter et al. 1999; Osorio et al. 2009).

In the Rayleigh-Jeans approximation, equation 4.1 gives

$$\left[ \frac{M_{\text{gas}}}{M_\odot} \right] = 432.0 \left[ \frac{F_\nu}{\text{Jy}} \right] \left[ \frac{D}{\text{kpc}} \right]^2 \left[ \frac{T}{\text{K}} \right]^{-1} \quad (4.2)$$

$$\left[ \frac{N_{\text{H}_2}}{\text{cm}^{-2}} \right] = \frac{1.0 \times 10^{27}}{\theta} \left[ \frac{F_\nu}{\text{Jy}} \right] \left[ \frac{T}{\text{K}} \right]^{-1} \quad (4.3)$$

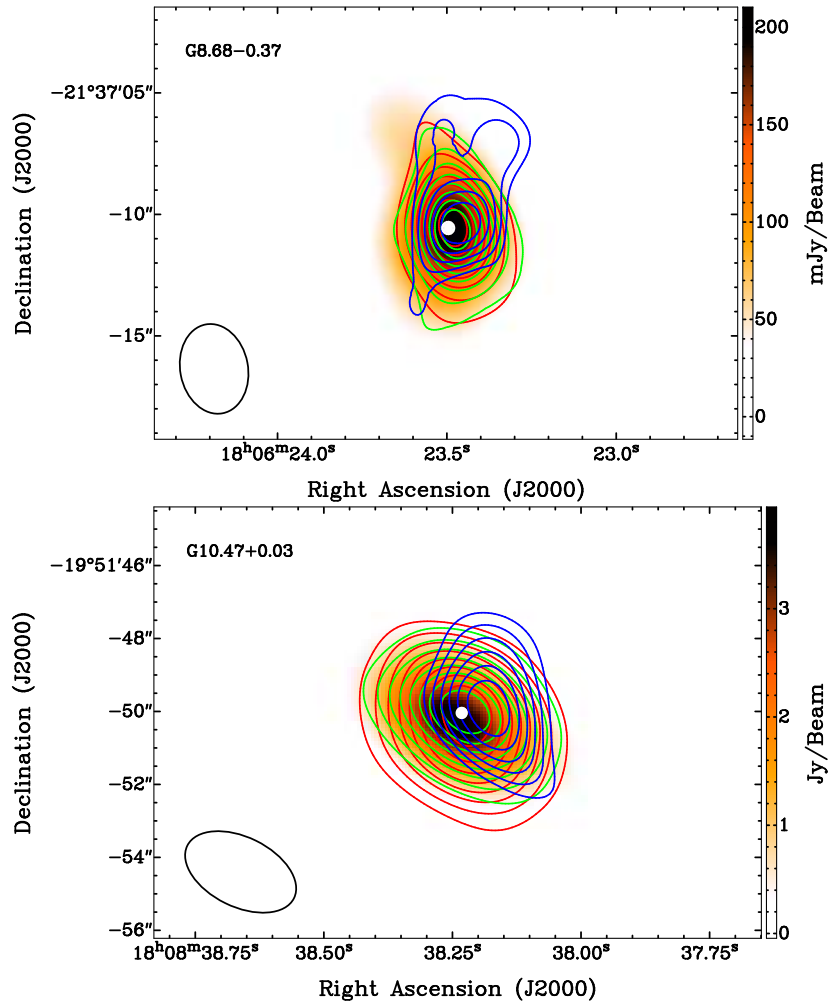


FIG. 4.3: Same as Figure 4.1. Contour levels for G8.68 begin at 20% ( $K = 3$  and  $K = 5$ ) and 50% ( $K = 7$ ). Contour levels for G10.47 begin at 20% ( $K = 3$  and  $K = 5$ ) and 40% ( $K = 7$ ).

where  $\theta$  is the source size ( $\theta = \sqrt{\theta_A \theta_B}$ , where  $\theta_A$  and  $\theta_B$  correspond to the beam sizes of the telescope) in arcsecond and we used the common gas-to-dust ratio of 100 (see Section 2.2). At the high densities of HMCs, dust and gas are probably well-coupled through collisions and we can assume that they are in thermal equilibrium (Kaufman et al. 1998). Thus, we used the high temperatures derived from the  $\text{CH}_3\text{CN}$  (see Section 4.3.3) to obtain  $M_{\text{gas}}$  and  $N_{\text{H}_2}$ . These values, obtained from the estimated 1.3 mm dust emission, are presented in Table 4.3.

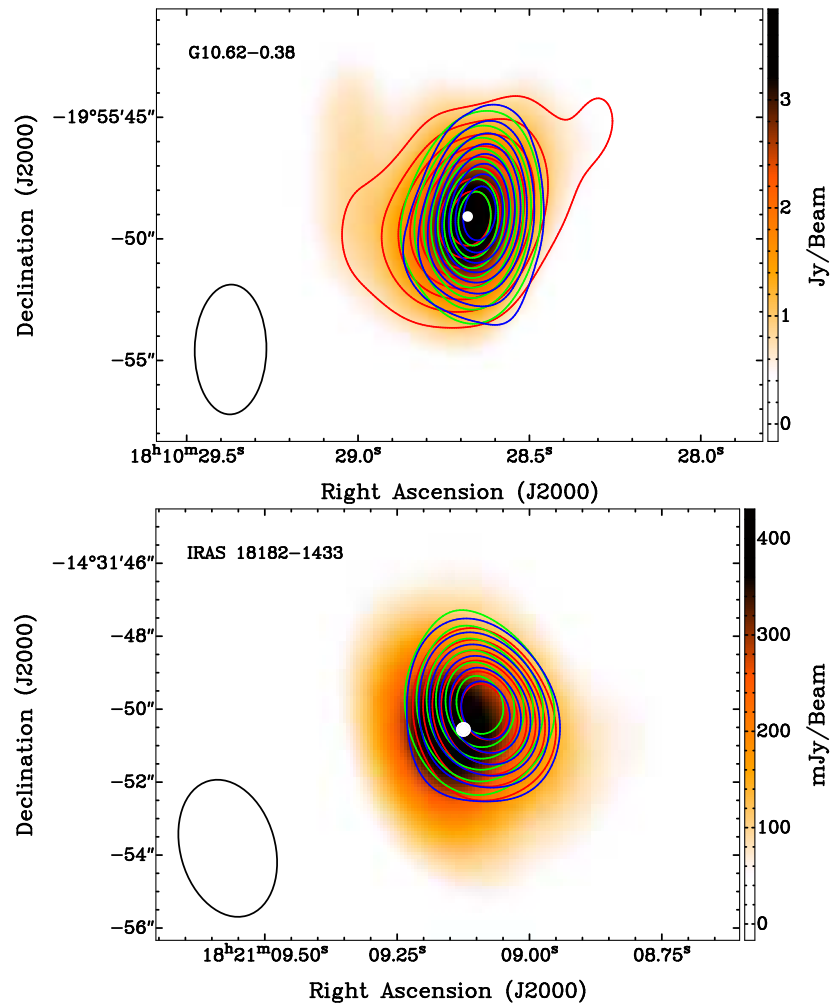


FIG. 4.4: Same as Figure 4.1. For G10.62 contour levels begin at 20% ( $K = 3$ ,  $K = 5$ , and  $K = 7$ ). For I18182 we used the  $K$ -lines 3, 5 and 6 with contour levels beginning at 50%.

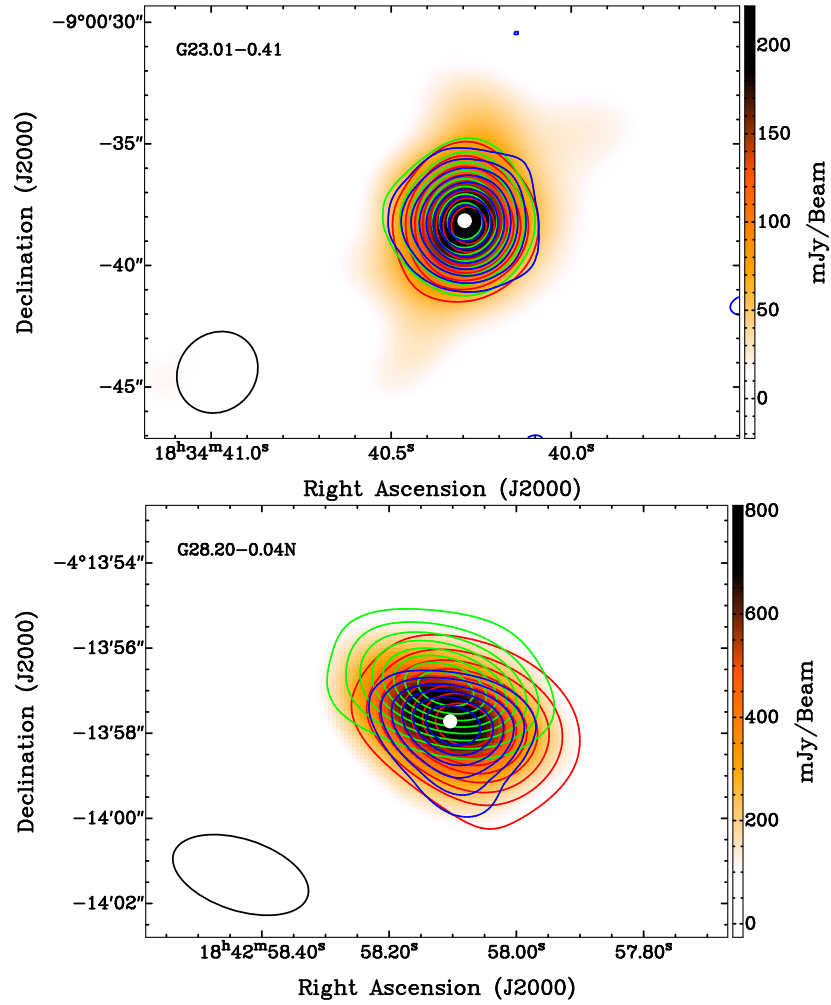


FIG. 4.5: Same as Figure 4.1. For G23.01 contour levels begin at 20% ( $K = 3$ ,  $K = 5$ , and  $K = 7$ ). For G28.20N contour levels begin at 20% ( $K = 3$  and  $K = 5$ ), and 40% ( $K = 7$ ).

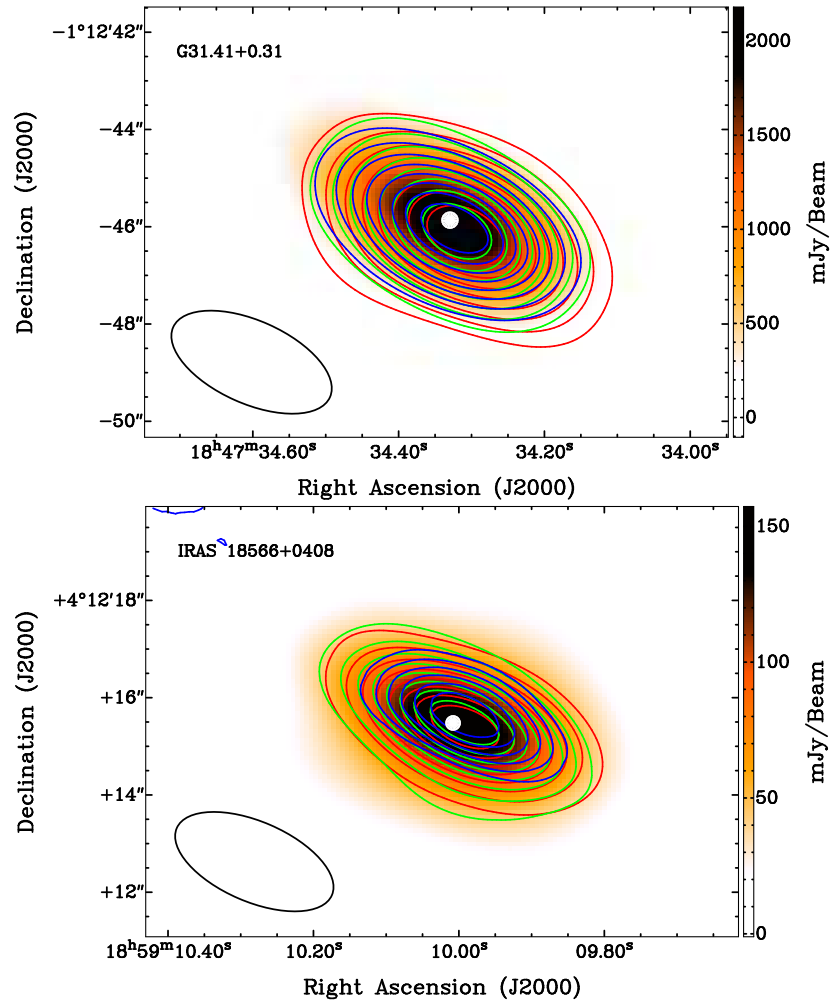


FIG. 4.6: Same as Figure 4.1. For G31.41 contour levels begin at 40% ( $K = 3$ ,  $K = 5$ , and  $K = 7$ ). For I18566 contour levels begin at 20% ( $K = 3$  and  $K = 5$ ), and 40% ( $K = 7$ ).

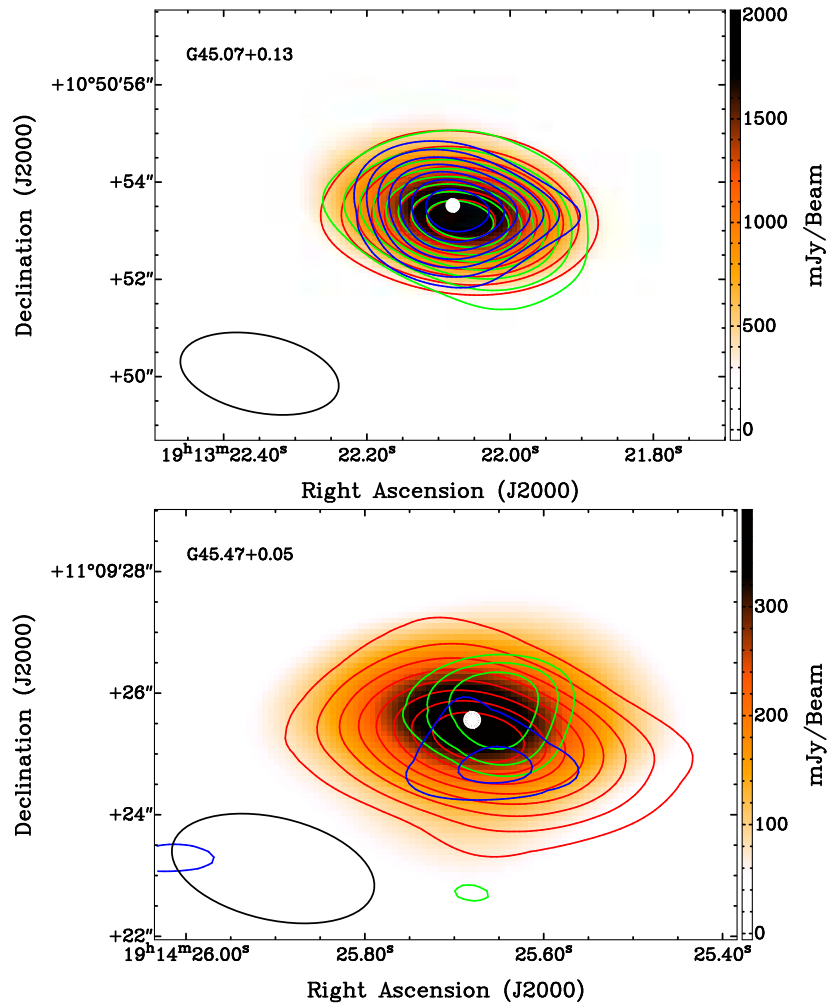


FIG. 4.7: Same as Figure 4.1. For G45.07 contour levels begin at 20% ( $K = 3$  and  $K = 5$ ), and 30% ( $K = 7$ ). For G45.47 contour levels begin at 20% ( $K = 3$ ), 70% ( $K = 5$ ), and 50% ( $K = 7$ ).

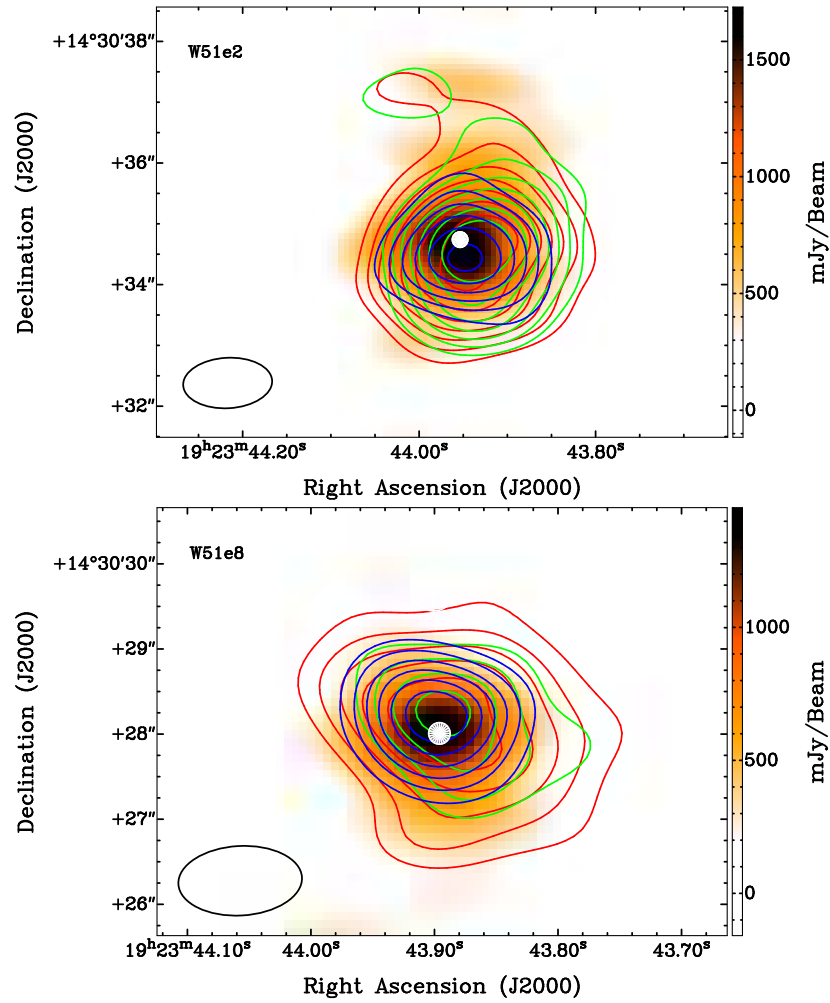


FIG. 4.8: Same as Figure 4.1. For W51e2 contour levels begin at 30% ( $K = 3$  and  $K = 5$ ), and 40% ( $K = 7$ ). For W51e8 contour levels begin at 30% ( $K = 3$ ), and 40% ( $K = 5$  and  $K = 7$ ).

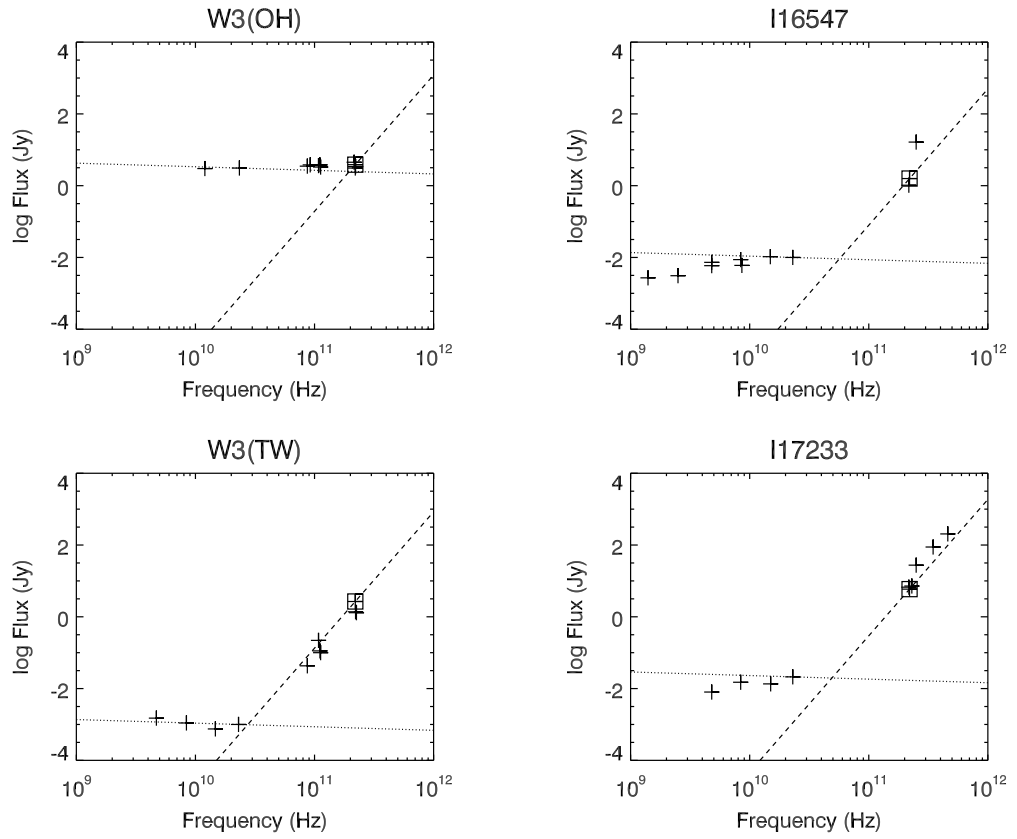


FIG. 4.9: Flux density distribution for the HMCs, from data given in this work (the square symbol;  $\sim 220$  GHz) and compiled (the plus symbol). Dotted line represent the flux density with a gradient  $S_\nu \propto \nu^{-0.1}$ . Dashed line represents the flux from a warm dust component with  $S_\nu \propto \nu^2$ .



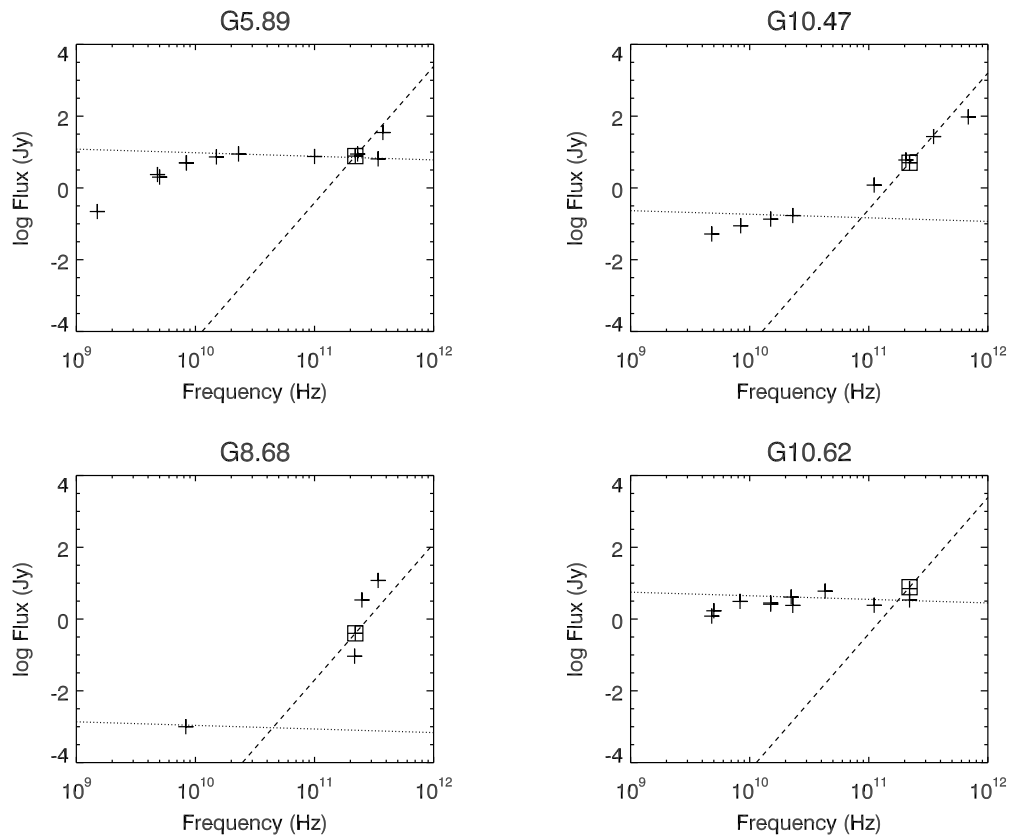


FIG. 4.10: The same as figure 4.9.

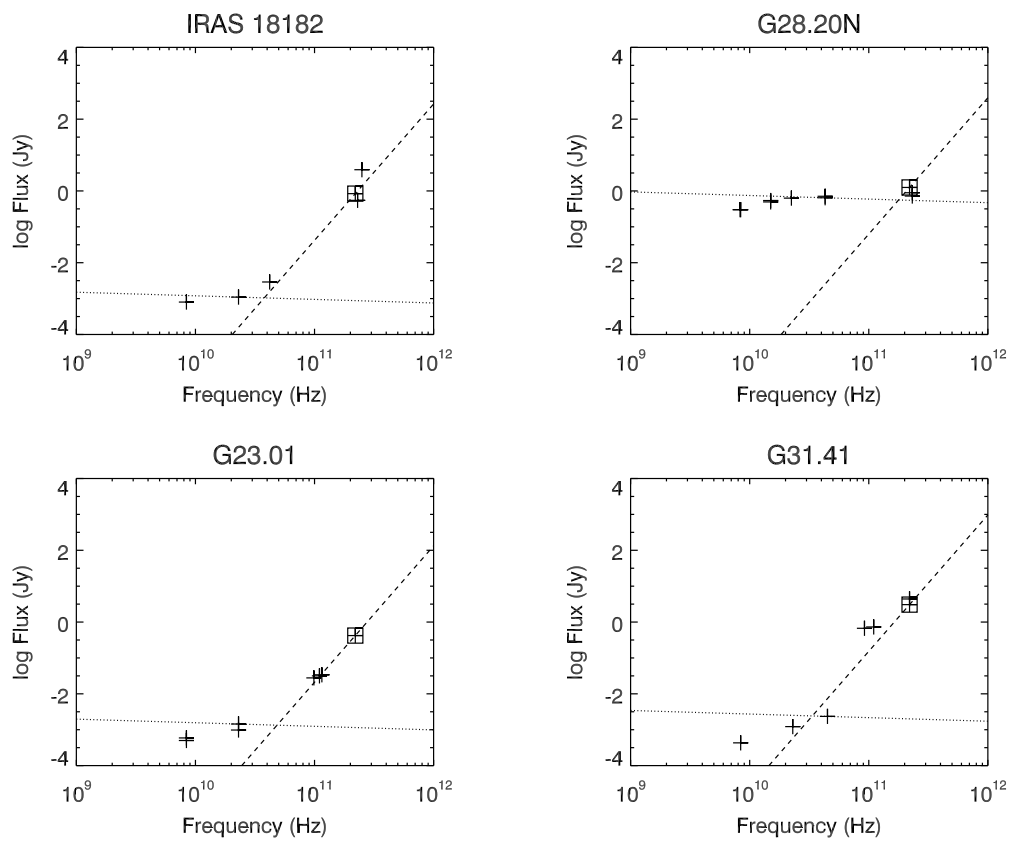


FIG. 4.11: The same as figure 4.9.

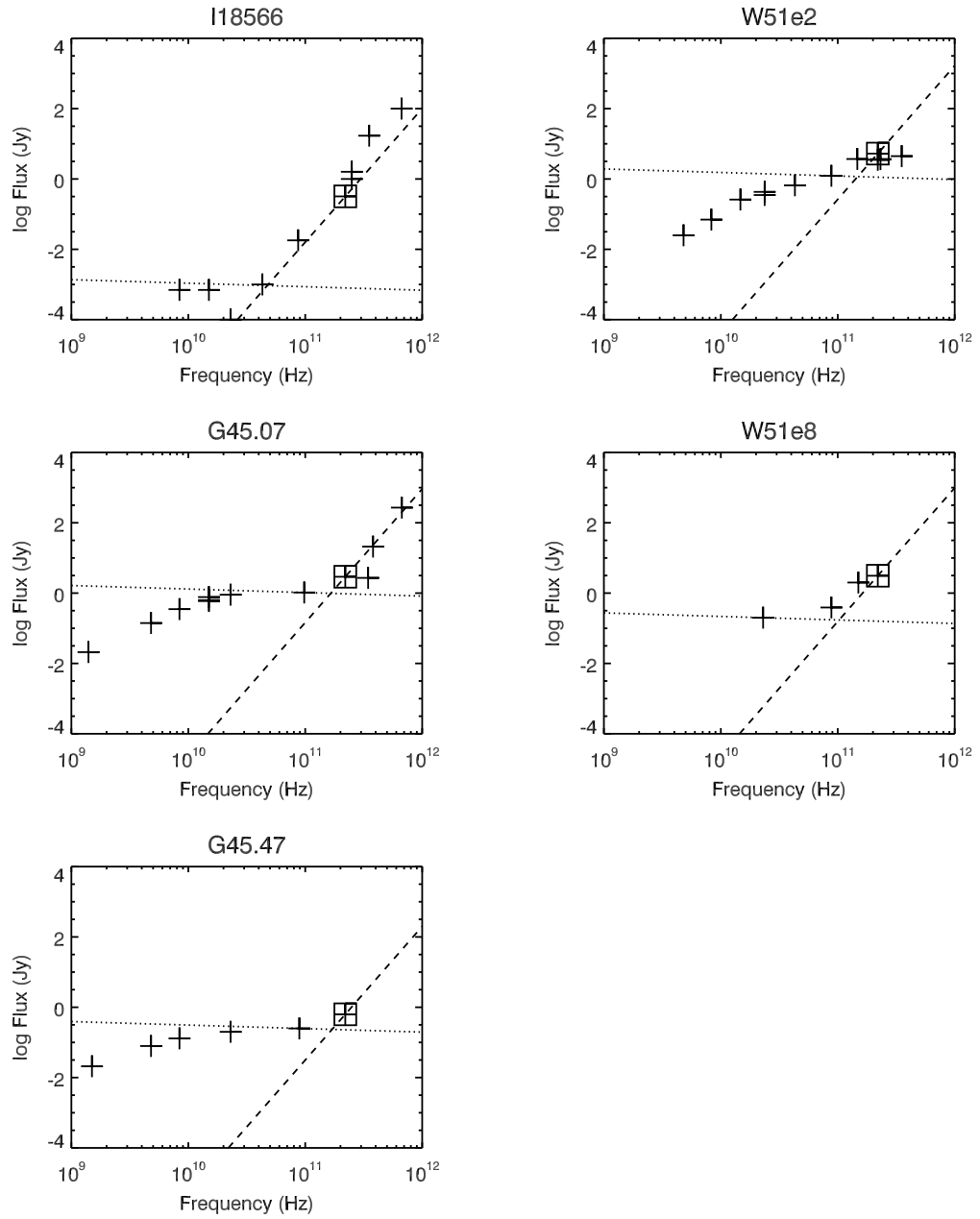


FIG. 4.12: The same as figure 4.9.

TABLE 4.3: 1.3 mm continuum results

Source	R.A.(a) (J2000)	Dec.(a) (J2000)	$S_{\nu}^{\text{Peak}}$ (Jy/beam)	$S_{\nu}^{\text{Total}}$ (Jy)	$S_{\nu}^{\text{dust}}$ (Jy)	$\theta_s$ (b) (arcsec)	Physical Size(c) ( $10^{-3}$ pc)	$M_{\text{gas}}$ (d) ( $M_{\odot}$ )	$N_{H_2}$ ( $10^{24}$ cm $^{-2}$ )	$n_{H_2}$ ( $10^7$ cm $^{-3}$ )
W3OH	02 27 03.862	+61 52 24.60	2.42±0.089	3.85±0.77	1.37±0.27	3.2×2.0	30.9 ×19.6	19	1.74	5.00
W3TW	02 27 04.611	+61 52 24.74	1.23±0.055	2.67±0.53	2.66±0.53	3.1×2.0	30.5 ×18.8	12	1.18	3.49
I16547	16 58 17.242	-42 52 07.97	0.20±0.029	1.58±0.32	1.57±0.31	4.0×3.0	56.8 ×41.6	21	0.48	0.70
I17233	17 26 42.480	-36 09 17.66	2.23±0.132	5.90±1.18	5.88±1.18	4.7×2.6	22.8 ×12.9	7	1.35	5.57
G5.89	18 00 30.428	-24 04 01.62	2.15±0.136	7.72±1.54	0.69±0.14	4.5×3.5	65.0 ×51.5	16	0.26	0.32
G8.68	18 06 23.492	-21 37 10.64	0.17±0.010	0.40±0.08	0.39±0.08	4.6×3.0	106.8 ×68.6	14	0.10	0.08
G10.47	18 08 38.238	-19 51 50.21	3.85±0.137	5.04±1.00	4.90±0.98	1.6×1.1	65.5 ×46.6	375	6.69	8.61
G10.62	18 10 28.687	-19 55 49.17	3.70±0.178	7.07±1.41	4.45±0.89	5.0×3.4	120.7 ×81.9	116	0.63	0.37
I18182	18 21 09.128	-14 31 50.56	0.39±0.025	0.84±0.17	0.83±0.17	3.4×3.2	60.4 ×56.5	21	0.33	0.41
G23.01	18 34 40.297	-09 00 38.19	0.20±0.009	0.42±0.08	0.41±0.08	4.0×2.9	90.3 ×63.8	16	0.14	0.13
G28.20N	18 42 58.112	-04 13 57.56	0.75±0.032	1.25±0.25	0.70±0.14	1.9×1.6	53.0 ×43.9	33	0.77	1.13
G31.41	18 47 34.334	-01 12 45.85	2.09±0.070	3.06±0.61	3.05±0.61	2.0×1.3	77.7 ×49.8	251	3.53	4.01
I18566	18 59 10.001	+04 12 15.46	0.13±0.009	0.32±0.06	0.31±0.06	3.0×2.4	99.3 ×78.3	16	0.11	0.08
G45.07	19 13 22.073	+10 50 53.41	1.92±0.085	2.92±0.58	1.96±0.39	1.8×1.3	69.4 ×49.6	173	2.73	3.29
G45.47	19 14 25.679	+11 09 25.54	0.35±0.024	0.63±0.13	0.40±0.08	2.6×1.5	95.9 ×55.2	66	0.67	0.65
W51e2	19 23 43.947	+14 30 34.88	1.82±0.140	5.27±1.05	4.14±0.83	1.5×1.4	37.3 ×35.3	96	4.00	7.70
W51e8	19 23 43.883	+14 30 27.82	1.36±0.107	3.12±0.62	2.96±0.59	1.4×1.0	35.8 ×24.9	86	5.27	12.44

**Notes.**— (a) Positions of the 1.3 mm continuum peak emission. (b) Deconvolved sizes from Gaussian fit. (c) Sizes at distances in Table 1. (d) Gas mass derived from the estimated 1.3 mm continuum dust emission ( $S_{\nu}^{\text{dust}}$ ) assuming the temperature of the CH<sub>3</sub>CN gas in the compact component.

We caution that the calculated values for the mass and column density are sensitive to both the dust emissivity index and the temperature assumed for each region. For example, decreasing  $\beta$  to 1.0 (while keeping the same temperature) lowers the results by a factor of  $\sim 3.3$ . Also, we note that distance uncertainties may be significant for some sources. For other sources (i.e., W3OH/TW, G5.89, G10.47, G10.62, I18182, G23.01, G45.07, and the W51 region) trigonometric parallaxes have been measured (Reid et al. 2009, 2014); these distances are more accurate.

### 4.3.2 Molecular line emission

We detected many molecular lines toward the 17 HMCs, but the strength of each species and transition detected varies from source to source. We used the SPLATALOGUE<sup>3</sup> website to identify by eye the main lines in the LSB spectra which are mostly dominated by species such as  $^{13}\text{CO}$  and  $\text{C}^{18}\text{O}$ , plus  $\text{CH}_3\text{CN}$ . Other species frequently detected were  $\text{SO}$ ,  $\text{SO}_2$ ,  $\text{H}_2^{13}\text{CO}$ ,  $\text{CS}$  and  $\text{HNCO}$ . In figures 4.13 and 4.14 we show the SMA spectra extracted from the line data-cubes. Except for G23.01, all spectra are the lower-sideband. The spectra are averaged over one beam centered on the peak of continuum. We set the spectra in the rest frame in order to compare the different frequency ranges of observations. We marked in all sources the  $\text{CH}_3\text{CN}$  ( $12_K\text{--}11_K$ )  $K$ -ladders. As a reference, we marked some molecular transitions with strong emission in I17233 and G23.01. A summary of three transitions of  $\text{CH}_3\text{CN}$  ( $12_K\text{--}11_K$ ),  $\text{CH}_3\text{OH}$ ,  $\text{SO}$ , and  $\text{HNCO}$  lines in the lower sideband is presented in Table 4.4.

In Figures 4.15 and 4.16 we show part of the spectrum—in the  $\text{CH}_3\text{CN}$  ( $12_K\text{--}11_K$ ) region—for each source, obtained from the integrated emission over the region of gas traced by the  $K = 3$  line. We detected  $K$ -components in all seventeen sources at least up to the  $K = 5$  line, which traces gas at  $\sim 247$  K. For six sources, I17233, G10.47, G10.62, G31.41, W51e2, and W51e8 we detected  $K = 8$  lines with  $E_u = 525$  K (See Table 4.5). The  $K = 9$  line is blended with the  $^{13}\text{CO}(2\text{--}1)$  line at  $\sim 220.4$  GHz, making its detection ambiguous.

A complete line identification and chemical analysis is beyond the scope of this work. Nevertheless, we note that there is substantial chemical differentiation in some sources,

---

<sup>3</sup><http://www.splatalogue.net/>

including pairs of objects as closely spaced as W3TW-W3OH or W51e2-W51e8. These differences have been explained as due to different physical conditions in each region, different chemical composition of ice-mantles on dust grains or different ages of HMCs (e.g., [Herbst & van Dishoeck 2009](#)).

In Table 4.5 we present the results from the fit of Gaussian profiles to each CH<sub>3</sub>CN  $K$ -component detected. We used the CLASS software package<sup>4</sup> to estimate the line width ( $\Delta V$ ), the integrated intensity ( $\int T dv$ ), and the LSR velocity ( $V_{\text{LSR}}$ ) for each line. We show in Table 4.5 the average  $K$ -component values for  $\Delta V$  and  $V_{\text{LSR}}$  toward each HMC.

TABLE 4.4: Detection Summary of three CH<sub>3</sub>CN ( $12_K$ – $11_K$ ) transitions, CH<sub>3</sub>OH, SO, and HNC lines in the lower sideband

Source	CH <sub>3</sub> CN			CH <sub>3</sub> OH( $8_{0,8}$ - $7_{1,6}$ )-E	SO ( $6_5$ - $5_4$ )	HNC ( $10_{0,10}$ - $9_{0,9}$ )
	$K = 3$ (133 K)	$K = 5$ (247 K)	$K = 7$ (418 K)	220.078 GHz (97 K)	219.949 GHz (35 K)	219.798 GHz (58 K)
W3OH	Y	Y	Y	Y	Y	Y
W3TW	Y	Y	N	Y	Y	?
I16547	Y	Y	Y	Y	Y	Y
I17233	Y	Y	Y	Y	Y	Y
G5.89	Y	Y	Y	Y	Y	Y
G8.68	Y	Y	N	–	–	–
G10.47	Y	Y	Y	–	–	–
G10.62	Y	Y	Y	–	–	–
I18182	Y	Y	Y	Y	Y	Y
G23.01	Y	Y	Y	Y	Y	Y
G28.20N	Y	Y	Y	–	–	–
G31.41	Y	Y	Y	Y	Y	Y
I18566	Y	Y	Y	Y	Y	Y
G45.07	Y	Y	Y	Y	Y	Y
G45.47	Y	Y	N	N	Y	Y
W51e2	Y	Y	Y	–	–	–
W51e8	Y	Y	Y	–	–	–

Notes.— (a) Positions. (d) Gas.

<sup>4</sup>CLASS is part of the GILDAS software package developed by IRAM

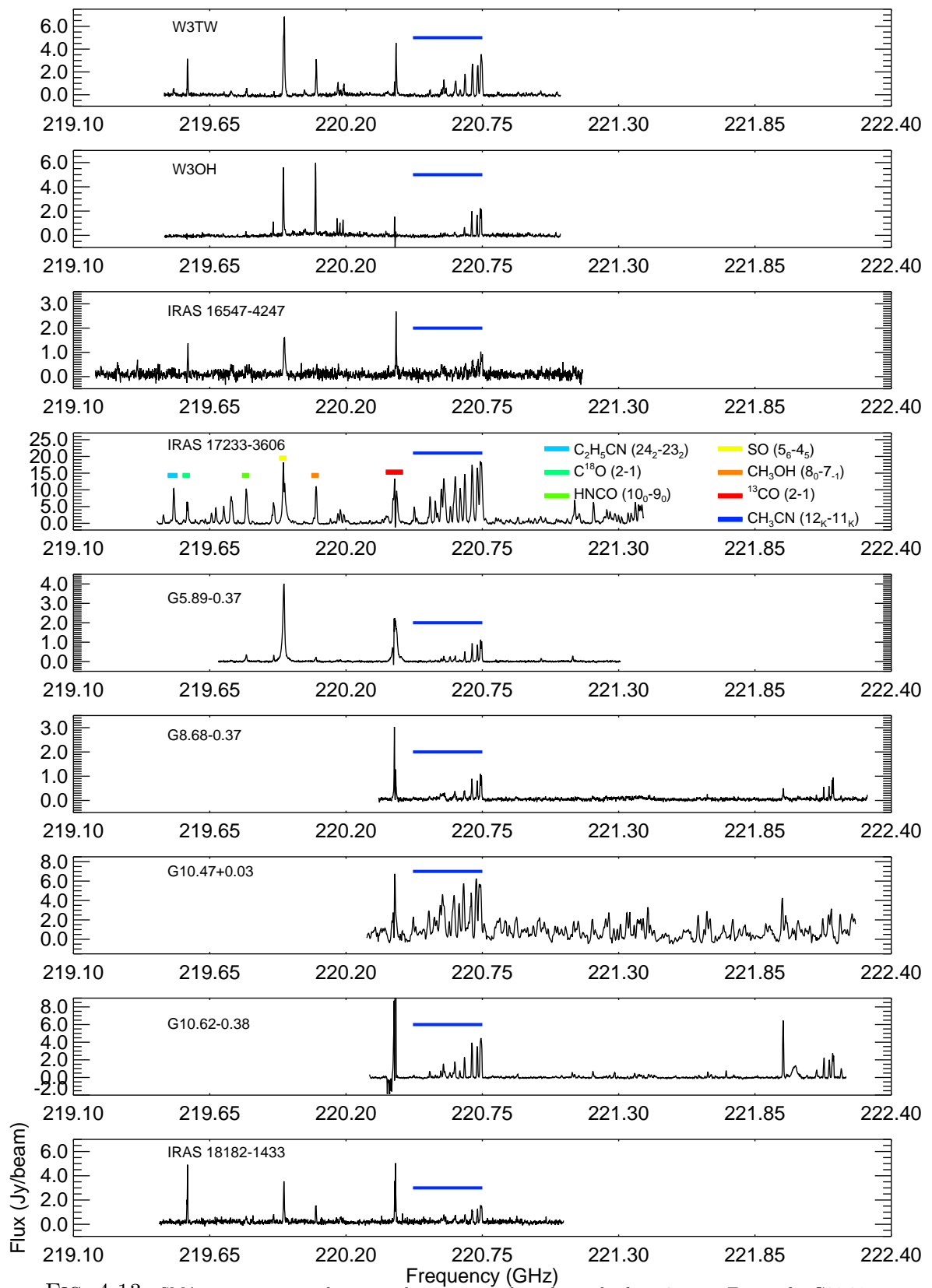


FIG. 4.13: SMA spectra averaged over one beam centered on the peak of continuum. Except for G23.01, all spectra are the lower-sideband. The horizontal axis is the frequency in the rest frame. As a reference, we marked some molecular transitions with strong emission in I17233. The  $CH_3CN$  ( $12_K-11_K$ )  $K$ -ladder is marked in all sources.

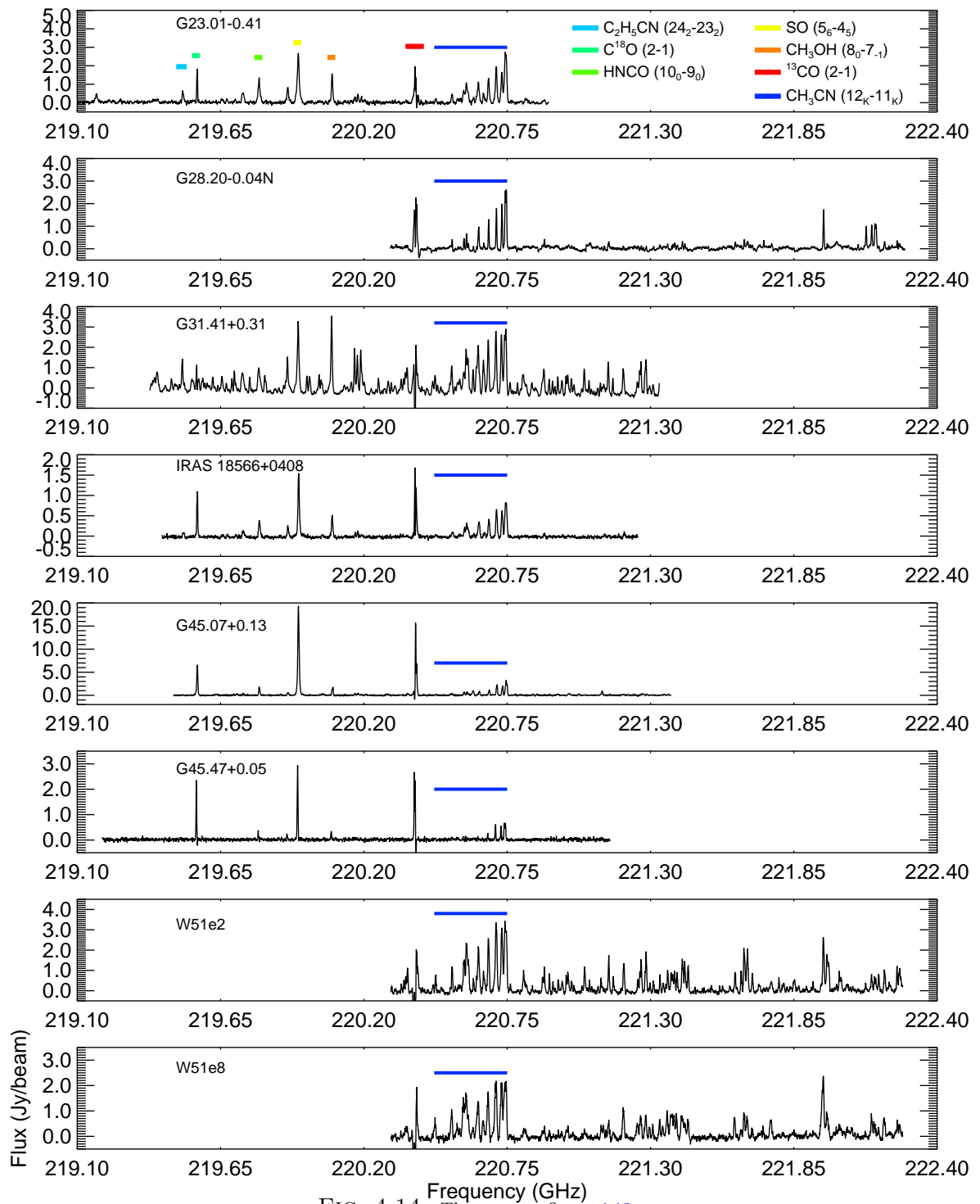


FIG. 4.14: The same as figure 4.13.



TABLE 4.5: Observed Line Parameters of CH<sub>3</sub>CN ( $12_K-11_K$ )

Source	$V_{\text{LSR}}^{(a)}$ (km s <sup>-1</sup> )	$\Delta V^{(a)}$ (km s <sup>-1</sup> )	$\int T dv$ (K km s <sup>-1</sup> )								
			$K=0$	$K=1$	$K=2$	$K=3$	$K=4$	$K=5$	$K=6$	$K=7$	$K=8$
W3OH	-46.2	5.3	21.5±0.5	32.2±0.7	22.8±0.4	24.1±0.4	9.4±0.6	4.8±1.1	2.2±1.2	...	...
W3TW	-49.7	6.5	35.3±18.9	58.5±19.8	40.1±3.0	39.1±0.5	25.9±4.6	22.2±5.4	13.8±13.0	4.3±3.1	...
I16547	-31.9	7.6	81.6±3.8	69.8±2.5	66.2±2.9	79.4±7.3	51.4±5.4	30.7±3.7	12.0±4.2	...	...
I17233	-3.51	9.8	201.3±15.5	241.0±0.6	230.9±1.8	269.9±3.1	195.2±0.7	119.9±10.9	157.2±9.0	89.5±0.6	46.8±2.0
G5.89	9.69	3.9	2.4±0.4	4.3±0.5	2.2±0.1	2.4±0.2	1.0±0.1	0.4±0.1	0.3±0.1	...	...
G8.68	39.2	5.4	4.9±0.2	6.3±0.2	3.8±0.1	5.2±0.1	2.9±0.1	2.8±0.3	1.2±0.5	0.7±0.1	...
G10.47	74.5	9.3	199.1±4.0	195.6±2.2	284.6±6.2	147.7±4.5	176.3±2.3	166.3±9.8	139.7±3.4	103.1±8.8	60.2±4.5
G10.62	-3.3	6.1	22.9±0.4	35.7±0.1	25.4±0.1	30.3±0.2	15.6±0.1	12.4±0.1	8.1±0.5	5.1±0.4	1.4±0.1
I18182	59.1	6.6	12.4±2.0	20.7±2.2	12.7±0.4	17.4±0.8	9.0±0.7	8.2±0.7	8.3±0.8	...	...
G23.01	78.3	8.0	20.9±0.3	31.8±0.2	18.3±1.9	23.5±0.5	15.0±0.3	10.2±0.2	11.5±0.7	4.6±0.2	...
G28.20N	95.3	5.0	38.9±1.6	40.0±1.6	28.5±0.7	33.3±0.4	20.9±0.2	19.4±1.0	12.3±0.5	4.8±0.6	...
G31.41	99.6	7.6	65.8±1.3	63.3±7.6	71.3±1.2	69.8±1.0	58.8±0.6	47.5±3.1	35.4±0.7	20.8±1.4	12.4±0.2
I18566	84.6	8.0	13.5±1.0	11.9±0.5	13.5±0.2	13.8±0.2	8.0±0.3	7.4±0.2	4.9±0.9	...	...
G45.07	58.5	7.4	47.6±5.9	52.4±0.7	38.3±0.4	47.0±0.3	20.4±0.2	19.2±1.0	13.3±1.0	5.2±0.8	...
G45.47	64.3	4.2	9.5±0.9	9.3±0.9	7.0±0.3	7.7±0.2	2.4±0.3	1.3±0.2	1.1±0.2	1.1±0.2	...
W51e2	55.7	8.0	252.0±9.8	408.8±9.5	413.8±5.5	449.2±5.1	270.2±5.2	235.4±9.1	236.6±9.3	89.5±3.2	47.2±2.9
W51e8	58.5	9.0	191.3±3.3	318.0±9.4	311.1±2.2	311.8±2.2	191.8±3.9	109.5±9.9	191.9±6.7	91.5±3.6	27.7±7.8

**Notes.**—(a) Average values from all detected  $K$ -components.

### 4.3.3 Temperature and density of the CH<sub>3</sub>CN gas

CH<sub>3</sub>CN is considered to be a good tracer of warm-hot and high density gas (e.g., [Araya et al. 2005a](#)). Its symmetric-top molecular structure works as a rotor, emitting in multiple  $K$ -levels within a specific  $J$  transition, all within a narrow bandwidth ( $\sim 0.2$  GHz). This spectral characteristic is very useful in order to avoid certain systematic errors that occur when comparing lines of very different frequencies. The  $K$ -levels are radiatively decoupled, and are populated only through collisions ([Solomon et al. 1971](#)), thus the rotational temperature of CH<sub>3</sub>CN is close to the kinetic temperature of the gas.

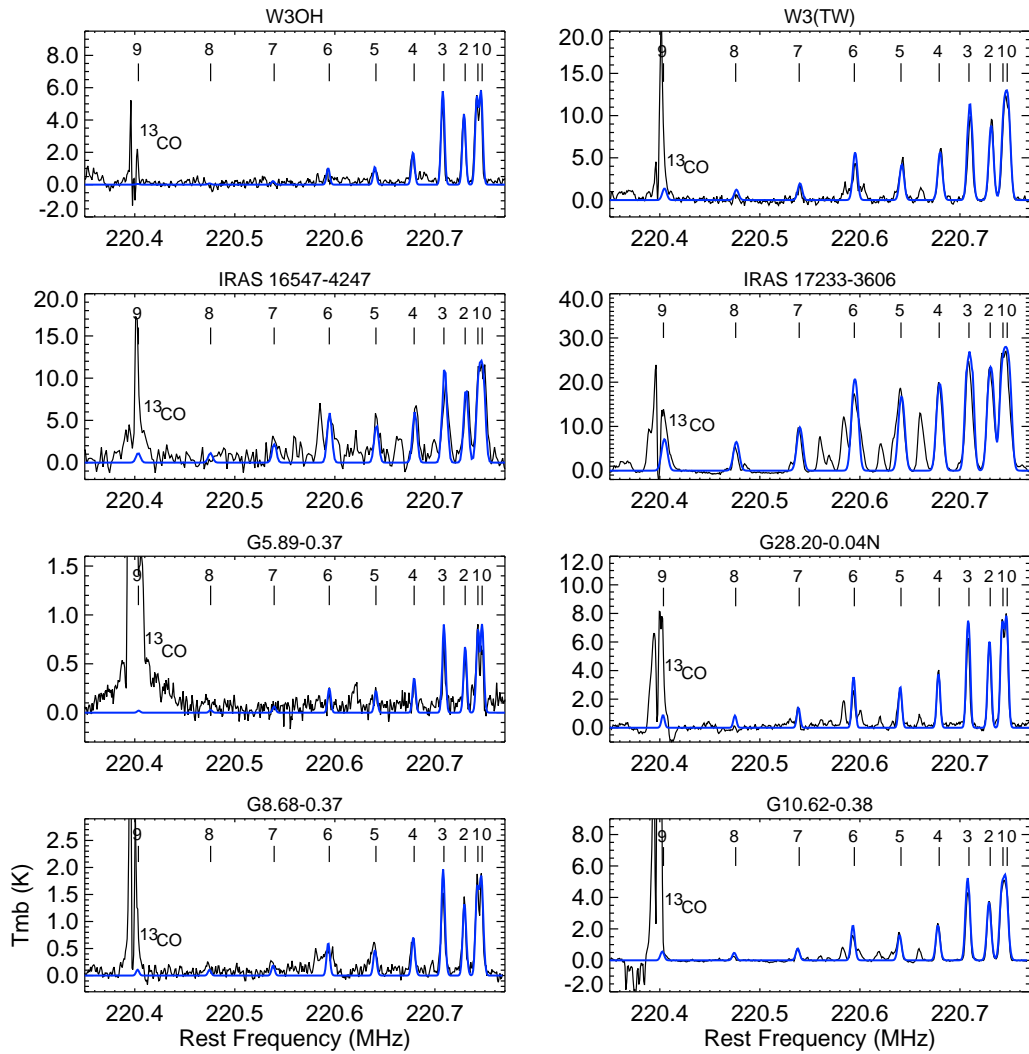


FIG. 4.15: Observed  $\text{CH}_3\text{CN}$  ( $12_K-11_K$ ) spectra (black) and synthetic model (blue) spectra obtained with XCLASS. The fit parameters are given in Table 4.6. The numbers in each panel represent the  $K$ -ladder quantum numbers. The line at  $\sim 220.4$  GHz is  $^{13}\text{CO}(2-1)$  and is overlapped with the  $K = 9$  line.

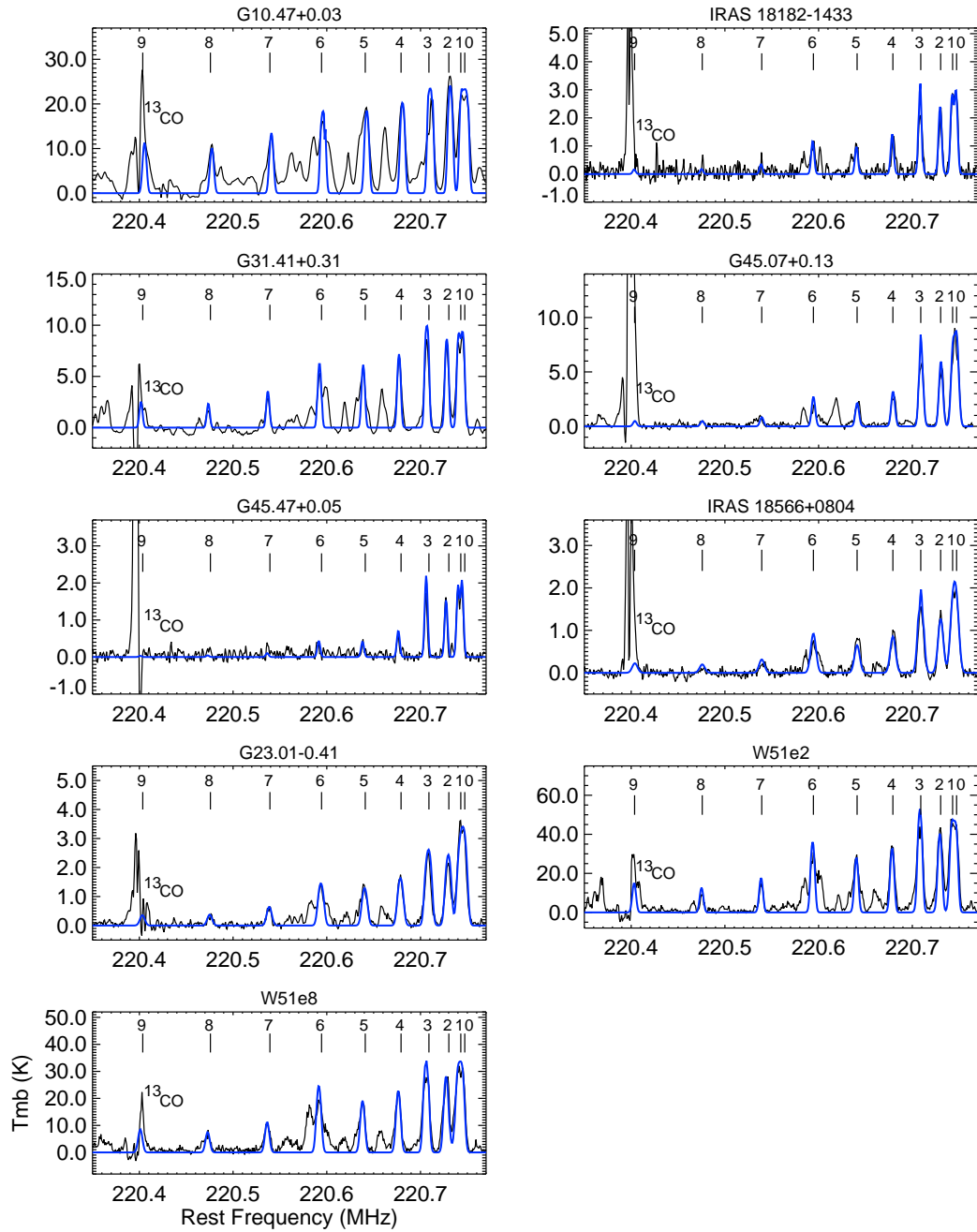


FIG. 4.16: Continuation of Figure 4.15.

If we assume local thermodynamic equilibrium (LTE) and optically thin gas,  $\text{CH}_3\text{CN}$  is an excellent tracer of kinetic temperature using methods such as rotation diagrams (RDs; Linke et al. 1979; Turner 1991), population diagrams (PDs, which consider the optical depth of lines; Goldsmith & Langer 1999; Araya et al. 2005a), and simultaneous fitting of multiple lines in a spectrum (Comito et al. 2005; Schilke et al. 1999). In

general, no background radiation is considered, and in the RD and PD methods, uniform temperature and density are assumed.

Following the procedure outlined in Turner (1991) and Araya et al. (2005a) one obtains the linear equation  $\ln(N_u/g_u) = \ln(N_{\text{tot}}/Q_{\text{rot}}) - E_u/kT_{\text{rot}}$ , in which the slope is  $(-1/T_{\text{rot}})$  and  $\ln(N_{\text{tot}}/Q_{\text{rot}})$  the intercept (see section 3.3.1) The left-hand side of this equation contains the column density per statistical weight of the molecular energy levels and represents the integrated intensity per statistical weight. In this way, plotting the natural logarithm of  $N_u/g_u$  versus  $E_u/k$  of each  $K$ -level of CH<sub>3</sub>CN and calculating the best linear fit,  $T_{\text{rot}}$  and  $N_{\text{tot}}$  can be inferred. In thermodynamic equilibrium the rotational temperature closely approximates the kinematic temperature of the gas.

As a first approximation we estimated the column density and rotational temperature by means of the RD method. The rotation diagrams are shown in Figure 4.17 and the results of the linear fits are listed in Table 4.6. The error bars come from the integrated intensity errors in the fitting to each  $K$ -transition with CLASS and are shown in Table 4.5.

In the case of mildly optically thick lines, RDs underestimate the upper level column density and overestimate the rotational temperatures. To first order, problems in these estimations can be overcome using the PD method which accounts for optical depth and the source filling factor as proposed in Goldsmith & Langer (1999). Finally, in the RDs method we assumed one region with a single temperature  $T_{\text{rot}}$ .

A more sophisticated approach is to simultaneously fit multiple lines as outlined by Comito et al. (2005) and Schilke et al. (1999). Their XCLASS program<sup>5</sup> generates a synthetic spectrum for multiple molecular species, assuming multiple emission regions, all assumed to be in LTE. Also, XCLASS accounts for line blends and optical depth. For each emission region the program requires inputs for the source size, column density, rotation temperature, line width, and velocity offset from the  $V_{\text{LSR}}$ . XCLASS uses the CDMS and JPL spectral line database (Pickett et al. 1998; Müller et al. 2005, 2001) for line identification. (See Comito et al. 2005, and Section 3.3.2 in this thesis for details of the procedure).

---

<sup>5</sup><http://astro.uni-koeln.de/projects/schilke/XCLASS>

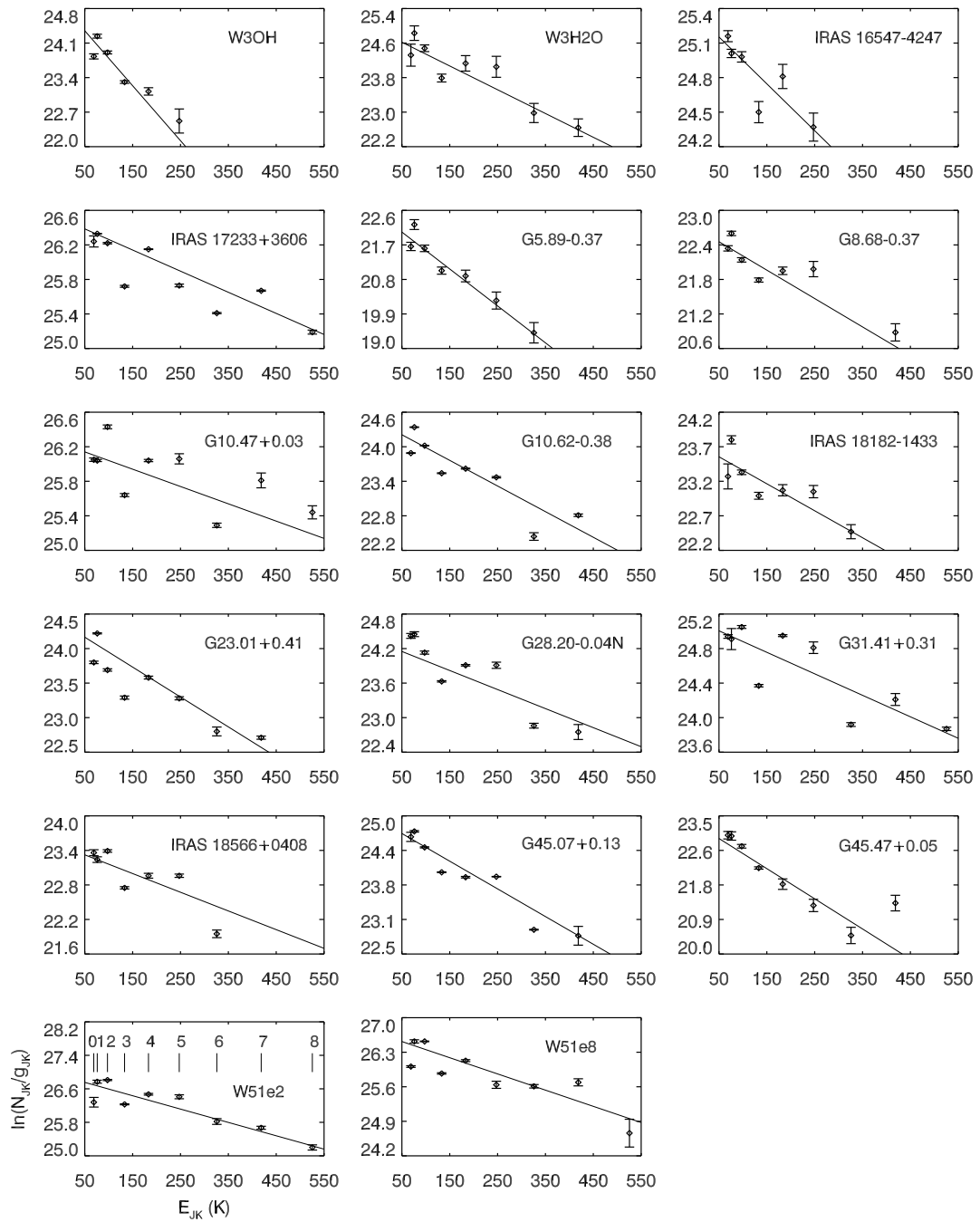


FIG. 4.17: Rotation diagrams for  $\text{CH}_3\text{CN}$  ( $12_K-11_K$ ). The line is the linear fit of all data points in the plots. The numbers in the lower left panel, of W51e2, represent the  $K$ -ladder quantum numbers.

TABLE 4.6: Physical parameters derived from CH<sub>3</sub>CN (12<sub>K</sub>-11<sub>K</sub>).

Source	XCLASS Program(a)					Rotational Diagram(b)		$M_{vir}$ (c) ( $M_{\odot}$ )
	$\theta_s$ (arcsec)	$T_{rot}$ (K)	$N_{tot}$ ( $\text{cm}^{-2}$ )	$\Delta v$ (km/s)	$X_{\text{CH}_3\text{CN}}^{\text{core}}$	$T_{rot}$ (K)	$N_{tot}$ ( $\text{cm}^{-2}$ )	
W3OH	1.1	$122^{+56}_{-12}$	$3.3^{+2.1}_{-3.5}$ (15)	5.0	1.9(-9)	90	2.2(14)	58
	5.5	$68^{+22}_{-25}$	$7.5^{+1.1}_{-2.0}$ (13)	6.0				
W3TW	0.8	$367^{+102}_{-6}$	$3.9^{+0.6}_{-1.1}$ (16)	7.0	3.2(-8)	182	6.9(14)	85
	3.5	$108^{+43}_{-6}$	$7.1^{+2.5}_{-0.6}$ (14)	8.0				
I16547	0.7	$272^{+93}_{-59}$	$2.2^{+0.4}_{-0.6}$ (16)	7.0	4.5(-8)	245	2.0(15)	235
	2.4	$78^{+20}_{-38}$	$8.8^{+2.2}_{-1.3}$ (13)	8.0				
I17233	0.9	$346^{+137}_{-105}$	$2.4^{+1.9}_{-3.2}$ (17)	9.0	1.8(-7)	408	2.0(16)	138
	6.3	$132^{+97}_{-100}$	$9.1^{+1.9}_{-0.9}$ (13)	9.0				
G5.89	0.9	$165^{+70}_{-33}$	$9.6^{+1.0}_{-2.2}$ (14)	5.0	3.6(-9)	104	2.5(13)	74
	7.0	$40^{+20}_{-15}$	$1.6^{+0.2}_{-3.1}$ (13)	7.0				
G8.68	1.0	$281^{+92}_{-79}$	$4.2^{+0.9}_{-1.2}$ (15)	5.0	4.2(-8)	202	9.5(13)	209
	4.7	$77^{+28}_{-30}$	$1.9^{+0.6}_{-0.9}$ (14)	6.0				
G10.47	0.6	$408^{+96}_{-108}$	$5.1^{+2.4}_{-1.9}$ (17)	6.0	6.1(-8)	499	2.5(16)	400
	4.0	$82^{+20}_{-22}$	$4.1^{+0.9}_{-0.6}$ (14)	7.0				
G10.62	1.9	$415^{+55}_{-123}$	$6.7^{+0.7}_{-0.4}$ (15)	6.0	1.0(-8)	224	6.5(14)	310
	6.6	$95^{+25}_{-45}$	$3.0^{+2.0}_{-0.8}$ (14)	8.0				
I18182	1.1	$219^{+102}_{-110}$	$7.3^{+2.6}_{-1.8}$ (15)	5.0	2.1(-8)	256	4.3(14)	213
	4.4	$75^{+45}_{-50}$	$8.2^{+2.2}_{-1.3}$ (13)	6.0				
G23.01	0.4	$237^{+93}_{-39}$	$1.5^{+0.7}_{-0.7}$ (17)	7.0	1.0(-7)	231	6.6(14)	407
	4.6	$58^{+92}_{-28}$	$1.7^{+1.1}_{-0.5}$ (14)	8.0				
G28.20N	0.6	$295^{+98}_{-92}$	$6.2^{+1.1}_{-0.9}$ (16)	5.0	8.0(-8)	302	1.1(15)	100
	5.0	$59^{+31}_{-30}$	$2.4^{+1.5}_{-1.8}$ (14)	6.0				
G31.41	0.4	$327^{+173}_{-97}$	$1.5^{+1.3}_{-1.3}$ (17)	5.0	4.2(-8)	402	4.8(15)	300
	4.6	$95^{+75}_{-55}$	$9.1^{+5.9}_{-5.0}$ (13)	7.0				
I18566	1.1	$382^{+107}_{-90}$	$7.1^{+1.2}_{-2.1}$ (15)	8.0	6.4(-8)	308	4.9(14)	473
	4.2	$110^{+62}_{-60}$	$5.2^{+1.0}_{-1.0}$ (13)	9.0				
G45.07	1.1	$290^{+89}_{-65}$	$5.4^{+0.9}_{-2.1}$ (15)	6.0	2.0(-9)	200	8.5(14)	270
	3.7	$82^{+25}_{-39}$	$4.1^{+1.1}_{-1.8}$ (14)	7.0				
G45.47	1.2	$155^{+95}_{-60}$	$6.8^{+1.8}_{-1.3}$ (14)	5.0	1.0(-9)	131	8.0(13)	108
	4.0	$65^{+18}_{-23}$	$3.8^{+1.2}_{-0.7}$ (13)	5.0				
W51e2	0.5	$485^{+121}_{-130}$	$2.8^{+2.3}_{-1.9}$ (17)	6.0	7.0(-8)	314	1.6(16)	194
	3.0	$118^{+44}_{-42}$	$1.0^{+1.4}_{-1.7}$ (15)	8.0				
W51e8	0.5	$384^{+126}_{-150}$	$1.8^{+0.8}_{-0.5}$ (17)	7.0	3.4(-8)	304	1.2(16)	203
	3.2	$85^{+95}_{-35}$	$1.8^{+0.3}_{-0.4}$ (14)	9.0				

**Notes.**— (a) Final values of source sizes, rotational temperatures, column densities, and line widths for the best fit of the synthetic to the observed spectrum. All sources fit with two components. (b) Rotational temperatures and column densities from the best linear fit, in which we included the  $K$ -lines 0 and 1. (c) Virial mass was estimated using  $\Delta V$  from Table 4.5.

To form the synthetic spectra we model each source as two distinct emission regions: one extended and warm, with relatively low density, and the other compact and hot, with high density. The size of the regions is degenerate with temperature and column density, depending on the optical depth (See Eq. 6 and 7 of Comito et al. 2005, and Section 3.3.2 of this thesis). To avoid this degeneracy, the size of the extended component was fixed and we varied the compact component size from 0.5 to 0.25 the size of the extended component. We fixed the offset from  $V_{\text{LSR}}$  as estimated directly from the observed spectrum (Table 4.5).

We probed the parameter space with temperatures between 100 K and 500 K for the compact component, and from 50 K to 150 K for the extended component. For the column density we probed  $10^{14}$ – $10^{18}$   $\text{cm}^{-2}$  for the compact component, and  $10^{12}$ – $10^{15}$   $\text{cm}^{-2}$  for the extended component. The best fit of the synthetic to the observed spectrum was determined by a  $\chi^2$  analysis. As we approached a better fit we used step sizes of 1 K in temperature and  $1 \times 10^{12}$   $\text{cm}^{-2}$  in column density. For  $\Delta V$  we probed steps of  $\pm 2$ ,  $\pm 1$  and 0  $\text{km s}^{-1}$  from a near value to the observed average (Table 4). Most of the sources showed a better fit when we used larger line widths for the compact component than for the extended one. In order to estimate errors, we modeled new synthetic spectra perturbing separately temperatures and column densities until we measured an under/overestimation in 20% of the brightness temperature for the  $K = 2$  transition (20% is the estimated upper limit flux uncertainty of observations), since such a line is mostly optically thin and not blended by other lines.

In Table 4.6 we present the final fit values and in Figures 4.15 and 4.16 we show the observed and synthetic spectra, respectively. All HMCs showed reasonable fits with observations using the two-component model.

#### 4.3.4 Virial masses and velocity gradients

Virial mass,  $M_{vir}$ , can be estimated using the line width and source size. Assuming a power-law density distribution with index  $p = 1.5$  in a spherical core, we use the expression (See Eq. 1 of Beltrán et al. 2004b; MacLaren et al. 1988):

$$\left[ \frac{M_{vir}}{M_{\odot}} \right] = 0.40 \left[ \frac{d}{\text{kpc}} \right] \left[ \frac{\theta_{\text{CH}_3\text{CN}}}{''} \right] \left[ \frac{\Delta V}{\text{km s}^{-1}} \right]^2 \quad (4.4)$$

This is the central mass assuming that the core has gravitationally bound motion. For  $\Delta V$  we used the average line width from the observed spectrum (Column 3 in Table 4.5), and for the source size we used the extended component from the XCLASS analysis (Table 4.6).

In the last column of Table 4.6 we present the calculated  $M_{vir}$ , which ranges from 60 to  $473 M_{\odot}$ , with a median of  $209 M_{\odot}$ . We note that most of the  $M_{vir}$  values are greater than  $M_{gas}$ . This imbalance would still hold even if we used the smaller source



size of the compact component to calculate  $M_{vir}$ . We caution that many of the HMCs probably are not in dynamical equilibrium owing to complicated kinematics, multiple star forming sites, and large rotating structures such as toroids and disks. Also, large optical depths, outflowing gas, and systematic velocity gradients will increase the line width and thus the virial mass.

In this regard, each of our observed HMC present evidence of large movement of gas, some times showing evidence for a velocity gradient across the emission region (see figures 4.18 to 4.25). Similar velocity gradients have previously been detected toward some of the sources (e.g., Sollins et al. 2005; Zhang & Ho 1997; Klaassen et al. 2009; Leurini et al. 2011; Furuya et al. 2008; Beltran et al. 2011; Franco-Hernandez et al. 2009; Galvan-Madrid et al. 2009). These works suggest that rotation of the molecular material is responsible for the velocity gradients. If these rotational motions are indicative of large scale toroids or the external region of a smaller scale disk, these inner-most structures may be similar to the well-known scenario of low-mass stars.

## 4.4 Comments on Individual Sources

In this Section we comment the main properties of each source on the basis of previous observations and describe the results obtained in this work.

### 4.4.1 W3OH

It is a well-known shell UC HII region harboring OB stars at about 2.0 kpc, rich in OH and CH<sub>3</sub>OH maser emission associated with ionized gas and weak molecular lines (Wink et al. 1994; Wilner et al. 1995). We measure a 1.3 mm flux density of  $\sim 3.85$  Jy, similar to reported values at different wavelengths: 3.5 Jy at 3 mm (Wilner et al. 1995), 3.4 and 3.6 Jy at 1.4 and 2.8 mm, respectively (Chen et al. 2006). This is consistent with a large contribution of optically-thin free-free emission and minimal dust emission. We estimated a gas mass of  $\sim 19 M_{\odot}$  and column density of  $1.7 \times 10^{24} \text{ cm}^{-2}$ . From interferometric observations of CH<sub>3</sub>CN(5-4) Wink et al. (1994) estimated a rotation temperature of  $90 \pm 40$  K. From the LTE analysis using XCLASS we calculated rotation temperatures between 68 and 122 K; consistent with the results of Wink et al. (1994).

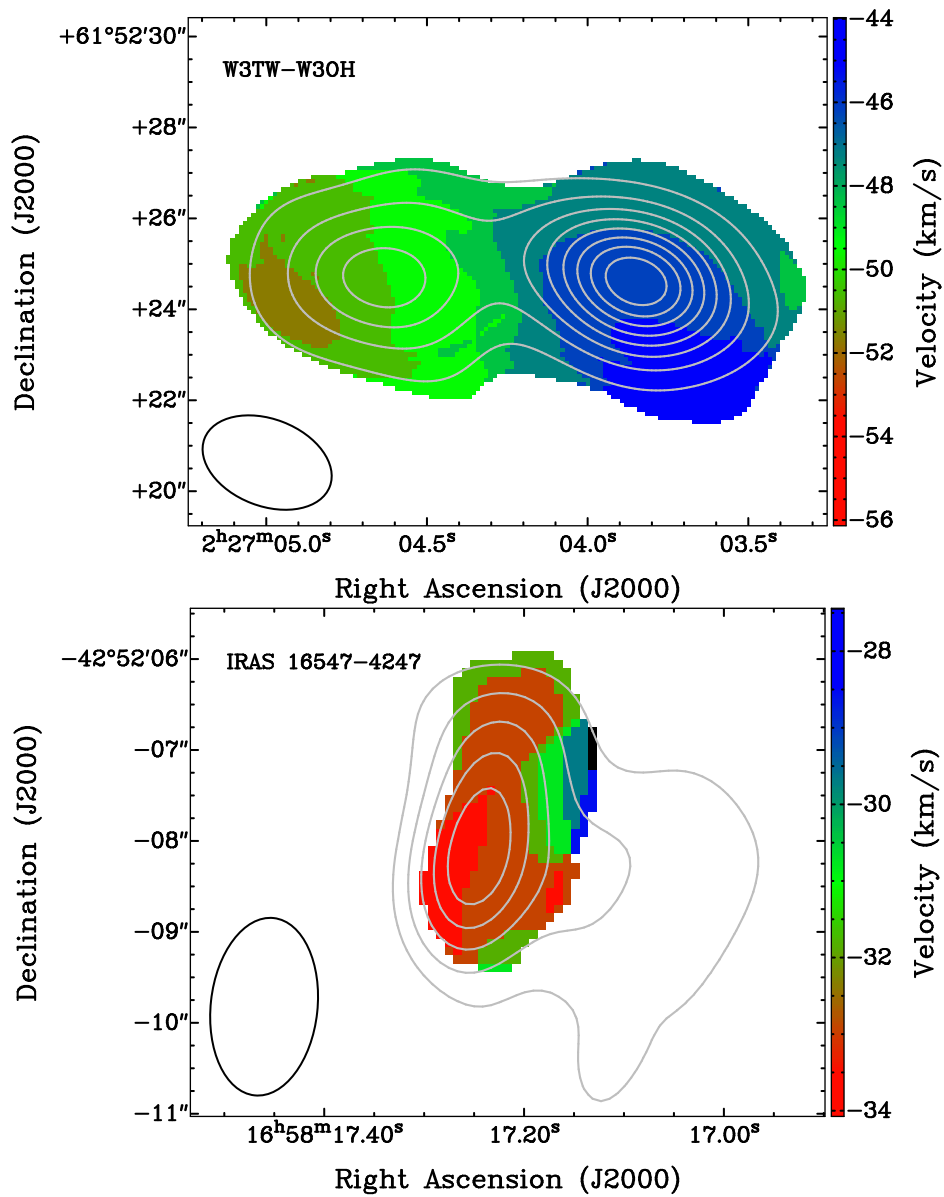


FIG. 4.18: Intensity-weighted mean velocity (moment 1, color scale) map of the  $K = 3$  transition. The 1.3 mm continuum (grey contours) is overlaid with levels for W3OH-region (*top*) from 10% to 90% of the integrated emission (see Table 4.3) with steps of 10%. Contour levels for I16547 (*bottom*) from 50% to 90% of the integrated emission with steps of 10%.

Notably, W3OH shows the lowest temperature in our survey.  $\text{CH}_3\text{CN}$  column densities of  $3.3 \times 10^{15}$  and  $7.5 \times 10^{13} \text{ cm}^{-2}$  were estimated for the compact and extended regions. We estimated a  $\text{CH}_3\text{CN}$  abundance of  $\sim 2 \times 10^{-9}$ .

#### 4.4.2 W3TW

Is a young source, resolved into three components by [Wyrowski et al. \(1999b\)](#), associated with strong dust and molecular emission at (sub)millimeter wavelengths. Using BIMA observations, [Chen et al. \(2006\)](#) report continuum flux densities of 1.38 and 0.22 Jy at 1.4 and 2.8 mm, respectively. Our higher estimate of 2.67 Jy at 1.3 mm may result from our lower angular resolution. [Chen et al. \(2006\)](#) found a protobinary system with a mass of  $\sim 22 M_\odot$  for the pair. Using an LTE model for the  $\text{CH}_3\text{CN}$  ( $12_K$ – $11_K$ ) emission, they found rotation temperatures of 200 K and 182 K for sources A and C, respectively. Our data cannot resolve these two sources. From the 1.3 mm dust emission we estimate a gas mass of  $12.4 M_\odot$  and  $\text{H}_2$  column density of  $1.2 \times 10^{24} \text{ cm}^{-2}$ . Using XCLASS, we estimate temperatures of 108 and 367 K for the extended and compact components. We find a  $\text{CH}_3\text{CN}$  abundance of  $3.2 \times 10^{-8}$ .

#### 4.4.3 I16547

Is a MSFR with a central source of  $\sim 30 M_\odot$ . It hosts a thermal radio jet, outflowing gas, knots of shocked gas and  $\text{H}_2\text{O}$  masers ([Garay et al. 2003](#); [Franco-Hernández et al. 2009](#)). Although the 1.3 mm continuum emission is extended toward the west it is dominated by a core of emission with the central source (see [Figure 4.1](#)). Our continuum analysis ( $S_\nu^{\text{dust}} \sim 1.57 \text{ Jy}$ ) estimates a gas mass of  $\sim 20 M_\odot$  toward the eastern core. The  $\text{CH}_3\text{CN}$  ( $12_K$ – $11_K$ ) analysis shows kinetic temperatures from 78 to 272 K with XCLASS and  $\sim 245 \text{ K}$  using RDs. The molecular emission from  $K = 3, 5, 7$ –lines is detected mainly toward the eastern region, coincident with the 1.3 mm continuum peak. We estimated  $\text{CH}_3\text{CN}$  column densities of  $2.1 \times 10^{16}$  and  $8.8 \times 10^{13} \text{ cm}^{-2}$  for the compact and extended regions, respectively, and a fractional abundance of  $4.5 \times 10^{-8}$  toward the compact component.

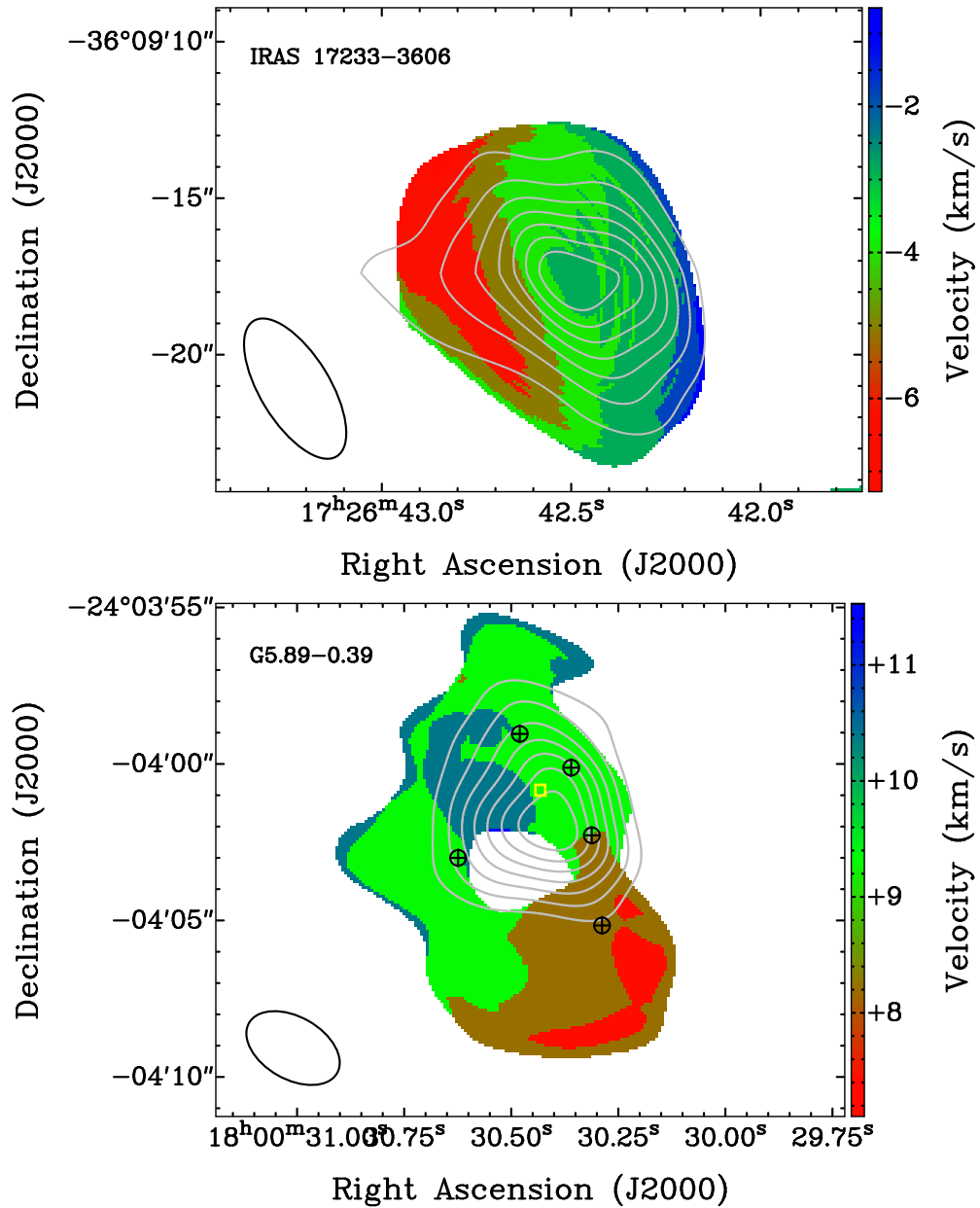


FIG. 4.19: Same as Figure 4.18, but for I17233 and G5.89. For I17233 (*top*) contour levels are from 30% to 90% with steps of 10%. Contour levels for G5.89 (*bottom*) are from 30% to 90% of the integrated emission with steps of 10%.

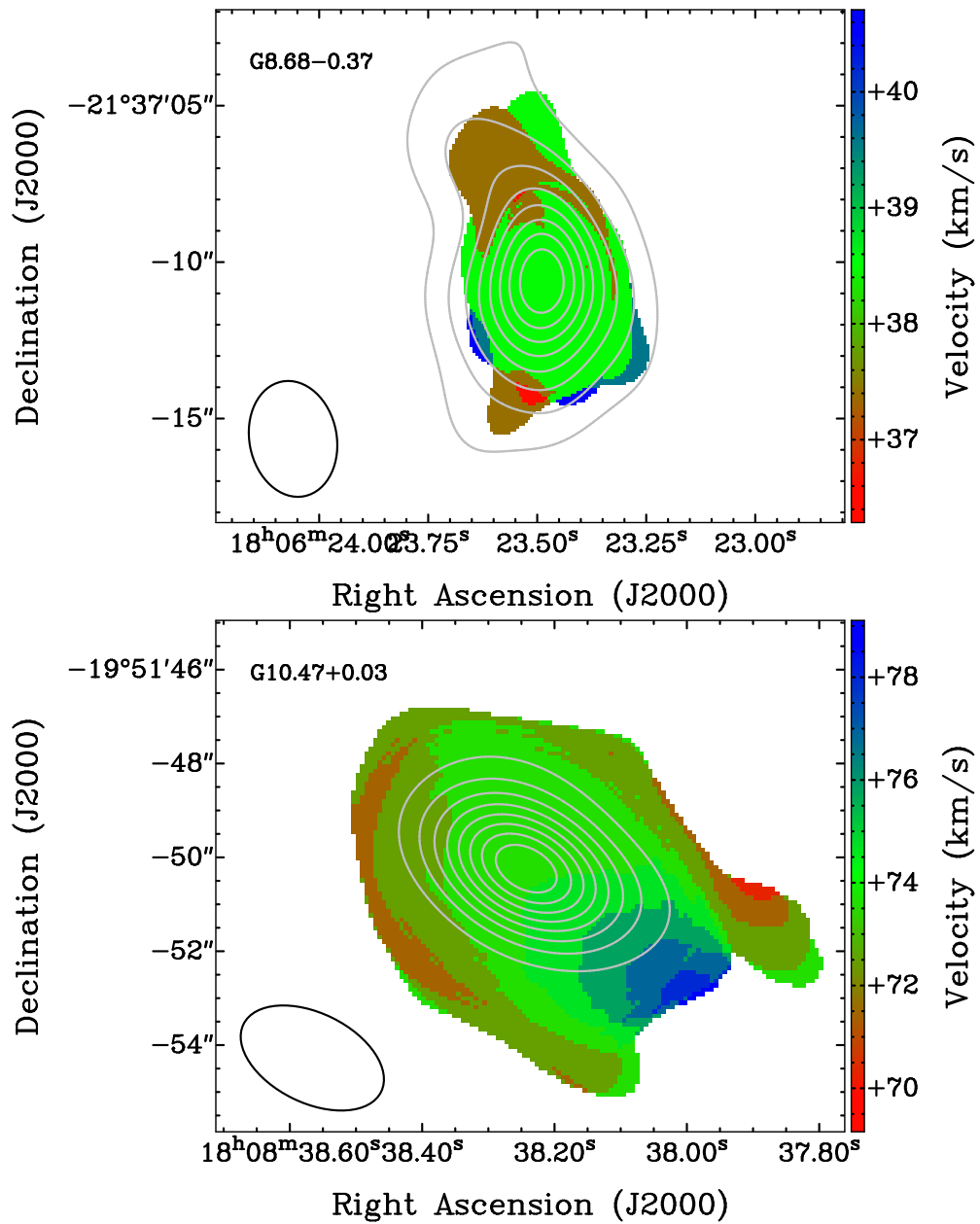


FIG. 4.20: Same as Figure 4.18, but for G8.68 and G10.47. For G8.68 (*top*) contour levels are from 20% to 90% with steps of 10%. Contour levels for G10.47 (*bottom*) are from 20% to 90% of the integrated emission with steps of 10%.

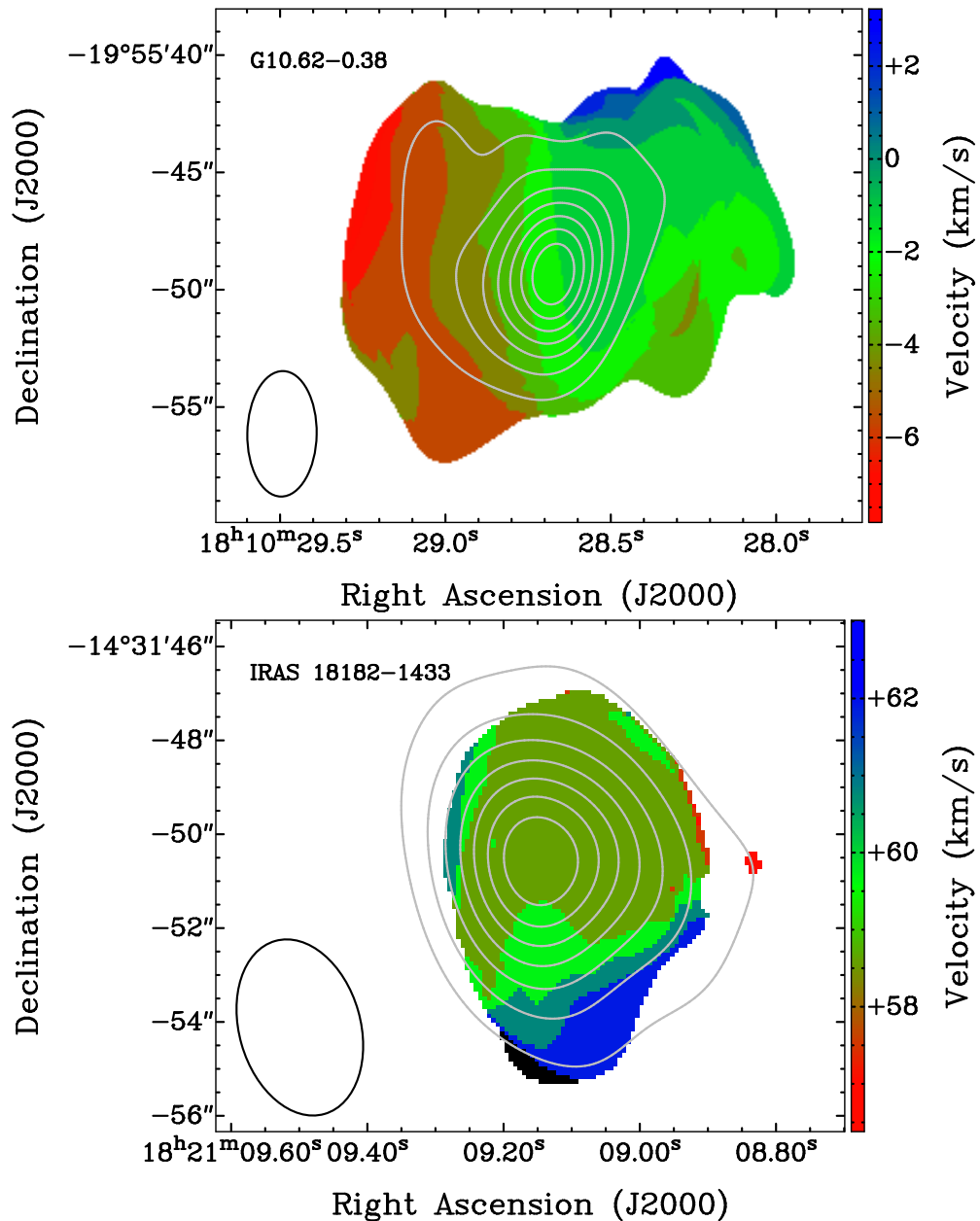


FIG. 4.21: Same as Figure 4.18 but for G10.62 and I18182. For G10.62 (*top*) contour levels are from 30% to 90% with steps of 10%. Contour levels for I18182 (*bottom*) are from 20% to 90% of the integrated emission with steps of 10%.

#### 4.4.4 I17233

Shows maser emission in OH (Fish et al. 2005), CH<sub>3</sub>OH (Walsh et al 1998) and H<sub>2</sub>O (Zapata et al. 2008a), and multiple outflows from several HC HII regions (Leurini et al. 2009; Zapata et al. 2008a). Large-scale movement of NH<sub>3</sub> gas suggests a rotating

core (Beuther et al. 2009). However, SMA observations of CH<sub>3</sub>CN (12<sub>K</sub>–11<sub>K</sub>) reported by Leurini et al. (2011) show that this molecular tracer is probably influenced by molecular outflows. Leurini et al. (2011) used XCLASS with a two-component model similar to ours and report temperatures of 200 K and 50–70 K for the compact and extended components, respectively. Our higher values of 346 K and 132 K result from using smaller component sizes in the modeled spectrum. We estimated a CH<sub>3</sub>CN abundance of  $\sim 2 \times 10^{-7}$ .

#### 4.4.5 G5.89

Is a shell-type UC HII region probably ionized by an O5 star offset  $\sim 1''$  from the center of the HII region (Feldt’s star; Feldt et al. 2003). Also present are strong molecular outflows, maser activity, five (sub)millimeter dust emission sources, and little molecular line emission (Hunter et al. 2008; Sollins et al. 2004). The locations of the five dusty objects are indicated in Figure 4.1. The molecular gas appears to form a cavity that encircles the ionized gas. Intriguingly, the peak position of the 1.3 mm continuum emission, the CH<sub>3</sub>CN (12<sub>K</sub>–11<sub>K</sub>) emission, and Feldt’s star do not coincide. However, most of the continuum emission probably comes from the free-free process, instead of thermal dust. The  $K = 3$ -line emission structure is much more extended than the continuum, while the  $K = 5$  and 6-lines trace hotter gas to the northeast of Feldt’s star and the 1.3 mm emission. The CH<sub>3</sub>CN spectrum of G5.89 does not show emission in  $K$ -lines  $> 6$ . Su et al. (2009) originally reported the SMA CH<sub>3</sub>CN (12<sub>K</sub>–11<sub>K</sub>) data. They found a decreasing temperature structure from 150 to 40 K with respect to the position of Feldt’s star. Using the same SMA data, we estimated temperatures of 165 and 40 K for the compact and extended components. We find a fractional abundance of  $3.6 \times 10^{-9}$  toward the compact component.

#### 4.4.6 G8.68

Is associated with the MSFR IRAS 18032-2137. Also, H<sub>2</sub>O, class II CH<sub>3</sub>OH, and OH maser emission, strong millimeter continuum emission, but no centimeter continuum compact sources or free-free emission are detected (Longmore et al. 2011). Infall profiles traced with HCO<sup>+</sup>, HNC and <sup>13</sup>CO at 3 mm (Purcell et al. 2006) and strong

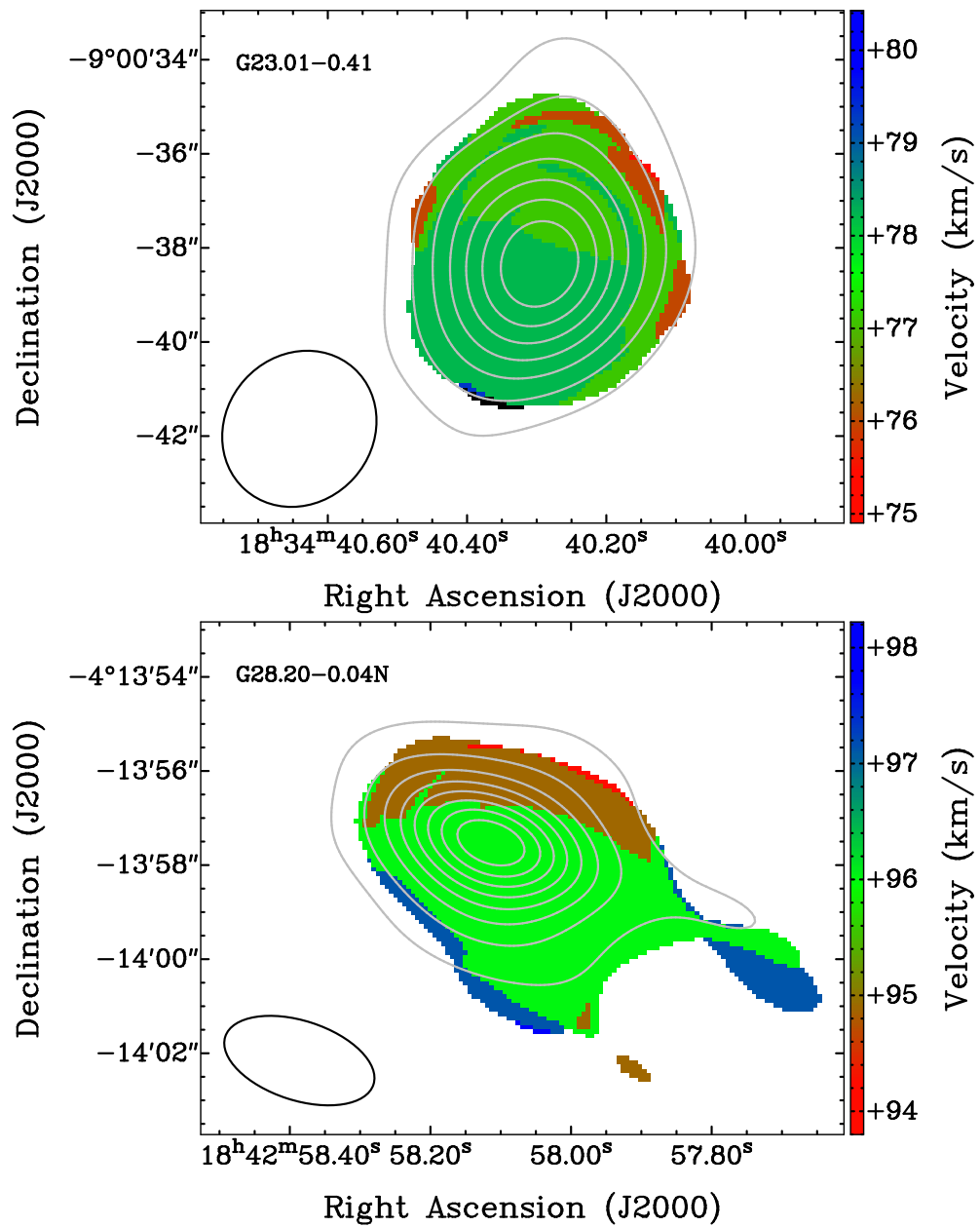


FIG. 4.22: Same as Figure 4.18. For G23.01 (*top*) contour levels are from 30% to 90% with steps of 10%. Contour levels for G28.20N (*bottom*) are from 10% to 90% of the integrated emission with steps of 10%.



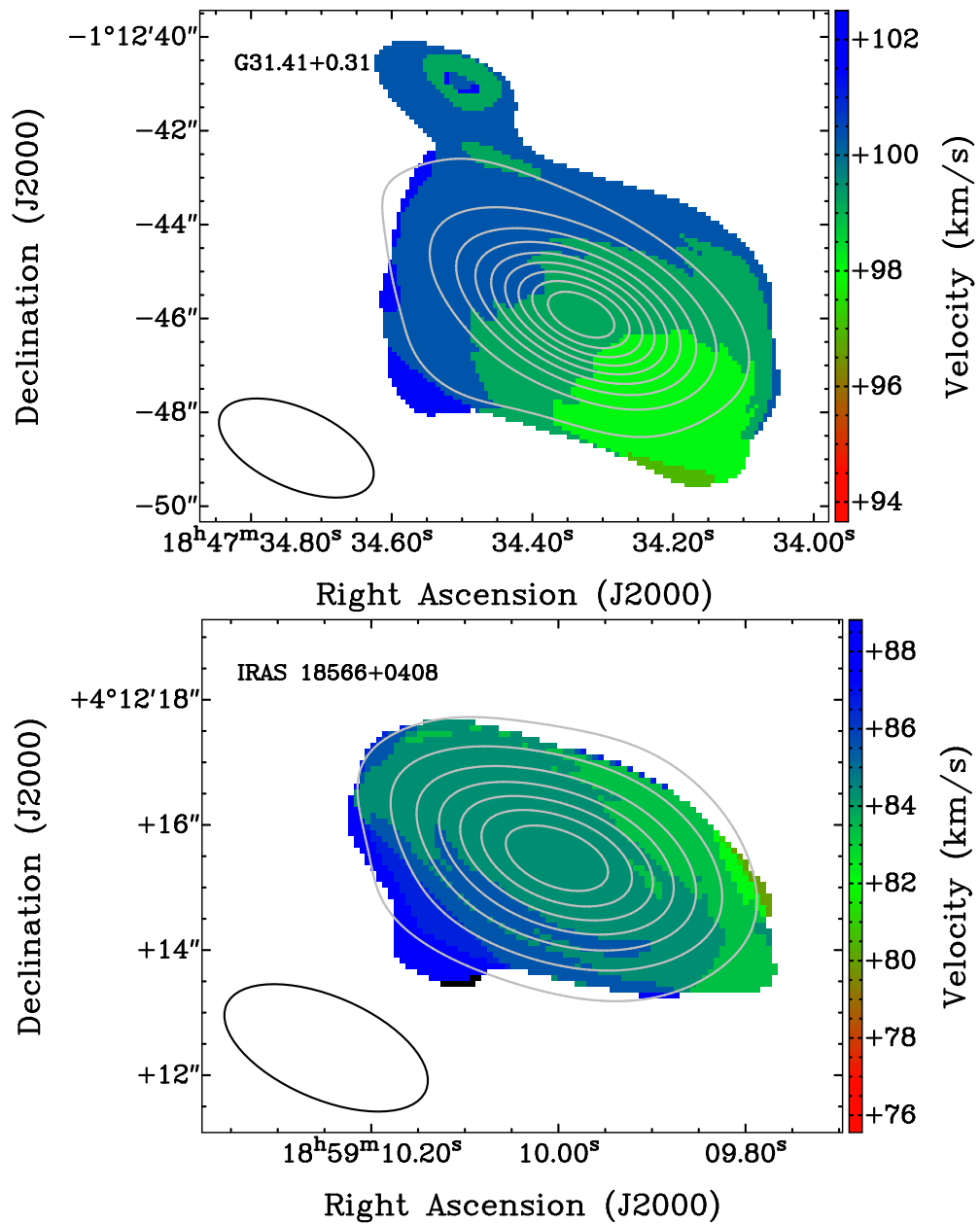


FIG. 4.23: Same as Figure 4.18, but for G31.41 and I18566. For G31.41 (*top*) contour levels are from 10% to 90% with steps of 10%. Contour levels for I18566 (*bottom*) are from 30% to 90% of the integrated emission with steps of 10%.

SiO indicative of shocks are detected (Harju et al. 1998). From the 1.3 mm continuum analysis, Longmore et al. (2011) estimated a mass of  $\sim 21 M_{\odot}$  and an  $\text{H}_2$  column density of at least  $10^{24} \text{ cm}^{-2}$ , assuming dust temperatures of 100-200 K. Using the same data as Longmore et al. (2011) but assuming a higher temperature of 281 K, corresponding to the compact component, we estimate a mass of  $14 M_{\odot}$  and a  $\text{H}_2$  column density of  $10^{23} \text{ cm}^{-2}$ . From the  $\text{CH}_3\text{CN}$  data Longmore et al. (2011) estimated a 200 K upper limit for the rotation temperature and  $10^{16} \text{ cm}^{-2}$  for the column density. We obtain  $\text{CH}_3\text{CN}$  column densities of  $4.2 \times 10^{15}$  and  $1.9 \times 10^{14} \text{ cm}^{-2}$  for the compact and extended components, respectively. We estimate a  $\text{CH}_3\text{CN}$  abundance of  $\sim 4 \times 10^{-8}$ , which is consistent with the result of Longmore et al. (2011).

#### 4.4.7 G10.47

Is one of the brightest HMCs and nursery of several OB stars. This source shows four UCHII regions embedded in the hot gas traced by  $\text{NH}_3$ ,  $\text{CH}_3\text{CN}$  and many other complex molecules (Olmi et al. 1996; Cesaroni et al. 1998; Hatchell et al. 1998; Wyrowski et al. 1999a; Rolffs et al. 2011). There is strong millimeter continuum emission toward two of the UCHII regions. We adopt a distance of 8.5 kpc (Reid et al. 2014). Olmi et al. (1996), using 30 m plus PdBI merged observations of  $\text{CH}_3\text{CN}(6-5)$ , obtained rotation temperatures of 240 and 180 K for separate spectra of a core and extended components, respectively. They obtained  $\text{CH}_3\text{CN}$  column densities of  $6.0 \times 10^{16}$  and  $3.6 \times 10^{15} \text{ cm}^{-2}$ , toward these regions. Using the  $\text{NH}_3(4,4)$  line Cesaroni et al. (1998) estimated kinetic temperatures of 250-400 K toward the central regions. We estimate rotation temperatures of 408 and 82 K, and  $\text{CH}_3\text{CN}$  column densities of  $5.1 \times 10^{17}$  and  $4.1 \times 10^{14} \text{ cm}^{-2}$ , for the compact and extended components, respectively. From the 1.3 mm continuum emission, G10.47 shows the largest gas mass in our survey,  $\sim 375 M_{\odot}$ . We find a  $\text{CH}_3\text{CN}$  abundance of  $7.6 \times 10^{-8}$ .

#### 4.4.8 G10.62

Is a well-studied MSFR and associated with a UCHII region,  $\text{H}_2\text{O}$  and OH maser emission, and multiple molecular lines, including  $\text{CH}_3\text{CN}$  (Keto et al. 1987, 1988; Sollins & Ho 2005; Sollins et al. 2005b; Fish et al. 2005; Liu et al. 2011). From

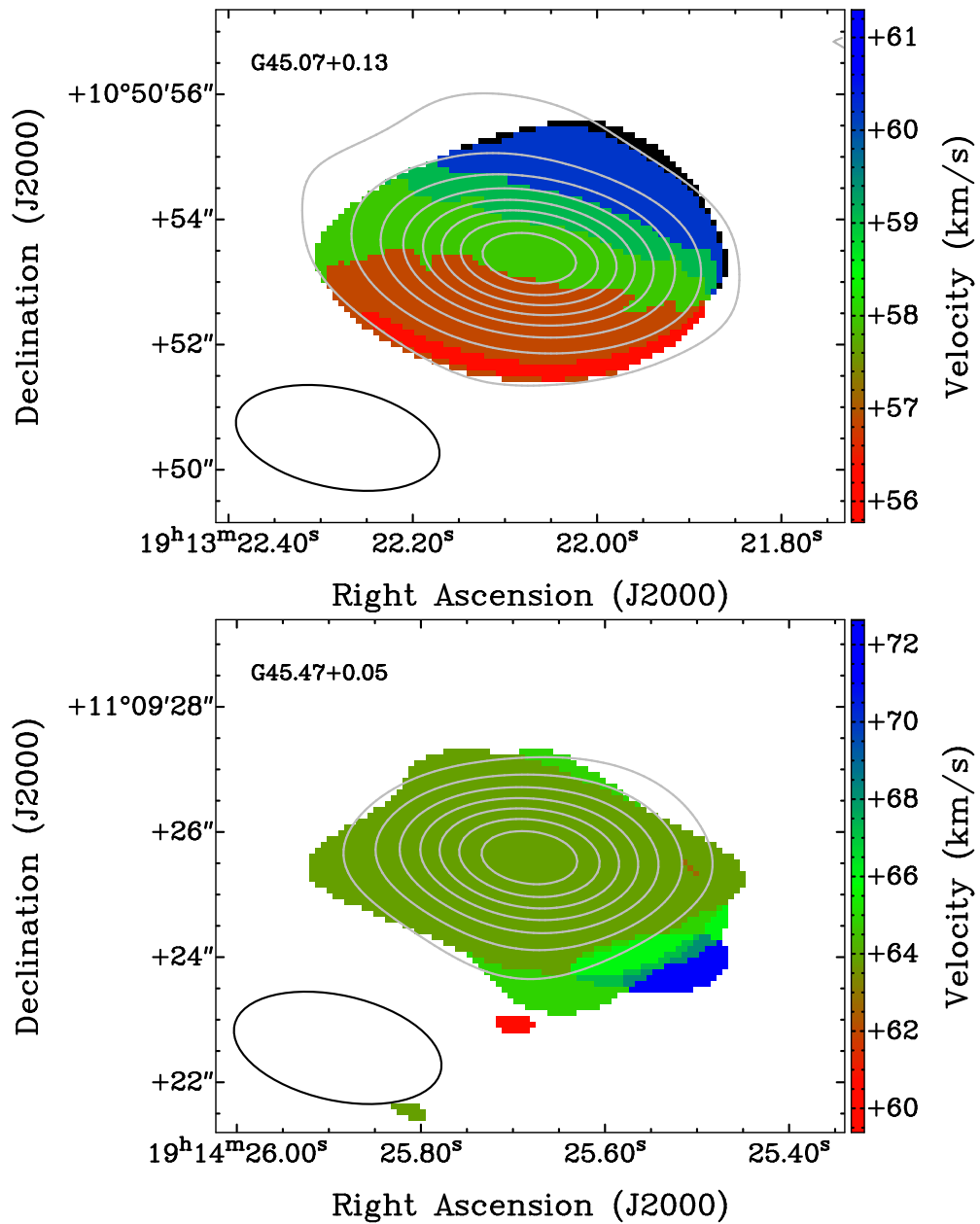


FIG. 4.24: Same as Figure 4.18, but for G45.07 and G45.74. For G45.07 (*top*) contour levels are from 10% to 90% with steps of 10%. Contour levels for G45.47 (*bottom*) are from 20% to 90% of the integrated emission with steps of 10%.

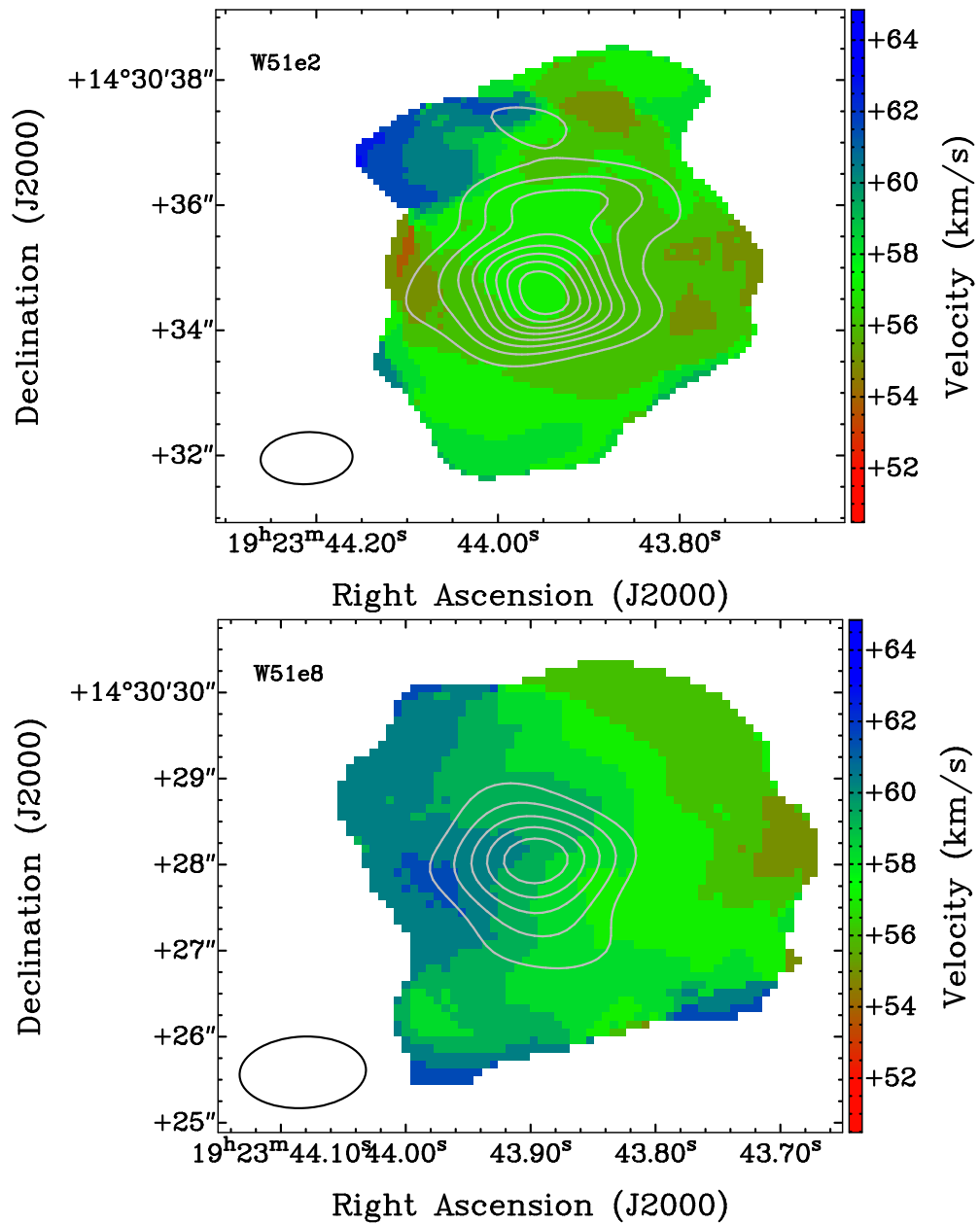


FIG. 4.25: Same as Figure 4.18, but for W51e2 and W51e8. For W51e2 (*top*) contour levels are from 10% to 90% with steps of 10%. Contour levels for W51e8 (*bottom*) are from 30% to 90% with steps of 10%.

the thermal dust emission and adopting a distance of 5 kpc (Reid et al. 2014), we derived a mass of  $116 M_{\odot}$  and  $N_{\text{H}_2} = 6.3 \times 10^{23} \text{ cm}^{-2}$ . Klaassen et al. (2009) and Beltrán et al. (2011) derived  $136 M_{\odot}$  and  $82 M_{\odot}$  also using the 1.3 mm continuum with distances of 6 and 3.4 kpc, respectively. Our rotation temperatures estimated from the XCLASS program are 415 and 95 K for the compact and extended components, respectively; column densities were  $6.7 \times 10^{15}$  and  $3.0 \times 10^{14} \text{ cm}^{-2}$ . Beltrán et al. (2011) obtained a rotation temperature of 87 K and column density of  $2 \times 10^{15} \text{ cm}^{-2}$  using vibrationally excited  $\text{CH}_3^{13}\text{CN}$  and  $\text{CH}_3\text{CN}$  transitions. (Klaassen et al. 2009), using only the rotational transitions, derived a temperature of  $323 \pm 105$  K and column density of  $1 \times 10^{15} \text{ cm}^{-2}$ . We find a  $\text{CH}_3\text{CN}$  abundance of  $1 \times 10^{-8}$ .

#### 4.4.9 I18182

Shows OH, Class II  $\text{CH}_3\text{OH}$ , and  $\text{H}_2\text{O}$  maser emission, weak cm continuum emission, and multiple molecular outflows (Walsh et al. 1998; Zapata et al. 2006; Beuther et al. 2006). High-density gas tracers ( $\text{CH}_3\text{CN}$ ,  $\text{CH}_3\text{OH}$ , and  $\text{HCOOCH}_3$ ) appear offset from the mm continuum peak, but they are associated with the outflows (Beuther et al. 2006). Beuther et al. (2006) found gas masses of 47.6 and  $12.4 M_{\odot}$  from the 1.3 mm continuum emission using dust temperatures of 43 and 150 K, respectively. They estimated  $\text{H}_2$  column densities of  $5.7 \times 10^{23}$  and  $1.5 \times 10^{23} \text{ cm}^{-2}$  at the same temperatures. Their XCLASS analysis of the  $\text{CH}_3\text{CN}$  ( $12_K-11_K$ ) shows a rotation temperature of 150 K and a column density of  $3.5 \times 10^{14} \text{ cm}^{-2}$ , using a single component model. With the same data and assuming a temperature of 219 K, we obtained a gas mass of  $\sim 21 M_{\odot}$  and an  $\text{H}_2$  column density of  $3.3 \times 10^{23} \text{ cm}^{-2}$ . Assuming two components for the XCLASS analysis, we obtain rotation temperatures of 219 and 75 K, and column densities of  $7.3 \times 10^{15}$  and  $8.2 \times 10^{13} \text{ cm}^{-2}$ . We estimated  $X_{\text{CH}_3\text{CN}} = 2.1 \times 10^{-8}$ .

#### 4.4.10 G23.01

Is a relatively isolated MSFR showing complex OH,  $\text{H}_2\text{O}$ , and  $\text{CH}_3\text{OH}$  class II maser emission (Caswell & Haynes 1983; Forster & Caswell 1989; Polushkin & Val'Tts 2011) but no free-free emission. Masers are clustered within 2000 AU in a probable disk,

from which an outflow emerges. A 1.3 cm continuum source likely traces a thermal jet driving the massive CO outflow observed at large scales (Sanna et al. 2010). From the analysis of CH<sub>3</sub>CN(6-5) transitions Furuya et al. (2008) found a rotation temperature of  $\sim 121$  K and a column density of  $4.6 \times 10^{14} \text{ cm}^{-2}$ , using the RD method. They found a gas mass of  $\sim 380 M_{\odot}$  and H<sub>2</sub> column density of  $3.6 \times 10^{23} \text{ cm}^{-2}$  from the 3 mm continuum emission. From 1.3 mm dust continuum emission, we estimate a gas mass of  $\sim 16 M_{\odot}$  and H<sub>2</sub> column density of  $1.4 \times 10^{23} \text{ cm}^{-2}$ . The difference in gas mass with Furuya et al. (2008) probably comes from our smaller size source and higher temperature. With the XCLASS analysis we calculate rotation temperatures of 237 and 58 K, and CH<sub>3</sub>CN column densities of  $1.5 \times 10^{17}$  and  $1.7 \times 10^{14} \text{ cm}^{-2}$ , for the compact and extended components. We estimated a CH<sub>3</sub>CN abundance of  $1 \times 10^{-7}$ .

#### 4.4.11 G28.20N

Is an HC III region showing H<sub>2</sub>O, OH, and CH<sub>3</sub>OH maser emission (Caswell & Vaile 1995; Argon et al. 2000). Rotation and probably infall motion of gas is detected with NH<sub>3</sub> (Sollins et al. 2005a). From SMA observations of CH<sub>3</sub>CN Qin et al. (2008) estimated a rotation temperature of 300 K, column density of  $1.6 \times 10^{16} \text{ cm}^{-2}$  and CH<sub>3</sub>CN fractional abundance of  $5 \times 10^{-9}$ , by rotation diagrams. From the 1.3 mm dust continuum emission, we estimate a gas mass of  $33 M_{\odot}$  and H<sub>2</sub> column density of  $7.7 \times 10^{24} \text{ cm}^{-2}$ . Using the XCLASS program, we estimate rotation temperatures of 295 and 59 K, and CH<sub>3</sub>CN column densities of  $6.25 \times 10^{16}$  and  $2.4 \times 10^{14} \text{ cm}^{-2}$ , for the compact and extended regions, and we calculate  $X_{\text{CH}_3\text{CN}} = 8 \times 10^{-8}$ .

#### 4.4.12 G31.41

Is a prototypical HMC imaged in multiple high-excitation molecular transitions such as NH<sub>3</sub>(4,4), CH<sub>3</sub>CN(6-5) and (12-11), CH<sub>3</sub>OH, CH<sub>3</sub>CCH, and others (Cesaroni et al. 1994b; Araya et al. 2008; Hatchell et al. 1998). Cesaroni et al. (1994b) detected CH<sub>3</sub>CN(6-5), CH<sub>3</sub><sup>13</sup>CN(6-5), and vibrationally excited CH<sub>3</sub>CN(6-5), and estimated a rotation temperature of 200 K. Hatchell et al. (1998) observed CH<sub>3</sub>CN(13-12) and (19-18) and report temperatures of 149 and 142 K, respectively, and a column density  $> 0.5 \times 10^{14} \text{ cm}^{-3}$ . Olmi et al. (1996), using observations with the IRAM 30 m of several

CH<sub>3</sub>CN transitions, estimated a rotation temperature of  $\sim 140$  K and a column density of  $2.3 \times 10^{17} \text{ cm}^{-2}$ . [Cesaroni et al. \(1998\)](#) found kinetic temperatures of 250-400 K toward the cores, using the NH<sub>3</sub>(4,4) line. Recently, with two SMA configurations and IRAM 30m observations of CH<sub>3</sub>CN(12-11) and CH<sub>3</sub><sup>13</sup>CN, [Cesaroni et al. \(2011\)](#) confirmed the existence of a velocity gradient, explained as a rotating toroid. Using only the compact SMA configuration data as [Cesaroni et al. \(2011\)](#), we obtain a gas mass  $\sim 250 M_{\odot}$  and H<sub>2</sub> column density of  $3.5 \times 10^{24} \text{ cm}^{-2}$ . With the XCLASS analysis we calculate rotational temperatures of 327 and 95 K, and column densities of  $1.5 \times 10^{17}$  and  $9.1 \times 10^{13} \text{ cm}^{-2}$  for the compact and extended regions. We estimate a CH<sub>3</sub>CN abundance of  $4.2 \times 10^{-8}$ .

#### 4.4.13 I18566

Shows H<sub>2</sub>O, CH<sub>3</sub>OH and H<sub>2</sub>CO maser emission, CS, an outflow traced by NH<sub>3</sub> and SiO, and weak emission at 3.6 cm and 2 cm, probably coming from an ionized jet ([Zhang et al. 2007b](#); [Araya et al. 2005b](#); [Beuther et al. 2002b](#)). This source harbors a 6 cm H<sub>2</sub>CO maser that flared in 2002 ([Araya et al. 2007](#)). From 43 and 87 GHz continuum emission, [Zhang et al. \(2007b\)](#) estimate a gas mass of  $\sim 70 M_{\odot}$  for the core. Also, they detected significant heating of the NH<sub>3</sub> gas (70 K) as a consequence of the outflow. From the 1.3 mm dust continuum we estimate a gas mass  $\sim 16 M_{\odot}$  and H<sub>2</sub> column density of  $1.1 \times 10^{23} \text{ cm}^{-2}$ . Our XCLASS analysis gives rotation temperatures of 382 and 110 K, and CH<sub>3</sub>CN column densities of  $7.1 \times 10^{15}$  and  $5.1 \times 10^{13} \text{ cm}^{-2}$ . We detected broad linewidths for most of the CH<sub>3</sub>CN-*K* components, with an average FWHM of  $8.2 \text{ km s}^{-1}$ . We find a CH<sub>3</sub>CN abundance of  $6.4 \times 10^{-8}$ .

#### 4.4.14 G45.07

Is a pair of spherical UC HII regions showing OH, H<sub>2</sub>O, and CH<sub>3</sub>OH maser emission. At least three continuum sources are observed in the mid-infrared ([De Buizer et al. 2005](#)). [Hunter et al. \(1997\)](#) observed CS and CO probably tracing an outflow; the H<sub>2</sub>O masers are roughly in the same direction as the axis. From the 1.3 mm dust continuum emission, we estimate a gas mass of  $172 M_{\odot}$  and H<sub>2</sub> column density of  $2.7 \times 10^{24} \text{ cm}^{-2}$ . The physical parameters obtained from XCLASS are 290 and 82 K

and  $\text{CH}_3\text{CN}$  column densities of  $5.4 \times 10^{15}$  and  $4.1 \times 10^{14} \text{ cm}^{-2}$ , for the compact and extended regions. We estimate a  $\text{CH}_3\text{CN}$  abundance of  $1.9 \times 10^{-9}$ .

#### 4.4.15 G45.47

Is a MSFR associated with an UC HII region, multiple molecular lines and OH,  $\text{H}_2\text{O}$ , and  $\text{CH}_3\text{OH}$  maser emission (Cesaroni et al. 1992; Remijan et al. 2004a; Olmi et al. 1993). Olmi et al. (1993) detected  $\text{CH}_3\text{CN}(6-5)$ , (8-7), and (12-11) transitions using the IRAM 30 m, and estimated upper limits of 51 K for the rotation temperature and  $2.5 \times 10^{13} \text{ cm}^{-2}$  for the column density. From  $\text{NH}_3(2,2)$  and (4,4), Hofner et al. (1999) estimated a rotation temperature of 59 K and column density of  $1.8 \times 10^{17} \text{ cm}^{-2}$ . From the ammonia absorption, they suggested that molecular gas is infalling onto the UC HII region. From their molecular line surveys Hatchell et al. (1998) and Remijan et al. (2004a) report that G45.47 is line-poor; they do not see evidence for a HMC in this field. However, the UC HII region and relatively high luminosity ( $\sim 10^6 L_\odot$ ) suggest a more-evolved MSFR. From the 1.3 mm we estimate a gas mass of  $\sim 66 M_\odot$  and  $\text{H}_2$  column density of  $6.7 \times 10^{23} \text{ cm}^{-2}$ . From the XCLASS analysis we estimate rotation temperatures between 155 K and 65 K, column densities of  $6.8 \times 10^{14}$  and  $3.8 \times 10^{13} \text{ cm}^{-2}$ , and  $X_{\text{CH}_3\text{CN}} = 1 \times 10^{-9}$ . Consistent with the molecular line surveys mentioned above, we find little molecular line emission from this source, compared to the rest of our sample.

#### 4.4.16 W51e2

Is an UC HII region associated with warm gas and  $\text{H}_2\text{O}$ , OH,  $\text{NH}_3$ , and  $\text{CH}_3\text{OH}$  maser emission (Gaume & Mutel 1987; Gaume et al. 1993; Zhang & Ho 1995, 1997; Zhang et al. 1998a). From the 1.3 mm continuum analysis, Klaassen et al. (2009) estimated a gas mass of  $140 M_\odot$  assuming a dust temperature of 400 K. They calculated from the  $\text{CH}_3\text{CN}$  a rotation temperature of 460 K and column density of  $2.1 \times 10^{16} \text{ cm}^{-2}$ . Using the same data, we estimate a gas mass of  $95 M_\odot$  and column density of  $3.9 \times 10^{16} \text{ cm}^{-2}$ . Differences probably come from our higher temperature for the dust emission. Using the RD method, Zhang et al. (1998a) found a  $\text{CH}_3\text{CN}$  column density of  $2.8 \times 10^{14} \text{ cm}^{-2}$  and rotation temperature of 140 K; they estimated a



CH<sub>3</sub>CN fractional abundance of  $5 \times 10^{-10}$ . From multiple CH<sub>3</sub>CN transitions at 3 mm and 1 mm, and using a LTE model for each transition, [Remijan et al. \(2004b\)](#) estimated a rotation temperature of 153 K and column density of  $3.8 \times 10^{16} \text{ cm}^{-2}$ . They calculated an H<sub>2</sub> column density of  $8.3 \times 10^{22} \text{ cm}^{-2}$  and CH<sub>3</sub>CN fractional abundance,  $X_{\text{CH}_3\text{CN}} = 4.6 \times 10^{-7}$ . With XCLASS we estimate rotation temperatures of 458 and 118 K, and CH<sub>3</sub>CN column densities of  $2.8 \times 10^{17}$  and  $1.0 \times 10^{15} \text{ cm}^{-2}$ , for the compact and extended components. We calculated  $X_{\text{CH}_3\text{CN}} = 7 \times 10^{-8}$ . The discrepancies with [Remijan et al. \(2004b\)](#) probably arise from differences in the methods used to estimate temperatures and H<sub>2</sub> and CH<sub>3</sub>CN column densities. The much lower abundances reported by [Zhang et al. \(1998a\)](#) are a direct consequence of the much lower column density that they report from CH<sub>3</sub>CN.

#### 4.4.17 W51e8

Is a MSFR located to the south of W51e2, and is associated with H<sub>2</sub>O and OH maser emission and multiple molecular lines such as HCO<sup>+</sup>, NH<sub>3</sub>, and CH<sub>3</sub>CN ([Zhang & Ho 1997](#); [Zhang et al. 1998a](#)). Observing with the Nobeyama Millimeter Array at 2 mm, [Zhang et al. \(1998a\)](#) detected molecules such as CS, CH<sub>3</sub>OCH<sub>3</sub>, HCOOCH<sub>3</sub>, and CH<sub>3</sub>CN. From the latter, they estimated a rotation temperature of 130 K and CH<sub>3</sub>CN column density of  $2.0 \times 10^{14} \text{ cm}^{-2}$ . [Klaassen et al. \(2009\)](#) estimated a dust-derived mass of  $82 M_{\odot}$ , assuming an average temperature of 400 K. They estimated a rotation temperature of 350 K and a CH<sub>3</sub>CN column density of  $8 \times 10^{15} \text{ cm}^{-2}$  through rotation diagrams. With the same method, [Remijan et al. \(2004b\)](#) (W51e1 in their nomenclature) estimated a rotation temperature of 123 K, column density of  $1.4 \times 10^{16}$ , and fractional abundances of  $1.3 \times 10^{-7}$ . With the set of data at 1.3 mm of [Klaassen et al. \(2009\)](#), we calculate an H<sub>2</sub> gas mass of  $86 M_{\odot}$  and a column density of  $5.8 \times 10^{24} \text{ cm}^{-2}$ . Using the XCLASS program we estimate rotation temperatures of 384 and 85 K, and column densities of  $1.8 \times 10^{17}$  and  $1.8 \times 10^{14} \text{ cm}^{-2}$ , for the compact and extended regions. For the compact component, we estimate  $X_{\text{CH}_3\text{CN}}$  of  $3.4 \times 10^{-8}$ . As in the case of W51e2, the differences with [Remijan et al. \(2004b\)](#) come from the methods used to obtain the physical parameters.

## 4.5 Discussion

### 4.5.1 Mass and density from 1.3 mm continuum

The range for gas masses estimated from the 1.3 mm emission is from 7 to  $375 M_{\odot}$ , and for column densities from  $1.0 \times 10^{23}$  to  $6.7 \times 10^{24} \text{ cm}^{-2}$ . The median value for the mass is  $21 M_{\odot}$  and for the column densities  $8 \times 10^{23} \text{ cm}^{-2}$ . Using the physical size of a deconvolved beam, we obtained  $\text{H}_2$  number densities from  $8 \times 10^5$  to  $1.4 \times 10^8 \text{ cm}^{-3}$ , assuming that the gas is distributed uniformly. Except for G5.89, all sources are above the classic  $\sim 10 M_{\odot}$  lower limit for HMCs.

The size of the dusty structures goes from  $\sim 3500$  to  $20500 \text{ AU}$  ( $0.017$  to  $0.10 \text{ pc}$ ). In general, the dust-emission structures shown in Figures 4.1 and 4.2 have similar sizes, gas masses and column densities to other HMCs (e.g., Beltrán et al. 2011).

From table 4.3 we see that the estimated thermal dust contribution to the total 1.3 mm flux ranges from 8% in G5.89, to  $>98\%$  in sources W3TW, I16547, I17233, G8.68, I18182, G23.01, G31.41, and I18566. The latter sources show a high fraction of dust emission because they have essentially no free-free emission from ionized gas. Since even this sub-group has luminosities  $> 10^4 L_{\odot}$  (corresponding to an early B-type star) we would expect a more substantial amount of ionization. Possible reasons for the lack of such ionization include young sources in early evolutionary stages, very high mass accretion rates, or the presence of a stellar cluster whose luminosity is dominated by late-B-type stars. Sources such as G10.47, G31.41, G45.07, G45.47, and W51e2 clearly show UCHII regions embedded in the dusty molecular gas, indicating much higher levels of ionization.

One of the assumptions implicit in Equations 5.2 and 4.3 is that the gas and dust are well-coupled. As a test, we calculate the gas-dust relaxation time,  $t_{\text{gd}}$ . We follow Chen et al. (2006), who estimated the time-scale necessary for thermal coupling of the dust and gas, and obtained  $t_{\text{gd}} = 2.5 \times 10^{16} / n_{\text{H}}$ , in seconds, where  $n_{\text{H}}$  is the number density of H nuclei in  $\text{cm}^{-3}$ . For the values of  $n_{\text{H}_2}$  in Table 4.3, the gas-dust relaxation time ranges from 3 to 500 yr. Thus,  $t_{\text{gd}}$  is much shorter than the expected HMC lifetime.

With respect to the LTE condition, the  $\text{CH}_3\text{CN}$  critical density is  $\sim 10^6 \text{ cm}^{-3}$  for the  $J_{\text{up}} = 12$  transition (Wang et al. 2010). We therefore conclude that the LTE

approximation is valid and the rotation temperature of CH<sub>3</sub>CN can be taken as the kinematic temperature of the H<sub>2</sub> gas.

### 4.5.2 Spatial distribution with respect to the CH<sub>3</sub>CN

In Figures 4.1 to 4.3 we compare the spatial distribution of the 1.3 mm continuum emission with the velocity-integrated emission (moment 0) of  $K$ -lines 3, 5 and 7 of CH<sub>3</sub>CN. These  $K$ -components trace kinetic temperatures of 133 K, 247 K, and 418 K, respectively. For G5.89 and I18182 we use the  $K$ -lines 3, 5 and 6, owing to the lack of  $K = 7$  emission.

At the resolution and sensitivity of our data, the 1.3 mm continuum emission and the hot CH<sub>3</sub>CN emission coincide closely and have similar spatial extents for most of the sources. Notably, G5.89 has a more complicated morphology.

The close spatial coincidence between dust and molecular gas can be explained if embedded protostellar heat the dust grains, thus evaporating the ice mantles, and subsequent gas-phase chemical reactions produce species such as CH<sub>3</sub>CN. This scenario has been observed toward HMCs, specially with nitrogen-bearing molecules (e.g., [Qin et al. 2010](#)). In Section 5.4 we will explore various scenarios to explain the molecular abundances.

We note that the displacement of some CH<sub>3</sub>CN lines from the continuum peak for sources such G5.89, G10.47, G28.20N and G45.47 (see Figures 4.1 to 4.3) could be due to factors such as multiple star forming points, unresolved continuum sources or molecular gas heated externally. Since, higher- $K$  transitions should be excited in denser, hotter and probably more compact regions, clumpy cores, with different physical conditions, are an alternative explanation for the displacements. Sub-arcsecond observations will be necessary to test these alternative explanations.

### 4.5.3 Temperature, density, and virial mass

The CH<sub>3</sub>CN analysis, using the rotational diagrams and XCLASS, indicates high temperatures and densities for all sources. However, from Figure 4.17, large deviations

TABLE 4.7: Velocity-integrated emission (moment 0) of CH<sub>3</sub>CN (12<sub>K</sub>–11<sub>K</sub>).

Sources	CH <sub>3</sub> CN Transitions		
	$K = 3$ (Jy beam <sup>-1</sup> km s <sup>-1</sup> )	$K = 5$ (Jy beam <sup>-1</sup> km s <sup>-1</sup> )	$K = 7$ (a) (Jy beam <sup>-1</sup> km s <sup>-1</sup> )
W3OH and TW	29.1	17.4	3.9
I16547	6.2	4.8	2.3
I17233	224.7	206.6	78.6
G5.89	5.8	2.5	1.8 <sup>a</sup>
G8.68	7.6	4.2	1.4
G10.47	63.1	100.6	45.4
G10.62	33.6	19.1	6.2
I18182	11.8	6.5	8.0 <sup>a</sup>
G23.01	18.7	11.3	3.5
G28.20N	13.9	8.9	2.5
G31.41	32.8	31.1	11.8
I18566	7.3	4.7	1.3
G45.07	10.8	4.2	1.6
G45.47	3.5	0.6	0.9
W51e2 and W51e8	34.6	26.6	13.0

Notes.— (a) For G5.89–0.37 and I18182 we present the line  $K = 6$ .

are clearly seen to the linear fit for some of the  $K = 3, 6$ -lines, toward sources such IRAS17233, G10.47, G10.62, G31.41, IRAS16547, and IRAS18566; this indicates that these lines are optically thick and hence there is probably a mixture of optically thin and thick lines in our spectra. This occurs because the  $K = 0, 3, 6, \dots$ , ladders are doubly degenerate compared to the  $K = 1, 2, 4, 5, \dots$  ladders. Thus the former lines will have higher optical depths than the latter. As we mention below, the homogeneous assumption of the RD method probably is inadequate.

Moreover, Figures 4.15 and 4.16 show similar brightness temperatures of low  $K$ -ladders ( $K = 0-4$ ), including the  $K = 3$ -line, toward some sources (e.g., IRAS17233, G28.20N, G10.47, G31.41, W51e2, and W51e8). This confirms that these lines are optically thick.

We find good agreement between the observed spectra and the synthetic models using XCLASS, with a two-component model. This result, along with the close coincidence between the molecular gas and dust emission, suggest that most of the HMCs are internally heated.

We consider the two-component model to be more realistic than a single homogeneous structure. The reality is probably even more complex; Cesaroni et al. (2010, 2011), for example, report sub-arcsecond observations that indicate gradients in both temperature and density. We note that the two-component model overestimate the  $K = 3$ -line for some sources, suggesting that even this model is too simplistic.

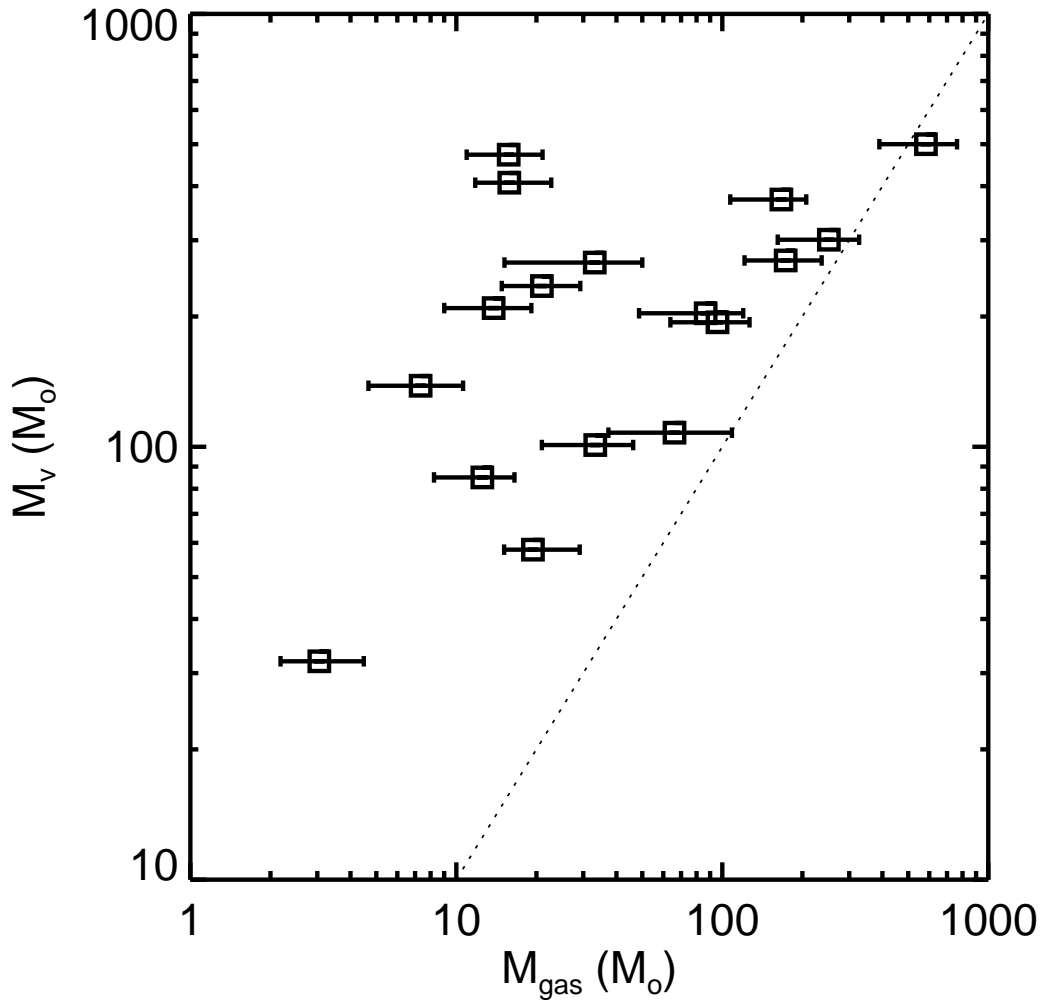


FIG. 4.26: Plot of virial mass versus gas mass.  $M_{\text{gas}}$  is estimated from the 1.3 mm continuum emission using the high temperature of the  $\text{CH}_3\text{CN}$  analysis (Table 5).  $M_{\text{vir}}$  is estimated using  $\Delta V$  from the observed linewidth (Table 4.5). The dotted line represents  $M_{\text{vir}}/M_{\text{gas}} = 1$ .

We summarize our results from the XCLASS program as follows. For the extended component, the temperature ranges from 40 to 132 K, with an average of 85 K, and median of 82 K; the mean size is 0.10 pc; the average column density  $N_{\text{CH}_3\text{CN}} = 2.4 \times 10^{14} \text{ cm}^{-2}$ , with a median of  $1.7 \times 10^{14} \text{ cm}^{-2}$ . For the compact component, the temperature ranges from 122 to 485 K, with an average of 303 K, and median of 295 K; the mean size is 0.02 pc; the average column density  $N_{\text{CH}_3\text{CN}} = 8.5 \times 10^{16} \text{ cm}^{-2}$ , with a median of  $2.2 \times 10^{16} \text{ cm}^{-2}$ .

In Tables 3 and 5 we present  $M_{\text{gas}}$  and  $M_{\text{vir}}$ , which provide information about the stability and structure of the HMCs. The ratio of the virial mass to gas mass,  $M_{\text{vir}}/M_{\text{gas}}$ , is greater than unity for all sources but G10.47 (see Figure 10). The ratio ranges from 29.6 to 1.1, with an average of 8.3. This suggests that the cores are not in virial equilibrium and a traditional interpretation of this result is that the HMCs are expanding, since  $E_k > 2E_g$ . However, another interpretation is that these cores are still collapsing, as suggested by recent models of molecular cloud formation and evolution (see [Ballesteros-Paredes et al. 2011](#)). This possibility will be explored in a future work.

#### 4.5.4 Fractional Abundances

Adopting the  $\text{H}_2$  column densities from the 1.3 mm continuum emission, we find  $\text{CH}_3\text{CN}$  abundances,  $X_{\text{CH}_3\text{CN}}$ , from  $\sim 1 \times 10^{-9}$  to  $\sim 2 \times 10^{-7}$  toward the hot-inner components. These results span a range of fractional abundances that agrees with other estimates toward HMCs, such as the Orion hot core with  $10^{-10}$ - $10^{-9}$  ([Wilner et al. 1994](#)), G20.08N with  $5 \times 10^{-9}$  to  $2 \times 10^{-8}$  ([Galván-Madrid et al. 2009](#)), Sgr B2(N) with  $\sim 3 \times 10^{-8}$  ([Nummelin et al. 2000](#)), and W51e8 and W51e2 with  $1.3 \times 10^{-7}$  and  $4.6 \times 10^{-7}$ , respectively ([Remijan et al. 2004b](#)).

At the high dust temperatures of the compact components ( $T > 122$  K), most of the organic molecules are probably evaporated from the grain mantles and incorporated into the gas phase ([Herbst & van Dishoeck 2009](#)). Moreover, these temperatures are high enough to form many new organic species by chemical reactions—if the chemical time scales are short enough. For any given molecular species, one can ask if it was formed 1) in a dense, cold gas phase prior to any protostellar object, 2) on the grains by surface reactions or 3) in gas phase processes after evaporation (see the review by [Herbst & van Dishoeck 2009](#)). In the case of  $\text{CH}_3\text{CN}$  all three of these scenarios have been studied using both chemical models and observations (e.g., [MacDonald & Habing 1995](#); [Ohishi & Kaifu 1998](#); [Rodgers & Charnley 2001](#); [Wang et al. 2010](#)).

Observations toward cold dense gas show  $\text{CH}_3\text{CN}$  abundances of  $\sim 10^{-10}$  ([Ohishi & Kaifu 1998](#)) i.e., substantially lower than the abundances that we find. Thus, the scenario in which  $\text{CH}_3\text{CN}$  is formed in a cold gas phase, then adsorbed by dust grains

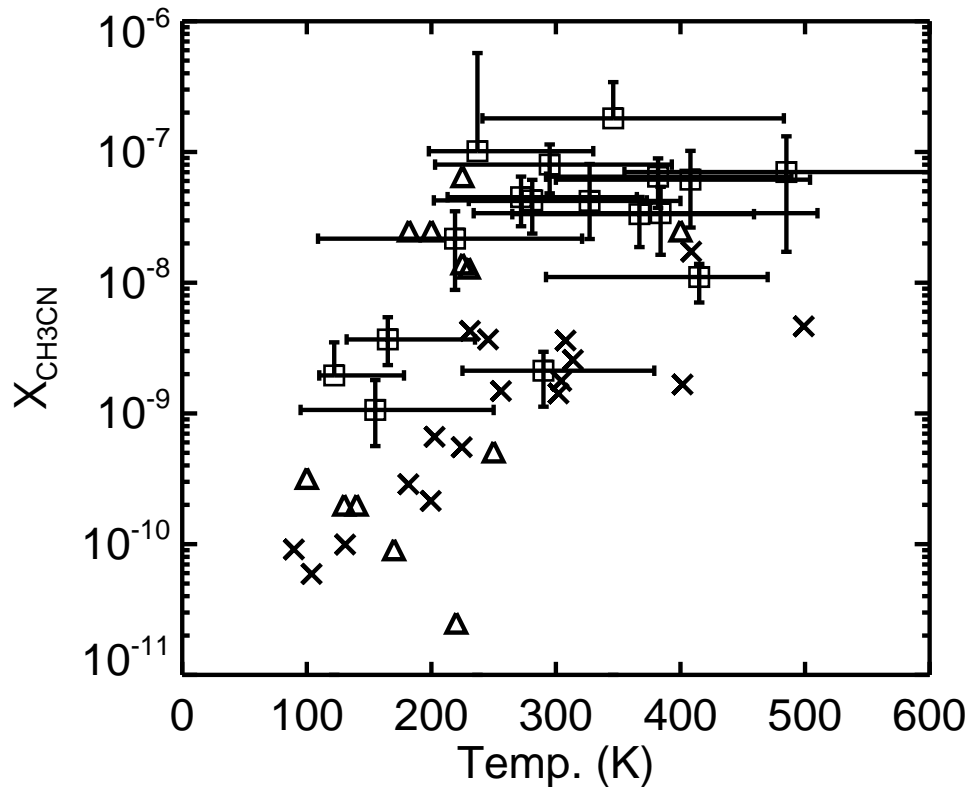


FIG. 4.27: Fractional abundance of  $\text{CH}_3\text{CN}$  versus temperature of the compact hot and dense region estimated with XCLASS (squares). For comparison, we plot our results from the rotational diagrams (crosses) and reported values for other HMCs (triangles). Reported data from the literature are taken from Galvan-Madrid et al. 2009, Chen et al. 2006, Wilner et al. 1994, Zhang et al. 1998, and Wang et al. 2010.

and released by heating from young protostars appears not to contribute to the high abundances observed toward these HMCs.

Alternatively, formation of  $\text{CH}_3\text{CN}$  on grain surfaces and/or in the hot gas after evaporation of “parent” species represent better possibilities. The former process tends to underestimate the final abundances (e.g., Caselli et al. 1993), while the chain of mantle-surface-gas reactions yields good agreement with HMC abundances at times  $> 10^5$  yr (e.g., Hasegawa & Herbst 1993). Moreover, if we consider the grain-surface process as the main path to form  $\text{CH}_3\text{CN}$ , the abundances toward the inner regions of all HMCs should be very similar, because the high temperatures would sublime most of the ice on the dust (e.g., Viti et al. 2004; Herbst & van Dishoeck 2009)

Chemical models, suggest that  $\text{CH}_3\text{CN}$  is synthesized from  $\text{NH}_3$  and  $\text{HCN}$ , once the ammonia is released from ice mantles, and via the ion-molecule reaction of  $\text{CH}_3^+ + \text{HCN}$  and the radiative association reaction of  $\text{CH}_3$  with  $\text{CN}$  (Charnley et al. 1992). The process occurs once the dusty regions reach temperatures  $>100$  K (e.g., Rodgers & Charnley 2001; Herbst & van Dishoeck 2009). Moreover, at temperatures  $>300$  K the environment is optimal to form  $\text{CH}_3\text{CN}$  from the parent nitrogenated species  $\text{HCN}$  and  $\text{NH}_3$  (Rodgers & Charnley 2001). For example, Doty et al. (2002) found that the  $\text{HCN}$  abundance increases with temperature, and at  $T > 200$  the formation of  $\text{HCN}$  proceeds quickly. This temperature dependence in the reactions of N-bearing molecules, including  $\text{HCN}$  and  $\text{CH}_3\text{CN}$ , has been observed in other chemical models and HMCs (Rodgers & Charnley 2001).

In Figure 4.27 we plot  $X_{\text{CH}_3\text{CN}}$  versus rotation temperature estimated for the compact components with XCLASS, and our RD results. We observe that fractional abundances increase with higher temperatures. This result can be understood with the chemical scenario in which  $\text{CH}_3\text{CN}$  molecules mainly form in a hot gas phase and its production is optimized at higher temperatures. A similar dependence between  $\text{CH}_3\text{CN}$  abundance and temperature was detected toward Orion-KL and the Compact Ridge (Wilner et al. 1994; Wang et al. 2010). High angular resolution, multi-species molecular line observations with ALMA would provide valuable constraints for chemical models to confirm this hypothesis.

#### 4.5.5 HMC and UC HII regions

From observations and theoretical models, HMCs have been proposed as the cradle of massive stars. Once massive stars produce enough UV photons, the surrounding atomic and molecular material will be ionized, forming UC HII regions. In our sample there are five HMCs (41%) with little or no centimeter free-free emission. They could represent young objects on the verge of becoming UC HII regions.

The evolutionary sequence of HMCs and the time scales involved are not fully understood. Using the ratio of the number of HMCs to the number of UC HII regions, Wilner et al. (2001) and Furuya et al. (2005) estimated that HMCs live at least 25%



of the UCHII region lifetime, i.e., some  $10^4$  yr. Similarly, [Kurtz et al. \(2000\)](#) estimated a lifetime between  $1.9 \times 10^3$  and  $5.7 \times 10^4$  yr, based in the number of HMC and UCHII regions known at that time.

On the other hand, chemical models require  $10^4 - 10^5$  yr to reach the chemical richness observed in HMCs (e.g., [Charnley et al. 1992](#); [Herbst & van Dishoeck 2009](#)). If the chemical models of [Rodgers & Charnley \(2001\)](#) are correct, chemically rich HMCs should have lifetimes between  $10^4$  and  $10^5$  yr, and hence a larger ratio of HMCs to UCHII would be expected. Although we are approaching a complete census of UCHII regions ([Purcell et al. 2013](#)), the statistics of HMCs are not yet known with sufficient accuracy to constrain the chemical models.

# Chapter 5

## APEX observations of CH<sub>3</sub>OH emission toward MSFRs

*This chapter is based on the paper in preparation Hernandez-Hernandez, V., Kurtz, S., Garay, G., Kalenskii, S. & Zapata, L. 2014*

### 5.1 Introduction

Massive stars ( $M > 8 M_{\odot}$ ) play a fundamental role in the life of the Universe and they are a cornerstone in the evolution of galaxies. Dynamics in the form of molecular outflows, ionized jets and stellar winds, push their surroundings, promoting additional star formation and stirring the interstellar medium (See [Arce et al. 2007](#); [Zinnecker & Yorke 2007](#)).

Many studies show that massive star forming regions (MSFRs) contain massive cores with typical masses of  $\sim 120 M_{\odot}$ , sizes of  $< 0.5$  pc, column densities of  $\sim 10^{23} - 10^{25} \text{ cm}^{-2}$ , and temperatures of 15-30 K. While most of these massive cores show no evidence for the early stages of massive star formation, others show bright  $24 \mu\text{m}$  emission, molecular line emission, and maser emission. These latter cores are probably actively forming massive stars ([Garay et al. 2004](#); [Chambers et al. 2009](#)).

More evolved objects are the so-called hot molecular cores, showing higher temperatures ( $>100$  K), densities ( $\sim 10^5 - 10^8 \text{ cm}^{-3}$ ), luminosities ( $> 10^4 L_{\odot}$ ), masses ( $\sim 10-1000 M_{\odot}$ ), compact sizes ( $<0.1$  pc) and a very rich chemistry. These hot molecular cores are probably heated by internal massive protostars (Kurtz et al. 2000; Cesaroni 2005). Also, energetic outflows and accretion material have been observed and estimated from models; these intense mass accretion mass are enough to quench the development of HII regions (Walmsley et al. 1995; Osorio et al. 2009). Thus, it is thought that HMCs are predecessors to UC HII regions.

Some molecular species in HMCs show both thermal and maser emission, such as  $\text{H}_2\text{O}$ ,  $\text{H}_2\text{CO}$ ,  $\text{NH}_3$ , and  $\text{CH}_3\text{OH}$ . In particular,  $\text{CH}_3\text{OH}$  (methanol) as an asymmetric rotor presents a complex spectrum with multiple lines in bandwidths from radio-frequencies to IR. Such lines are sensitive to the molecular gas conditions in MSFRs, allowing detailed analysis of physical parameters. Also,  $\text{CH}_3\text{OH}$  masers are important tracers of the early stages toward MSFRs, and are associated with molecular outflows, disks, shocks and deeply embedded objects (Minier et al. 2005; Ellingsen 2006, and references therein).

Methanol masers are grouped into two classes (I and II; e.g., Menten 1991). Class I masers are typically somewhat distant ( $\sim 0.1$  pc; Kurtz et al. 2004) from the protostellar position and are thought to be collisionally pumped (Cragg et al. 1992). Class II masers are usually found very near to the protostellar position and are thought to be radiatively pumped (Cragg et al. 2005). Methanol maser surveys have shown the Class II masers to be exclusively associated with MSFRs (Minier et al. 2003) The strongest Class II masers are observed in the centimeter wave range, whilst weaker lines are detected at 3 and 2 mm.

Theoretical models of methanol excitation suggest that maser intensity diminishes at higher frequencies due to lesser degrees of inversion and line opacities. In order to constrain such models it is necessary to observe the shortest wavelengths and establish which transitions are found to mase.

Sobolev et al. (1997) and Cragg et al. (2005) have developed a model to predict Class II masing for methanol transitions in the 6 to 700 GHz range. At high frequencies one of the best candidates is the  $4_2-5_1$   $A^+$  transition at 247.228 GHz. The models

TABLE 5.1: Observed Sources.

Source	Short Name	$\alpha$ (J2000)	$\delta$ (J2000)	$V_{LSR}$ (km s <sup>-1</sup> )	Distance (kpc)	$L$ (10 <sup>5</sup> $L_{\odot}$ )	Comments	Refs
NGC6334I(N)	N6334IN	17 20 55.0	-35 45 05	-3	1.7	0.32	HMC-UCHII	
IRAS17233-3606	I17233	17 26 43.0	-36 09 15	-3	1.0	0.14	HMC	1
G10.47+0.03	G10.47	18 08 38.2	-19 51 49	+67	8.5	3.9	HMC-UCHII	2
G10.62-0.38	G10.62	18 10 28.7	-19 55 49	-3	5.0	11.0	HMC	3
G20.08-0.14N	G20.08N	18 28 10.3	-11 28 48	+42	12.3	6.6	HMC-UCHII	
G29.96-0.02	G29.96	18 46 03.9	-02 39 21	+97	7.4	4.35	HMC	
G34.26+0.15	G34.26	18 53 18.5	+01 14 57	+58	3.7	5.22	HMC-UCHII	
G45.07+0.13	G45.07	19 13 22.0	+10 50 53	+60	8.8	4.40	HMC-UCHII	2
G24.33+0.11MM1	G24.33	18 35 08.1	-07 35 04	+53	3.8	0.47	MC <sup>b</sup>	4
G28.53-0.25MM2	G28.53	18 44 15.7	-03 59 41	+87	5.7	0.005	MC <sup>c</sup>	4
G30.97+0.14MM1	G30.97	18 48 22.0	-01 48 27	+79	5.1	0.04	MC <sup>c</sup>	4
G31.97+0.07MM1	G31.97	18 49 36.6	-00 45 45	+97	6.9	0.36	MC <sup>c</sup>	4

**Notes.**— Units of right ascension are hours, minutes, and seconds, and for declination are degrees, arcminutes, and arcseconds. Positions,  $V_{LSR}$ , distances, and luminosities are taken from the cited references. (a) Hot molecular cores (HMC), some of them showing ultracompact HII regions (UCHII), and massive cores (MC) associated with infrared dark clouds.

**References.**— (1) Leurini et al. 2011; (2) Pandian et al. 2008; (3) Sollins & Ho 2005; (4) Rathborne et al. 2006

indicate brightness temperatures as high as  $10^{6.2}$  K for this line. Moreover, the model conditions predicting this maser (kinetic temperatures of 30-50 K, dust temperatures of 175 K, and gas densities of  $10^6$ - $10^7$  cm<sup>-2</sup>) are quite consistent with the environment of massive cores (Ellingsen 2006; Cyganowski et al. 2008, e.g.).

To test the predictions of the Sobolev/Cragg model, we observed 12 MSFRs associated with massive cores, HMCs, or HMC-UCHII-regions with the APEX antenna. The latter sources are associated with hot temperatures, high densities and luminosities, and rich abundances of organic molecules from previous studies. Our observations with APEX and the reduction procedure are presented in Sect. 4.2. Results and discussion are presented in Sect. 4.3.

## 5.2 Observations and Data Reduction

Of the twelve MSFRs observed, four are associated with massive cores, three are HMCs, and five are HMC-UCHII-regions. The HMCs are associated with hot temperatures, high densities and luminosities, and rich abundances of organic molecules. We list in table 5.1 the observed sources.

The massive cores were selected from a sample of cores associated with IRDCs (Rathborne et al. 2007). These four sources have masses above  $400 M_{\odot}$ , show  $4.5 \mu\text{m}$  emission (associated with shocks and outflows) and strong  $8.0 \mu\text{m}$  emission, and have  $\text{CH}_3\text{OH}$  maser emission at cm wavelengths. The HMCs and UCHII-regions were selected from the literature and are well-known MSFRs with luminosities in excess of  $10^4 L_{\odot}$ .

The observations were made using the 12 m APEX<sup>1</sup> telescope on Llano del Chajnantor, Chile, during 2010 August–December. We used the APEX-1 receiver and the Fast Fourier Transform Spectrometer (FFTS) configured with two units, each with a bandwidth of 1 GHz and 8192 channels. To obtain the maximum spectral coverage we overlapped the units to achieve 1.8 GHz total bandwidth, centered at 247228.73 MHz (1.21 mm wavelength) which is the rest frequency of the  $\text{CH}_3\text{OH}(4_{2,2}-5_{1,5})$  line. The channel width was  $0.15 \text{ km s}^{-1}$ , with a total velocity coverage of  $\sim 2300 \text{ km s}^{-1}$ . At the observing frequency of 247 GHz the APEX forward efficiency is 0.95, the beam efficiency is  $\eta_{\text{mb}}=0.75$ , and the primary beamwidth is  $\theta_{\text{FWHM}}=25''.2$ .

We converted the antenna temperature,  $T_{\text{A}}^*$ , to main-beam brightness temperature,  $T_{\text{mb}}$ , through  $T_{\text{mb}} = T_{\text{A}}^*/\eta_{\text{mb}}$ . We observed in position switching mode, using RAFGL2135 and NGC6302 as pointing sources in different epochs.

The data reduction was done with the CLASS software package<sup>2</sup>. First, we inspected the raw data for any bad spectra in either of the FFTS units. Then we combined the spectra to obtain a single  $\sim 1.8$  GHz spectral window. To fit a baseline, we made windows avoiding any obvious line emission and fitted a polynomial of order 3 or less. The data were smoothed by 6 channels to obtain a velocity resolution of  $0.9 \text{ km s}^{-1}$  in the final spectra.

<sup>1</sup>Atacama Pathfinder EXperiment. APEX is a collaboration between the Max-Planck-Institut für Radioastronomie, the European Southern Observatory, and Onsala Space Observatory.

<sup>2</sup>CLASS is part of the GILDAS software package developed by IRAM.

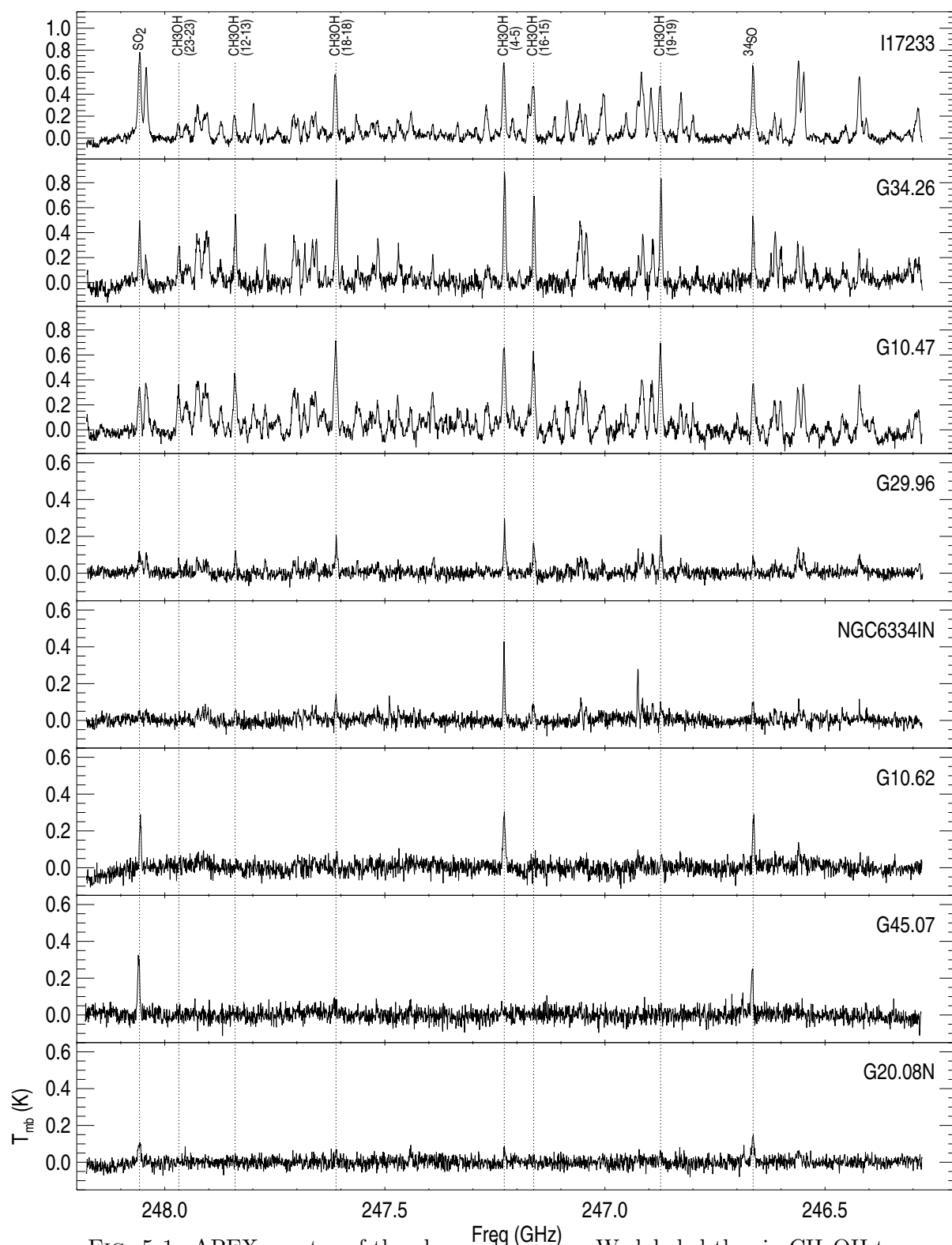


FIG. 5.1: APEX spectra of the observed sources. We labeled the six  $\text{CH}_3\text{OH}$  transitions, the  $^{34}\text{SO}$ , and the  $\text{SO}_2$  transitions.

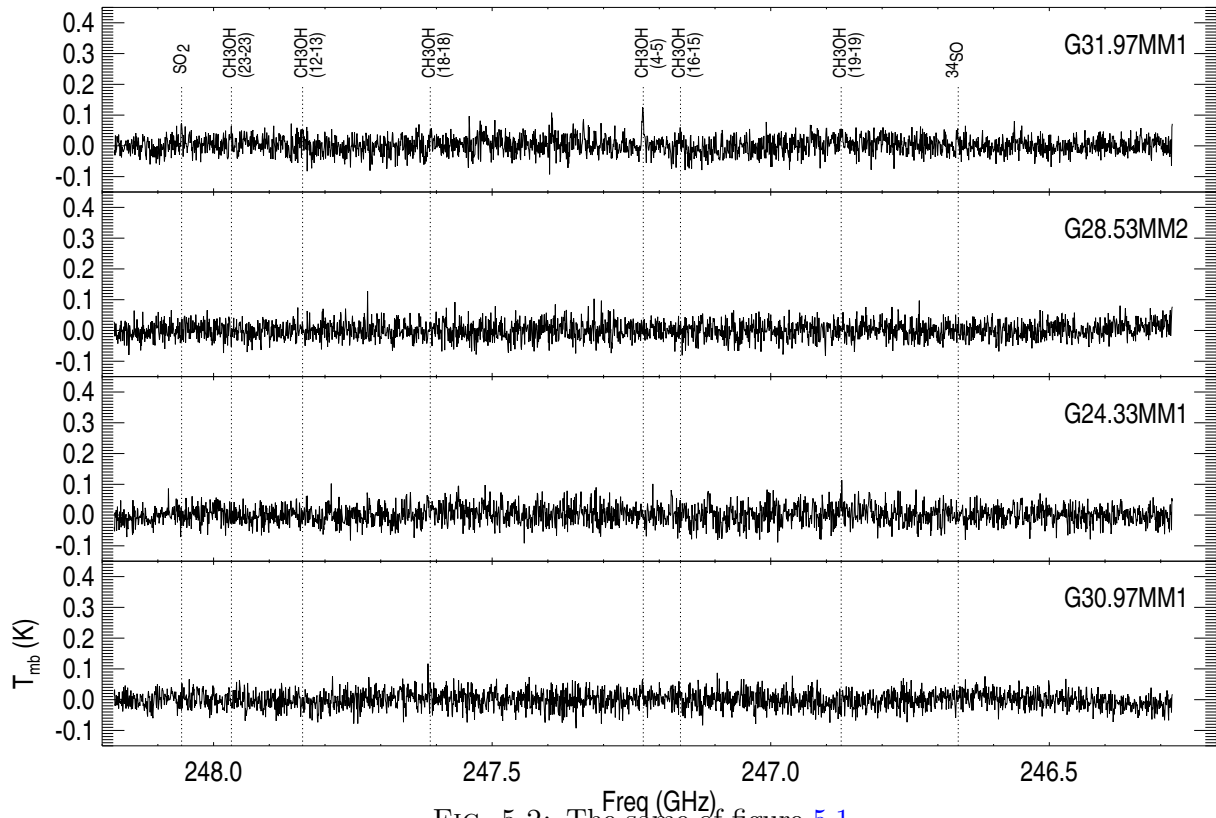


FIG. 5.2: The same of figure 5.1

## 5.3 Results and Discussion

### 5.3.1 Detection of molecular line emission

In Figures 5.1 and 5.2 we show the spectra of the twelve cores and in Table 5.2 we present a summary of the detected lines for all the cores. From our sample, I17233, G34.26 and G10.47 show the most line emission and the richest chemistry. Among the species we detected are  $\text{HC}_3\text{N}$ ,  $\text{CH}_3\text{OH}$ ,  $\text{SO}_2$ ,  $^{33}\text{SO}_2$ ,  $^{34}\text{SO}$ ,  $\text{CH}_3\text{OCHO}$ ,  $\text{CH}_3\text{CHCN}$  and  $\text{CH}_3\text{CH}_2\text{CN}$ . In Table 5.3 we show the properties of the more prominent lines found toward the hot core I17233.

We find that 3 sources, I17233, G34.26, and G10.47, contain numerous emission lines from oxygenated, nitrogenated, and sulfured species, and some isotopomers. On the other hand G29.96, NGC6334IN, G10.62, G45.07, and G20.08N, show a less-rich chemistry in their spectra. The remaining four, G31.97MM1, G28.53MM2, G24.33MM1, and G30.97MM1, show little molecular line emission. We labeled in Figures 5.1 and





---

5.2 the five CH<sub>3</sub>OH transitions used to estimate rotation temperature and column density through the rotation diagram method for I17233, G34.26, G10.47, and G29.96 and NGC6334IN (see section 5.2).

TABLE 5.2: APEX Detection Summary of Main Molecular lines

Freq (GHz)	Line	HMCs								Massive Cores			
		NGC6334IN	I17233	G10.47	G10.62	G20.08	29.96	G34.26	G45.07	G24.33	G28.5MM2	G30.9MM1	G31.9MM1
247.2100	HC <sub>3</sub> N <sub>v7=2</sub>	...	Y	Y	...	...	...	...	...	...	...	...	...
247.1136	HC <sub>3</sub> N <sub>v7=2</sub>	...	Y	Y	...	...	...	...	...	...	...	...	...
246.5607	HC <sub>3</sub> N <sub>v7=1</sub>	Y	Y	Y	Y	Y	Y	Y	...	...	...	...	...
247.9679	CH <sub>3</sub> OH <sub>vt=0</sub>	Y?	Y	Y	...	...	Y	Y	...	...	...	...	...
247.8402	CH <sub>3</sub> OH <sub>vt=1</sub>	Y	Y	Y	...	...	Y	Y	...	...	...	...	...
247.6110	CH <sub>3</sub> OH <sub>vt=0</sub>	Y	Y	Y	Y?	...	Y	Y	...	...	...	...	...
247.2287	CH <sub>3</sub> OH <sub>vt=0</sub>	Y	Y	Y	Y	Y	Y	Y	...	...	...	...	Y
247.1619	CH <sub>3</sub> OH <sub>vt=0</sub>	Y	Y	Y	...	...	Y	Y	...	...	...	...	...
246.8735	CH <sub>3</sub> OH <sub>vt=0</sub>	Y	Y	Y	Y?	...	Y	Y	...	Y	...	...	...
248.0574	SO <sub>2</sub>	...	Y	Y	Y	Y	Y	Y	Y	...	...	...	...
247.1697	SO <sub>2</sub>	...	Y	Y	...	...	...	...	...	...	...	...	...
246.4566	<sup>33</sup> SO <sub>2</sub>	...	Y	Y	...	...	...	Y	...	...	...	...	...
246.6861	<sup>34</sup> SO <sub>2</sub>	...	...	...	Y	Y	...	...	Y	...	...	...	...
247.4403	<sup>34</sup> SO <sub>2</sub>	...	Y	Y	...	Y	...	...	...	...	...	...	...
246.4045	SO 3Σ <sub>v</sub>	...	Y	...	...	...	...	...	...	...	...	...	...
246.6634	<sup>34</sup> SO	Y	Y	Y	Y	Y	Y	Y	Y	...	...	...	...
248.0425	CH <sub>3</sub> CH <sub>2</sub> CN	...	Y	Y	...	...	Y	Y	...	...	...	...	...
246.5487	CH <sub>3</sub> CH <sub>2</sub> CN	...	Y	Y	...	...	Y	Y	...	...	...	...	...
246.4219	CH <sub>3</sub> CH <sub>2</sub> CN	Y	Y	Y	...	...	...	Y	...	...	...	...	...

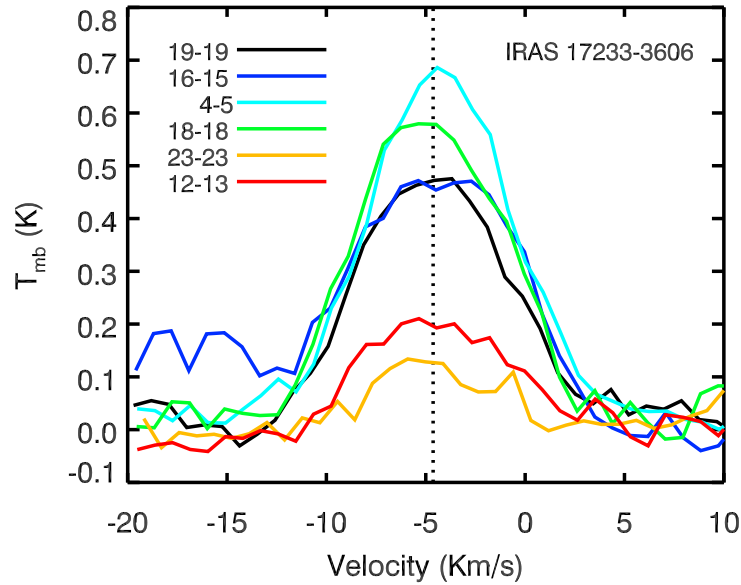


FIG. 5.4: Methanol lines toward I17233.

We used the SPLATALOGUE<sup>3</sup> website to identify the main lines in the I17233 spectra and they are labeled in Figure 5.3. We note that the large number of emission lines may produce blending of several species; thus, our list of detected transitions is not complete. High resolution ALMA observations would improve this situation, since its better angular resolution would allow spatial, as well as spectral, separation of the lines. Molecular emission coming from outflows, envelopes and toroids could be resolved and separated, for example.

TABLE 5.3: Molecular lines toward IRAS 17233

Freq (GHz)	Line transition	$E_u$ (K)	$S\mu^2$ ( $D^2$ )
247.2099	$\text{HC}_3\text{N } v_7=2(27-26, l=2f)$	811	370.40
247.1146	$\text{HC}_3\text{N } v_7=2(27-26, l=0v)$	807	372.41
246.5607	$\text{HC}_3\text{N } v_7=1(27-26, l=1f)$	486	373.64
247.9679	$\text{CH}_3\text{OH } vt=0(23_1, 22-23_0, 23)$	661	11.74
247.8402	$\text{CH}_3\text{OH } vt=1(12_{-2, 10}-13_{-3, 10})$	545	8.86
247.6110	$\text{CH}_3\text{OH } vt=0(18_3, 15-18_2, 16)$	446	17.36
247.2287	$\text{CH}_3\text{OH } vt=0(4_2, 2-5_1, 5)$	70	1.08
247.1619	$\text{CH}_3\text{OH } vt=0(16_2, 14-15_3, 12)$	338	4.83
246.8735	$\text{CH}_3\text{OH } vt=0(19_3, 16-19_2, 17)$	490	18.42
248.0574	$\text{SO}_2(15_2, 14-15_1, 15)$	119	14.05
247.1697	$\text{SO}_2(31_9, 23-32_8, 24)$	654	11.34
246.6861	$^{34}\text{SO}_2 v=0 4(3, 1)-4(2, 2)$	30	4.30
247.4403	$^{34}\text{SO}_2 v=0 5(3, 3)-5(2, 4)$	35	6.03
248.0425	$\text{CH}_3\text{CH}_2\text{CN}(28_1, 27-27_1, 26)$	176	412.53
246.5487	$\text{CH}_3\text{CH}_2\text{CN}(27_3, 24-26_3, 23)$	174	395.51
246.4219	$\text{CH}_3\text{CH}_2\text{CN}(28_2, 27-27_2, 26)$	177	412.23

<sup>3</sup><http://www.splatalogue.net/>

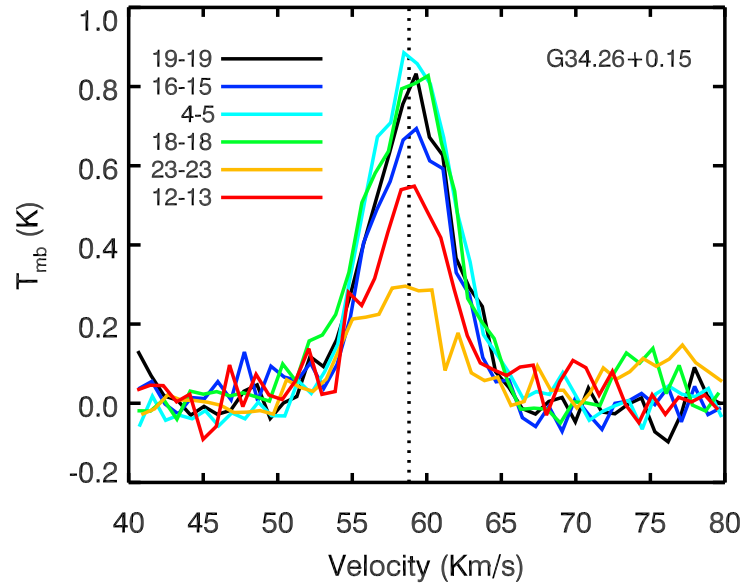


FIG. 5.5: Methanol lines toward G34.26

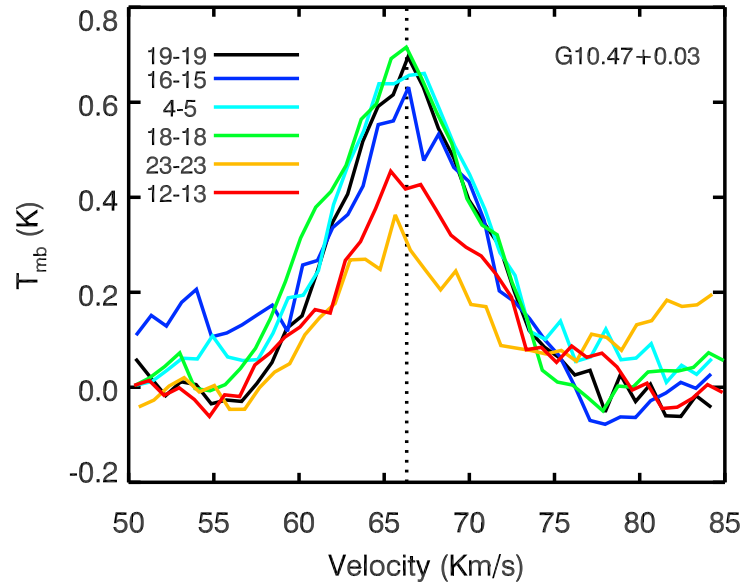


FIG. 5.6: Methanol lines toward G10.47

It is worth noting that I17233, G34.26, G10.47, and G29.96 show richer spectra than NGC6334IN, G10.62, G45.07, and G20.08N, although all eight are classified in the literature as hot cores. Moreover, we see differentiation in some molecular lines toward the latter four cores. For example, NGC6334IN and G10.62 show important emission from the  $\text{CH}_3\text{OH}v_t=0(4_{2,2}-5_{1,5})$  transition, in comparison to G45.07 and G20.08N.

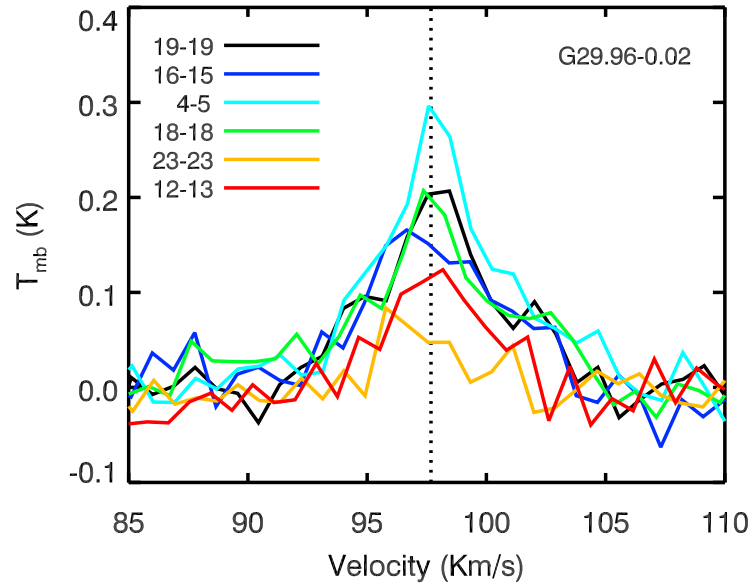


FIG. 5.7: Methanol lines toward G10.47

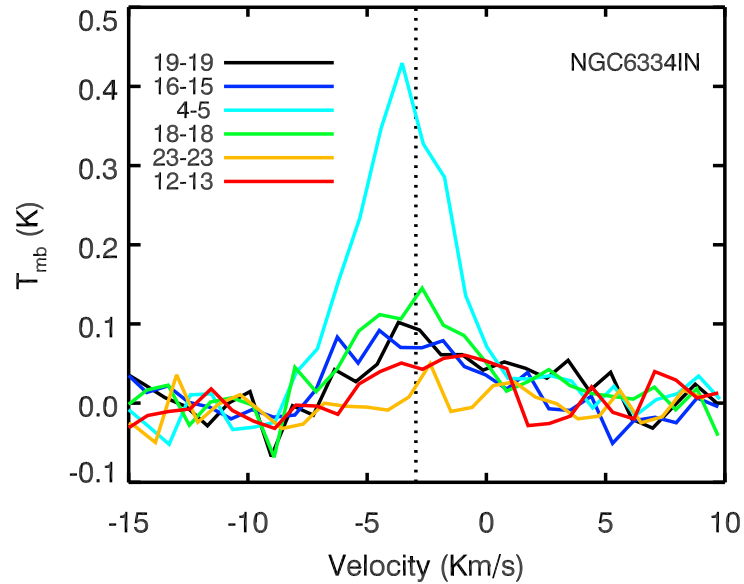


FIG. 5.8: Methanol lines toward NGC6334IN

On the other hand, G45.07 and G20.08N show a prominent  $\text{SO}_2$  line at 248.05 GHz, while the former two do not show significant emission. In any case, for all the HMCs we can see molecular transitions of  $\text{CH}_3\text{OH}(4-5)$  and  $\text{SO}(15-15)$  that have excitation temperatures of 70 and 120 K respectively, confirming the HMC nature of these sources. Chemical differences in the number of transitions and their emission have been detected toward other MSFRs such as the Orion hot core and the W3(OH)–(TW) region, and have been explained as the result of different physical conditions, different composition

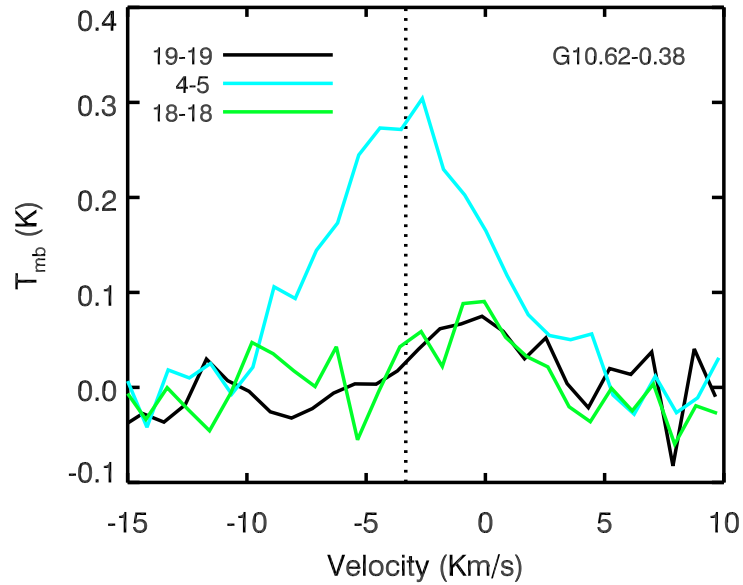


FIG. 5.9: Methanol lines toward G10.62

of ice-mantles on dust grains or, different ages of HMCs (e.g., Liu et al. 2002; Beuther et al. 2005).

TABLE 5.4: Physical parameters from lines and rotational diagrams

Source	$T_{\text{rot}}$ (K)	$N_{\text{CH}_3\text{OH}}$ ( $\text{cm}^{-2}$ )	FWHM ( $\text{km s}^{-1}$ )	$M_{\text{vir}}$ ( $M_{\odot}$ )
I17233	136	2.0(14)	8.4	709
G34.26	152	2.1(14)	6.7	2625
G10.47	168	2.6(14)	10.0	6032
G29.96	140	5.1(13)	5.7	5250
NGC6334IN	106	4.5(13)	4.5	1206
G10.62	87	4.7(13)	5.4	3550
G20.08N	...	...	...	...
G31.97MM1	...	...	...	...

**Notes.**— FWHM is the average value for detected lines.  $M_{\text{vir}}$  is calculated from the FWHM for each source.

### 5.3.2 Rotation diagram analysis

The multiple  $\text{CH}_3\text{OH}$  lines can be used to estimate the rotational temperature and column density via a rotation diagram (RD) analysis (Turner 1991), assuming the methanol gas is optically thin and molecules in local thermodynamic equilibrium (LTE). No background radiation is considered, and uniform temperature and density

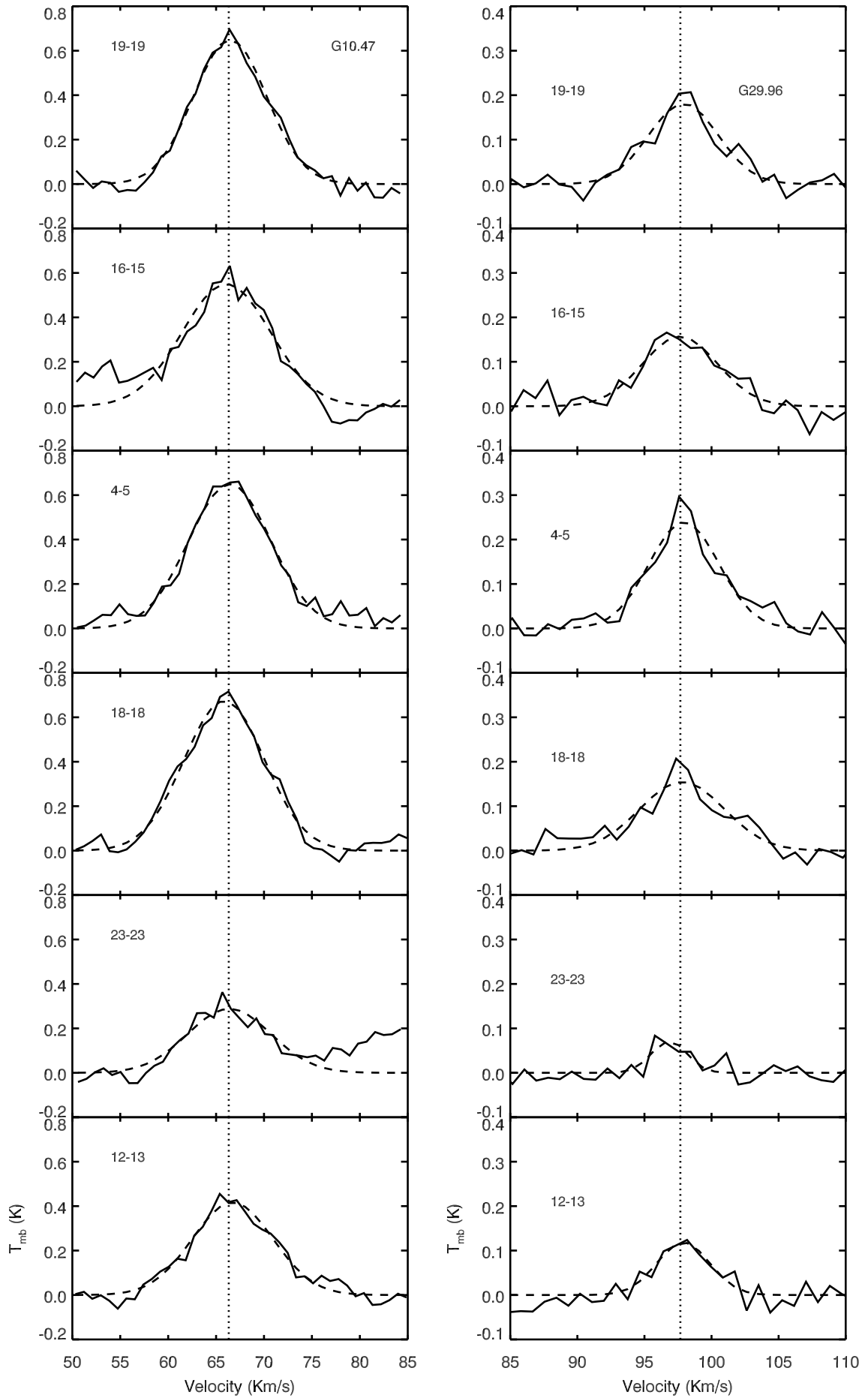


FIG. 5.10: Gaussian fits of methanol lines toward G10.47 (left) and G29.96 (right).

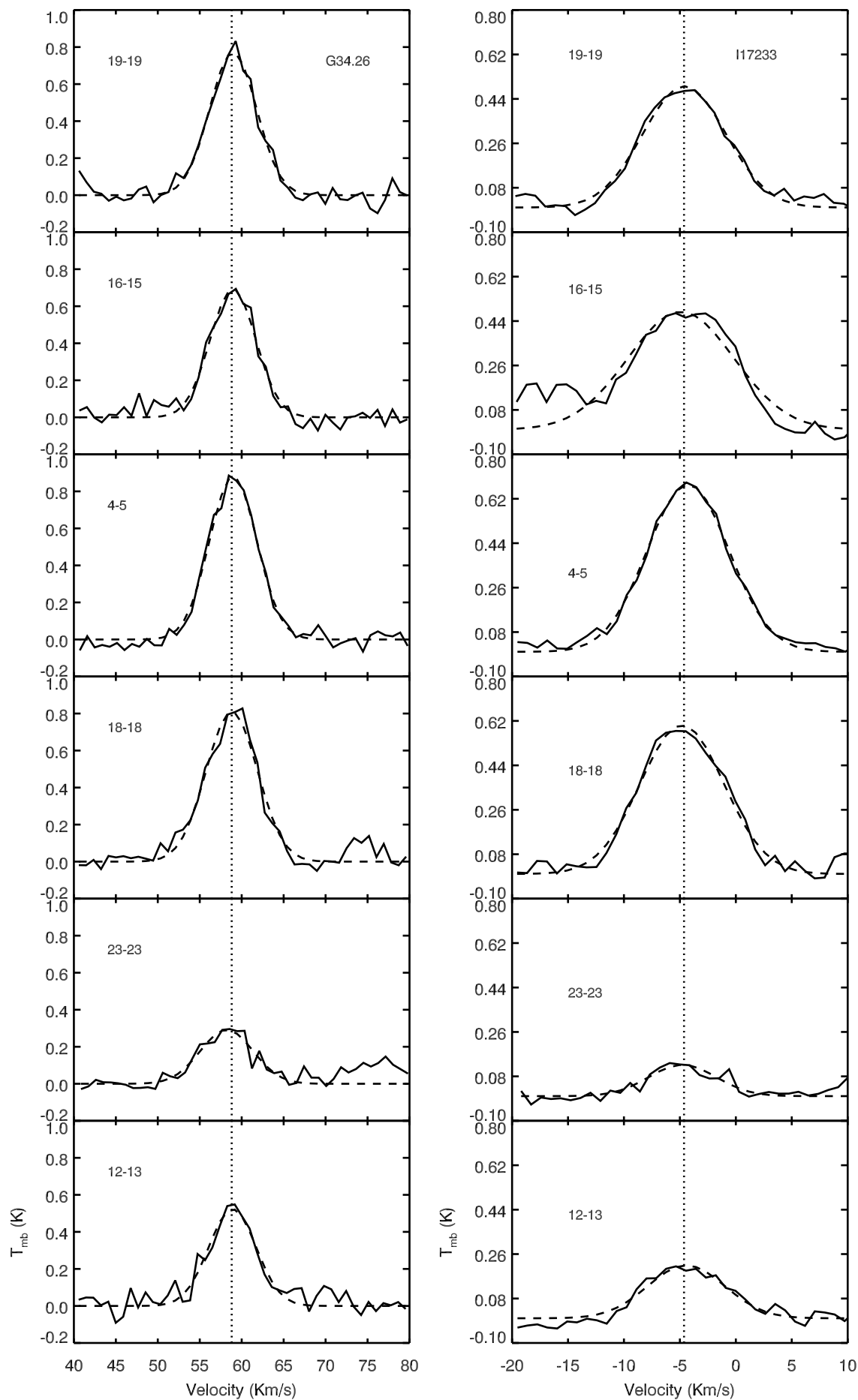


FIG. 5.11: Gaussian fits of methanol lines toward G34.26 (*left*) and I17233 (*right*).



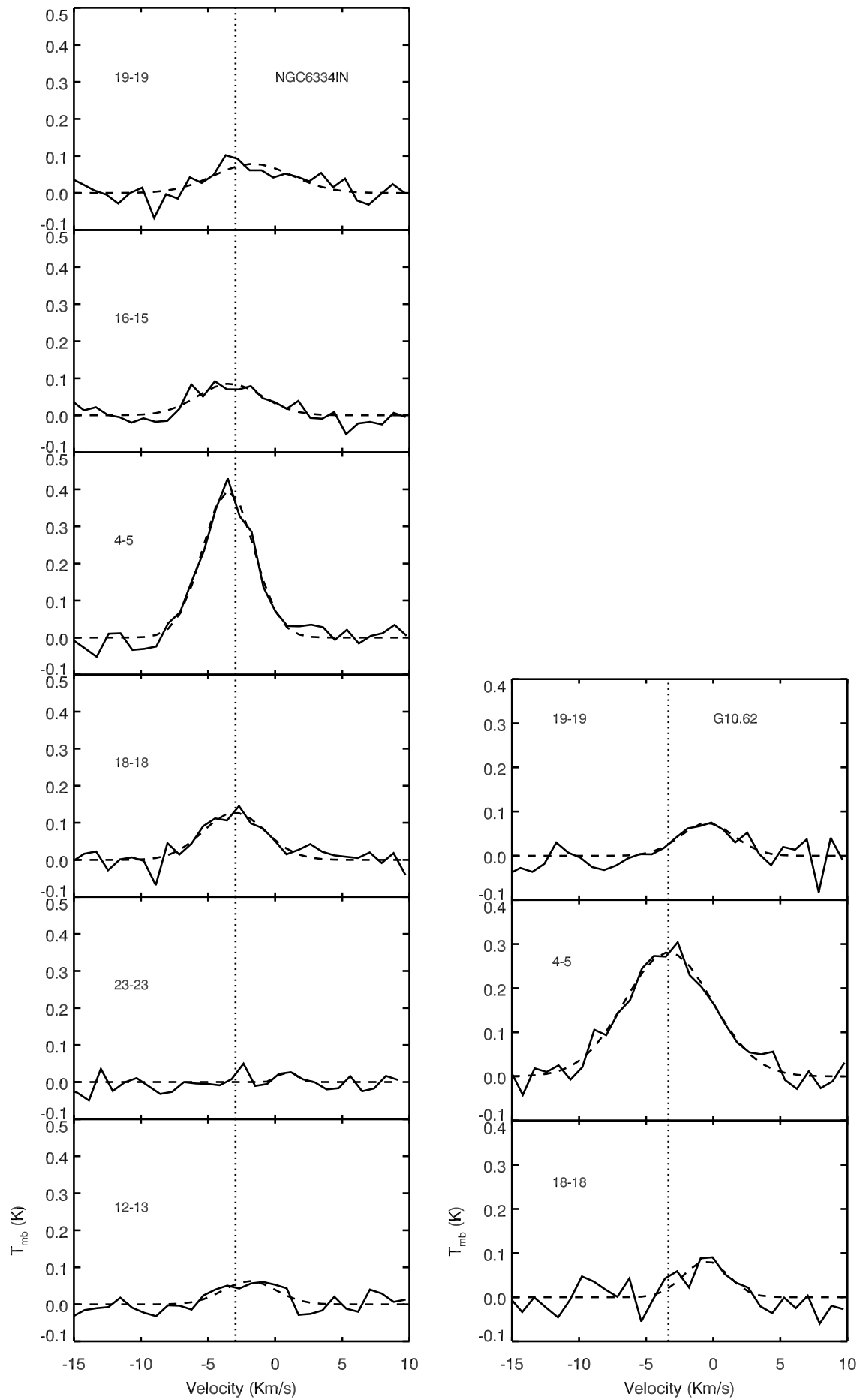


FIG. 5.12: Gaussian fits of methanol lines toward NGC6334IN (*left*) and G10.62 (*right*).

are assumed. If the molecular transitions are thermalized, the rotational temperature will be close to the kinematic temperature of the gas.

The RD method starts from the Boltzmann equation in which the measured integrated main-beam brightness temperature,  $\int T_{\text{mb}} dv$ , is related to the column density of the species in the upper level  $N_u$  by

$$\ln \left( \frac{3k \int T_{\text{mb}} dv}{8\pi^3 \mu^2 \nu S} \right) = \ln \left( \frac{N_u}{g_u} \right) = \ln \left( \frac{N_{\text{tot}}}{Q_{\text{rot}}} \right) - \frac{E_u}{kT_{\text{rot}}} \quad (5.1)$$

where  $\nu$  is frequency,  $\mu$  the dipole moment,  $S$  is the line strength,  $g_u$  is the total degeneracy of the upper state,  $N_{\text{tot}}$  is the column density of the molecule, and  $E_u$  is the upper energy level. The rotational partition function,  $Q_{\text{rot}}$ , for the  $A$ - and  $E$ -methanols (see Section 3.1) can be approximated from Turner (1991) and for an asymmetric rotor,

$$Q_0 \approx \sqrt{\frac{\pi}{ABC} \left( \frac{kT_{\text{rot}}}{h} \right)^3} \quad (5.2)$$

where  $A$ ,  $B$  and  $C$  are the rotational constants. Thus in Eq. 5.1, we can use  $Q_{\text{rot}} \approx Q_0^A + Q_0^E \approx 2Q_0 \approx 1.24T_{\text{rot}}^{1.5}$  where  $Q_0^A$  and  $Q_0^E$  refers to the symmetries of the  $A$  and  $E$  lines (section 3.1). This value is similar to others used in the literature (Menten et al. 1986; Buckle & Fuller 2000; Turner 1991).

Equation 5.1 is a linear equation with slope  $(-1/T_{\text{rot}})$  and intercept  $\ln(N_{\text{tot}}/Q_{\text{rot}})$ . The RD is the result of plotting the left part of eq. 5.1 versus  $E_u/k$  for each molecular transition. Using a linear fit, the temperature and column density can be determined.

CH<sub>3</sub>OH rotation diagrams and the fit to six transitions are shown in figure 5.13. The rotational temperatures determined from these CH<sub>3</sub>OH transitions range from 106 K to 168 K, and column densities range from  $4.5 \times 10^{13}$  to  $2.6 \times 10^{14} \text{ cm}^{-2}$ . These values are presented in table 5.4.

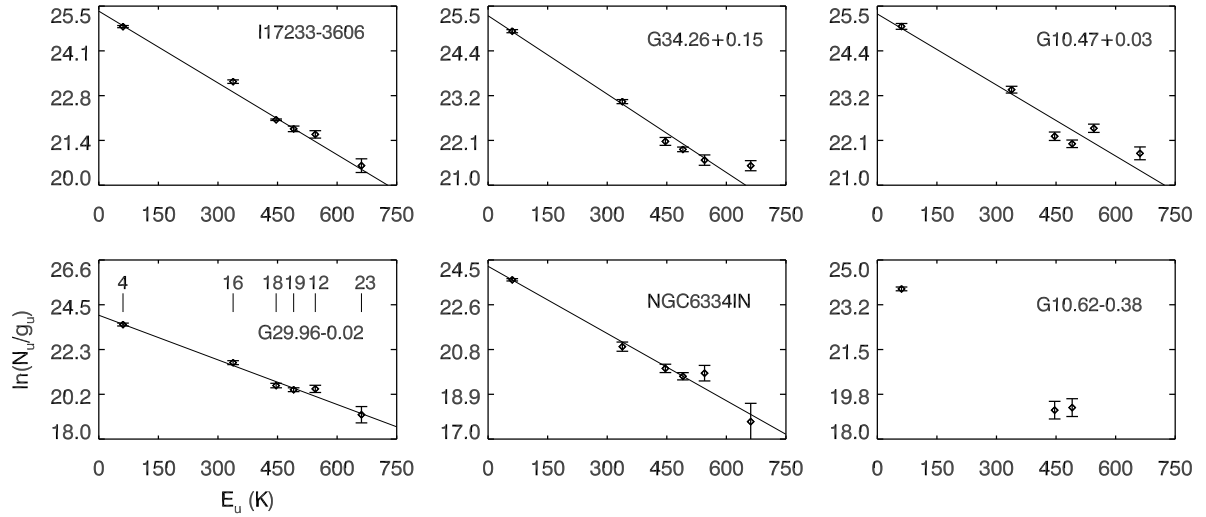


FIG. 5.13: Rotation diagram fits for methanol transitions. The solid line is for the best linear fit to the data. Results of rotational temperature and column density are shown in table 5.4

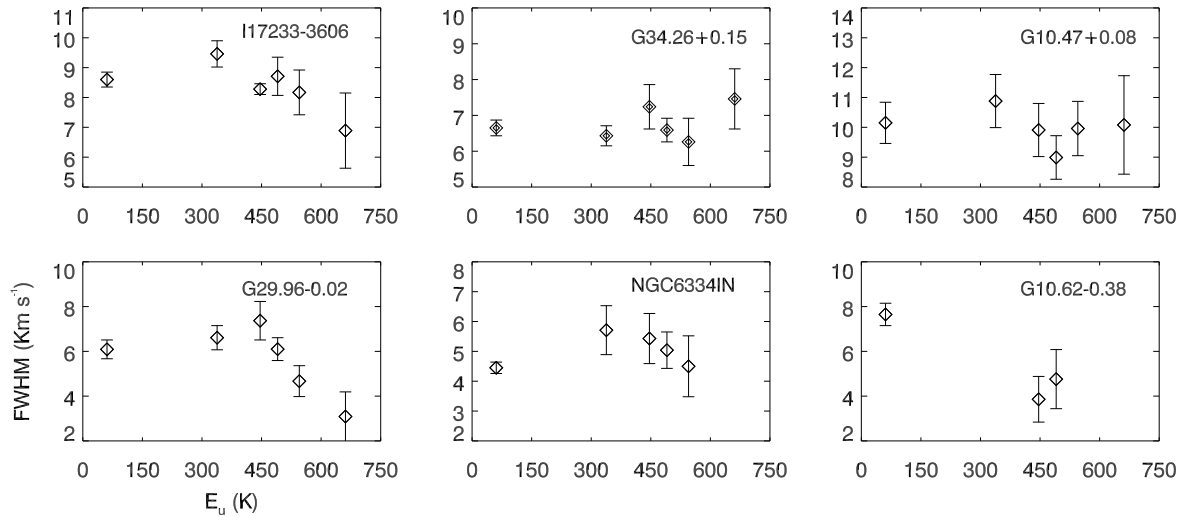


FIG. 5.14: Plots of the FWHM *vs.* upper energy level for the methanol lines.

### 5.3.3 Detection of CH<sub>3</sub>OH toward our sample

It is worth noting that G24.33MM1, G28.53MM2, G30.97MM1 and G31.97MM1 are massive cores embedded in IRDCs and show masses estimated from 1.2 mm continuum emission of 1760, 2115, 417, and 1890  $M_{\odot}$ , respectively (Rathborne et al. 2006). G24.33MM1 shows bright 8.0  $\mu\text{m}$  emission and is associated with H<sub>2</sub>O and CH<sub>3</sub>OH maser emission (Chambers et al. 2009), while G28.53MM2, G30.97MM1 and

G31.97MM1 are associated with “green fuzzies” that show  $4.5\ \mu\text{m}$  emission (classified as green in IRAC-Spitzer camera) and postulated as emission due to shocks and molecular outflows (Chambers et al. 2009; Noriega-Crespo et al. 2004). G28.53MM2 is not associated with either  $\text{H}_2\text{O}$  or  $\text{CH}_3\text{OH}$  maser emission, G30.97MM1 shows only  $\text{H}_2\text{O}$  maser emission, and G31.97MM1 is associated with both  $\text{H}_2\text{O}$  and  $\text{CH}_3\text{OH}$  maser emission (Chambers et al. 2011). Of these four massive cores only G31.97MM1 shows a weak line of  $\text{CH}_3\text{OH}(4_{2,2}-5_{1,5})$  emission, consistent with a young source probably associated with shocks and outflow phenomena.

$\text{CH}_3\text{OH}$  is an abundant molecule, mainly in MSFRs, where its formation is thought to occur through grain surface chemical reactions during an early cold stage in massive cores. Subsequently, these mantles evaporate and sublime as temperatures increase due to thermal heating and dynamical shocks from outflows, enriching the molecular gas (e.g., Caselli et al. 1993, Bachiller et al. 1998, Buckle et al. 2000). Production of  $\text{CH}_3\text{OH}$  at temperatures  $< 100\ \text{K}$  in the gas phase, go mainly through radiative association of  $\text{CH}_3^+$  and  $\text{H}_2\text{O}$ . However, this pathway via is inefficient, yielding abundances of only  $\sim 10^{-11}$  relative to  $\text{H}_2$  (Lee et al. 1996). Moreover, warm gas-phase processes are not enough to account for the observed abundances and chemistry on grain surfaces is invoked to reach the large abundances observed (Millar et al. 1991, 1995).

Bachiller et al. (1998) found that the  $\text{CH}_3\text{OH}$  abundance is enhanced by a factor  $\sim 300$  in the outflow lobes of the Class 0 object NGC 1333/IRAS 2 (See Kontinen et al. (2000) for more results toward protostellar cores). On the other hand, toward massive objects, van der Tak et al. (2000) found that  $\text{CH}_3\text{OH}$  abundance increases due to shocks in low-luminosity objects, but radiation processes are more efficient in luminous regions. Furthermore, they found that abundance profiles of  $\text{CH}_3\text{OH}$  present three different stages: (1) flat profiles and low abundances in coldest sources, (2) steeper profiles and high abundances in warmer ones, and (3) flat profiles and medium abundances toward HMCs. These results suggest a rapid evaporation of ice mantles above  $T \sim 100\ \text{K}$ , followed by destruction in gas-phase reactions during the HMC stage. Thus, van der Tak et al. (2000) suggest that  $T_{rot}(\text{CH}_3\text{OH})$  could be used as evolutionary indicator in MSFRs.

From the above, the four massive cores reported here should be associated with early stages of star formation, but G31.97MM1 probably represents a more evolved object

showing  $4.5\ \mu\text{m}$  emission, both  $\text{H}_2\text{O}$  and  $\text{CH}_3\text{OH}$  maser emission and a weak line of  $\text{CH}_3\text{OH}(4_{2,2}-5_{1,5})$  emission. On the other hand, G28.53MM2 and G30.97MM1 should be younger cores. Even though G24.33MM1 shows  $8.0\ \mu\text{m}$ ,  $\text{H}_2\text{O}$  and  $\text{CH}_3\text{OH}$  maser emission we do not detected more complex molecular tracers with our APEX observations.

In the case of the HMCs, we found very different richness of  $\text{CH}_3\text{OH}$  molecule and their transitions. In the case of the  $\text{CH}_3\text{OH}(4_{2,2}-5_{1,5})$  lines, for example, only G45.07 and G20.08N do not show emission. NGC6334IN and G10.62 both show the line, but they do not present enough lines to estimate the temperature and column density by the RD method.

### 5.3.4 Nature of the $\text{CH}_3\text{OH}$ emission

One of our goals in this work was to search for possible  $\text{CH}_3\text{OH}$  Class II maser emission at (sub)millimetric wavelengths. Class II masers are typically associated with UCHII regions, HMCs and MSFRs in general (Walsh et al. 1997; Ellingsen 2006)

High frequency Class II maser emission has been detected, mainly toward dense MSFRs, some of them associated with HMCs. For example, at 156-157 GHz Slysh et al. (1995) detected Class II masers toward W3(OH), G345.01, W48, and Cep A. At 107-108 GHz Val'tts et al. (1995, 1999) detected Class II maser emission toward several MSFRs, that are consistent with a maser model with radiative excitation and collisional de-excitation. Below  $\sim 100$  GHz Class II methanol maser is much more common (e.g., Sutton et al. 2001; Wilson et al. 1984, 1985; Menten 1991).

Our selected  $\text{CH}_3\text{OH}(4_{2,2}-5_{1,5})$  line is a good candidate to show maser emission according to maser models (Sobolev et al. 1997; Cragg et al. 2005).

In our APEX observations we found that methanol emission is thermal in most of our sources. However, the HMCs and massive cores observed have adequate physical conditions to generate the maser emission. For example, we detected the  $12_{-2,10}-13_{-3,10}$  transition in the first torsionally excited state ( $v_t = 1$ ) toward I17233, NGC6334IN, G10.47, G29.96, and G34.26. This  $\text{CH}_3\text{OH}$  line has an upper-state energy of 545 K and

its excitation mechanism involves radiative excitation. At least in these five sources, the physical conditions of dust and gas are more favourable to produce maser emission.

A possible explanation for the not definitive detection of maser is that the large size beam of APEX ( $\sim 25''$ ) covers multiple components of gas. For example, early observations have shown some Class II maser accompanied by broad thermal features from larger molecular clumps (e.g., [Slysh et al. 1995](#)).

### 5.3.5 Virial Masses

Virial masses can be estimated assuming that the cores are in virial equilibrium. If we do not consider magnetic fields or external forces, the virial mass,  $M_{\text{vir}}$ , for a spherical cloud is

$$\left[ \frac{M_{\text{vir}}}{M_{\odot}} \right] = 0.40 \left[ \frac{d}{\text{kpc}} \right] \left[ \frac{\theta_{\text{CH}_3\text{CN}}}{''} \right] \left[ \frac{\Delta V}{\text{km s}^{-1}} \right]^2 \quad (5.3)$$

where  $d$  is the distance,  $\theta_{\text{CH}_3\text{OH}}$  is the angular diameter and  $\Delta V$  the line width, in kpc, arcsecond, and  $\text{km s}^{-1}$ , respectively. For  $\Delta V$  we used the average line width from the observed  $\text{CH}_3\text{OH}$  lines (Column 4 in Table 5.4), and for the source size we used the FWHM of the APEX primary beam at 247 GHz, i.e.,  $25''$ . We show the results of  $M_{\text{vir}}$  in Table 5.4, which range from 700 to  $6030 M_{\odot}$ . We found these values are 709, 1200, 6030, 5250, and 2625 for I17233, NGC6334I(N), G10.47, G29.96, and G34.26 respectively, and an average of  $\sim 3200 M_{\odot}$ .

We note that virial masses are relatively high, but consistent with MSFRs observed with low angular resolution (e.g., [Zinchenko et al. 1997](#)).

# Chapter 6

## Conclusions

We have studied a group of MSFRs using both interferometric and single dish observations in continuum and molecular line emission. Here we present our main conclusions.

### 6.1 SMA observations of Hot Molecular Cores

We studied 17 hot molecular cores in the CH<sub>3</sub>CN ( $12_K$ – $11_K$ ) lines and the 1.3 mm continuum. The sources were observed with the SMA at 220 GHz, with either the compact or extended configuration.

From the 1.3 mm continuum, we detected dusty structures with physical sizes of 0.01–0.1 pc, gas masses of 7–375  $M_\odot$ , and column densities of 0.1– $6.7 \times 10^{24}$  cm<sup>-2</sup>. The continuum emission coming from dust ranges from 8% to 98% of the total flux.

All 17 sources show multiple molecular lines but different molecular richness. All sources show five or more  $K$ -components of CH<sub>3</sub>CN ( $12_K$ – $11_K$ ). Some spectra showed emission up to the  $K = 8$ -component, which traces gas at  $\sim 525$  K.

Based on these emission lines we estimated rotational temperatures, column densities, and fractional abundances, using both rotation diagrams and the XCLASS program that generates synthetic spectra. From the rotation diagram method we find temperatures from 90 to 500 K, and column densities from  $2.5 \times 10^{13}$  to  $2.5 \times 10^{16}$  cm<sup>-2</sup>. With XCLASS we find temperatures from 40 to 132 K and column densities from  $1.6 \times 10^{13}$

to  $1.0 \times 10^{15} \text{ cm}^{-2}$  for the extended component, and temperatures from 122 to 485 K and column densities from  $6.8 \times 10^{14}$  to  $5.1 \times 10^{17} \text{ cm}^{-2}$  for the compact component.

We used the rotation temperatures estimated with XCLASS to derive the gas mass from the 1.3 mm continuum. With the multiple  $K$ -lines of  $\text{CH}_3\text{CN}$  we find a good fit between observed and synthetic spectra for the two-component XCLASS model. These results, together with the close spatial coincidence between the molecular gas and the continuum emission, suggest that most of these HMC are internally heated. Sub-arcsecond observations are necessary to explore their structure in greater detail.

The fractional abundance of  $\text{CH}_3\text{CN}$  toward the hot-inner components shows a marked increase with temperature. This can be understood if we consider that  $\text{CH}_3\text{CN}$  molecules form in the hot gas phase when parent N-bearing species, such as  $\text{NH}_3$ , are evaporated from grain mantles.

These results have been published in [Hernández-Hernández et al. \(2014\)](#).

## 6.2 APEX observations of $\text{CH}_3\text{OH}$

We performed single dish submillimeter observations with the APEX antenna toward twelve MSFRs, grouped in three different evolutionary stages: massive cores associated with IRDCs, HMCs, and UCHII regions associated with hot molecular cores.

To search for possible  $\text{CH}_3\text{OH}$  Class II maser emission we observed the  $\text{CH}_3\text{OH}(4_{2,2}-5_{1,5})$  transition at 247.2 GHz.

Although the HMCs and massive cores observed have adequate physical conditions to generate the maser emission, we conclude that methanol emission is thermal in most of our sources. In only two cases does maser emission seem plausible; follow-up interferometric observations are needed to confirm this.

We detected up to six methanol lines, and multiple transitions of O-bearing, N-bearing and S-bearing molecules. The methanol emission lines have upper-state energies from 70 K to 660 K, confirming the presence of warm-hot gas toward some targets. In particular, the  $4_{2,2}-5_{1,5}$  transition tracing gas at 70 K was detected toward eight of the twelve sources observed, and the  $12_{-2,10}-13_{-3,10}$  transition in the first torsionally



excited state and upper-state energy of 545 K was detected in five sources, all of them HMCs.

We used the methanol line emission to estimate rotational temperatures and column densities by the rotation diagram method. Our analysis shows high densities and temperatures in five of the HMCs. The temperatures lie in the range of 105-170 K and column densities from  $4 \times 10^{13}$  to  $2 \times 10^{14} \text{ cm}^{-2}$ . Using the average line parameters from CH<sub>3</sub>OH we estimate virial masses from 700 to 6000  $M_{\odot}$ .

As general conclusions, we confirm that evaporation of grain-mantles followed by chemical reactions in hot molecular gas play an important role in the abundance of the CH<sub>3</sub>CN. The results of our survey will be constructive for chemical models in the warm/hot gas-phase. We found observational evidence of internal heating in our HMCs. These kinds of “a posteriori” surveys are important to be undertaken since it is difficult to obtain the necessary observing time in a single project. Interferometers such as SMA and ALMA will continue providing high angular resolution data from which statistical studies can be done.

Finally, more high frequency observations of CH<sub>3</sub>OH maser candidates are necessary in order to disentangle the physical conditions under which these important tracers emit radiation.

# Bibliography

- Andersson, M., & Garay, G. 1986, *A&A*, 167, L1
- Araya, E., Hofner, P., Kurtz, S., Bronfman, L., & DeDeo, S. 2005a, *ApJS*, 157, 279
- Araya, E., Hofner, P., Kurtz, S., et al. 2005b, *ApJ*, 618, 339
- Araya, E., Hofner, P., Kurtz, S., Olmi, L., & Linz, H. 2008, *ApJ*, 675, 420
- Araya, E., Hofner, P., Sewiło, M., et al. 2007, *ApJ*, 654, L95
- Araya, E. D., Kurtz, S., Hofner, P., & Linz, H. 2009, *ApJ*, 698, 1321
- Arce, H. G., Shepherd, D., Gueth, F., et al. 2007, *Protostars and Planets V*, 245
- Argon, A. L., Reid, M. J., & Menten, K. M. 2000, *ApJS*, 129, 159
- Bachiller, R., Codella, C., Colomer, F., Liechti, S., & Walmsley, C. M. 1998, *A&A*, 335, 266
- Ballesteros-Paredes, J., Hartmann, L. W., Vázquez-Semadeni, E., Heitsch, F., & Zamora-Avilés, M. A. 2011, *MNRAS*, 411, 65
- Bally, J., Cunningham, N. J., Moeckel, N., et al. 2011, *ApJ*, 727, 113
- Bayandina, O. S., Val'tts, I. E., & Larionov, G. M. 2012, *Astronomy Reports*, 56, 553
- Behrend, R., & Maeder, A. 2001, *A&A*, 373, 190
- Beltrán, M. T., Cesaroni, R., Codella, C., et al. 2006, *Nature*, 443, 427
- Beltrán, M. T., Cesaroni, R., Neri, R., & Codella, C. 2011, *A&A*, 525, A151
- Beltrán, M. T., Cesaroni, R., Neri, R., et al. 2004a, *ApJ*, 601, L187
- . 2005, *A&A*, 435, 901
- Beltrán, M. T., Girart, J. M., Estalella, R., & Ho, P. T. P. 2004b, *A&A*, 426, 941
- Beuther, H., Schilke, P., Menten, K. M., et al. 2002a, *ApJ*, 566, 945
- Beuther, H., & Sridharan, T. K. 2007, *ApJ*, 668, 348
- Beuther, H., Walsh, A., Schilke, P., et al. 2002b, *A&A*, 390, 289
- Beuther, H., & Walsh, A. J. 2008, *ApJ*, 673, L55
- Beuther, H., Walsh, A. J., & Longmore, S. N. 2009, *ApJS*, 184, 366

- Beuther, H., Walsh, A. J., Thorwirth, S., et al. 2007, *A&A*, 466, 989
- Beuther, H., Zhang, Q., Sridharan, T. K., & Chen, Y. 2005, *ApJ*, 628, 800
- Beuther, H., Zhang, Q., Sridharan, T. K., Lee, C., & Zapata, L. A. 2006, *A&A*, 454, 221
- Blake, G. A., Mundy, L. G., Carlstrom, J. E., et al. 1996, *ApJ*, 472, L49
- Bonnell, I. A., & Bate, M. R. 2006, *MNRAS*, 370, 488
- Bonnell, I. A., Bate, M. R., & Zinnecker, H. 1998, *MNRAS*, 298, 93
- Bourke, T. L., Hyland, A. R., & Robinson, G. 1995, *MNRAS*, 276, 1052
- Brand, J., Cesaroni, R., Caselli, P., et al. 1994, *A&AS*, 103, 541
- Bronfman, L., Nyman, L.-A., & May, J. 1996, *A&AS*, 115, 81
- Carey, S. J., Feldman, P. A., Redman, R. O., et al. 2000, *ApJ*, 543, L157
- Carlstrom, J. E., & Vogel, S. N. 1989, *ApJ*, 337, 408
- Caselli, P., Hasegawa, T. I., & Herbst, E. 1993, *ApJ*, 408, 548
- Caswell, J. L. 1996, *MNRAS*, 279, 79
- Caswell, J. L., & Haynes, R. F. 1983, *JRASC*, 77, 257
- Caswell, J. L., & Vaile, R. A. 1995, *MNRAS*, 273, 328
- Cesaroni, R. 2005, *Proceedings of the International Astronomical Union*, 1, 59
- Cesaroni, R., Beltrán, M. T., Zhang, Q., Beuther, H., & Fallscheer, C. 2011, *A&A*, 533, A73
- Cesaroni, R., Churchwell, E., Hofner, P., Walmsley, C. M., & Kurtz, S. 1994a, *A&A*, 288, 903
- Cesaroni, R., Galli, D., Lodato, G., Walmsley, M., & Zhang, Q. 2006, *Nature*, 444, 703
- Cesaroni, R., Hofner, P., Araya, E., & Kurtz, S. 2010, *A&A*, 509, A50
- Cesaroni, R., Hofner, P., Walmsley, C. M., & Churchwell, E. 1998, *A&A*, 331, 709
- Cesaroni, R., Neri, R., Olmi, L., et al. 2005, *A&A*, 434, 1039
- Cesaroni, R., Olmi, L., Walmsley, C. M., Churchwell, E., & Hofner, P. 1994b, *ApJ*, 435, L137
- Cesaroni, R., Walmsley, C. M., & Churchwell, E. 1992, *A&A*, 256, 618
- Cesaroni, R., Walmsley, C. M., Koempe, C., & Churchwell, E. 1991, *A&A*, 252, 278
- Chambers, E. T., Jackson, J. M., Rathborne, J. M., & Simon, R. 2009, *ApJS*, 181, 360
- Chambers, E. T., Yusef-Zadeh, F., & Ott, J. 2014, *A&A*, 563, A68
- Chambers, E. T., Yusef-Zadeh, F., & Roberts, D. 2011, *ApJ*, 733, 42
- Charnley, S. B. 1995, *Ap&SS*, 224, 251

- . 1997, *ApJ*, 481, 396
- Charnley, S. B., Tielens, A. G. G. M., & Millar, T. J. 1992, *ApJ*, 399, L71
- Chen, H.-R., Welch, W. J., Wilner, D. J., & Sutton, E. C. 2006, *ApJ*, 639, 975
- Chen, X., Shen, Z.-Q., Li, J.-J., Xu, Y., & He, J.-H. 2010, *ApJ*, 710, 150
- Churchwell, E. 2002, *ARA&A*, 40, 27
- Churchwell, E., Walmsley, C. M., & Cesaroni, R. 1990, *A&AS*, 83, 119
- Churchwell, E., Walmsley, C. M., & Wood, D. O. S. 1992, *A&A*, 253, 541
- Codella, C., Testi, L., & Cesaroni, R. 1997, *A&A*, 325, 282
- Comito, C., Schilke, P., Phillips, T. G., et al. 2005, *ApJS*, 156, 127
- Comoretto, G., Palagi, F., Cesaroni, R., et al. 1990, *A&AS*, 84, 179
- Cragg, D. M., Johns, K. P., Godfrey, P. D., & Brown, R. D. 1992, *MNRAS*, 259, 203
- Cragg, D. M., Sobolev, A. M., & Godfrey, P. D. 2005, *MNRAS*, 360, 533
- Cyganowski, C. J., Brogan, C. L., & Hunter, T. R. 2007, *AJ*, 134, 346
- Cyganowski, C. J., Brogan, C. L., Hunter, T. R., & Churchwell, E. 2009, *ApJ*, 702, 1615
- Cyganowski, C. J., Brogan, C. L., Hunter, T. R., Churchwell, E., & Zhang, Q. 2011, *ApJ*, 729, 124
- Cyganowski, C. J., Koda, J., Rosolowsky, E., et al. 2013, *ApJ*, 764, 61
- Cyganowski, C. J., Whitney, B. A., Holden, E., et al. 2008, *AJ*, 136, 2391
- De Buizer, J. M., Osorio, M., & Calvet, N. 2005, *ApJ*, 635, 452
- De Buizer, J. M., Radomski, J. T., Telesco, C. M., & Piña, R. K. 2003, *ApJ*, 598, 1127
- de Vicente, P., Martín-Pintado, J., Neri, R., & Colom, P. 2000, *A&A*, 361, 1058
- Dedes, C., Röllig, M., Mookerjee, B., et al. 2010, *A&A*, 521, L24
- Doty, S. D., van Dishoeck, E. F., & Tan, J. C. 2006, *A&A*, 454, L5
- Doty, S. D., van Dishoeck, E. F., van der Tak, F. F. S., & Boonman, A. M. S. 2002, *A&A*, 389, 446
- Egan, M. P., Shipman, R. F., Price, S. D., et al. 1998, *ApJ*, 494, L199
- Ellingsen, S. P. 2005, *MNRAS*, 359, 1498
- . 2006, *ApJ*, 638, 241
- Ellingsen, S. P., von Bibra, M. L., McCulloch, P. M., et al. 1996, *MNRAS*, 280, 378
- Faúndez, S., Bronfman, L., Garay, G., et al. 2004, *A&A*, 426, 97
- Feldt, M., Puga, E., Lenzen, R., et al. 2003, *ApJ*, 599, L91
- Fernández-López, M., Girart, J. M., Curiel, S., et al. 2011, *AJ*, 142, 97
- Fish, V. L., Reid, M. J., Argon, A. L., & Zheng, X.-W. 2005, *ApJS*, 160, 220

- Forster, J. R., & Caswell, J. L. 1989, *A&A*, 213, 339
- Franco-Hernández, R., Moran, J. M., Rodríguez, L. F., & Garay, G. 2009, *ApJ*, 701, 974
- Furuya, R. S., Cesaroni, R., & Shinnaga, H. 2011, *A&A*, 525, A72
- Furuya, R. S., Cesaroni, R., Takahashi, S., et al. 2008, *ApJ*, 673, 363
- . 2005, *ApJ*, 624, 827
- Galván-Madrid, R., Keto, E., Zhang, Q., et al. 2009, *ApJ*, 706, 1036
- Garay, G., Brooks, K. J., Mardones, D., & Norris, R. P. 2003, *ApJ*, 587, 739
- Garay, G., Faúndez, S., Mardones, D., et al. 2004, *ApJ*, 610, 313
- Garay, G., & Lizano, S. 1999, *PASP*, 111, 1049
- Garay, G., Mardones, D., Bronfman, L., et al. 2010, *ApJ*, 710, 567
- Garay, G., Reid, M. J., & Moran, J. M. 1985, *ApJ*, 289, 681
- Garay, G., & Rodríguez, L. F. 1990, *ApJ*, 362, 191
- Garay, G., Rodríguez, L. F., & de Gregorio-Monsalvo, I. 2007, *AJ*, 134, 906
- Garay, G., Rodríguez, L. F., Moran, J. M., & Churchwell, E. 1993, *ApJ*, 418, 368
- Garrod, R. T., & Herbst, E. 2006, *A&A*, 457, 927
- Garrod, R. T., Weaver, S. L. W., & Herbst, E. 2008, *ApJ*, 682, 283
- Garrod, R. T., & Widicus Weaver, S. L. 2013, *Chemical Reviews*, 113, 8939
- Gaume, R. A., Johnston, K. J., & Wilson, T. L. 1993, *ApJ*, 417, 645
- Gaume, R. A., & Mutel, R. L. 1987, *ApJS*, 65, 193
- Genzel, R., & Stutzki, J. 1989, *ARA&A*, 27, 41
- Gibson, D., Plume, R., Bergin, E., Ragan, S., & Evans, N. 2009, *ApJ*, 705, 123
- Goddi, C., Greenhill, L. J., Humphreys, E. M. L., Chandler, C. J., & Matthews, L. D. 2011, *ApJ*, 739, L13
- Goldsmith, P. F., & Langer, W. D. 1999, *ApJ*, 517, 209
- Gomez, Y., Garay, G., & Lizano, S. 1995, *ApJ*, 453, 727
- Guesten, R., Chini, R., & Neckel, T. 1984, *A&A*, 138, 205
- Guesten, R., & Fiebig, D. 1988, *A&A*, 204, 253
- Harju, J., Lehtinen, K., Booth, R. S., & Zinchenko, I. 1998, *A&AS*, 132, 211
- Hasegawa, T. I., & Herbst, E. 1993, *MNRAS*, 263, 589
- Hatchell, J., Thompson, M. A., Millar, T. J., & MacDonald, G. H. 1998, *A&AS*, 133, 29
- Heaton, B. D., Matthews, N., Little, L. T., & Dent, W. R. F. 1985, *MNRAS*, 217, 485
- Henkel, C., Haschick, A. D., & Guesten, R. 1986, *A&A*, 165, 197

- Henkel, C., Wilson, T. L., & Johnston, K. J. 1984, *ApJ*, 282, L93
- Henkel, C., Wilson, T. L., & Mauersberger, R. 1987, *A&A*, 182, 137
- Henning, T., Michel, B., & Stognienko, R. 1995, *PLANSS*, 43, 1333
- Herbst, E., & van Dishoeck, E. F. 2009, *ARA&A*, 47, 427
- Hernández-Hernández, V., Zapata, L., Kurtz, S., & Garay, G. 2014, *ApJ*, 786, 38
- Hildebrand, R. H. 1983, *QJRAS*, 24, 267
- Ho, P. T. P., Genzel, R., & Das, A. 1983, *ApJ*, 266, 596
- Ho, P. T. P., Moran, J. M., & Lo, K. Y. 2004, *ApJ*, 616, L1
- Hofner, P., & Churchwell, E. 1996, *A&AS*, 120, 283
- Hofner, P., Kurtz, S., Churchwell, E., Walmsley, C. M., & Cesaroni, R. 1996, *ApJ*, 460, 359
- Hofner, P., Peterson, S., & Cesaroni, R. 1999, *ApJ*, 514, 899
- Hogerheijde, M. R. 2005, *Ap&SS*, 295, 179
- Hunter, T. R., Brogan, C. L., Indebetouw, R., & Cyganowski, C. J. 2008, *ApJ*, 680, 1271
- Hunter, T. R., Brogan, C. L., Megeath, S. T., et al. 2006, *ApJ*, 649, 888
- Hunter, T. R., Churchwell, E., Watson, C., et al. 2000, *AJ*, 119, 2711
- Hunter, T. R., Phillips, T. G., & Menten, K. M. 1997, *ApJ*, 478, 283
- Hunter, T. R., Testi, L., Zhang, Q., & Sridharan, T. K. 1999, *AJ*, 118, 477
- Jackson, J. M., Finn, S. C., Rathborne, J. M., Chambers, E. T., & Simon, R. 2008, *ApJ*, 680, 349
- Jiménez-Serra, I., Caselli, P., Tan, J. C., et al. 2010, *MNRAS*, 406, 187
- Jiménez-Serra, I., Martín-Pintado, J., Rodríguez-Franco, A., et al. 2007, *ApJ*, 661, L187
- Kalenskii, S. V., Dzura, A. M., Booth, R. S., Winnberg, A., & Alakoz, A. V. 1997, *A&A*, 321, 311
- Kalenskii, S. V., Promislov, V. G., Alakoz, A., Winnberg, A. V., & Johansson, L. E. B. 2000, *A&A*, 354, 1036
- Kaufman, M. J., Hollenbach, D. J., & Tielens, A. G. G. M. 1998, *ApJ*, 497, 276
- Keto, E., & Klaassen, P. 2008, *ApJ*, 678, L109
- Keto, E., & Wood, K. 2006, *ApJ*, 637, 850
- Keto, E., & Zhang, Q. 2010, *MNRAS*, 406, 102
- Keto, E. R., Ho, P. T. P., & Haschick, A. D. 1987, *ApJ*, 318, 712
- . 1988, *ApJ*, 324, 920

- Klaassen, P. D., & Wilson, C. D. 2007, *ApJ*, 663, 1092
- Klaassen, P. D., Wilson, C. D., Keto, E. R., & Zhang, Q. 2009, *ApJ*, 703, 1308
- Krumholz, M. R., Klein, R. I., & McKee, C. F. 2007, *ApJ*, 656, 959
- Kurtz, S., Cesaroni, R., Churchwell, E., Hofner, P., & Walmsley, C. M. 2000, *Protostars and Planets IV*, 299
- Kurtz, S., Churchwell, E., & Wood, D. O. S. 1994, *ApJS*, 91, 659
- Kurtz, S., Hofner, P., & Álvarez, C. V. 2004, *ApJS*, 155, 149
- Kurtz, S. E., Watson, A. M., Hofner, P., & Otte, B. 1999, *ApJ*, 514, 232
- Lada, C. J., & Lada, E. A. 2003, *ARA&A*, 41, 57
- Leurini, S., Beuther, H., Schilke, P., et al. 2007a, *A&A*, 475, 925
- Leurini, S., Codella, C., Zapata, L., et al. 2011, *A&A*, 530, A12
- Leurini, S., Hieret, C., Thorwirth, S., et al. 2008, *A&A*, 485, 167
- Leurini, S., Schilke, P., Wyrowski, F., & Menten, K. M. 2007b, *A&A*, 466, 215
- Leurini, S., Codella, C., Zapata, L. A., et al. 2009, *A&A*, 507, 1443
- Lim, W., Lyo, A.-R., Kim, K.-T., & Byun, D.-Y. 2012, *AJ*, 144, 151
- Linke, R. A., Frerking, M. A., & Thaddeus, P. 1979, *ApJ*, 234, L139
- Lintott, C. J., Viti, S., Rawlings, J. M. C., et al. 2005, *ApJ*, 620, 795
- Liu, H. B., Zhang, Q., & Ho, P. T. P. 2011, *ApJ*, 729, 100
- Longmore, S. N., Burton, M. G., Barnes, P. J., et al. 2007a, *MNRAS*, 379, 535
- Longmore, S. N., Maercker, M., Ramstedt, S., & Burton, M. G. 2007b, *MNRAS*, 380, 1497
- Longmore, S. N., Pillai, T., Keto, E., Zhang, Q., & Qiu, K. 2011, *ApJ*, 726, 97
- López, C., Bronfman, L., Nyman, L.-Å., May, J., & Garay, G. 2011, *A&A*, 534, A131
- MacDonald, G. H., & Habing, R. J. 1995, in *Lecture Notes in Physics*, Berlin Springer Verlag, Vol. 459, *The Physics and Chemistry of Interstellar Molecular Clouds*, ed. G. Winnewisser & G. C. Pelz, 291–293
- MacLaren, I., Richardson, K. M., & Wolfendale, A. W. 1988, *ApJ*, 333, 821
- Massi, M., Felli, M., & Churchwell, E. 1988, *A&A*, 194, 116
- Mauersberger, R., Henkel, C., & Wilson, T. L. 1987, *A&A*, 173, 352
- Mauersberger, R., Henkel, C., Wilson, T. L., & Walmsley, C. M. 1986a, *A&A*, 162, 199
- Mauersberger, R., Wilson, T. L., & Henkel, C. 1986b, *A&A*, 160, L13
- Mayen-Gijon, J. M., Anglada, G., Osorio, M., et al. 2014, *MNRAS*, 437, 3766
- McKee, C. F., & Ostriker, E. C. 2007, *ARA&A*, 45, 565

- McKee, C. F., & Tan, J. C. 2002, *Nature*, 416, 59  
— 2003, *ApJ*, 585, 850
- Menten, K. M. 1991, *ApJ*, 380, L75
- Mezger, P. G., & Henderson, A. P. 1967, *ApJ*, 147, 471
- Millar, T. J., MacDonald, G. H., & Gibb, A. G. 1997, *A&A*, 325, 1163
- Minier, V., Ellingsen, S. P., Norris, R. P., & Booth, R. S. 2003, *A&A*, 403, 1095
- Miralles, M. P., Rodriguez, L. F., & Scalise, E. 1994, *ApJS*, 92, 173
- Mookerjea, B., Casper, E., Mundy, L. G., & Looney, L. W. 2007, *ApJ*, 659, 447
- Motte, F., Schilke, P., & Lis, D. C. 2003, *ApJ*, 582, 277
- Müller, H. S. P., Schlöder, F., Stutzki, J., & Winnewisser, G. 2005, *Journal of Molecular Structure*, 742, 215
- Müller, H. S. P., Thorwirth, S., Roth, D. A., & Winnewisser, G. 2001, *A&A*, 370, L49
- Nakano, T., Hasegawa, T., Morino, J.-I., & Yamashita, T. 2000, *ApJ*, 534, 976
- Nomura, H., & Millar, T. J. 2004, *A&A*, 414, 409
- Noriega-Crespo, A., Moro-Martin, A., Carey, S., et al. 2004, *ApJS*, 154, 402
- Nummelin, A., Bergman, P., Hjalmarsen, Å., et al. 2000, *ApJS*, 128, 213
- Ohishi, M., & Kaifu, N. 1998, *Faraday Discussions*, 109, 205
- Olmi, L., Cesaroni, R., & Walmsley, C. M. 1993, *A&A*, 276, 489  
— 1996, *A&A*, 307, 599
- Osorio, M., Anglada, G., Lizano, S., & D'Alessio, P. 2009, *ApJ*, 694, 29
- Osorio, M., Lizano, S., & D'Alessio, P. 1999, *ApJ*, 525, 808
- Ossenkopf, V., & Henning, T. 1994, *A&A*, 291, 943
- Palla, F., Brand, J., Comoretto, G., Felli, M., & Cesaroni, R. 1991, *A&A*, 246, 249
- Palla, F., Cesaroni, R., Brand, J., et al. 1993, *A&A*, 280, 599
- Pandian, J. D., Momjian, E., & Goldsmith, P. F. 2008, *A&A*, 486, 191
- Pankonin, V., Churchwell, E., Watson, C., & Bieging, J. H. 2001, *ApJ*, 558, 194
- Perault, M., Omont, A., Simon, G., et al. 1996, *A&A*, 315, L165
- Pickett, H. M., Poynter, R. L., Cohen, E. A., et al. 1998, *JQSRT*, 60, 883
- Pillai, T., Wyrowski, F., Carey, S. J., & Menten, K. M. 2006, *A&A*, 450, 569
- Polushkin, S. V., & Val'Tts, I. E. 2011, *Astronomy Reports*, 55, 445
- Pratap, P., Batrla, W., & Snyder, L. E. 1989, *ApJ*, 341, 832
- Purcell, C. R., Balasubramanyam, R., Burton, M. G., et al. 2006, *MNRAS*, 367, 553
- Purcell, C. R., Hoare, M. G., Cotton, W. D., et al. 2013, *ApJS*, 205, 1
- Qin, S.-L., Huang, M., Wu, Y., Xue, R., & Chen, S. 2008, *ApJ*, 686, L21



- Qin, S.-L., Wu, Y., Huang, M., et al. 2010, *ApJ*, 711, 399
- Ragan, S. E., Bergin, E. A., & Gutermuth, R. A. 2009, *ApJ*, 698, 324
- Ragan, S. E., Bergin, E. A., Plume, R., et al. 2006, *ApJS*, 166, 567
- Ragan, S. E., Henning, T., & Beuther, H. 2013, *A&A*, 559, A79
- Rathborne, J. M., Garay, G., Jackson, J. M., et al. 2011, *ApJ*, 741, 120
- Rathborne, J. M., Jackson, J. M., Chambers, E. T., et al. 2005, *ApJ*, 630, L181
- Rathborne, J. M., Jackson, J. M., & Simon, R. 2006, *ApJ*, 641, 389
- Rathborne, J. M., Jackson, J. M., Simon, R., & Zhang, Q. 2009, *Ap&SS*, 324, 155
- Rathborne, J. M., Jackson, J. M., Zhang, Q., & Simon, R. 2008, *ApJ*, 689, 1141
- Rathborne, J. M., Simon, R., & Jackson, J. M. 2007, *ApJ*, 662, 1082
- Reid, M. J., Menten, K. M., Zheng, X. W., et al. 2009, *ApJ*, 700, 137
- Reid, M. J., Menten, K. M., Brunthaler, A., et al. 2014, *ArXiv e-prints*, arXiv:1401.5377
- Remijan, A., Shiao, Y.-S., Friedel, D. N., Meier, D. S., & Snyder, L. E. 2004a, *ApJ*, 617, 384
- Remijan, A., Sutton, E. C., Snyder, L. E., et al. 2004b, *ApJ*, 606, 917
- Rodgers, S. D., & Charnley, S. B. 2001, *ApJ*, 546, 324
- Rodríguez, L. F., Moran, J. M., Franco-Hernández, R., et al. 2008, *AJ*, 135, 2370
- Rolffs, R., Schilke, P., Zhang, Q., & Zapata, L. 2011, *A&A*, 536, A33
- Sakai, T., Sakai, N., Kamegai, K., et al. 2008, *ApJ*, 678, 1049
- Sandell, G., & Wright, M. 2010, *ApJ*, 715, 919
- Sanhueza, P., Garay, G., Bronfman, L., et al. 2010, *ApJ*, 715, 18
- Sanna, A., Moscadelli, L., Cesaroni, R., et al. 2010, *A&A*, 517, A78
- Schilke, P., Phillips, T. G., & Mehringer, D. M. 1999, in *The Physics and Chemistry of the Interstellar Medium*, ed. V. Ossenkopf, J. Stutzki, & G. Winnewisser, 330
- Shi, H., Zhao, J.-H., & Han, J. L. 2010, *ApJ*, 710, 843
- Shu, F. H., Adams, F. C., & Lizano, S. 1987, *ARA&A*, 25, 23
- Simon, R., Rathborne, J. M., Shah, R. Y., Jackson, J. M., & Chambers, E. T. 2006, *ApJ*, 653, 1325
- Slysh, V. I., Kalenskii, S. V., & Val'tts, I. E. 1995, *ApJ*, 442, 668
- Snell, R. L., Dickman, R. L., & Huang, Y.-L. 1990, *ApJ*, 352, 139
- Sobolev, A. M., Cragg, D. M., & Godfrey, P. D. 1997, *MNRAS*, 288, L39
- Sollins, P. K., & Ho, P. T. P. 2005, *ApJ*, 630, 987
- Sollins, P. K., Zhang, Q., Keto, E., & Ho, P. T. P. 2005a, *ApJ*, 631, 399

- . 2005b, *ApJ*, 624, L49
- Sollins, P. K., Hunter, T. R., Battat, J., et al. 2004, *ApJ*, 616, L35
- Solomon, P. M., Jefferts, K. B., Penzias, A. A., & Wilson, R. W. 1971, *ApJ*, 168, L107
- Sridharan, T. K., Beuther, H., Schilke, P., Menten, K. M., & Wyrowski, F. 2002, *ApJ*, 566, 931
- Sridharan, T. K., Williams, S. J., & Fuller, G. A. 2005, *ApJ*, 631, L73
- Su, Y.-N., Liu, S.-Y., Wang, K.-S., Chen, Y.-H., & Chen, H.-R. 2009, *ApJ*, 704, L5
- Sutton, E. C., Sobolev, A. M., Ellingsen, S. P., et al. 2001, *ApJ*, 554, 173
- Swings, P., & Rosenfeld, L. 1937, *ApJ*, 86, 483
- Torrelles, J. M., Ho, P. T. P., Rodriguez, L. F., & Canto, J. 1985, *ApJ*, 288, 595
- . 1986, *ApJ*, 305, 721
- Turner, B. E. 1991, *ApJS*, 76, 617
- Ungerechts, H., Winnewisser, G., & Walmsley, C. M. 1986, *A&A*, 157, 207
- Val'tts, I. E., Dzura, A. M., Kalenskii, S. V., et al. 1995, *A&A*, 294, 825
- Val'tts, I. E., Ellingsen, S. P., Slysh, V. I., et al. 1999, *MNRAS*, 310, 1077
- van der Tak, F. F. S., van Dishoeck, E. F., & Caselli, P. 2000, *A&A*, 361, 327
- Viti, S., Collings, M. P., Dever, J. W., McCoustra, M. R. S., & Williams, D. A. 2004, *MNRAS*, 354, 1141
- Wakelam, V., Caselli, P., Ceccarelli, C., Herbst, E., & Castets, A. 2004, *A&A*, 422, 159
- Walmsley, C. M., Baudry, A., Guilloteau, S., & Winnberg, A. 1986, *A&A*, 167, 151
- Walmsley, C. M., Cesaroni, R., Olmi, L., Churchwell, E., & Hofner, P. 1995, *Ap&SS*, 224, 173
- Walsh, A. J., Burton, M. G., Hyland, A. R., & Robinson, G. 1998, *MNRAS*, 301, 640
- Walsh, A. J., Hyland, A. R., Robinson, G., & Burton, M. G. 1997, *MNRAS*, 291, 261
- Wang, K.-S., Kuan, Y.-J., Liu, S.-Y., & Charnley, S. B. 2010, *ApJ*, 713, 1192
- Wang, Y., Zhang, Q., Pillai, T., Wyrowski, F., & Wu, Y. 2008, *ApJ*, 672, L33
- Wang, Y., Zhang, Q., Rathborne, J. M., Jackson, J., & Wu, Y. 2006, *ApJ*, 651, L125
- Ward-Thompson, D., Scott, P. F., Hills, R. E., & Andre, P. 1994, *MNRAS*, 268, 276
- Williams, J. P., Aguirre, J., Bally, J., et al. 2007, in *Bulletin of the American Astronomical Society*, Vol. 39, American Astronomical Society Meeting Abstracts #210, 110
- Wilner, D. J., De Pree, C. G., Welch, W. J., & Goss, W. M. 2001, *ApJ*, 550, L81
- Wilner, D. J., Welch, W. J., & Forster, J. R. 1995, *ApJ*, 449, L73+

- Wilner, D. J., Wright, M. C. H., & Plambeck, R. L. 1994, *ApJ*, 422, 642
- Wilson, T. L., & Walmsley, C. M. 1989, *A&A Rev.*, 1, 141
- Wilson, T. L., Walmsley, C. M., Jewell, P. R., & Snyder, L. E. 1984, *A&A*, 134, L7
- Wilson, T. L., Walmsley, C. M., Menten, K. M., & Hermsen, W. 1985, *A&A*, 147, L19
- Wink, J. E., Duvert, G., Guilloteau, S., et al. 1994, *A&A*, 281, 505
- Wolfire, M. G., & Cassinelli, J. P. 1987, *ApJ*, 319, 850
- Wood, D. O. S., & Churchwell, E. 1989a, *ApJ*, 340, 265
- . 1989b, *ApJS*, 69, 831
- Wright, M. C. H., Plambeck, R. L., & Wilner, D. J. 1996, *ApJ*, 469, 216
- Wu, Y. W., Xu, Y., Pandian, J. D., et al. 2010, *ApJ*, 720, 392
- Wyrowski, F., Schilke, P., & Walmsley, C. M. 1999a, *A&A*, 341, 882
- Wyrowski, F., Schilke, P., Walmsley, C. M., & Menten, K. M. 1999b, *ApJ*, 514, L43
- Yorke, H. W., & Sonnhalter, C. 2002, *ApJ*, 569, 846
- Zapata, L. A., Ho, P. T. P., Rodríguez, L. F., Schilke, P., & Kurtz, S. 2007, *A&A*, 471, L59
- Zapata, L. A., Ho, P. T. P., Schilke, P., et al. 2009a, *ApJ*, 698, 1422
- Zapata, L. A., Leurini, S., Menten, K. M., et al. 2008a, *AJ*, 136, 1455
- Zapata, L. A., Palau, A., Ho, P. T. P., et al. 2008b, *A&A*, 479, L25
- Zapata, L. A., Rodríguez, L. F., Ho, P. T. P., Beuther, H., & Zhang, Q. 2006, *AJ*, 131, 939
- Zapata, L. A., Schmid-Burgk, J., Ho, P. T. P., Rodríguez, L. F., & Menten, K. M. 2009b, *ApJ*, 704, L45
- Zapata, L. A., Schmid-Burgk, J., & Menten, K. M. 2011, *A&A*, 529, A24
- Zapata, L. A., Tang, Y.-W., & Leurini, S. 2010, *ApJ*, 725, 1091
- Zhang, Q., & Ho, P. T. P. 1995, *ApJ*, 450, L63
- . 1997, *ApJ*, 488, 241
- Zhang, Q., Ho, P. T. P., & Ohashi, N. 1998a, *ApJ*, 494, 636
- Zhang, Q., Hunter, T. R., Beuther, H., et al. 2007a, *ApJ*, 658, 1152
- Zhang, Q., Hunter, T. R., & Sridharan, T. K. 1998b, *ApJ*, 505, L151
- Zhang, Q., Sridharan, T. K., Hunter, T. R., et al. 2007b, *A&A*, 470, 269
- Zhang, Q., Wang, Y., Pillai, T., & Rathborne, J. 2009, *ApJ*, 696, 268
- Zinchenko, I., Henkel, C., & Mao, R. Q. 2000, *A&A*, 361, 1079
- Zinchenko, I., Henning, T., & Schreyer, K. 1997, *A&AS*, 124, 385
- Zinnecker, H., & Yorke, H. W. 2007, *ARA&A*, 45, 481